Dissertation zur Erlangung des Doktorgrades
der Fakultät für Chemie und Pharmazie
der Ludwig-Maximilians-Universität München

Structural and Biochemical Characterization of

Ciliary Targeting Complexes

Reveals a Novel Dual Effector Bound Mechanism

for the Rab11:GTP - FIP3 - Rabin8 Module

Melanie Anja Vetter

aus

Ludwigsburg, Deutschland

2016

"If you're not failing every now and again, it's a sign you're not doing anything very innovative."

- Woody Allen -

Dedicated to my beloved Mum, Dad and Grandma.

Table of Content

Summary

Eukaryotic cells possess a characteristic organization into several compartments, which enable efficient separation of various cellular functions. One such compartment is the cilium, a versatile organelle, which can be described as a hair-like projection, found on nearly all cells in the human body. Cilia serve important functions including motility and sensory reception and are required for normal organismic development and tissue homeostasis. Defects in cilium formation or function are linked to an increasing number of human disorders, which are now commonly referred to as ciliopathies with phenotypes that include retinal degeneration, kidney failure, cerebral anomalies and many more. To perform their diverse functions, cilia possess a unique protein and lipid composition distinct from that of the plasma membrane. However, given that cilia are devoid of ribosomes, both soluble and membrane proteins important for ciliary assembly and function have to be synthesized elsewhere in the cell, selectively recruited and transported to the cilium. Small GTPases of the Arf and Rab family regulate multiple steps of intracellular membrane trafficking events including transport of membrane proteins from the Golgi to the cilium. At least three macromolecular complexes have been implicated in ciliary targeting, which are controlled by small GTPases: IFT complex, the BBSome and the Arf4-based ciliary targeting complex. Upon cargo binding the Arf4-based ciliary targeting complex assembles at the trans-Golgi network (TGN) and regulates the first stages of ciliary targeting that include sorting and packaging of ciliary membrane proteins. Subsequently members of the conserved ciliogenesis cascade are recruited to the TGN to form a ciliary targeting module, which enables delivery of cargo-associated vesicles to the base of the cilium. Although, some progress has been made regarding identification and characterization of putative ciliary cargo and key players implicated in ciliary targeting of membrane proteins, the molecular basis for selection and packaging of ciliary cargo, the high resolution-architecture of ciliary targeting complexes and the underlying regulatory mechanisms remain elusive. My doctorial thesis mainly investigates the biochemical and structural properties of complexes implicated in ciliary targeting.

The small GTPase Rab11 binds to several effector proteins including Rabin8 and FIP3, which are essential for ciliary membrane trafficking pathways. Whereas interaction of active Rab11 to the Rabin8 C-terminal domain was demonstrated in pull-down experiments, complex reconstitution attempts using size-exclusion

chromatography (SEC) did not result in stable complex formation, suggesting a low affinity interaction. Despite low affinity, nevertheless crystals were obtained, when mixing the two proteins in high concentrations. Solving the crystal structure of the human Rab11-Rabin8 complex at 2.6 Å resolution by molecular replacement revealed that the Rabin8 C-terminal domain adopts a previously undescribed fold, which interacts with Rab11 at an unusual effector binding site to form heterotetramers. The small and unusual Rabin8 effector binding surface on Rab11, utilizing only two residues of the switch I region and four residues of a non-switch-region loop not only explains the weak affinity of Rabin8 towards Rab11 but would, in principle, allow for simultaneous binding of a different effector such as FIP3 at the canonical effector-binding site of Rab11. Indeed, pull-down and size exclusion experiments demonstrated that both FIP3 and Rabin8 effectors associate with Rab11 at the same time. In addition, dissociation constant (K_D) determination by Isothermal titration calorimetry (ITC) revealed that the Rab11-effector domain of Rabin8 binds a preformed Rab11-FIP3 complex with a four-fold higher affinity than Rab11 alone, which is likely a result of direct contacts of the two effectors. To elucidate the molecular basis of how the two effectors Rabin8 and FIP3 bind Rab11 simultaneously, the crystal structure of Rab11 in complex with the Rab11-binding domain of FIP3 and the C-terminal Rabin8 domain at 3.0 Å resolution was determined. Formation of the dual effector bound complex is facilitated through neighboring recognition sites at the switch regions of Rab11 and conformational changes of the subunits. Analysis of the crystal structure, SEC and small-angle X-ray scattering (SAXS) experiments revealed that the Rab11-FIP3-Rabin8 complex exists in a concentration-dependent equilibrium between different oligomeric states ranging from heterohexamer (2:2:2) to larger dodecameric assemblies *in vitro.*

Taken together, my doctorial thesis provides a structural and biochemical characterization of two human ciliary targeting complexes and unravels a novel regulatory mechanism of dual effector binding by the Rab11 GTPase, which might not only result in higher stabilized ciliary targeting complexes, but may also be utilized by other small GTPases of the Arf and Rab family to control distinct membrane trafficking pathways.

Preface

The work presented in this doctorial thesis was performed in the laboratory of Dr. Esben Lorentzen at the Max Planck Institute of Biochemistry in Martinsried. This study has led to several publications including one review that will be presented in a cumulative manner.

Preceding the result section, chapter 1 gives a detailed introduction into the biological background, attempting to take into account the current state of the research. The topics that will be addressed include a structural and function description of eukaryotic cilia, deals with important underlying mechanisms of ciliary cargo transport and introduces key players that are required for proper cilia function, which in turn is essential for human health.

The result section (chapter 2) comprises three original and published manuscripts, which present distinct, but related projects that have been divided into three subchapters. The first manuscript (subchapter 2.1) presents the key findings of this thesis, providing structural insights into ciliary targeting complex assemblies and elucidates underlying mechanisms. The manuscript was published as a research article in the journal *Nature Structure and Molecular Biology* with the title: 'Structure of Rab11–FIP3–Rabin8 reveals simultaneous binding of FIP3 and Rabin8 effectors to Rab11'.

The second subchapter (2.2) describes a project on the structural characterization of the human α-tubulin acetyltransferase and provides mechanistic insights into lysine 40 acetylation of α-tubulin. The enzyme has a conserved role in several microtubule-based processes including cilia formation. The resulting manuscript with the title: 'Atomic resolution structure of human α-tubulin acetyltransferase bound to acetyl-CoA' was published as an article in the journal *Proceedings of the National Academy of Sciences, USA*. My colleague Dr. Michael Taschner was lead author and I contributed as a second author.

In subchapter 2.3 a study is presented, which was initiated from a team of investigators of an international consortium led by the Michael J. Fox Foundation for Parkinson's Research and has been published as an article in the journal *elife* with the title: 'Phosphoproteomics reveals that Parkinson's disease kinase LRRK2 regulates a subset of Rab GTPases'. The study identified a group of Rab GTPases as key targets of the Leucine-rich repeat kinase 2 (LRRK2) and unravels a new Rab regulatory mechanism. These findings link Rab GTPases, master regulators of intracellular transport including ciliary membrane trafficking, to Parkinson's disease, a

human degenerative disorder. I contributed to this project and have been listed as a co-author. Subchapters 2.2 - 2.3 are introduced with a short summary.

I contributed as a co-author to two additional studies with the titles: 'Biochemical mapping of interactions within the intraflagellar transport protein (IFT) B core complex: IFT52 binds directly to four other IFT-B subunits' and 'Intraflagellar transport proteins 172, 80, 57, 54, 38, and 20 form a stable tubulin-binding IFT-B2 complex' published as an article in the *Journal of Biological Chemistry* and in the *EMBO journal*, respectively. The two manuscripts present an updated architectural map as well as a structural and biochemical characterization of the IFT-B subcomplex, which is required for a transport process essential for cilia assembly and maintenance. Since contributed results are already partially covered in my diploma thesis, the two studies are not presented in the result sections.

Chapter 3 features an extended discussion that examines insights gained from the publication of my main PhD project (2.1). Major parts of the discussion have been published as a review in the Journal *Small GTPases* with the title: 'Novel topography of the Rab11-effector interaction network within a ciliary membrane targeting complex'.

A brief outlook is presented in chapter 4, which aims to provide potential future directions and long-term perspectives based on insights gained from this study and the current state of knowledge. Open questions will be formulated, giving rise to further investigation and research.

List of Publications and Contributions

1) **Vetter, M.,** Stehle, R., Basquin, C. & Lorentzen, E. (2015). Structure of Rab11–FIP3–Rabin8 reveals simultaneous binding of FIP3 and Rabin8 effectors to Rab11. *Nature Structural and Molecular Biology* (22(09), pages 695-702).

M.V. carried out all the protein biochemistry and the structural biology. M.V. and E.L. wrote the paper with input form R.S. and C.B.

2) **Vetter, M.,** Wang, J., Lorentzen, E., & Deretic, D. (2015). Novel topography of the Rab11-effector interaction network within a ciliary membrane targeting complex. *Small GTPases* (6(4), pages 165-173). (Review).

3) Taschner, M., **Vetter, M.**, & Lorentzen, E. (2012). Atomic resolution structure of human α-tubulin acetyltransferase bound to acetyl-CoA. *Proc Natl Acad Sci USA* (109(48), pages 19649–19654).

M.V. cloned and purified various αTAT1 mutants. She purified and solved the crystal structure of the Q58A mutant and was involved in analyzing data.

4) Taschner, M., Bhogaraju, S., **Vetter, M.,** Morawetz, M. & Lorentzen E. (2011). Biochemical mapping of interactions within the intraflagellar transport protein (IFT) B core complex: IFT52 binds directly to four other IFT-B subunits. *J Biol Chem*. (286(30), pages 26344-26352).

M.V. cloned and purified an N-terminal IFT52 construct that was subjected to functional analysis including a glycan microarray screen.

5) Taschner, M., Weber, K., Mourão, A**., Vetter, M.,** Awasthi, M., Stiegler M., Bhogaraju, S. & Lorentzen E. (2016). Intraflagellar transport proteins 172, 80, 57, 54, 38, and 20 form a stable tubulin-binding IFT-B2 complex. *EMBO journal* (10.15252/embj.201593164).

M.V. helped with purification and crystal structure determination of the IFT52 N-terminal domain.

6) Steger, M., Tonelli, F., Ito, G., Davies, P., Trost, M., **Vetter, M.,** Wachter, S., Lorentzen, E., Duddy, G., Wilson, S., Baptista, M., Fiske, B., Fell, M., Morrow, J., Reith, A., Alessi, D., Mann, M. (2016). Phosphoproteomics reveals that Parkinson's disease kinase LRRK2 regulates a subset of Rab GTPases. *eLife* ((5), e12813).

M.V. cloned, purified and provided human WT and mutant Rab8 proteins as well as human Rabin8 constructs. She separated and enriched phosphorylated Rab8 confirmed by ESI-TOF MS (Fig. 5 – figure supplement 2E). M.V. performed guanine-nucleotide exchange (GEF) assays (Fig. 5D) and provided Ni^{2+}-NTA Rabin8 pull-down samples (Fig. 5 – figure supplement 2G). M.V. discussed the results, analyzed and interpreted the contributed data.

1   Introduction

1.1   Compartmentalization of eukaryotic cells

A hallmark of eukaryotes is their complex and extensive intracellular compartmentalization. In contrast to prokaryotes, the cytoplasm of a common eukaryotic cell contains a variety of membrane-enclosed organelles including the endoplasmic reticulum (ER), the Golgi apparatus, the nucleus, mitochondria, endosomes and lysosomes. Approximately half of the volume of an eukaryotic cell is compartmentalized via selectively permeable membranes (Alberts *et al.*, 2002). This characteristic organization into membrane-enclosed compartments or organelles provides a lot of benefits to the cell. It enables efficient separation of cellular processes such as degradation of cellular debris in lysosomes or calcium storage in the ER, permitting the coexistence of multiple biochemical environments within the same cell. It does, however, at the same time introduce a major challenge for these organisms. The complexity of compartmentalization requires a versatile intracellular membrane trafficking system that not only enables communication of the cell with its environment but also the exchange of material between the various membrane-enclosed organelles. Malfunctioning of cellular organelles such as lysosomes and mitochondria are well-known causes of human disease (Taylor and Turnbull, 2005; Duchen and Szabadkai, 2010; Settembre *et al.*, 2013). Hence, a complex network of interconnected intracellular trafficking pathways, an active transport machinery, and a molecular surveillance mechanism are crucial for normal tissue and organ function. Besides extensive research on well-studied organelles such as lysosomes, research into a less-well known organelle termed the cilium has undergone a renaissance over the past decade. Reasons for this development and implications of cilia for eukaryotes, in particular humans are further described in the following sections.

1.2   The cilium – a versatile eukaryotic organelle

Cilia or flagella (interchangeable terms) are hair-like cellular organelles that protrude from the surface of most eukaryotic organisms and cell types. They are ancient evolutionarily conserved structures present in unicellular organisms such as the green algae *Chlamydomonas reinhardtii* as well as in higher metazoans including humans where they are found on the surface of almost all cells (Fig. 1). However,

cilia are absent in some plants (e.g. *Arabidopsis thaliana*) and in fungi (e.g. *Saccharomyces cerevisiae*) (Raven *et al.*, 1999). The appearance of cilia on different cell types varies a lot regarding shape and morphology. Furthermore, the number of cilia on a given cell can range from one to thousands (Fig. 1e). Besides diversity in their appearance, cilia perform a wide range of functions. The first described and most prominent function of cilia is locomotion. In addition, non-motile cilia, which usually occur as a single copy on a large number of different human cells and typically referred to as "primary cilia" were already discovered a century ago. However, primary cilia did not receive a lot of attention, because no obvious function could be assigned to them. Thus, for a long time primary cilia were regarded as evolutionary remnants much like the appendix. This view changed, when it was discovered that non-motile/primary cilia are involved in sensory reception including chemosensation or mechanosensation and play important roles in various signaling pathways (Huangfu *et al.*, 2003; Dabdoub and Kelley, 2005; Hirokawa *et al.*, 2006; Fliegauf *et al.*, 2007; Satir and Christensen, 2007; Gerdes *et al.*, 2009). Hence, defects in cilium formation or function are linked to an increasing number of human disorders, which are now commonly referred to as ciliopathies with phenotypes that include retinal degeneration, kidney failure, infertility and many more (Badano *et al.*, 2006; Waters and Beales, 2011). Taken together, these facts make the cilium a versatile organelle that after decades of relative disregard has emerged at the center of interest and intense research.
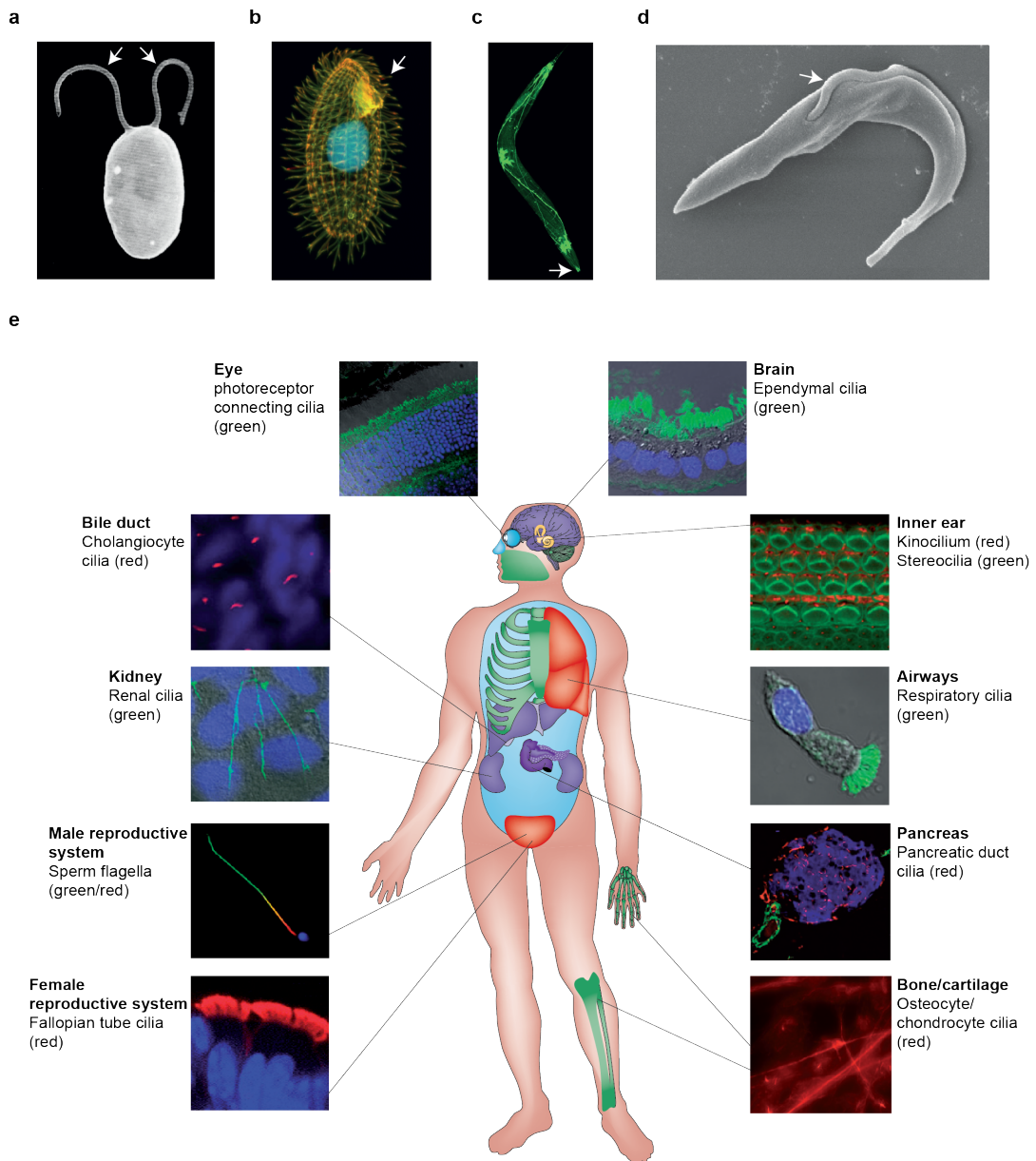
Figure 1: Cilia are present in most eukaryotic organisms ranging from single-celled organisms up to humans. *(a-d) White arrows point at cilia found in various eukaryotes. a) Scanning electron micrograph (SEM) of two flagella that extend from a Chlamydomonas cell is depicted. b) The surface of the single-celled organism Tetrahymena thermophila is covered with rows of cilia. c) The nervous system including the sensory cilia located in the head region of Caenorhabditis elegans are illuminated with GFP. d) SEM shows the procyclic pathogen Trypanosoma brucei containing a single flagellum that is attached along the cell body. e) A graphical illustration of a human body showing diverse organs that contain cilia. Strokes connecting the ciliated organs with panels of indirect immunofluorescence stained cilia using an antibody. Ciliary axonemes are stained in red or green respectively. Nuclei are stained using Hoechst or DAPI (4',6-diamidino-2-phenylindole). SEM shown in a) is obtained from (Rosenbaum and Witman, 2002), b) from (Robinson, 2006), c) from (Scholey, 2012) and d) from (Ralston and Hill, 2008). The graphical illustration of the human body (e) is modified from (Goetz and Anderson, 2010). All panels and their descriptions presented in e) originate from (Fliegauf et al., 2007).*

1.2.1 Structure of the cilium

Despite diverse morphologies of cilia, they all share a remarkably similar and highly ordered basic architecture. Cilia nucleate from a centriole-derived basal body onto which a microtubule cytoskeleton, the axoneme, is built, surrounded by a ciliary membrane (Fig. 2). A detailed analysis of the structural elements of the cilium and their potential functional roles are described in the following sections.

Figure 2: Structure of eukaryotic cilia. *a) Transmission electron micrograph (TEM) of a primary cilium in retinal pigment epithelial (RPE) cells. Several elements of the ciliary ultrastructure are labelled with arrows. BB, basal body; CiPo, ciliary pocket; Ax, axoneme. b) Immunofluorescence image of primary cilia of inner medullary collecting duct cells. Primary cilia (green), which extend from the basal body (magenta), are present in only one copy per cell). c) & d) SEMs of mouse nodal motile monocilia (c) and mouse tracheal motil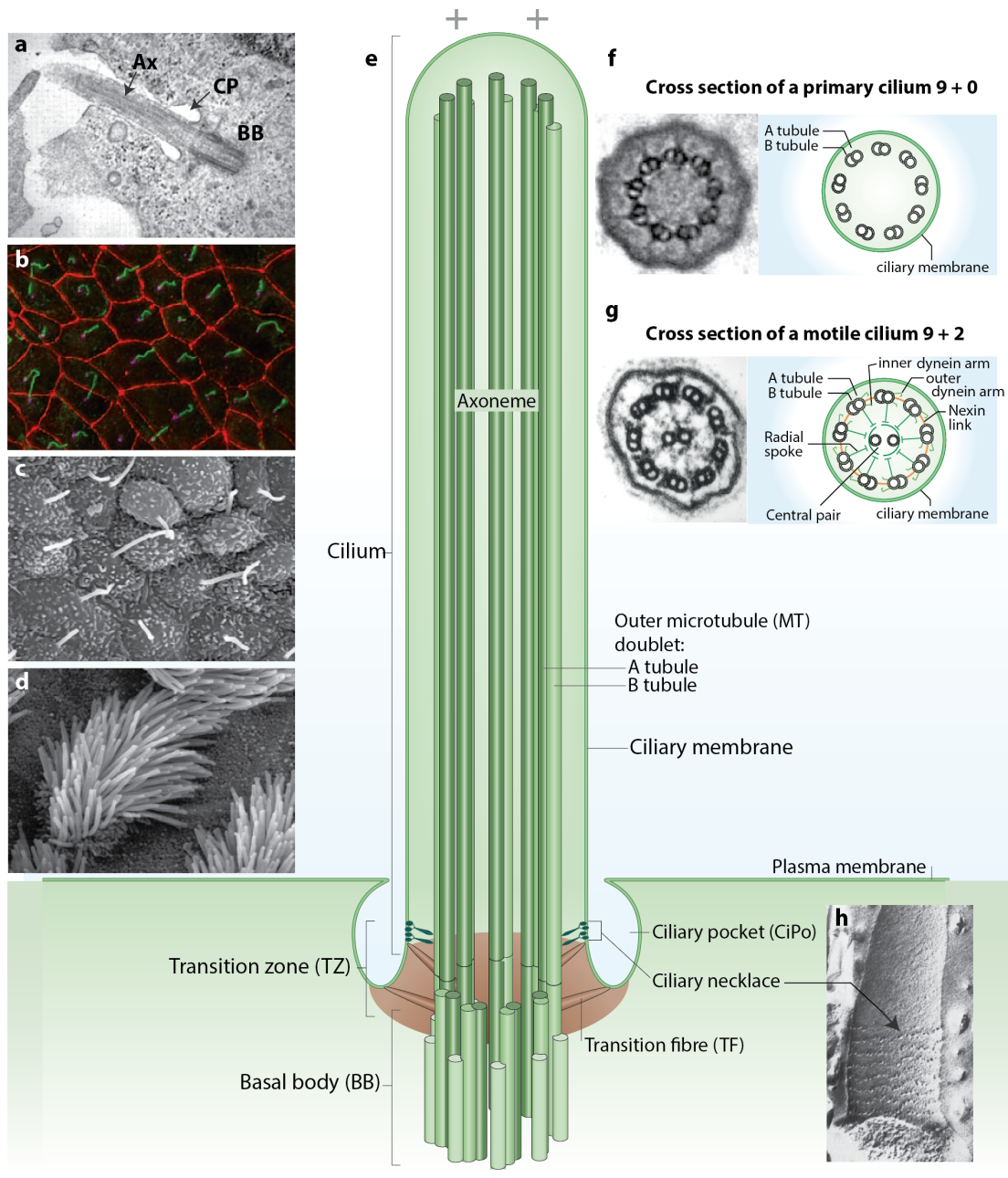e cilia (d). e) Schematic illustration of a cilium. Different structural elements are labelled. f) (Right) Cross-section of a conventional non-motile cilium with a 9+0 axoneme. (Left) TEM of a human oviduct cilium, which lacks the central pair of singlet microtubules (MTs). g) (Right) Cross-section of a conventional motile cilium with a 9+2 axoneme, which possesses additional structural elements required for ciliary movement and beat regulation. (Left) EM of a Chlamydomonas flagellum axoneme that contains a central pair of MTs. h) Freeze-fracture SEM of a hamster respiratory cilium, which shows the ciliary necklace as bead-like, ring forming particles on the membrane (arrow points to one of the membrane particles). TEM in a), image in b), SEMs in c) and d), graphical illustrations in e), f) and g) are adopted from (Ishikawa & Marshall, 2011). TEM in f) is taken from (Reiter et al., 2012) and TEM in g) from (Rosenbaum and Witman, 2002). Graph in h) is obtained from (Reiter et al., 2012).*

1.2.1.1 The ciliary axoneme – structural core of the cilium

The axoneme constitutes the structural core of the cilium to which it owes its cylindrical appearance. It is formed by two major patterns both composed of a radial array of nine doublet microtubules (MTs) either with or without a central pair of singlet microtubules, referred to as 9+2 or 9+0 arrangement, respectively (Figs. 2f,g) (Satir and Christensen, 2007). Conventionally, the 9+0 arrangement is associated with non-motile cilia, which are also missing the molecular dynein motors required for ciliary beat. Examples in humans are, among others, non-motile cilia found on epithelial cells, such as those of the kidney tubule, the bile duct and the endocrine pancreas as well as the connecting cilium of photoreceptor cells (Figs. 1e, 2b) (Fliegauf *et al.*, 2007). One exception represents the motile 9+0 cilium on nodal cells of developing mammalian embryos, which lacks the central pair of MTs, but possesses molecular dynein motors to generate a ciliary beat (Hirokawa *et al.*, 2006). This ciliary beat creates a directional flow, which is required for establishment of left-right asymmetry (Hirokawa *et al.*, 2006). In contrast, 9+2 cilia are usually motile and possess in addition to their two extra MTs in the center, molecular complexes such as the inner and outer dynein arms (IDAs and ODAs), radial spokes and nexin links (Fig. 2g) (Gibbons and Rowe, 1965; Lindemann and Lesich, 2010). Ciliary movement and beat regulation is enabled by the interplay of MT-attached dynein arms, nexin links, which connect the MT doublets and radial spokes that project from each outer doublet towards the central pair to hold them in place (Satir and Christensen, 2007). Motile cilia are present in large numbers on the epithelial cell surface of the trachea

and the oviduct (Figs. 1e, 2d). Non-motile 9+2 kinocilia are found on hair cells of the inner ear (Fig. 1e) (Dabdoub and Kelley, 2005) constituting an exception to the conventional distinction.

1.2.1.2   The basal body and the transition zone – ciliary ground floor

All cilia arise from a basal body (BB) derived from the mother centriole. The basal body serves as MT-organization center just beneath the cell membrane and is used as a template from which the ciliary axoneme extends (Sorokin, 1968; Beisson and Wright, 2003). A ring of nine MT-triplets, designated A, B, and C tubules with respect to increasing distance from the center is a typical characteristic of the BB. Conversion of the triplet microtubular structure of the basal body into the axonemal doublet structure is achieved in the transition zone (TZ) (Fig. 2e). The TZ is further composed of Y-shaped linkers, that span from the axoneme to the ciliary membrane, transitional fibers (TFs) and the ciliary necklace (see 1.2.1.3 The ciliary necklace) (Gilula and Satir, 1972; Robinson, 2006; Satir and Christensen, 2007; Reiter *et al.*, 2012). TFs represent features of both, the TZ and the basal body. They anchor the BB to the proximal region of the ciliary membrane and contact the TZ, which result in a pinwheel-like structure. Thus, TFs, also referred to as alar sheets, demarcate the boundary between the cytoplasmic and the ciliary compartment (Anderson, 1972). Together, TFs and structures of the TZ region are proposed to function as a 'ciliary gate', which regulates entry to the ciliary compartment (1.3.1 The ciliary gate) (Reiter *et al.*, 2012).

1.2.1.3   The ciliary necklace – a ciliary membrane specialization

The ciliary necklace is located distal to the transition fibers and was visualized by freeze-fracture electron microscopy as multiple rows of intramembranous protein particles (Gilula and Satir, 1972). The ciliary necklace particles can be further described as a circumferential strand of intramembranous 'decorations', which line the edges of the ciliary membrane. Cup-like structures link these particles to the center of each basal body doublet at the transition zone below the origin of the axoneme, together forming the ciliary necklace (Figs. 2e,h). This specialized feature is found on all mammalian and invertebrate cilia but not universally present on sperm cells (Gilula and Satir, 1972). Proteins, which are involved in ciliary cargo transport have been localized to the ciliary necklace implying that this domain apart from TFs

and structures of the TZ represents a specialized zone for assembly and controlled insertion of ciliary membrane components and axonemal cargos (Deane *et al.*, 2001).

1.2.1.4 The ciliary pocket – a putative endocytic membrane domain

All cilia share a similar architecture containing previously described elements including the axoneme, the basal body and the ciliary membrane. However, the ciliary pocket (CiPo), a structural feature that is found at the root of the cilium, is not ubiquitously present in ciliated organisms (Poole *et al.*, 1985; Molla-Herman *et al.*, 2010). The CiPo can be described as a membrane domain, formed by invagination of the plasma membrane, which encircles the base of the cilium (Figs. 2a,e). The name 'ciliary pocket' is adapted from the flagellar pocket (FP) of trypanosomes due to morphological and functional similarity (Fig. 1d) (Molla-Herman *et al.*, 2010; Benmerah, 2013). Trypanosomes are parasitic protozoans with a high rate of endocytosis and exocytosis, which is important for evasion of the host immune response and for nutrient acquisition (Engstler *et al.*, 2004; Overath and Engstler, 2004; Field and Carrington, 2009). To shield the rest of the cell from the environment, the parasite restricts both endocytosis and exocytosis to the FP (Morgan *et al.*, 2002b; 2002c; Allen *et al.*, 2003; Engstler *et al.*, 2004; Overath and Engstler, 2004).

A similar role for the ciliary pocket in endocytosis and/or exocytosis has been suggested (Overath *et al.*, 1997; Gadelha *et al.*, 2009), which was further strengthens by the findings that the CiPp is enriched with both clathrin-coated pits (CCPs) and vesicles. Thus, the CiPo might function as a specialized endocytic membrane domain and a platform for vesicular trafficking in and out of the cilium (Molla-Herman *et al.*, 2010; Ghossoub *et al.*, 2011; Benmerah, 2013; Clement *et al.*, 2013). However, the CiPo is not an omnipresent feature in ciliated organisms and vesicular trafficking of ciliary cargo also occurs at cilia, which lack the CiPo. Furthermore, interaction of the actin-based cytoskeleton with the CiPo was reported, which likely mediates the position of the cilium (Molla-Herman *et al.*, 2010; Benmerah, 2013). Taken together, the exact role and function of the ciliary pocket still remain to be elucidated.

1.2.1.5 The ciliary membrane – separation of a unique cilia specific protein and lipid composition

The ciliary membrane closely sheathes both the 9+0 and 9+2 ciliary axonemes, usually resulting in a cylindrical shape (Fig. 2). In some special cases the ciliary membrane has different morphologies. For instance, both vertebrate photoreceptor

cells and neurons of *C. elegans* contain specialized cilia. The outer segment (OS) of photoreceptor cells represents an extended tip of a highly modified cilium, which is composed of an elaborated array of photosensitive disc membranes formed into membrane stacks to enable detection of light (Fig. 7a) (Horst *et al.*, 1990). *C. elegans* have ciliary sensory neurons, which are located to their heads. The ciliary membrane at the distal end of these cilia exhibit unusual fork and fan-like specialization (Ward *et al.*, 1975; Perkins *et al.*, 1986; Mukhopadhyay *et al.*, 2008). Even though the ciliary membrane extends from and is continuous with the plasma membrane, this domain possesses a unique set of molecules. This composition includes, but is not limited to specific receptors, ion channels and lipids defining the ciliary membrane as a privileged compartment. A growing interest in ciliary membrane composition arose with the discovery of signaling factors such as polycystin-1/2, which specifically localize to the ciliary compartment (Yoder *et al.*, 2002; Pazour *et al.*, 2002b; Nauli *et al.*, 2003). Enrichment of signaling receptors suggests a pivotal role of cilia in sensory reception and in several signaling pathways important for development and tissue homeostasis. To date, more than 1000 proteins, which function inside the cilium and the ciliary membrane have been identified (Pazour *et al.*, 2005; Gherman *et al.*, 2006). Diverse functions or roles of cilia that can be derived from ciliary protein and lipid composition will be described in detail in the upcoming section.

1.2.2 Diverse functions of cilia make the organelle indispensible for eukaryotes

Cilia, motile and in particular non-motile ones, have been already discovered more than a century ago (van Leeuwenhoek, 1677; Zimmermann, 1898). The role of motile cilia, e.g. in cell locomotion and in the generation of fluid flow over epithelia is well established and defects in ciliary motility are the underlying cause of several human pathologies (Afzelius, 1976; Nonaka *et al.*, 1998; Ibañez-Tallon *et al.*, 2003; Afzelius, 2004; Ibanez-Tallon *et al.*, 2004; Badano *et al.*, 2006). Although, non-motile/primary cilia are present on almost all cells of the human body, they have been considered to be evolutionary remnants that fell into oblivion until last decade (Wheatley *et al.*, 1996). Cilia were brought back into the focus of interest due to the discovery that various important functions in sensory reception and involvement in signaling pathways are carried out by both motile and in particular by immotile primary cilia (Pazour *et al.*, 2000; Yoder *et al.*, 2002; Pazour *et al.*, 2002b; Singla and Reiter, 2006; Christensen *et al.*, 2007; Eggenschwiler and Anderson, 2007; Berbari

et al., 2009). Despite their overall structural similarity, cilia exert various tissue-specific functions during development, tissue morphogenesis and homeostasis. In the following sections a detailed summary of the diverse functions of motile and immotile/primary cilia is presented.

1.2.2.1 Motile functions of cilia

Cellular and organismal locomotion

Cilia appeared early in eukaryotic evolution to provide locomotion for unicellular organisms including many aquatic protozoans. For instance, the green algae *C. reinhardtii* uses its long pair of flagella to move in response to light (phototaxis) and is a widely used model organism to study ciliary assembly and motility (Kozminski *et al.*, 1993; Witman, 1993). A large number of cilia protrude from the external surface of various species like *Paramecium* or *Tetrahymena thermophila* (Fig. 1b) exerting primarily movement, in most cases swimming (Lynn, 2008; Rajagopalan *et al.*, 2008). The mammalian sperm cell (spermatozoon) also contains a single flagellum that is required to propel the cell via successive waves of bending through the female reproductive system (Fig. 1e) (Afzelius and Eliasson, 1982; Fliegauf *et al.*, 2007). Consequently, impaired or defective assembly of the sperm flagellum is a well known cause of male sterility (Afzelius and Eliasson, 1982; Fliegauf *et al.*, 2007).

Generation of fluid flow

Multiple motile cilia are found in the fallopian tubes and the uterine lining of the female reproductive system, required for the transport of the zygote from the ovary to the uterus (Fig. 1e). Dysfunction of motile cilia in the female reproductive system can lead to reduced fertility along with an increased risk of ectopic pregnancy, which, however, occur less frequently than male infertility (Afzelius and Eliasson, 1982; Lyons *et al.*, 2006). Furthermore, the ependymal cells lining the ventricles of the brain carry multiple motile cilia that are essential for circulating cerebrospinal fluid (Fig. 1e) (Ibanez-Tallon *et al.*, 2002). Impaired beating of ependymal cilia can cause hydrocephalus ('water in the brain') and other developmental cerebral abnormalities (Ibanez-Tallon *et al.*, 2004; Banizs *et al.*, 2005). In addition, motile cilia are also very abundant in the airway epithelium (Figs. 1e & 2d), where they constantly beat in coordinated waves thus playing a crucial role in mucus transport and airway clearance (Duchateau *et al.*, 1985).

Primary ciliary dyskinesia (PCD), also known as immotile cilia syndrome, was the first human disease linked to dysfunction of motile cilia (Afzelius, 1976; Eliasson et al., 1977). Characteristic symptoms of the disease are recurrent respiratory tract infections, often combined with male infertility and left-right asymmetry defects, which mainly result from impaired airway, sperm or nodal cilia that are immotile, absent or display abnormal beat pattering (Afzelius, 1976; Munro et al., 1994; van's Gravesande and Omran, 2005). In PCD patients, the most prevalent structural defects, which affect both ciliary beat generation and regulation, involve total or partial absence of outer and inner dynein arms, absence or dislocation of central tubules or defects of radial spokes (Olbrich et al., 2002; Ibañez-Tallon et al., 2003; Satir and Christensen, 2007).

Left-right asymmetry

Monocilia cover the ventral surface of the embryonic node, a cup-like structure, which is found during mammalian embryonic development (Fig. 2c) (Nonaka et al., 1998). These cilia display an ultrastructure with 9+0 axonemes, but are still motile, which can be attributed to the presence of dynein arms (Nonaka et al., 1998). However, absence of the central pair of MTs in nodal cilia results in a clockwise directed unique rotational movement rather than the conventional back-and-forth motion of other 9+2 motile cilia (Chilvers et al., 2003). It is generally assumed that during early embryonic development, the rotational movement of nodal cilia generates a leftward fluid flow or nodal flow, which in turn results in a left-sided release of calcium (Ca^{2+}) that is critical in controlling left-right asymmetry of the viscera (Nonaka et al., 2002; Nauli et al., 2003). First evidence of a functional role of nodal cilia in the correct positioning of visceral organs was provided by a study in which disruption of the intraciliary transport motor Kif3b led to loss of nodal cilia and to randomized left-right asymmetry as a consequence (Nonaka et al., 1998). Hence, impairment of ciliary motility in the embryonic node may cause phenotypes such as *situs solitus, situs inversus totalis* or the less common *situs inversus abdominalis* and *situs inversus thoracalis* whereby vital internal organs such as lungs, heart, stomach and spleen have all or partly inverted positions (Witman, 1993; Ibanez-Tallon et al., 2002; Hornef et al., 2006; Zariwala et al., 2006; Kennedy et al., 2007). Approximately, half of the patients with PCD exhibit *situs inversus totalis*, which together with chronic rhinitis and infertility, was identified as Kartagener syndrome (Afzelius, 1976; Rajagopalan et al., 2008).

1.2.2.2 Sensory functions of cilia

Additional functions of cilia unrelated to motility involve sensing of environmental cues, which have led to the view of cilia as 'signaling antennas' enriched with signaling receptors. It is generally assumed that all cilia, including motile and nonmotile/primary cilia, perform sensory functions.

Mechanosensation

Mechanosensation is one of the key sensory functions of primary cilia. Glomerulus and tubular cells of the kidney carry non-motile (9+0) monocilia that extend into the tubular lumen, being able to sense movement and flow (ANDREWS, 1975; Lynn, 2008). During normal kidney function, urine (mechanical stress) moves along the kidney epithelial cells and induces ciliary bending (Afzelius and Eliasson, 1982; Schwartz *et al.*, 1997; Fliegauf *et al.*, 2007). The functional role of renal cilia in mechanosensation was first described in cultured renal collecting epithelial cells, which showed an increase of intracellular Ca^{2+} upon flow-mediated ciliary bending (Afzelius and Eliasson, 1982; Praetorius and Spring, 2001) (Fig. 3). Cilia, not only in the kidney, but also in other organs, have been recently designated as specialized Ca^{2+} signaling organelles, which are functionally distinct from the cytoplasm (Delling *et al.*, 2013). Furthermore, measurements of ion current revealed that primary cilia contain a six-fold higher Ca^{2+} concentration than found in the cytoplasm under resting conditions (Delling *et al.*, 2013). Polycystin-1 (PC1, Pkd1) and polycystin-2 (PC2, Pkd2), two membrane proteins implicated in the pathogenesis of polycystic kidney disease (PKD), localize to primary cilia of kidney cells and were shown to be required for the described Ca^{2+} influx (Ibanez-Tallon *et al.*, 2002; Pazour *et al.*, 2002b; Nauli *et al.*, 2003; Lyons *et al.*, 2006). Pkd1 and Pkd2 comprise a mechanosensory complex in which PKD1 a transmembrane G protein-coupled receptor (GPCR) (Parnell *et al.*, 2002; Ibanez-Tallon *et al.*, 2004) acts as a flow sensor and transmits the signal from the extracellular fluid environment to the Ca^{2+} interaction channel Pkd2 (Koulen *et al.*, 2002; Nauli *et al.*, 2003; Banizs *et al.*, 2005). DeCaen and colleagues further established the direct interaction of PKD1-L1 (PKD1L1/Pkd1l1) and PKD2-L1 (PKD2L1/Pkd2l1) isoforms, which form a Ca^{2+}-permeable ion channel that initiate ciliary Ca^{2+} transduction (DeCaen *et al.*, 2013). Loss or dysfunction of Pkd1 or Pkd2 interrupts the Ca^{2+} signaling pathway in renal cells, which is required for tissue morphogenesis and normal cell proliferation. Consequently, aberrant intracellular Ca^{2+} allows cyclic AMP (cAMP) activation of the MEK/ERK pathway resulting in

increased cell proliferation, thereby inducing cyst formation and kidney enlargement, which are hallmarks of PKD (Duchateau *et al.*, 1985; Nauli *et al.*, 2003; Nagao *et al.*, 2008). In addition to liver cells, cells in the bile and pancreas also contain non-motile monocilia that extend into the lumen. All three organs play an important role in fluid or secretion transport, respectively. Hence, dysfunction of monocilia in these organs affects the correct detection and transmission of flow stimuli into intracellular Ca^{2+} signals, which might lead to pancreatic or choledochal cyst formation (Afzelius, 1976; Cano *et al.*, 2004; van's Gravesande and Omran, 2005; Masyuk *et al.*, 2006).
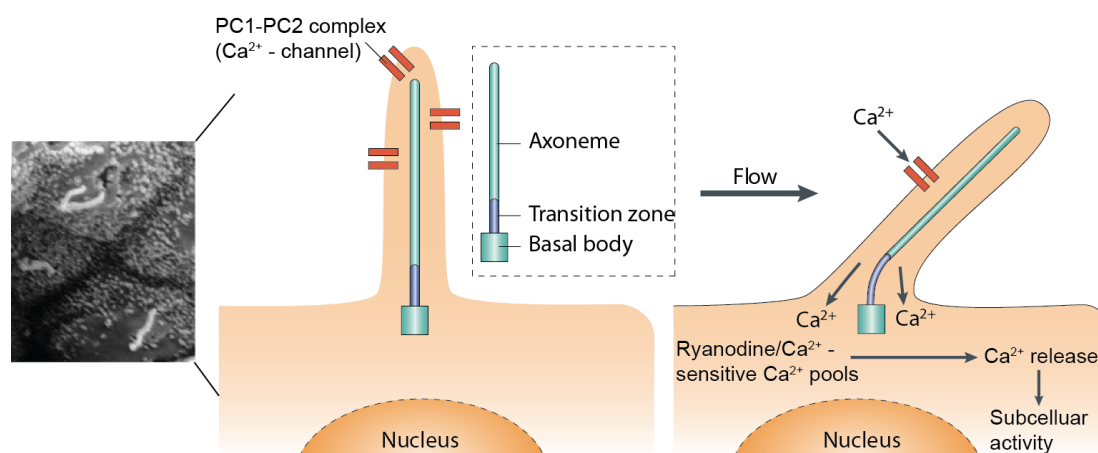
Figure 3: The mechanosensation-based cilia signaling model. (Left) SEM of non-motile monocilia found in the tubules of renal epithelial cells. (Middle & right) Schematic illustration of a mechanosensation-based cilia signaling model is presented, exemplified for renal cilia. In tubules, cilia are constantly exposed to urine flow, which induces passive ciliary bending and results in an increase of the cytoplasmic Ca^{2+} level. Polycystin-1 (PC1) and polycystin-2 (PC2) form Ca^{2+}-permeable heteromeric ion channels, which localize to the ciliary membrane. (Right) PC1-PC2 channels are sensitive to mechanical stress and mediate transduction of an extracellular mechanical stimulus into a Ca^{2+} signaling response inside kidney epithelial cells. SEM picture (left) is obtained from (Badano et al., 2006) and schematic representation (middle & right) from (Fliegauf et al., 2007).

Motile monocilia of the embryonic node resemble non-motile monocilia of renal cells. As mentioned previously (Left-right asymmetry), directional beating of nodal cilia generates a leftward flow of extraembryonic fluid, followed by a left-sided Ca^{2+} release, which is critical for left-right development (Nonaka *et al.*, 1998; 2002; Nauli *et al.*, 2003). However, the resulting 'nodal flow' needs to be sensed. Two models for left-right axis determination have been proposed aiming to explain this issue (McGrath *et al.*, 2003; Tanaka *et al.*, 2005). The nodal vesicular parcel (NVP) model suggests the presence of vesicles filled with morphogens, which are secreted at the

right side of the embryonic node and transported leftward by nodal flow (Tanaka *et al.*, 2005). Upon arrival on the left side on the embryonic node, vesicles are smashed open to release their contents. Subsequently, specific transmembrane receptors are proposed to bind to the morphogens, which in turn initiates a left-sided intracellular Ca^{2+} release (Tanaka *et al.*, 2005). On the contrary, in 2003 McGrath and colleagues predicted a 'two-cilia model', which was further supported by Yoshiba and colleagues in 2012. Both groups suggest the co-existence of two populations of cilia in the node, motile (found in the center of the node) and immotile (present at the edge of the node) cilia, whereas the former generate nodal flow and the latter sense the flow (Nonaka *et al.*, 1998; McGrath *et al.*, 2003; Yoshiba *et al.*, 2012) (Fig. 4). However, it remains unclear, if only immotile cilia that are non-motile at the time when left-right symmetry is broken are exclusively involved in sensing the Ca^{2+} influx or motile nodal cilia as well. In accordance to renal cilia, Pkd2 has been also localized to nodal cilia, in particular to the crown cells at the edge of the ventral node. Mutations affecting ciliary localization of Pkd2 at the embryonic node disrupt left-right development. Hence, both ciliary motility and the Ca^{2+}-permeable cation channel Pkd2 are required to establish an increase in cytoplasmic mesendodermal Ca^{2+} at the left side of the embryonic node (Chilvers *et al.*, 2003; Takao *et al.*, 2013). Recently, it was demonstrated that in response to ciliary motility dynamic, intraciliary calcium oscillations (IOCS) occur along the left side of the embryonic node, which is initiated by Pkd2. The asymmetric IOCS represent the first described molecular signal, which is functionally required for establishment of left-right asymmetry (Nonaka *et al.*, 2002; Nauli *et al.*, 2003; Yuan *et al.*, 2015).
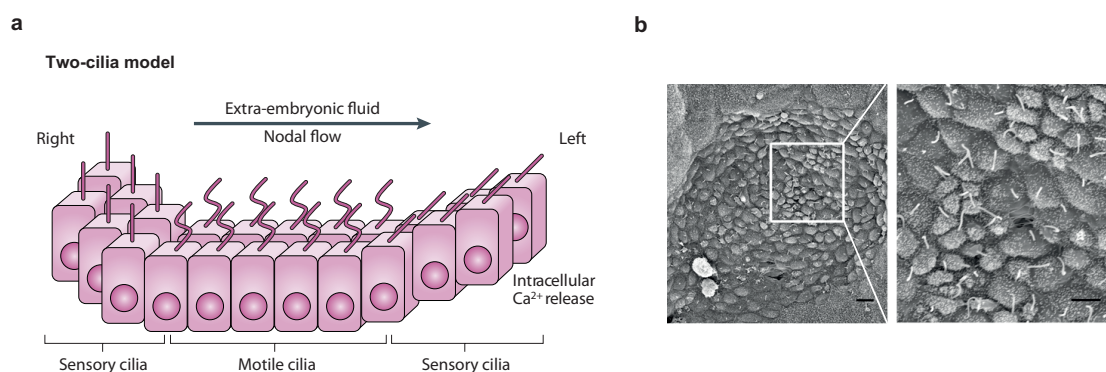
Figure 4: Establishment of left-right asymmetry by nodal cilia. a) Schematic drawing of the 'two-cilia model'. Motile nodal cilia in the center of the embryonic node generate a directional leftward nodal flow that is mechanosensed by passive bending of immotile cilia on the left side of the embryonic node. Bending of nodal cilia results in a left-sided Ca^{2+} release required for establishment of left-right asymmetry. b) SEM of the embryonic node and nodal cilia. The boxed region on the left SEM shows a

It was suggested that polycystins along with the cilium conduct ciliary calcium changes into the cytoplasm thereby having an important impact on cellular responses (Praetorius and Spring, 2001; Yoshiba *et al.*, 2012). However, when monitoring changes in ciliary calcium concentration Delling and colleagues found that the cytoplasmic calcium concentration remained unaffected (Delling *et al.*, 2013). Further investigations are needed to elucidate the functional role of the cilium as a calcium enriched organelle and to shed light on the mechanisms that regulate Ca^{2+} signaling in the cell.

1.2.2.3 Cilia and signaling pathways

Enrichment of signaling receptors to the ciliary membrane and the fact that most cells in the mouse embryo possess primary cilia raised the possibility of ciliary implication in developmental signaling pathways such as Hedgehog or Wingless signaling. Indeed, several lines of evidence including *in vivo* and *in vitro* studies indicate a role of cilia in these signal transduction pathways.

Wingless (Wnt) signaling

Wnt signaling represents an important pathway during embryonic development and regulation of adult tissue maintenance. The Wnt signaling pathway can be divided into two separated signal transduction pathways known as the canonical and the non-canonical branches (Clevers, 2006). The canonical Wnt/β-catenin pathway signals through controlled stabilization of the transcription coactivator β-catenin, which regulates expression of genes that control a number of embryonic and adult processes (Logan and Nusse, 2004). The non-canonical β-catenin independent pathway also known as the planar cell polarity (PCP) pathway plays an important role in the regulation of cytoskeletal architectures associated with cell polarity and movement (Veeman *et al.*, 2003).

Studies of the ciliary protein inversin (Inv) provided one of the first functional link between the cilium and Wnt signaling (Saadi-Kheddouci *et al.*, 2001; Otto *et al.*, 2003; Simons *et al.*, 2005). Inv is localized to primary cilia in kidney epithelial cells (Morgan *et al.*, 2002a), to nodal cilia, to fibroblast cilia in cell cultures and to the pituitary gland (Watanabe *et al.*, 2003). Furthermore, mutations in Inv result in cilia-related phenotypes including altered left-right laterality and the autosomal recessive

cystic kidney disease nephronophthisis type2, which lead to chronic renal failure in children (Otto *et al.*, 2003). In renal epithelial cells and in *Xenopus laevis* embryos an inhibitory role for Inv in the canonical Wnt signaling upstream of the β-catenin degradation complex was demonstrated, which results in activation of the non-canonical pathway (Fig. 5) (Simons *et al.*, 2005). Thus, cilia-mediated signaling through Inv may function as a molecular switch between the canonical and the non-canonical pathways by regulating the degradation of cytoplasmic dishevelled (Dsh) but not membrane-bound Dsh levels, a critical component found at the crossroad of both pathways (Wharton, 2003; Simons *et al.*, 2005) (Fig. 5). However, in addition to cilia, Inv also localizes to other cellular compartments such as cell junctions and the nucleus, which raises the possibility that observed Inv activities might originate from a non-ciliary site (Nurnberger *et al.*, 2002; 2004).
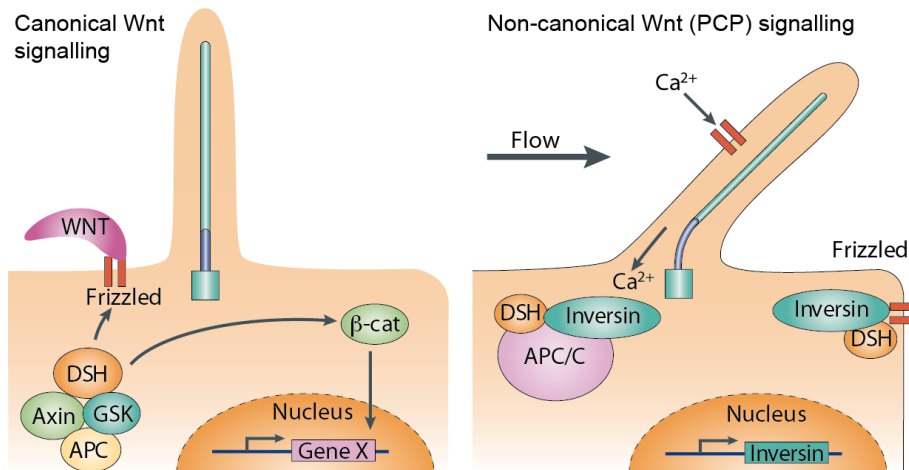
Figure 5: Involvement of cilia in Wnt signaling. The Wnt pathway can be divided into canonical (left) and non-canonical (right) arms. (Left) The canonical pathway predominates in the absence of physiological flow. Binding of WNTs, secreted lipoproteins to the Frizzled receptors, results in recruitment of dishevelled (DSH) and inactivation of the β-catenin (β-cat) multiprotein destruction complex consisting of the glycogen synthase kinase-3β (GSK3β) and the tumor suppressors Axin and adenomatous polyposis coli (APC). The transcriptional cofactor β-cat subsequently translocates to the nucleus to induce transcription of WNT target genes. (Right) Fluid flow-induced (e.g. urine flow) ciliary bending triggers the opening of calcium-sensitive channel proteins to allow calcium ions (Ca^{2+}) to enter the cilium. Intracellular Ca^{2+} release leads to an increase of inversin (Inv) expression. Inv induces degradation of cytoplasmic DSH by the anaphase-promoting complex/cyclosome (APC/C), making DSH unavailable for the canonical Wnt signaling pathway, thus promoting non-canonical Wnt signaling (Simons et al., 2005). The graphical illustration of the Wnt signaling model is obtained from (Fliegauf et al., 2007) .

An additional connection between cilia and non-canonical PCP signaling has been suggested by Ross and colleagues (Ross *et al.*, 2005). The Bardet-Biedl Syndrome (BBS) is a genetic disorder associated with ciliary dysfunction due to mutations in BBS genes, and shares phenotypes with PCP mutants including neural tube defects and renal cyst formation (Ross *et al.*, 2005). Observed genetic interactions between BBS genes and a PCP gene, led to the localization of the PCP protein Vangl2 to the ciliary axoneme and the basal body (Ross *et al.*, 2005). In addition, genetic interactions between BBS genes and Wnt11 or Wnt5a genes, which are also involved in PCP signaling, have been reported. Together with the findings that suppression of BBS1/4/6 leads to increased cytoplasmic levels of Dsh and β-catenin, evidence is provided that BBS proteins participate in the non-canonical Wnt pathway (Ross *et al.*, 2005; Gerdes *et al.*, 2007). Additionally, disruption of Kif3a, an essential component of the ciliary kinesin-2 motor required for cilium formation (Marszalek *et al.*, 1999) causes constitutive phosphorylation of Dsh and hyper-response activation of the canonical pathway upon Wnt ligand stimulation (Gerdes *et al.*, 2007; Corbit *et al.*, 2008). Taken together, these studies suggest that the basal body and the cilium restrain canonical Wnt signaling and might be further enabling the switch to the non-canonical Wnt pathway (Simons *et al.*, 2005; Gerdes *et al.*, 2007; Corbit *et al.*, 2008). However, the described role of cilia in Wnt signaling remains controversial (He, 2008; Ocbina *et al.*, 2008). Further investigations are required to prove whether defects in non-canonical, rather than canonical signaling are driven by cilia-mediated Wnt phenotypes.

Hedgehog (Hh) signaling

The Hh signaling pathway plays an important role in numerous processes during embryonic development and in adult stem cell function (di Magliano and Hebrok, 2003; McMahon *et al.*, 2003). Dysregulation of the pathway can cause various birth defects including polydactyly, skeletal malformations and human cancer (McMahon *et al.*, 2003; Goetz and Anderson, 2010). First evidence of ciliary implication in vertebrate Hh signaling resulted from a phenotype-based screen for mutations, which altered the patterning of the mouse embryo including neural tube closure defects, abnormal brain morphology and preaxial polydactyly (Huangfu *et al.*, 2003). These mutations were mapped to genes required for cilia formation. Furthermore, the mammalian Smoothened (Smo), a transmembrane protein essential for Hh signaling, was shown to localize to the primary cilium of the mouse embryonic node (Corbit *et al.*, 2005). It was demonstrated that Smo is involved in left-right determination and

floor plate induction (Corbit *et al.*, 2005). In mammals, binding of secreted Hh ligands to the patched 1 (Ptch1) receptors, which initially localize to the cilium, activates the Hh signaling pathway (Rohatgi *et al.*, 2007). Upon Hh stimulation the inhibitory effect of Ptch1 on Smo is abolished resulting in translocation of Smo to the cilium. Accumulation of Smo allows for cilia-mediated signal transduction via ciliary localized glioma transcription factors (Gli). Subsequently, Gli activates the expression of Hh target genes (Fig. 6) (Haycraft *et al.*, 2005).
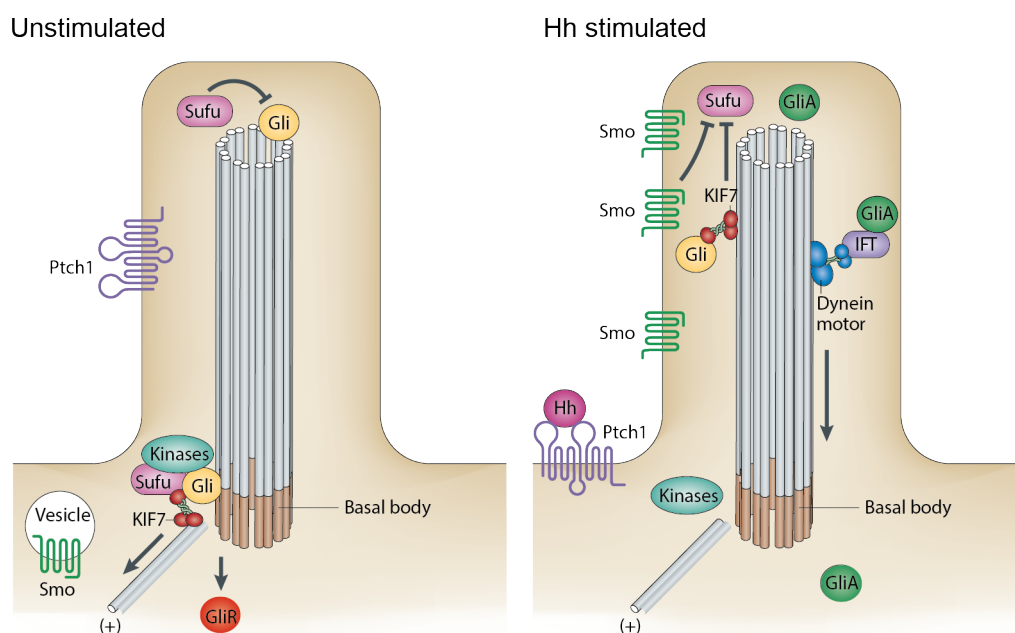
Figure 6: Vertebrate Hh signaling is linked to the cilium. (Left) In the absence of Hh ligands, patched 1 (Ptch1) receptor resides to the cilium and blocks entry of the transmembrane protein Smoothened (Smo) to the ciliary compartment. Transcription factor Gli and suppressor of fused (Sufu) localize to the ciliary tip. Gli transcription factors are proteolytically processed to the Gli repressor form (GliR) that keep Hh target genes switched off. (Right) Upon activation of the pathway via Hh ligand binding to Ptch1 receptor, Smo moves to and accumulates at the ciliary membrane. Consequently, Smo turns off Gli processing by interacting with Sufu, which allow Gli activators (GliAs) to translocate to the nucleus to induce Hh target gene expression. The Hh signalling model was presented in (Goetz and Anderson, 2010).

As mentioned previously, sensory cilia have higher Ca^{2+} concentrations than found in the cytoplasm, which is controlled by ciliary Ca^{2+}-permeable Pkd1l1-Pkd2l1 ion channels (DeCaen *et al.*, 2013; Delling *et al.*, 2013). To elucidate if impaired Pkd1l1-Pkd2l1 ion channels have potential ciliary defects, *Pkd2l1$^{-/-}$* knockout mice were tested (Delling *et al.*, 2013). In half of the *Pkd2l1$^{-/-}$* knockout mice intestinal malrotation was observed, a phenotype that is associated with sonic hedgehog (Shh) pathway defects during early development (Ramalho-Santos *et al.*, 2000; Martin and Shaw-Smith, 2010). In addition, *Pkd2l1$^{-/-}$* MEFs (mouse embryonic fibroblasts) cells

exhibit decreased protein levels of Hh-activated Gli1 and impaired accumulation of Gli2 at the ciliary tip compared with wild-type cells (Delling *et al.*, 2013). Consequently, Pkd1l1-Pkd2l1 ion channels control the ciliary Ca^{2+} concentration and thereby modulating established hedgehog pathways (DeCaen *et al.*, 2013; Delling *et al.*, 2013). In conclusion, Hh signaling requires maintenance and function of cilia to sense Hh ligands and transduce downstream signals critical for development, carcinogenesis and stem cell function.

Platelet-derived growth factor receptor-α (PDGFRα) signaling

Signaling via platelet-derived growth factors (PDGFs) is essential for cell survival, growth control, cell migration during gastrulation, fetal development and maintenance of tissues in adults (Heldin and Westermark, 1999; Andrae *et al.*, 2008). It was demonstrated that primary cilia in mouse embryonic and NIH3t3 fibroblasts play an important role in growth control via the platelet-derived growth factor receptor alpha (PDGFRα) (Tucker *et al.*, 1979; Schneider *et al.*, 2005). PDGFRα forms homodimers and localizes to the primary cilium during growth arrest (G0) (Fredriksson *et al.*, 2004). Ligand-dependent activation of the PDGFRα within the ciliary membrane by PDGF-AA induces a phosphorylation cascade through the PI3K–AKT and MEK1/2–ERK1/2 pathways in and at the base of the cilium. Quiescent embryonic fibroblasts of *orpk* mutant mice fail to form normal cilia or cilia at all and are therefore unable to upregulate PDGFRα, implying that ciliary localization of PDGFRα is necessary for proper signal transduction (Schneider *et al.*, 2005). In addition, PDGFRα localizes to primary cilia of human embryonic stem cells (hESCs), nerve stem cells (NSCs) and neuroblasts in the rat brain (Danilov *et al.*, 2009). These findings support the conclusion that PDGFRα signaling required for cell cycle control of various cell types and tissues, is coordinated by the cilium in order to regulate developmental processes and to maintain normal tissue homeostasis (Christensen *et al.*, 2008).

1.2.2.4 Cilia as environmental sensors - Light, odorant and auditory detection

Sensing the extracellular environment is a major function of primary cilia and essential for photoreception, olfaction and audition. To facilitate their sensory roles, for instance receiving and transducing the stimuli of light or odorant to cells, cilia undergo specialization.

Phototransduction

In mammalian retina, photoreceptors cells, which represent polarized sensory neurons, utilize a modified non-motile (9+0) primary cilium for the reception and transduction of light. In rods and cones, the two classic photoreceptor cell types, the cilium represents the sole transport corridor between the inner segment (IS) and the outer segment (OS), thus referred to as connecting cilium (CC) (Fig. 7a) (Horst *et al.*, 1990). The IS contains the nucleus and other organelles including the Golgi and the ER, which allow synthesis of materials required for the formation, maintenance and function of the OS. The OS can be considered as an expanded tip of a specialized sensory cilium, composed of an elaborated array of photosensitive disc membranes organized into membrane stacks derived from the plasma membrane (Besharse *et al.*, 1977). Enormous amounts ($\sim 10^9$ molecules) of the photosensory GPCRs opsin and rhodopsin as well as other signaling molecules such as the trimeric G protein transducin or the cGMP gated channel concentrate in the OS, thereby acting as a collecting antenna for photons (Besharse *et al.*, 1977; Elias *et al.*, 2004). The OS is highly dynamic and undergoes continuous turnovers. Thus, all membrane and soluble proteins required for maintenance of the photoreceptor segment are synthesized in the IS and need to be transported to the OS via the CC, facilitated by a conserved transport machinery (Rosenbaum *et al.*, 1999; Rosenbaum and Witman, 2002). Impairment and mutations of key players involved in the transport of materials through the CC cause accumulation of opsin and arrestin in the IS, followed by degeneration of the OS, which can lead to severe retinal degeneration (Marszalek *et al.*, 2000; Pazour *et al.*, 2002a).
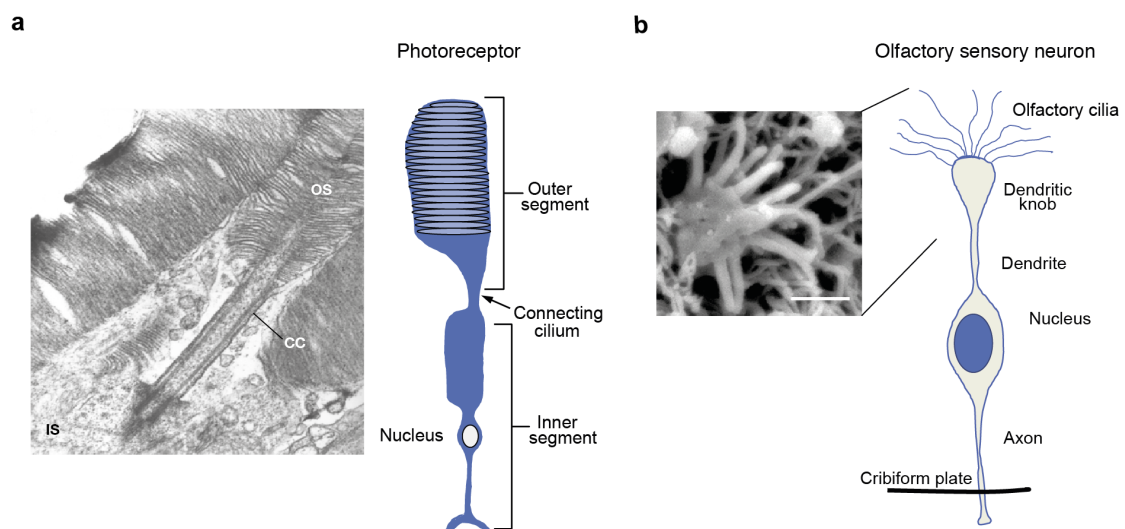
Figure 7: Modified sensory cilia. a) (Left) EM of a vertebrate photoreceptor cell showing the connecting cilium (CC) localized between the outer and inner segments (OS and IS, respectively). (Right) Schematic representation of a photoreceptor cell and its substructures. The light detecting protein machinery has to pass through the CC, which represents the sole corridor from the IS to the OS. b) An olfactory sensory neuron of vertebrates is depicted. SEM on the left shows a zoom-in of a single dendritic knob from which multiple cilia extend. Scale bar is 1 μm. EM in a) is obtained from (Rosenbaum and Witman, 2002), SEM in b) from (McEwen et al., 2007) and schematic illustrations in a) and b) from (Berbari et al., 2009).

Odorant detection

Detection of odorant, the initial step of olfaction, occurs in olfactory sensory neurons, which are located in the olfactory epithelium of the nasal cavity of vertebrates (Buck and Axel, 1991). The olfactory sensory neurons are bipolar structures in which the dendrite and the axon are directly connected to the cell body. The dendrite ends in a dendritic knob from which eight or more immotile olfactory cilia originate and elongate into mucus that covers the surface of the epithelium (Menco and Morrison, 2003) (Fig. 7b). The importance of cilia in olfaction has become apparent by the observation that cilia mouse mutants and Bardet-Biedl syndrome patients are usually unable to smell (Kulaga *et al.*, 2004). Olfactory signaling is initiated once odorants interact with the odorant GPCRs localized in the ciliary membrane of olfactory sensory neurons (Buck and Axel, 1991). These interactions trigger an increase in intraciliary concentration of the second messenger cAMP through the activation of the adenylyl cyclase (AC) (Boekhoff *et al.*, 1990; Wong *et al.*, 2000). Increase of cAMP causes opening of the olfactory cyclic nucleotide-gated (CNG) channels, which in turn results in depolarization of the neurons that are further amplified via Ca^{2+}-activated chloride channels, a process essential for sense of smell ((Nakamura and Gold, 1987) reviewed in (Ronnett and Moon, 2002)). All components necessary for odorant detection are localized to olfactory cilia implying that these cilia play a major role in odorant reception and signal amplification. Indeed, any perturbations affecting the cilium or the localization of ciliary olfaction components cause impaired olfactory function, which lead to disorders such as hyposmia (decreased ability to smell odorants) or anosmia (loss of the ability to smell) (Wong *et al.*, 2000; Kulaga *et al.*, 2004; Iannaccone *et al.*, 2005; Benton *et al.*, 2006; McEwen *et al.*, 2007).

Auditory detection

In vertebrates, the inner ear is comprised of two distinct regions the cochlea, which regulates auditory function and the vestibular system responsible for perception of motion and balance. In order to process sound and positional signals mechanosensory hair cells and non-sensory supporting cells are required. The apical part of hair cells carry multiple rigid microvilli-like structures called stereocilia or stereovilli, often referred to as stereociliary bundles. The name stereocilia is mis-leading as these structures are actin-based and only have superficial resemblance to MT-based cilia. Each bundle is comprised of tightly packed rows of stereovilli, which convert a mechanical stimulus into an electrical signal (Hudspeth, 1985; Purves *et al.*, 2001). Additionally, each hair cell possesses a 'true' single non-motile primary cilium with an unusual 9+2 axonemal arrangement, termed kinocilium that protrudes from behind the tallest row of stereovilli. Kinocilia are required for the correct orientation of the stereovilli and the organization of hair cells. Disruption of kinocilia formation leads to abnormal morphologies, mislocated basal bodies and misoriented stereovilli bundles (Axelrod, 2008; Jones *et al.*, 2008; Fukuda *et al.*, 2014). In contrast to stereovilli, the cochlear kinocilium of the inner ear hair cells is considered not to be involved in auditory perception. Nevertheless, a dependence of mechanosensitive responses of the kinocilium during development of hair cells was proposed (Kindt *et al.*, 2012). In addition, the kinocilium was demonstrated to be critical for the emergence of hair bundle polarity and thereby crucial for the hearing process (Grati *et al.*, 2015). Protein localization studies further revealed that the Usher interactome, a protein network including USH proteins, is present in stereovilli and the synaptic region of hair cells as well as in the synaptic region of photoreceptor cells providing a link to an autosomal recessive disorder, termed Usher syndrome, in which patients display deafness in combination with blindness (Adato *et al.*, 2005; Reiners *et al.*, 2006). In summary, whether motile or not, all types of cilia have important sensory functions critical for regulating and controlling various cellular and developmental processes (Christensen *et al.*, 2007).

1.3   Ciliary compartmentalization

Compartmentalization permits the existence of different biochemical environments and execution of specialized functions. Hence, the specific localization of proteins and lipids that are concentrated in the ciliary membrane has to be assured to enable efficient separation of various ciliary functions. However, cilia are devoid of

ribosomes, therefore missing the biosynthetic machinery for protein synthesis. Consequently, all proteins including axonemal building blocks and receptors, which are important for assembly and function of the cilium, have to be synthesized elsewhere in the cell, selectively recruited and transported to the ciliary base and finally imported to the ciliary compartment. Two aspects of ciliary trafficking will be described in the following sections. Firstly, structural features and components required for ciliary compartmentalization, which not only retain membrane proteins in the ciliary compartment, but also exclude nonciliary components, are presented. Secondly, a conserved bi-directional transport mechanism in the cilium required for ciliary assembly, maintenance and function, will be introduced. Mechanisms for selective recruitment and transport of proteins from their site of synthesis to the base of the cilium are the topics of the upcoming chapter 1.4 Ciliary targeting - Trafficking of proteins to the ciliary compartment.

1.3.1 The ciliary gate – checkpoint for the ciliary compartment

The specific protein and lipid composition concentrated in the ciliary membrane markedly differs from the cytoplasm, suggesting the existence of a selective barrier (Musgrave *et al.*, 1986; Hunnicutt *et al.*, 1990; Nachury *et al.*, 2007; Satir and Christensen, 2007; Pazour and Bloodgood, 2008). While the ciliary membrane covers most of the surface of the cilium, entry of proteins and lipids destined for the ciliary compartment has to occur at a small opening at the base of the cilium in form of a 'ciliary gate' (Rosenbaum and Witman, 2002). First hints for the presence of a diffusion barrier that separates the ciliary membrane from the plasma membrane (PM) has been reported in *Chlamydomonas,* in which cell body agglutinins were prevented from diffusion to the flagellum (Musgrave *et al.*, 1986; Hunnicutt *et al.*, 1990). It was further demonstrated that the ciliary membrane at the base of the cilium possesses a condensed lipid zone of high lipid order that differs from that of the PM, termed periciliary membrane domain (Pazour and Bloodgood, 2008). The periciliary membrane domain may contribute to a lateral diffusion barrier, since glycosylphosphatidylinositol (GPI) anchored proteins fail to diffuse from the apical plasma membrane into the ciliary compartment (Montesano, 1979; Vieira *et al.*, 2006). Good candidates that likely constitute a physical barrier are structural features of the basal body, the transition zone and associated structures including the ciliary necklace and transitional fibers (as previously described in 1.2.1 Structure of the cilium) (Rosenbaum and Witman, 2002; Satir and Christensen, 2007). The curved nature of the membrane at the base of the cilium and interactions of the TFs with the

ciliary membrane, impose geometric constraints on movement of lipids and membrane proteins across this region (Satir and Christensen, 2007). In accordance, docking and assembly sites for proteins destined for the ciliary compartment at or near the TFs, distal to the basal body, has been reported (Deane *et al.*, 2001; Williams *et al.*, 2011).

Moreover, components that are proposed to constitute a membrane diffusion barrier, are septins (Hu *et al.*, 2010). Septins comprise a conserved family of GTPases, which form large-order structures, including rings, bundles and filaments (Weirich *et al.*, 2008). Several studies in biological systems including the budding yeast indicate that septins form diffusion barriers, which regulate the distribution of membrane proteins between different cellular compartments (Myles *et al.*, 1984; Cesario and Bartles, 1994; Barral *et al.*, 2000; McMurray *et al.*, 2011). Septin 2 and septin 7, two members of the septin family that associate with each other, were found to localize at the ciliary base (Hu *et al.*, 2010). Depletion of septins causes defects in ciliogenesis and results in an increase of ciliary transmembrane proteins entering the cilium (Hu *et al.*, 2010). Similarly, knockdown of either septin 2 or 7, abrogates hedgehog signaling (Hu *et al.*, 2010; Kim *et al.*, 2010). Thus, septins represent likely components that constitute a membrane diffusion barrier at the ciliary base required for retaining receptor-signaling pathways in the cilium.

In addition, it became apparent that the transition zone at the ciliary base comprises an increasing number of ciliopathy-associated proteins, which likely act as modulators of a ciliary gate (Sharma *et al.*, 2008; Hu and Nelson, 2011; Chih *et al.*, 2012; Reiter *et al.*, 2012). For instance, the *Chlamydomonas* protein CEP290 (also known as nephrocystin-6/NPHP6) localizes to the Y-links, important structural features, which are required to connect MTs and the ciliary membrane at the flagellar transition zone (Craige *et al.*, 2010). Disruption of CEP290 results in defective linker structures and in abnormal flagellar protein content, indicating that CEP290 functions as a gatekeeper to regulate entry and exit of flagellar proteins (Betleja and Cole, 2010; Craige *et al.*, 2010). Meckel-Gruber syndrome (MKS) and nephronophthisis (NPHP) are two human disorders of a long list of known ciliopathies (Badano *et al.*, 2006; Sharma *et al.*, 2008). Eight ciliary TZ-localized MKS, MKSR and NPHP proteins out of two distinct modules were shown to functionally interact with each other and to be required for the early stage of ciliogenesis (Williams *et al.*, 2011). Moreover, these TZ proteins establish a gate, which modulates ciliary protein composition during ciliogenesis further implying that perturbations of these two modules may contribute to phenotypic features of the MKS/NPHP disease spectrum (Williams *et al.*, 2011). In consistency with these results, several recent studies

identified a number of additional transition zone ciliopathy-associated protein complexes or modules that are also involved in regulation of ciliogenesis and ciliary membrane composition, suggesting that TZ dysfunction represent the cause of diverse ciliopathies (Garcia-Gonzalo *et al.*, 2011; Chih *et al.*, 2012).

Furthermore, the nucleus and the cilium appear to share lot of similarities. The nuclear envelope constitutes a double-membrane barrier that separates the nucleus from the cytoplasm. Nuclear-cytoplasmic shuttling requires a complex cytoarchitecture, termed the nuclear pore. The nuclear pore complex (NPC) is embedded in the membrane of the nuclear envelope and facilitates nucleocytoplasmic transport via its pore-like structure (Fahrenkrog and Aebi, 2003). The physical and molecular nature of the NPC shows a high degree of homology with aforementioned features involved in regulation of ciliary permeation, which are therefore termed ciliary pore complex (CPC) (Satir and Christensen, 2007; Kee *et al.*, 2012). Moreover, it was proposed that NPC components including nucleoporins, importins and Ran GTPases localize to the base of the cilium (Dishinger *et al.*, 2010; Fan *et al.*, 2011; Hurd *et al.*, 2011). These components are suggested to regulate entry of soluble proteins including kinesin-2 KIF17 motor to the cilium (Kee *et al.*, 2012). A size-exclusion permeability barrier and NPC components are proposed to characterize a CPC, implying that cilia and the nucleus share similar import and transport machineries (Kee *et al.*, 2012). However, there is no evidence of a diffusion barrier at the connecting cilium of photoreceptor cells (Calvert *et al.*, 2010) leading to the assumption that steric effects may account for the observed size-dependent distribution of soluble proteins in cilia versus cytoplasm (Calvert *et al.*, 2010; Najafi *et al.*, 2012). Using a combination of permeabilized cell assays and *in vivo* studies, Breslow *et al*. further described a ciliary permeability barrier for soluble proteins that is size-dependent, but mechanically distinct from those of the NPC or the axon initial segment (Song *et al.*, 2009; Breslow *et al.*, 2013). In addition, NPC components, which have been suggested to localize to primary cilia where they are implicated in ciliary entry regulation (Kee *et al.*, 2012), have not been observed in the study from Breslow and colleagues (Breslow *et al.*, 2013), resulting in conflicting reports.

Finally, a recent study in *Tetrahymena pyriformis* identified a barrier-like structure at the base of the cilium that appears to fulfill all requirements for ciliary compartmentalization, therefore referred to as the ciliary partitioning system (CPS) (Ounjai *et al.*, 2013). The CPS comprises the cytosolic ciliary pore complex and a membrane domain that serves as a diffusion barrier, which directly associate to seal the cilia opening (Ounjai *et al.*, 2013). Electron tomography (ET) analysis revealed that the CPC is a plate-shaped structure containing nine symmetrically arranged

holes or pores through which the nine doublet MTs of the basal body protrude. Thus, the CPC represents a physical barrier that limits cytosolic movement while both a detergent-resistant periciliary membrane (ciliary pocket) and a ring complex, which connects the CPC to the membrane act as a membrane diffusion barrier. However, despite similar architecture of cilia, there is significant diversity of structural features present in the transition zone among different species, implying that the described CPS in *Tetrahymena* (Ounjai *et al.*, 2013) might be distinct or not even present in other ciliated organisms (Nachury *et al.*, 2007; Fisch and Dupuis-Williams, 2011).

In summary, there is strong evidence for the existence of a ciliary gate to ensure formation, maintenance and compartmentalization of cilia. The ciliary gate not only localizes to the TZ at the base of the ciliary membrane but is also supposed to consist of transition zone and basal body features (ciliary necklace, Y-links, TFs), a septin-based diffusion barrier and TZ ciliopathy-associated protein complexes (Hu and Nelson, 2011; Chih *et al.*, 2012; Reiter *et al.*, 2012). For soluble cytoplasmic proteins, transition zone gating might not involve a diffusion barrier mechanism such as the one proposed for membrane-associated proteins (Kee *et al.*, 2012; Najafi *et al.*, 2012; Breslow *et al.*, 2013). Instead, entry of soluble proteins likely occurs via a size-dependent permeability barrier (Kee *et al.*, 2012; Najafi *et al.*, 2012; Breslow *et al.*, 2013). Although, a lot of components, which constitute the ciliary gate, have been identified, additional candidates, their exact roles and the ultrastructural organization of the barrier are still fragmentary and remain to be determined. Nevertheless, the cilium, even though it is not fully membrane-enclosed, possesses all characteristics of a distinct compartment and can thus be considered as a cellular organelle.

1.3.2 Intraflagellar transport (IFT) – Trafficking system within the cilium

The cilium consists of a MT-based axoneme, which is continuous with the basal body at its proximal end. During ciliary growth, the axoneme is elongated by addition of new axonemal subunits exclusively to its distal tip (plus end) (Fig. 2e) (JL and Child, 1967). As mentioned previously, cilia are devoid of ribosomes, lacking the machinery required for protein synthesis. This poses problems for the delivery of new axonemal building blocks, which are synthesized far removed from their site of assembly. Thus, for maintenance and assembly of the cilium, an active transport process is required. The cell solved this logistical problem by means of Intraflagellar transport (IFT) (Kozminski *et al.*, 1993; Rosenbaum and Witman, 2002). IFT was first described, through differential interference contrast (DIC) microscopy, as the bi-directional movement of particles along the axoneme of the bi-flagellated algae

Chlamydomonas reinhardtii (Kozminski *et al.*, 1993). The observed membrane-bound particles consist of large multisubunit protein complexes referred to as IFT particles, which track along the axonemal doublet MTs from the base to the ciliary tip and back, just beneath the ciliary membrane (Fig. 8). Moreover, IFT was further visualized in different cell types and organisms including neuronal sensory cilia of *C. elegans* indicating that IFT and its associated components are highly conserved among ciliated organisms (Orozco *et al.*, 1999; Jékely and Arendt, 2006; Absalon *et al.*, 2008a). IFT is powered by opposing molecular motors. Members of the kinesin-2 family are required for anterograde movement (from the basal body to the tip) (Walther *et al.*, 1994; Kozminski *et al.*, 1995; Scholey, 2008) and cytoplasmic dynein 2/IFT dynein for retrograde transport (from the ciliary tip to the basal body) (Pazour *et al.*, 1999; Porter *et al.*, 1999; Perrone *et al.*, 2003; Hou *et al.*, 2004; Pfister *et al.*, 2005), respectively (Pedersen and Rosenbaum, 2008). The first step of IFT is to recruit and assemble IFT components and it cargo such as tubulin near the site where transition fibers contact the ciliary membrane (Deane *et al.*, 2001; Bhogaraju *et al.*, 2013) (Fig. 8). Secondly, IFT particles, which carry uploaded cargo and inactive retrograde IFT motor dynein 2, need to enter the ciliary compartment via the ciliary gate (Rosenbaum and Witman, 2002; Hu and Nelson, 2011). After crossing the barrier, the IFT complex moves anterogradely along the ciliary axoneme from the basal body to the tip (Iomini *et al.*, 2001; Qin *et al.*, 2004). At the tip, a yet poorly understood series of events, termed 'turnaround' takes places (Marshall and Rosenbaum, 2001). This process includes cargo release of the anterograde IFT trains, inactivation of kinesin-2, followed by significant remodeling of the IFT particles to prepare for retrograde IFT (Iomini *et al.*, 2001; Marshall and Rosenbaum, 2001; Dentler, 2005; Sloboda, 2005; Pedersen *et al.*, 2006; Pigino *et al.*, 2009). In addition, a 'flagellar tip complex', which contains the MT-plus-end-binding protein (EB1) is proposed to aid during the turnaround process (Sloboda, 2005). Cytoplasmic dynein 2, the motor that powers retrograde IFT gets activated, the retrograde IFT machinery assembles and ciliary turnover products are loaded onto the IFT particle (Iomini *et al.*, 2001; Rosenbaum and Witman, 2002; Qin *et al.*, 2004). Retrograde transport via dynein 2 from the distal tip to the base of the cilium takes place. Finally, the IFT machinery disassembles, ciliary turnover products are recycled or degraded and the IFT components are re-used for the next round of IFT (Hao and Scholey, 2009).
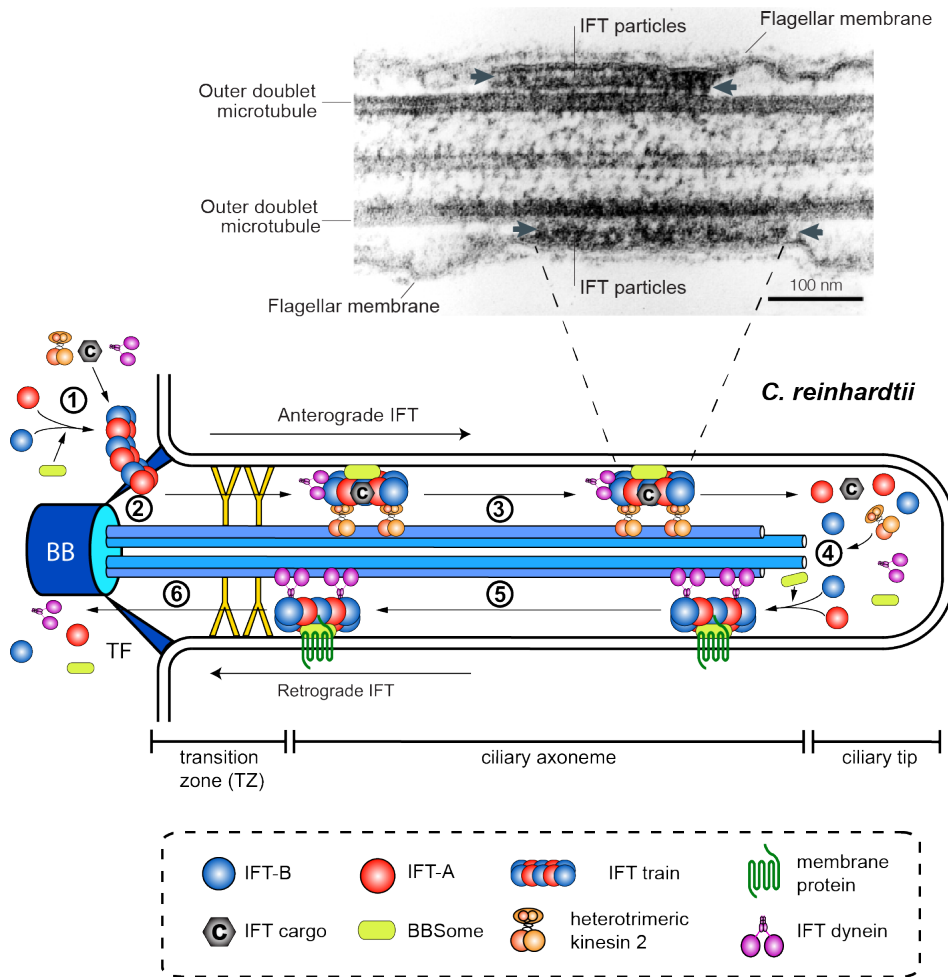
Figure 8: Intraflagellar transport machinery. (Upper image) EM of a longitudinal section through a Chlamydomonas flagellum shows two electron-dense complexes (grey arrows) between the outer doublet MTs and the flagellar membrane, identified as IFT particles. (Lower panel) Schematic representation of a cilium illustrates different steps of Intraflagellar transport: (1) Recruitment and assembly of the IFT machinery, (2) selective entry into the ciliary compartment via the ciliary gate, (3) anterograde transport along the axoneme by kinesin-2 mediated IFT, (4) turnaround, including IFT particle remodelling, (5) ciliary turnover products are retrogradely transported by IFT dynein, and (6) disassembly of the IFT machinery. BB: basal body, TFs: transition fibers. EM was slightly modified from (Rosenbaum and Witman, 2002) and the schematic presentiation was created and kindly provided from Dr. Michael Taschner (unpublished).

IFT particles were first isolated and characterized from *C. reinhardtii* flagella and were found to consist of a multisubunit protein complex (IFT complex) that can be further organized into two biochemically distinct sub-complexes, termed IFT-A and IFT-B (Piperno and Mead, 1997; Cole *et al.*, 1998). The IFT complex consists of at least 22 IFT proteins (named after their apparent molecular weight in SDS-PAGE), which are subdivided further into IFT-A and IFT-B members that contain 6 and 16 known subunits, respectively (Cole *et al.*, 1998; Piperno *et al.*, 1998; Wang *et al.*,

2009; Fan *et al.*, 2010; Ishikawa *et al.*, 2014). Functional studies of IFT proteins led to the conclusion that IFT-A and IFT-B sub-complexes are not only genetically and biochemically distinct, but also function in different parts of IFT. IFT-B contributes to anterograde trafficking, which is essential for ciliary assembly and maintenance. In all studied organisms, mutations that affect IFT-B proteins or the kinesin-2 motor lead to short or absent flagella (Fujiwara *et al.*, 1999; Pazour *et al.*, 2000; Brazelton *et al.*, 2001; Qin *et al.*, 2001; Haycraft *et al.*, 2003; Huangfu *et al.*, 2003; Follit *et al.*, 2006; Hou *et al.*, 2007). By contrast, perturbations of IFT-A proteins or cytoplasmic dynein 2 result in malformed cilia with shortened and abnormal bulges containing accumulation of IFT-B proteins (Perkins *et al.*, 1986; Piperno *et al.*, 1998; Pazour *et al.*, 1999; Iomini *et al.*, 2001; Schafer *et al.*, 2003; Efimenko *et al.*, 2006; Tran *et al.*, 2008; Tsao and Gorovsky, 2008; Absalon *et al.*, 2008b). Thus, IFT-A plays an important role in retrograde transport via returning proteins from the ciliary tip to the cell body, but appears not to be essential for ciliary assembly. The IFT complex is not only crucial in mediating contacts between the ciliary motors and the ciliary cargo but also plays an evolutionarily conserved role in the assembly of cilia (ciliogenesis).

1.4 Ciliary targeting - Trafficking of proteins to the ciliary compartment

Cilia, as well as other cellular organelles, utilize specific mechanisms and machinery for the delivery of proteins and lipids from their site of synthesis to their destined compartments. In general, ciliary membrane proteins are synthesized in the rough endoplasmic reticulum, processed in the Golgi and finally transported to the base of the cilium. Selective entry via the ciliary diffusion barrier and movement of membrane proteins along the ciliary axoneme is mainly regulated by Intraflagellar transport (IFT) as discussed in the previous chapter 1.3 Ciliary compartmentalization. Mechanisms and regulation of transport from the Golgi to the cilium and the machinery implicated in these processes are the main focus of this chapter. In contrast to other membrane trafficking routes, our knowledge about trafficking to the ciliary compartment remains in its infancy.

1.4.1 Vesicular transport – major trafficking pathway in eukaryotic cells

In eukaryotes, selective and efficient exchange of membrane receptors, lipids or neurotransmitters between organelles occurs by means of polarized vesicular transport (Bonifacino and Glick, 2004). Polarized vesicular trafficking is an ancient conserved and highly regulated delivery system essential to maintain normal cell function (Zerial and McBride, 2001). During this process, cargo is packed into carrier vesicles of different size, that bud from a donor membrane and fuse with an acceptor compartment (Palade, 1975). General mechanisms of vesicular trafficking can be further divided into several steps. Firstly, membrane-associated cargo has to be sorted and concentrated in a region of the donor compartment. During this process, cytosolic coat proteins form large supramolecular assemblies or coats, which enclose cargo molecules (Kirchhausen, 2000; Bonifacino and Lippincott-Schwartz, 2003). Subsequently, coating facilitates budding of the vesicle from the donor membrane. Movement of the vesicle towards its target compartment occurs along cytoskeleton filaments such as MTs or actins. Once at its destination, the vesicle docks or becomes tethered to the acceptor membrane, probably facilitated by multisubunit tethering complexes (Bröcker *et al.*, 2010). Subsequently, soluble N-ethylmaleimide-sensitive factor attachment protein receptors (SNAREs) promote fusion of the vesicle with the acceptor lipid bilayers. Finally, the transported cargo is delivered to the acceptor compartment (Cooper, 2000; Martens and McMahon, 2008; Stenmark, 2009). The Golgi apparatus was one of the first organelles consistently found in close proximity to the primary cilium and the basal body suggesting physiologically relevant interactions between these cellular compartments (Sorokin, 1962). Several lines of evidence further demonstrated that Golgi-derived vesicles are not only implicated in early cilia formation (ciliogenesis), but the constant trafficking of post-Golgi vesicles to the cilium is crucial for maintenance and function of the organelle (Sorokin, 1968; Pedersen *et al.*, 2008). It became apparent that vesicular transport is the major process by which cells deliver materials to the base of the cilium.

1.4.2 Regulation of vesicular transport by small GTPases

Polarized vesicular trafficking between specialized membrane-enclosed organelles is an important multi-step transport process regulated by small GTPases. Members of the superfamily of small GTPases have been also implicated in controlling membrane and protein traffic from the Golgi and the trans-Golgi network (TGN) to the cilium. General mechanisms, properties and structural features as well

as accessory factors critical for the control of small GTPases with focus on members of the Rab and Arf subfamily, key regulators of membrane traffic, will be described in detail in the following sections.

1.4.2.1   General features of small GTPases

Small guanine nucleotide-binding (G) proteins play a central role in the spatial and temporal organization of many cellular processes including signal transduction, cytoskeleton dynamics and membrane trafficking. They share a common biochemical mechanism and act as binary molecular switches and timers altering between a guanosine diphosphate (GDP)-bound and a guanosine triphosphate (GTP)-bound state, respectively (Fig. 9a) (Vetter and Wittinghofer, 2001). The GDP-bound conformation is considered to be inactive, whereas the GTP-bound one is generally regarded as active, as this is the form that interacts with downstream effector proteins (Stenmark *et al.*, 1994). The molecular switch between these two conformations is facilitated by a number of additional factors. Guanine nucleotide exchange factors (GEFs) catalyze the exchange of GDP for GTP, whereas GTPase activating proteins (GAPs) stimulate GTP hydrolysis (Bos *et al.*, 2007) (Fig. 9a).

All small GTPases are made of a conserved GTPase domain (G domain) composed of a six-stranded β-sheet flanked by five α-helices (Fig. 9b). G proteins can be further recognized by four to five conserved sequence elements, called G-motifs (G-binding motifs, G1-G5) important for GDP/GTP exchange, GTP-induced conformational change and GTP hydrolysis (Bourne *et al.*, 1991). Interaction of G proteins with guanine nucleotides and magnesium (Mg^{2+}), an essential cofactor, involves mainly residues from the G-motifs, which are lined up along the nucleotide binding site of the G domain (Bourne *et al.*, 1991; Vetter and Wittinghofer, 2001). The most important contribution to strong binding are the interactions of the nucleotide base with residues of the N/TKxD motif, whereas the GxxxxGK(S/T) motif in the P-loop (phosphate-binding loop) provides contacts to β,γ-phosphates of the guanine nucleotides (Fig. 9b) (Saraste *et al.*, 1990; Vetter and Wittinghofer, 2001). Structural comparison of the GDP- and GTP-bound state further revealed that small GTPases adopt different conformations with major nucleotide-induced differences occurring in regions of the G2/G3-motifs, denoted switch I and switch II (Milburn *et al.*, 1990; Stroupe and Brunger, 2000). The gamma phosphate of GTP interacts with elements of the switch I and switch II regions, thereby stabilizing their conformation. Switch regions can sense the nucleotide state and alter the outer shape of the G protein allowing not only for binding to effectors but also to GEFs and GAPs, which can

discriminate between the GDP- and GTP-bound forms (Ostermeier and Brunger, 1999; Cherfils and Zeghouf, 2013). Although the switch mechanism is a conserved and universally found module in G proteins, contributions of switch regions to nucleotide binding vary among small GTPases. The same applies to the G domain, whose structure, function and GTPase reaction are modified for many different pathways and processes.

The Ras superfamily of small GTPases is composed of more than 150 human members, which can be subclassified into five major braches on the basis of sequence and functional similarities: Ras, Rho, Ran, Rab and Arf families (Wennerberg *et al.*, 2005). Protein members of the Ras-like proteins in brain (Rab) and the ADP-ribosylation factor (Arf) families are master regulators of membrane trafficking and are involved in all steps of vesicular transport (Gillingham and Munro, 2007; Stenmark, 2009). Thus, Rab and Arf proteins represent likely candidates for the regulation of membrane trafficking to the cilium and will be described in detail in the following sections.
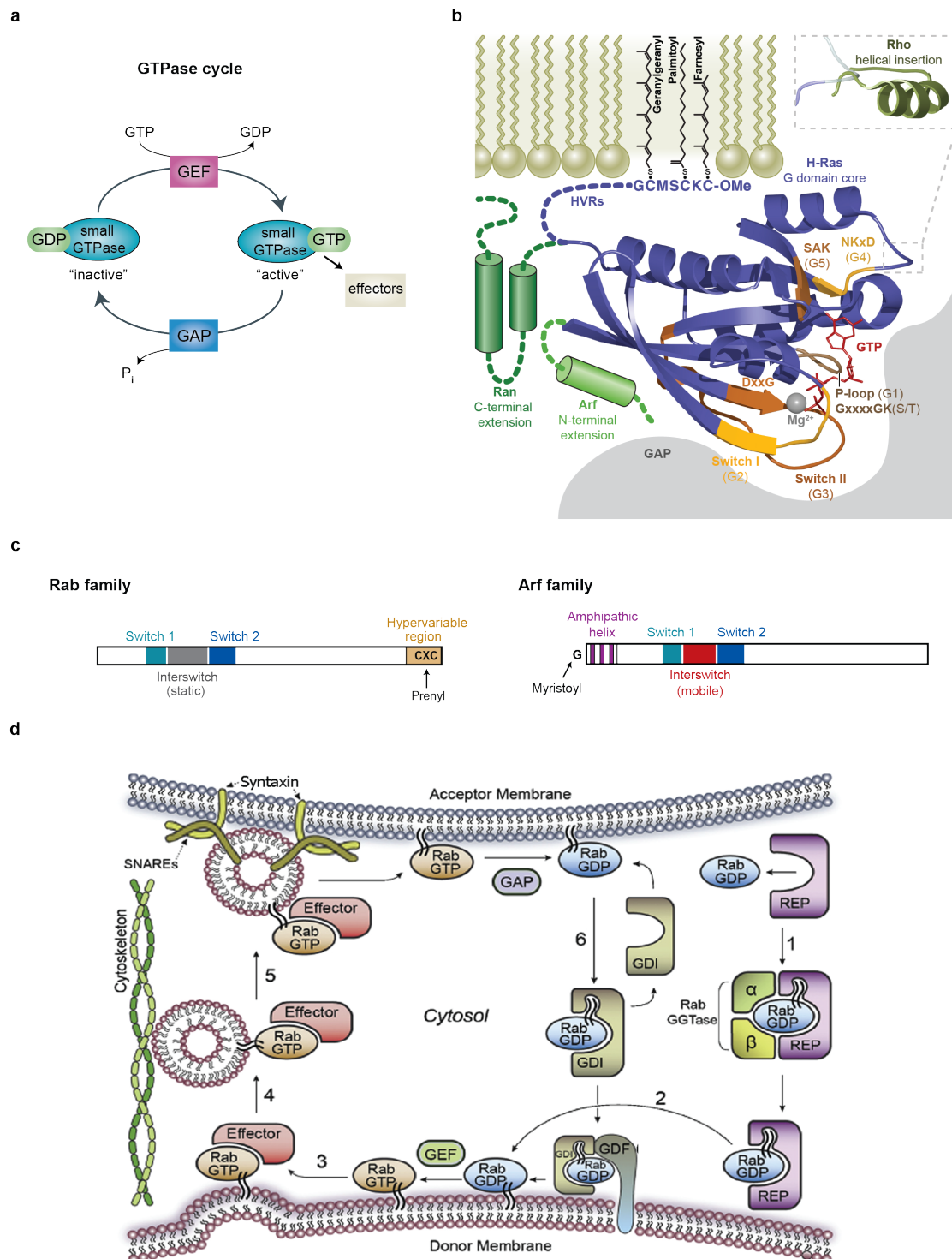
Figure 9: General and structural features of small GTPases. *a) Small GTPases undergo a cycle of GTP binding and hydrolysis mediated by guanine nucleotide exchange factors (GEFs) and GTPase activating proteins (GAPs), respectively. The GDP-bound form is considered to be inactive, whereas the active GTP-bound conformation recruits various effectors. b) Structure of the G domain core and variations found in different small GTPase subfamilies are presented. G proteins possess conserved G-motifs (G1-G5) including the nucleotide sensitive switch regions. In additional to G-motifs, nucleotide-binding usually requires Mg^{2+}, an*

38

essential cofactor. Hypervariable regions (HVRs) are found at the C-terminus and subjected to posttranslational lipid modifications e.g. attachment of geranylgeranyl groups, which are required for membrane attachment. c) Schematic representation of members of the Arf and the Rab family is depicted. The Arf proteins possess a conserved N-terminal amphipathic helix, which is often myristoylated, while Rab proteins have C-terminal hypervariable domains followed by prenyl-groups attached to one or two carboxy-terminal cysteine residues. Upon GTP-binding, switch regions change their conformation; in the case of Arf proteins the interswitch region is also mobile. d) The Rab GTPase cycle and involved regulators are presented. Rab proteins cycle between the cytosol and the membrane of its respective transport compartment. Newly synthesized Rabs bind to Rab escort proteins (REPs) in their GDP-bound form. REPs present the Rab to a Rab GGTase, which attaches geranylgeranyl groups to the Rabs (1) and delivers them to the donor membrane (2). GEFs activate the Rabs, which recruit various downstream effectors that allow for budding (3), movement (4), tethering/docking (5) and fusion of the vesicle with the acceptor membrane. Rab GTPases are inactivated by GAPs, followed by extraction via a guanine nucleotide dissociation inhibitor (GDI). GDIs deliver the Rabs back to the donor compartment membrane with assistance from GDI-displacement factors (GDFs), which destabilize the complex to allow for the start of a new cycle. Structural representation in b) is obtained from (Ligeti et al., 2012), schematics in c) from (Gillingham and Munro, 2007) and c) from (Seixas et al., 2013).

1.4.2.2 Arf and Rab GTPases are major regulators of membrane traffic

Rab GTPases

Rab GTPases constitute the largest family of the Ras superfamily with 11 members in yeast and more than 60 members in humans, which localize to specific intracellular compartments consistent with their functions in distinct membrane trafficking pathways (Pereira-Leal and Seabra, 2001; Zerial and McBride, 2001). Rabs ensure the precise delivery of cargos to their correct destinations by coordinating all consecutive stages of vesicular transport such as vesicle formation, budding, uncoating, vesicle and organelle motility, tethering and fusion of vesicles to their target compartments (Stenmark, 2009). Thus, Rab proteins are essential for cell signaling and involved in the control of cell proliferation, differentiation and tumor progression (Recchi and Seabra, 2012). They also regulate a number of basic cellular functions including growth control and maintain organelle homeostasis (Schwartz *et al.*, 2007). Rab proteins are highly compartmentalized in organelle membranes of the endomembrane system e.g. the endoplasmic reticulum, the Golgi apparatus and the early, late or recycling endosomes, but are also present on the nucleus and mitochondria, contributing to define organelle identity and determine transport specificity (Chavrier *et al.*, 1990; Zerial and McBride, 2001). As described previously, Rab GTPases, like other regulatory GTPases, cycle between a GTP-

bound active form and a GDP-bound inactive conformation. The latter is cytosolic, whereas the GTP-bound form associates with membranes of its respective transport compartment to recruit effectors that mediate their downstream functions (Donaldson and Jackson, 2011; Hutagalung and Novick, 2011). Thus, the nucleotide state of Rab proteins influence their localization and activity (Schwartz *et al.*, 2007). In the case of Rab proteins, the accessory factor Rab escort protein (REP) bind to newly synthesized cytosolic Rabs in their GDP-bound form (ALEXANDROV *et al.*, 1994). The REP presents the Rab to a Rab geranylgeranyl transferase (RabGGT), an enzyme, which attaches geranylgeranyl (prenyl-) lipid groups to one or two C-terminal cysteine residues (Seabra, 1996; Shen and Seabra, 1996). After the lipid transfer, the REP delivers the Rab protein to the donor membrane and recycles back to bind other nascent Rab proteins. The covalent modifications of Rabs allow them to attach to the donor membrane, where GEFs convert them into the active GTP-bound form. Active Rabs recruit effectors, which regulate various steps of vesicular transport including budding, vesicle movement, tethering/docking and SNARE-dependent fusion of carrier vesicles with the acceptor membrane (Stenmark, 2009). Consequently, Rabs are inactivated by GAPs and extracted from the donor membrane by guanine nucleotide dissociation inhibitors (GDIs). Similar to REPs, GDIs prevent release of GDP from Rab proteins thereby stabilizing the inactive form (Matsui *et al.*, 1990). They further shield the geranylgeranyl moiety of Rab GTPases and chaperone them to the cytosol (Ullrich *et al.*, 1993; Soldati *et al.*, 1994; Ullrich *et al.*, 1994). Finally, a set of membrane proteins known as GDI-displacement factors (GDFs) can promote GDI release and association of Rabs with the target membrane (Sivars *et al.*, 2003) (Fig. 9d). Thus, GEFs and GDFs might be the main determinants for the characteristic localization pattern of different Rab GTPases to distinct membranes (Sivars *et al.*, 2003; Pfeffer and Aivazian, 2004; Seabra and Wasmeier, 2004; Blümer *et al.*, 2013). However, the exact mechanism of Rab membrane targeting and subcellular localization of Rab GTPases are still a matter of debate.

Membrane attachment of Rab GTPases depends on their post-translational modifications of a cystine motif (CAAX) at the very carboxyl terminus with on or two hydrophobic geranylgeranyl groups (Anant *et al.*, 1998). C-terminal of the small GTPase fold, upstream of the conserved CAAX box, Rab GTPases contain a hypervariable region of about 34-40 amino acids that shows the greatest divergence in sequence among the Rab family (CHAVRIER *et al.*, 1991). The hypervariable regions of Rabs are considered to be flexible (Neu *et al.*, 1997; Ostermeier and Brunger, 1999) thus providing a relative motile polypeptide extension between the prenylation site and the GTPase domain. This characteristic feature suggests that

Rabs inserted into membranes via the C-terminus can extend some distance from the membrane (Figs. 9b,c).

As mentioned previously (1.4.2.1 General features of small GTPases) Rabs resemble other Ras-related GTPases in their overall core fold, comprising the minimal G domain. Although Rab GTPases are structurally very similar, their recruited set of proteins, which regulate their activity and carry out downstream functions, are not. This implies the existence of Rab specific selection features. Comparison of different active Rab structures revealed that the greatest structural heterogeneity is found in their switch regions and a loop that connects α helix 3 with β sheet 5 adjacent to the switch II domain, which can be attributed to effector specificity (Eathiraj *et al.*, 2005; Lee *et al.*, 2009). In addition, multiple sequence analysis of Rab sequences led to the identification of five so-called Rab family sequences, F1–F5, which are conserved among Rabs but absent in other Ras GTPase family members (Pereira-Leal and Seabra, 2000). Rab F-motifs cluster in and around the switch regions. Moreover, the same study identified four Rab subfamily conserved sequences, named SF1-4 that allow for grouping of Rabs into various subfamilies and were predicted to represent effector specific-interaction motifs (Ostermeier and Brunger, 1999; Pereira-Leal and Seabra, 2000; 2001).

Arf GTPases

Like Rab proteins, Arf GTPases play a central role in organizing intracellular membrane transport. Arf proteins not only control vesicular traffic and organelle structure by recruitment of cargo sorting coat proteins, but are also involved in regulating the membrane lipid composition and modulate cytoskeleton dynamics (Donaldson and Jackson, 2011). The complete Arf subfamily has 29 members in humans and comprises Arf, Arl (Arf-like) and Sar (secretion-associated and Ras related) proteins (Kahn *et al.*, 2006; Gillingham and Munro, 2007; Cherfils and Zeghouf, 2013). Although Arf and Rab GTPases have a lot in common, including the localization to specific organelles and the recruitment of a wide range of effectors, Arf proteins display several differences to Rab proteins. One characteristic feature of Arf family G proteins is the presence of an N-terminal amphipathic helix (Pasqualato *et al.*, 2002). A myristoyl group is usually attached to a glycine residue at the second position of the N-terminal amphipathic helix (Figs. 9b,c). In the GDP-bound conformation, the myristoylated amphipathic helix is tucked into a hydrophobic pocket on the core of the GTPase. Upon GTP-binding facilitated by GEFs, the myristoyl group and the associated amphipathic helix are inserted to the membrane

(Antonny *et al.*, 1997). In addition, the exchange of GDP to GTP induces a conformational change not only in the switch regions, but also affect the β2–β3 strands between the switch regions, called interswitch, which moves to displace the N-terminal helix out of its pocket (Goldberg, 1998; Pasqualato *et al.*, 2002; Chavrier and Menetrey, 2010). This mechanism allows the direct coupling of the nucleotide state with membrane association. After GTP hydrolysis facilitated by GAPs, membrane dissociation of Arfs occurs spontaneously without the need of a GDI. The mode of membrane attachment distinguishes Arf proteins from other subfamilies of the Ras superfamily including Rabs. While Rabs have a long flexible C-terminal hypervariable linker domain to which their lipid membrane anchor is attached, the distance between the myristoylated amphipathic helix to the rest of the Arf is very short. Therefore, Arf proteins and their recruited effectors are positioned closer to the membrane surface (Fig. 9c) (Neu *et al.*, 1997). Arf GTPases also undergo a cycle of GTP binding and hydrolysis mediated by GEFs and GAPs, respectively. However, members of the Arf family have a negligible intrinsic GTPase activity; therefore, ArfGAPs are particularly critical for the inactivation of Arf proteins (Randazzo *et al.*, 1992). In addition to a GAP domain and its role in regulating GTP hydrolysis, ArfGAPs have complex, multiple domains that affect the actin cytoskeleton and membranes by specific interactions with lipids and proteins, dependently or independently of their catalytic activity (Inoue and Randazzo, 2007; Donaldson and Jackson, 2011). Thus, ArfGAPs coordinate signaling through their function as scaffolds and act as downstream effectors in additional to signal termination. GTP-bound Arf family members recruit various downstream effectors involved in membrane trafficking that include protein adaptors, coat complexes such as COPI, COPII, GGA and clathrin adaptor proteins AP1-4 (Donaldson and Jackson, 2011). These coat proteins interact with cargo proteins, incorporate them into newly formed transport carriers and promote membrane curvature in preparation of vesicle budding (Gillingham *et al.*, 2004; Lee *et al.*, 2004; Donaldson and Jackson, 2011).

1.4.3 Transport mechanisms of ciliary membrane proteins from the Golgi to the cilium

Membrane proteins destined for the cilium are initially sorted at the trans-Golgi network before they traffic to the basal body or (sub)apical region of polarized cells. Subsequently, different trafficking pathways for the delivery of ciliary membrane proteins exist. Finally, at the periciliary membrane, cilium-bound cargos need to enter the ciliary compartment with or without the aid of the IFT machinery.

1.4.3.1 Ciliary targeting sequences – Sorting of membrane proteins

Proteins often contain sequence elements that serve as a type of cellular zip code to direct them to their destined compartments. For example, nuclear import of protein cargos relies on nuclear localization signals (NLSs) recognized by importin proteins, which promote translocation through the nuclear pore complex (Goldfarb *et al.*, 1986; Stewart, 2007). As mentioned previously similarities between nucleocytoplasmic and ciliary transport suggest that efficient localization of ciliary membrane proteins utilize the same mechanism. Indeed, several ciliary targeting sequences (CTSs) within the targeted proteins have been identified that appear to aid the translocation to the cilium and the ciliary compartment. The first defined CTS has been found in rhodopsin and has been extensively studied (Tam *et al.*, 2000). Rhodopsin, a photosensory GPCR, which localizes to the ciliary photoreceptor outer segment, harbors a CTS at the C-terminal cytoplasmic tail (Tam *et al.*, 2000) (Fig. 7a). The core element of the CTS is the VxPx-motif (where x is any amino acid), which is highly conserved among different species and appears to be responsible for the active sorting and transport of rhodopsin to the OS by regulating the budding of rhodopsin transport carriers (RTCs) vesicles from the trans-Golgi network (Sung *et al.*, 1994; Deretic, 1998; Concepcion *et al.*, 2002). Lack of sequence recognition due to absence or mutations clustered in this VxPx-motif result in rhodopsin mislocalization and lead to the most severe form of the human disease autosomal dominant retinitis pigmentosa (RP) (Deretic, 1998). In addition, a similar C-terminal RVxP-motif present in polycystin-1 and an N-terminal KVHPSST targeting sequence in polycystin-2 have been demonstrated to be critical for ciliary localization (Geng *et al.*, 2006; Ward *et al.*, 2011). Another common ciliary targeting motif is Ax(S/A)xQ identified in the third intracellular loop of a number of GPCRs such as somatostatin (Sstr3) and serotonin (Htr6) (Berbari *et al.*, 2008). Fibrocystin, the human autosomal

recessive polycystic kidney disease gene product is a large transmembrane receptor that is also localized to cilia (Ward *et al.*, 2002; 2003). The fibrocystin protein contains a 18-residue motif in the cytoplasmic tail, which acts as a CTS (Follit *et al.*, 2010). It was suggested that in the case of fibrocystin, rhodopsin and some other ciliary membrane proteins, post-translational modifications such as palmitoylation and myristoylation are additionally required for proper targeting to the cilium (Tam *et al.*, 2000; Tao *et al.*, 2009; Follit *et al.*, 2010). Thus, the sorting of ciliary membrane proteins may be achieved by ciliary targeting sequences but may also be influenced by post-translational modifications.

1.4.3.2 The Arf4-based ciliary targeting complex - Sorting Rhodopsin from the TGN

Targeting of ciliary membrane proteins likely depends on partitioning into specific lipid microdomains and on recognition of their ciliary targeting sequences by specific sorting machineries. A popular cargo to study sorting and trafficking to the cilium is the photosensory-enriched GPCR rhodopsin (Deretic *et al.*, 2005; Mazelova *et al.*, 2009a; Lodowski *et al.*, 2013). As described in the previous chapter, rhodopsin contains a CTS that enables its sorting at the TGN into carrier vesicles for the subsequent transport to the OS in photoreceptor cells (Li *et al.*, 1996; Deretic, 1998). Sorting of rhodopsin is mediated by the sequential formation of a ciliary targeting module (Fig. 10) (Mazelova *et al.*, 2009a). The first member shown to be involved in this process is Arf4, a small GTPase of the Arf family that also localizes to the TGN of photoreceptor cells, where the Arf GEF GBF1 activates it (Deretic *et al.*, 2005; Szul *et al.*, 2007; Lowery *et al.*, 2013). Activated Arf4 directly interacts with the VxPx-motif of rhodopsin (Deretic *et al.*, 2005). Upon binding, additional components are recruited, which form a ciliary targeting complex at the TGN thereby acting as an effector of Arf4 (Mazelova *et al.*, 2009a). The Arf4-based ciliary targeting complex is composed of three additional members: the Arf GTPase activating protein ASAP1 (Brown *et al.*, 1998; Randazzo and Hirsch, 2004), the small Rab GTPase Rab11a (Chen *et al.*, 1998), and the Arf/Rab effector FIP3 (Fig. 10) (Hales *et al.*, 2001; Junutula *et al.*, 2004; Schonteich *et al.*, 2007; Mazelova *et al.*, 2009a). After binding of Arf4 to rhodopsin via the VxPx-motif, ASAP1 appears to recognize a second FR ciliary targeting motif of rhodopsin and to form a tripartite complex with activated Arf4 and the cargo (Corbit *et al.*, 2005; Wang *et al.*, 2012). Moreover, the Arf4 mutant I46D, deficient in ASAP1 induced GTP hydrolysis, disrupts rhodopsin trafficking, which leads to retinal degeneration in transgenic animals (Mazelova *et al.*, 2009a).

ASAP1 is a large, multifunctional scaffold protein that not only possesses an Arf GAP domain to mediate GTP hydrolysis on Arf4, but also contains an N-terminal BAR (Bin/amphiphysin/Rvs) domain, a pleckstrin homology (PH) domain, an ankyrin repeat-containing domain, a proline-rich and a C-terminal SH3 domain, which enable protein-protein and protein-lipid interactions (Brown *et al.*, 1998; Peter *et al.*, 2004; Mazelova *et al.*, 2009a; Jian *et al.*, 2015). The BAR domain of ASAP1 mediates homodimerization, induces membrane curvature and has an autoinhibitory effect on the GAP activity (Nie *et al.*, 2006; Jian *et al.*, 2009). Through its BAR domain ASAP1 furthermore directly interacts with the Arf/Rab11 effector FIP3, which is supposed to stimulate the Arf GAP activity of ASAP1 (Inoue *et al.*, 2008). ASAP1 binds selectively Rab11 and FIP3 that also acts as a dimer (Eathiraj *et al.*, 2006; Inoue *et al.*, 2008; Wang *et al.*, 2012). The next step involves GTP hydrolysis by ASAP1, which results in inactivation and dissociation of Arf4, whereas ASAP1 and Rab11 are considered to remain associated at the TGN. Thus, the Arf4-based ciliary targeting complex sorts and packs rhodopsin into ciliary-targeted RTCs at the TGN.

Some time later, it became apparent that subsequent budding and transport of RTCs from the Golgi requires additional components of a conserved ciliogenesis cascade (Knödler *et al.*, 2010; Westlake *et al.*, 2011; Feng *et al.*, 2012; Wang *et al.*, 2012) (see 1.4.3.3 Conservation between exocytosis in yeast and ciliary targeting in mammals). Besides Rab11, a constituent of the Arf4-based ciliary targeting complex and the ciliogenesis cascade, another Rab GTPase, termed Rab8 and its GEF Rabin8 (Hattula *et al.*, 2002) facilitate transport of RTCs (Deretic *et al.*, 1995; Moritz *et al.*, 2001; Wang *et al.*, 2012). Rab8 is key regulator of ciliogenesis and controls the final stages of polarized membrane traffic by mediating docking and fusion of vesicles at the base of the cilium (Deretic *et al.*, 1995; Moritz *et al.*, 2001; Nachury *et al.*, 2007; Yoshimura *et al.*, 2007; Omori *et al.*, 2008). Furthermore it was suggested that Rab11 activates Rab8 via interaction with Rabin8, which together constitute a cascade of molecular interactions termed ciliogenesis cascade (Knödler *et al.*, 2010; Westlake *et al.*, 2011; Feng *et al.*, 2012). Rabin8 is recruited to the TGN, to interact with Rab11 and ASAP1 respectively, concomitant with the formation of post TGN-carriers (Wang *et al.*, 2012). Finally, Rab8, via Rabin8 interaction, associates with the budding vesicles, while ASAP1 may act as a scaffold protein for stepwise assembly of the ciliary targeting complex (Wang *et al.*, 2012). Besides rhodopsin, Arf4 and also Rab8 bind to other ciliary targeting sequences of membrane proteins destined for the cilium, which include fibrocystin-1 and polycystin-1 (Follit *et al.*, 2010; Ward *et al.*, 2011; Follit *et al.*, 2014). Deletion of the CTS in polycystin-1 or knockdown of the regulators Arf4 and Rab8 hinders delivery of polycystin-1 to the cilium implying that

GTPase-dependent ciliary targeting complexes utilize a trafficking mechanism that is conserved in diverse cell types and organisms (Ward *et al.*, 2011).
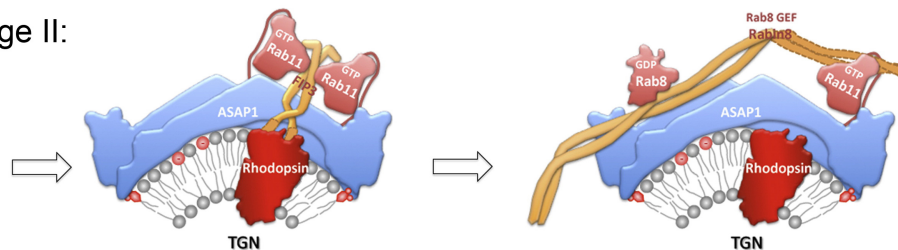
Stage I:
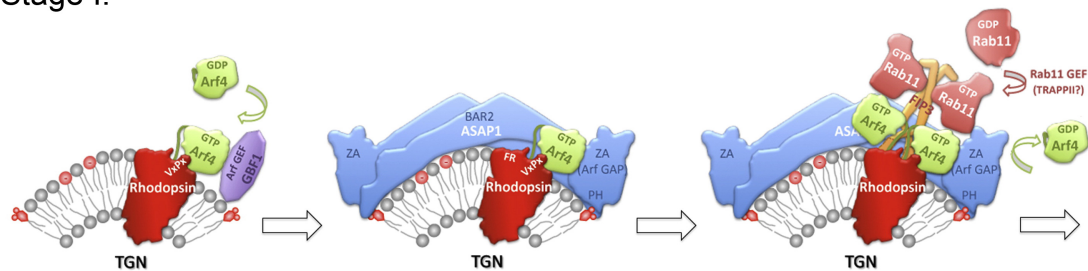
Stage II:

Figure 10: Ciliary targeting complex assembly at the TGN. At stage I, Arf4 is activated by the putative Arf GEF GBF1, becomes membrane-associated and interacts with rhodopsin via the VxPx ciliary targeting sequence (CTS). Active Arf4 and possibly rhodopsin recruit ASAP1, the Arf4 GAP, to the TGN. ASAP1 dimerizes through the BAR domain, which likely induce membrane curvature required for vesicle budding. ASAP1 binds to the Rab GTPase Rab11 and the Rab/Arf effector FIP3, which also acts as a dimer. In stage II, Arf4 is inactivated by ASAP1 and dissociates from the TGN while the remaining components stay associated. In the next step, ASAP1 and Rab11 recruit the Rab8 GEF Rabin8 and the inactive Rab GTPase Rab8. Activation of Rab8 likely takes places during budding of the rhodopsin transport carriers (RTC), which renders them competent for fusion with the periciliary membrane. The schematics are obtained from (Wang and Deretic, 2013).

1.4.3.3 Conservation between exocytosis in yeast and ciliary targeting in mammals

A plausible route or pathway of post-Golgi vesicles containing ciliary membrane proteins including rhodopsin relies on exocytosis at the periciliary base (Papermaster *et al.*, 1985; Rosenbaum and Witman, 2002; Pazour and Bloodgood, 2008). Studies of the yeast secretory pathway revealed that the delivery and fusion of Golgi-derived vesicles with the plasma membrane involves a regulatory mechanism, which is facilitated by a Rab GEF cascade (Ortiz *et al.*, 2002). In the budding yeast, Sec2p (Rabin8 homolog) acts as a GEF for Sec4p (Rab8 homolog) an important process

required for the regulation of the final stages of the exocytic pathway (Walch-Solimena *et al.*, 1997). Sec2p is recruited to the Golgi by phosphatidylinositol-4-phosphate (PI4P) and another active Rab GTPase, termed Ypt32p (Rab11 homolog), but shows no GEF activity towards Ypt32p, leading to the conclusion that Sec2p acts as an effector of the Ypt32p GTPase (Ortiz *et al.*, 2002). Interaction of Sec2p and Ypt32p promotes vesicle budding from the TGN, whereas Sec2p subsequently activates Sec4p to facilitate fusion of the secretory vesicle with the plasma membrane (Ortiz *et al.*, 2002; Mizuno-Yamasaki *et al.*, 2012). On arrival, vesicles have to be further tethered to the plasma membrane through association with the exocyst, an octameric protein complex (TerBush *et al.*, 1996). Members of the exocyst are evolutionarily conserved from yeast to human. Furthermore, the exocyst subunit Sec15p associates with secretory vesicles and interacts with the active form of Sec4p (Guo *et al.*, 1999; Hsu *et al.*, 2004). In addition, Sec15p and the GEF Sec2p directly bind to each other on the surface of vesicles. The interaction serves to couple nucleotide exchange on Sec4p and to recruit effectors of Sec4p (Medkova *et al.*, 2006). Furthermore, it was shown that Ypt32p and Sec15p compete for binding to Sec2p and that the switch from the Rab GEF cascade Ypt32p-Sec2p-Sec4p to a Sec2p-Sec4p-Sec15p positive-feedback loop is regulated by Golgi-associated PI4P levels (Medkova *et al.*, 2006; Mizuno-Yamasaki *et al.*, 2010; 2012). The yeast Rab cascade of Ypt32-Sec2p-Sec4p-Sec15p parallels the mammalian Rab11-Rabin8-Rab8-Sec15 ciliogenesis cascade demonstrating an evolutionarily conserved regulatory mechanism that applies not only for exocytosis but also for other stages of membrane traffic (Knödler *et al.*, 2010; Westlake *et al.*, 2011; Feng *et al.*, 2012; Mizuno-Yamasaki *et al.*, 2012). The exocyst localizes to the base of the cilium and different members of the tethering complex have been suggested to play an important role in ciliogenesis (Rogers *et al.*, 2004; Park *et al.*, 2008; Zuo *et al.*, 2009; Mazelova *et al.*, 2009b). In agreement with studies in the budding yeast, the exocyst component Sec15 interacts with active Rab8 and its GEF Rabin8, whereas inhibition of Sec15 function leads to impaired cilia formation (Das and Guo, 2011; Feng *et al.*, 2012). Sec15 is not only a downstream effector of Rab8, but also of Rab11, which differs from the yeast system (Zhang *et al.*, 2004; Wu *et al.*, 2005; Bryant *et al.*, 2010). The interplay of Rab11, Rabin8, Rab8 and Sec15 is required to regulate vesicle tethering and fusion during primary ciliogenesis.

1.5 Scope of the thesis

It is well established that cilia, found on nearly all cells in the human body, play an important role in organismic development and tissue homeostasis. Consistent with their almost ubiquitous presence on human cells, defects in the delivery of ciliary cargo required for assembly and proper function of the cilium are the underlying cause of various human disorders, commonly referred to as 'ciliopathies' with phenotypes that include kidney failures, infertility and many more. In order to carry out their diverse functions, cilia rely on a unique set of both soluble and membrane proteins. The absence of a biosynthetic machinery in the cilium requires a highly regulated sorting and transport machinery to achieve proper ciliary localization of these signaling factors. Some progress has been made in the past decade regarding the identification and characterization of the key players implicated in sorting and trafficking of ciliary membrane proteins. Nevertheless, several important details about direct protein-protein interactions within components of the ciliary sorting and transport machinery, the overall architecture of ciliary targeting complexes, as well as the underlying regulatory mechanism of membrane protein trafficking from the Golgi to the cilium remain elusive. Biochemical reconstitution and structural characterization of ciliary targeting complexes are important to shed light on these issues.

The work presented in this thesis aims to elucidate the regulated assembly of such ciliary targeting complexes, as well as their three-dimensional architecture, using biochemical and structural approaches. In particular, the main questions that will be addressed are: (1) How do individual subunits of ciliary targeting complexes including Rab11, ASAP1, FIP3, Rabin8 and Rab8 interact with each other and what are their functions regarding complex formation and/or stability? (2) Is Rabin8 an effector of the small GTPase Rab11, and if so, what are the crucial residues for complex formation? (3) What is the molecular basis for ciliary targeting complex assembly, and how does Rab11 recruit several effectors (such as FIP3 and Rabin8) simultaneously? (4) Can the findings made on the mechanism of ciliary cargo sorting and transport also be used for other cargo sorting and transport processes?

2 Results

2.1 Structure of Rab11–FIP3–Rabin8 reveals simultaneous binding of FIP3 and Rabin8 effectors to Rab11

Vetter, M., Stehle, R., Basquin, C. & Lorentzen, E. (2015). Structure of Rab11–FIP3–Rabin8 reveals simultaneous binding of FIP3 and Rabin8 effectors to Rab11. *Nature Structural and Molecular Biology* (22(09), pages 695-702).

Methods and supplementary material are attached at the end of the article.

Structure of Rab11–FIP3–Rabin8 reveals simultaneous binding of FIP3 and Rabin8 effectors to Rab11

Melanie Vetter[1], Ralf Stehle[2], Claire Basquin[1] & Esben Lorentzen[1]

The small GTPase Rab11 and its effectors FIP3 and Rabin8 are essential to membrane-trafficking pathways required for cytokinesis and ciliogenesis. Although effector binding is generally assumed to be sequential and mutually exclusive, we show that Rab11 can simultaneously bind FIP3 and Rabin8. We determined crystal structures of human Rab11–GMPPNP–Rabin8 and Rab11–GMPPNP–FIP3–Rabin8. The structures reveal that the C-terminal domain of Rabin8 adopts a previously undescribed fold that interacts with Rab11 at an unusual effector-binding site neighboring the canonical FIP3-binding site. We show that Rab11–GMPPNP–FIP3–Rabin8 is more stable than Rab11–GMPPNP–Rabin8, owing to direct interaction between Rabin8 and FIP3 within the dual effector–bound complex. The data allow us to propose a model for how membrane-targeting complexes assemble at the trans-Golgi network and recycling endosomes, through multiple weak interactions that create high-avidity complexes.

Trafficking of proteins via membrane-bound vesicles is vital to cellular functions such as ciliogenesis, secretion, autophagy, cytokinesis and cell adhesion[1–4]. Important and highly regulated steps of membrane trafficking are cargo recognition and sorting as well as vesicle formation and transport. These steps rely on a number of protein complexes that assemble on donor membranes and function to facilitate cargo selection and assist in vesicle formation and transport to the acceptor membrane where fusion occurs. Numerous small GTPases of the Rab, ADP-ribosylation factor (Arf) and Arf-like (Arl) families are essential components of membrane-trafficking complexes[1,2,5]. Rabs constitute the largest family of GTPases, comprising more than 70 members that interact with numerous downstream effectors to control vesicular transport at various stages[2,6]. Different Rabs generally regulate different membrane-trafficking events and are often specifically located to a particular intracellular organelle, although some Rabs are involved in multiple transport pathways. One such versatile Rab is Rab11, which localizes to endosomes and the trans-Golgi network (TGN) and is required for cleavage-furrow formation during cytokinesis, for ciliogenesis and for recycling of membrane receptors such as β1 integrins to the plasma membrane[7–12].

The extension of the ciliary membrane during ciliogenesis and the ciliary targeting of membrane proteins require the delivery of vesicles to the ciliary base[13–15]. This process relies on ciliary-targeting complexes that include Arf4, Rab11 family–interacting protein 3 (FIP3), Rabin8 and ASAP1 (refs. 15–17) in addition to Rab11. Genetic mutations in cilia-assembly factors cause a number of human ciliopathies including polycystic kidney disease, retinal degeneration and Bardet-Biedl syndrome[18–22]. An early step of vesicular transport to the cilium is the sorting of ciliary cargos such as rhodopsin[23] and fibrocystin[24] at the TGN; this process critically depends on the recognition of ciliary-targeting sequences (CTSs) by the small GTPase

Arf4 (ref. 25). Mutations clustered within the CTS of rhodopsin (C-terminal VxPx motif) lead to one of the most severe forms of autosomal-dominant retinitis pigmentosa, causing blindness[25,26]. Rab11 and Arf4 are linked by the common effector protein FIP3, which is required for the integrity of recycling endosomes and the transport of rhodopsin to cilia[15,27–31]. Additionally, ciliary-targeting complexes contain the protein ASAP1, which is an effector and a GTPase-activating protein (GAP) for Arf4 (ref. 15). ASAP1 also interacts with Rab11 and FIP3 and contains a Bin-amphiphysin-Rvs (BAR) domain, which is typically found in proteins that bind membranes to induce curvature[11,15,32]. Ciliary membrane extension requires Rab8 and its guanine nucleotide exchange factor (GEF), Rabin8, which presumably facilitates docking and fusion of post-Golgi vesicles at the ciliary base[13,14,33]. Strikingly, the inhibition of Rab8 function results in pronounced accumulation of rhodopsin carrier vesicles near the ciliary base of photoreceptor cells[34]. Rabin8, an effector of Rab11, is recruited to the ciliary-targeting complex (ref. 33), in which it presumably replaces the FIP3 effector[35], thus resulting in the activation of Rab8. The high-resolution architecture of ciliary-targeting-complex assembly is largely unknown.

We set out to elucidate the assembly and architecture of ciliary-targeting complexes. To this end, we reconstituted human ciliary-targeting complexes and determined the crystal structures of Rab11–Rabin8 and Rab11–FIP3–Rabin8. The C-terminal domain of Rabin8 adopts a previously undescribed fold that interacts with Rab11 via an unusual effector-binding site to form heterotetramers. In the dual effector–bound Rab11–FIP3–Rabin8 complex, the two effectors interact with Rab11 and with each other to form heterohexameric 2:2:2 assemblies. Contrary to previously proposed architectural models of ciliary-targeting complexes, our data show that binding of FIP3 and of Rabin8 effectors to Rab11 is not

mutually exclusive. Indeed, we find that Rabin8 has an affinity that is four times higher for Rab11–FIP3 than for Rab11 alone, thus demonstrating that dual effector–bound ciliary-targeting complexes have higher stability.

RESULTS

Structure of Rab11–Rabin8 reveals a heterotetramer

We purified constitutively active human Rab11a(Q70L)–5′-guanylyl imidodiphosphate (GMPPNP) (residues 6–186; hereafter referred to as Rab11) and crystallized it in complex with the purified C-terminal domain of human Rabin8 (Rabin8C, residues 270–460). Rabin8C is an effector of Rab11 (ref. 33), and the Rab11-Rabin8 interaction is required for the recruitment of Rabin8 to vesicles and the accumulation of vesicles at the ciliary base[14]. In addition to its C-terminal domain, Rabin8 contains a central coiled-coil domain that acts as a GEF toward Rab8 (refs. 33,36) (**Fig. 1a**). In agreement with the reported low affinity[37], we did not observe a stable complex between Rab11 and Rabin8C in size-exclusion chromatography (SEC) (**Supplementary Fig. 1a**), but we nevertheless obtained crystals of the complex when the proteins were mixed at high concentration. We found that Rabin8C alone formed a stable homodimer, as determined by SEC and analytical ultracentrifugation (AUC) (**Supplementary Fig. 1b**), a result in agreement with the central coiled-coil domain of Rabin8 adopting a parallel homodimeric structure[36]. The crystal structure of Rab11–Rabin8C at 2.6-Å resolution (R_{free} of 27.1%; **Table 1**) revealed that the Rabin8C dimer contains two Rab11-binding sites and forms a heterotetrameric complex organized around a dyad axis (**Fig. 1b**). This result is in agreement with isothermal titration calorimetry (ITC) experiments demonstrating that each Rabin8C homodimer contains two binding sites for Rab11 (**Fig. 1e**).

The K_d for the Rab11–Rabin8C complex was 40.2 ± 2.0 μM (mean ± s.d.), a value in agreement with previously published results (K_d of 54 μM; ref. 37). The stoichiometry (N) value close to 2 (1.93) indicates that each Rabin8C homodimer binds two Rab11 subunits, a result consistent with the quaternary structure observed in the crystal structure. We found that the structure of Rabin8C adopted a previously undescribed fold consisting of five α-helices and three strands of antiparallel β-sheet (**Fig. 1b** and **Supplementary Fig. 2**). The Rabin8C dimer is formed by residues from helices α2 and α5 as well as by domain-swapped two-stranded antiparallel β-sheets consisting of the N- and C-terminal residues of the Rabin8C construct (**Fig. 1c**). In the Rab11–Rabin8C complex, residues from helix α4 and β-strand β2 of Rabin8C contact residues from switch I and the loop connecting β5 and α4 of Rab11 (**Fig. 1b,d**). The guanine moiety of GMPPNP bound to Rab11 makes a hydrogen bond with the hydroxyl group of Y423 of Rabin8, thus contributing directly to complex formation (**Fig. 1d**). We note that residues 300–305 of Rabin8, whose deletion was reported to reduce Rab11 binding in a previous study[37], are found in helix α1, which is part of the Rabin8C core fold and does not interact directly with Rab11 in our crystal structure. Interestingly, each Rabin8 monomer interacts with both Rab11 subunits in the
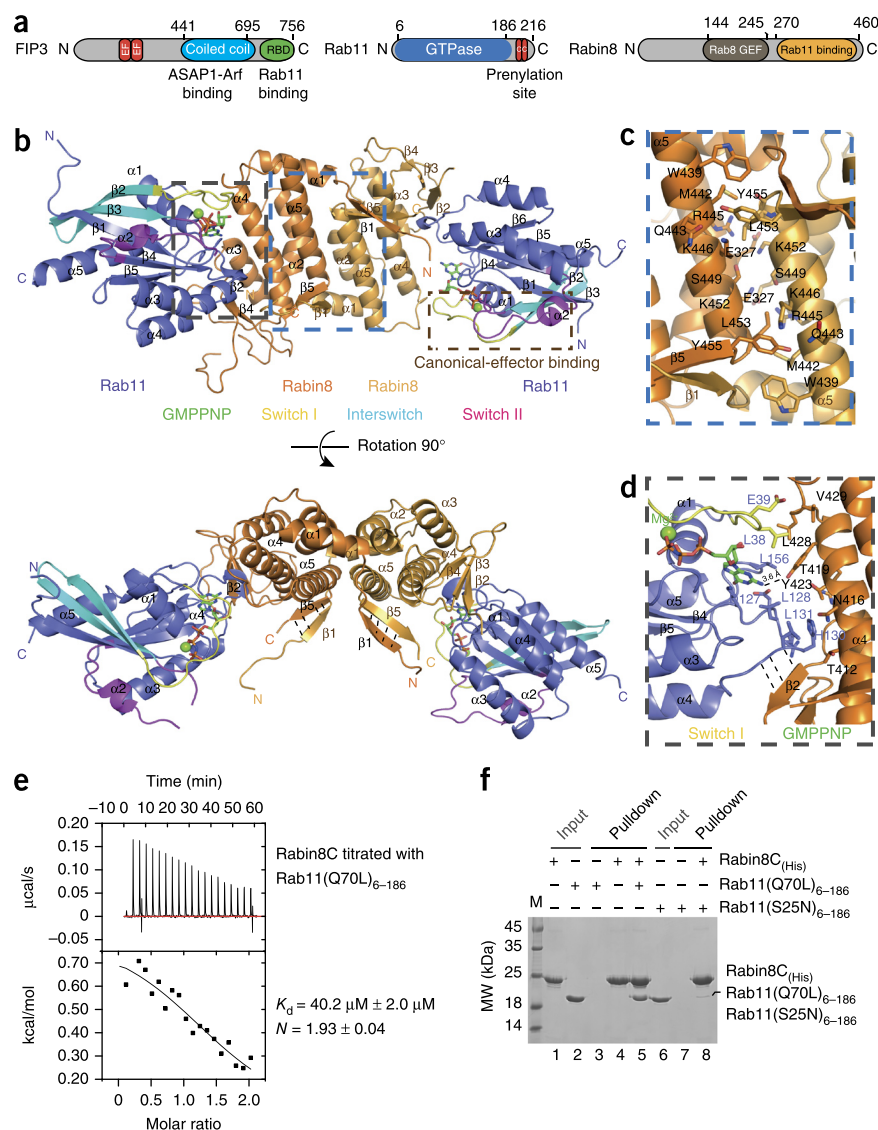

Figure 1 Crystal structure of heterotetrameric Rab11–Rabin8C. (**a**) Domain representation of the small GTPase Rab11 and its effectors FIP3 and Rabin8. Domains are indicated, and the numbers above the schematics annotate the constructs used in this study. EF, tandem repeat of EF hands. (**b**) The crystal structure of the Rab11–Rabin8C complex in two perpendicular orientations, shown in cartoon representation. Mg²⁺ ions are shown as balls and the GMPPNP as sticks. (**c**) Zoomed-in view of the Rabin8C homodimerization interface, showing interacting residues of helices α5. Domain-swapped β-strands 1 and 5 interact via main chain hydrogen bonds. (**d**) Zoomed-in view on the Rab11-Rabin8C interaction interface. Interactions between the hydroxyl group of Y423 and the guanine base of GMPPNP and backbone interactions between β2 of Rabin8C and loop β5–α4 of Rab11 are indicated with dashed lines. (**e**) ITC experiment in which Rabin8C was titrated with Rab11(Q70L)₆₋₁₈₆. The s.d. of 2.0 μM was calculated from 3 independent ITC experiments. (**f**) SDS-PAGE gel of an Ni²⁺-NTA pulldown of constitutively active Rab11(Q70L)₆₋₁₈₆ or nucleotide-free Rab11(S25N)₆₋₁₈₆. M, marker. Uncropped images are shown in **Supplementary Data Set 1**.

51

Table 1 Data collection and refinement statistics

	HsRab11–GMPPNP–Rabin8C	HsRab11–GMPPNP–FIP3$_{RBD}$–Rabin8C	HsRab11–GMPPNP–FIP3$_{RBD}$–Rabin8C_2
Data collection			
Space group	$P12_11$	$P12_11$	$P2_12_12_1$
Cell dimensions			
a, b, c (Å)	51.7, 108.2, 75.7	67.5, 165.4, 218.7	66.1, 161.7, 192,8
α, β, γ (°)	90.0, 102.8, 90.0	90.0, 95.9, 90.0	90.0, 90.0, 90.0
Resolution (Å)[a]	50–2.60 (2.70–2.60)	50–2.97 (3.14–2.97)	50–4.2 (4.40–4.20)
R_{sym}	0.037 (0.74)	0.045 (0.65)	0.13 (0.67)
$I / \sigma I$	13.8 (0.9)	19.4 (1.8)	10.6 (1.6)
Completeness (%)	94.5 (84.1)	94.6 (93.5)	93.7 (61.2)
Redundancy	3.5 (3.4)	6.8 (6.8)	4.2 (3.0)
Refinement			
Resolution (Å)	2.60	3.0	4.2
No. reflections	24,951 (2,382)	92,398 (13,704)	15,543 (1,540)
R_{work} / R_{free}	0.210 / 0.271	0.199 / 0.250	0.225 / 0.276
No. atoms			
Protein	5,464	23,494	11,772
Ligand/ion	2 Mg^{2+}, 2 GMPPNP, 1 SO$_4$	8 Mg^{2+}, 8 GMPPNP	4 Mg^{2+}, 4 GMPPNP
Water	160	62	–
B factors			
Protein	78.2	49.7	160.7
Ligand/ion	54.1	28.3	140.4
Water	60.1	34.4	–
r.m.s. deviations			
Bond lengths (Å)	0.010	0.006	0.006
Bond angles (°)	1.51	1.10	1.1

[a]One crystal was used for each measurement. Values in parentheses are for the highest-resolution shell. GMPPNP, 5′-guanylyl imidodiphosphate (nonhydrolyzable GTP analog). Hs, *Homo sapiens*.

heterotetramer as the domain-swapped N-terminal region of Rabin8C extends across the complex to contact helix α3 of the second Rab11 subunit (**Fig. 1b**). Whereas single point mutations of Rab11-interacting residues in Rabin8 to alanine did not abolish formation of the Rab11–Rabin8C complex, the triple point mutation T419A Y423A L428A (**Fig. 1d**) did substantially weaken complex formation, thus providing a biochemical validation of the Rab11–Rabin8C interface (**Supplementary Fig. 1c–e**). We conclude that Rabin8 interacts with Rab11 via a new fold to form a heterotetramer.

Unusual effector binding of the Rab11–Rabin8 complex
Effectors typically recognize the switch regions of active GTP-bound small GTPases[38]. That Rabin8C makes only two contacts with residues of switch I and no contacts with switch II makes it a rather unusual effector (**Fig. 1d**). However, pulldown experiments with affinity-tagged Rabin8C revealed a strong preference for GTP-bound active Rab11, thus confirming that Rabin8 is indeed an effector for Rab11 (**Fig. 1f**, **Supplementary Data Set 1** and ref. 33). Structural comparison with previously determined Rab11 structures revealed that the Rabin8-binding site on Rab11 is similar to that of the phosphatidylinositol 4-kinase PI4KIIIβ (ref. 39) (**Supplementary Fig. 3a**). Although PI4KIIIβ and Rabin8C adopt different folds, they use the same binding surface on Rab11. A prediction from the structural overlay (**Supplementary Fig. 3a**) is that binding of Rabin8 and PI4KIIIβ to Rab11 is mutually exclusive. PI4KIIIβ in complex with Rab11 is able to simultaneously bind the homodimeric effector FIP3, as demonstrated by the crystal structure of the ternary complex determined at 6-Å resolution[39]. Structural overlay of the Rab11–Rabin8C structure presented here with previously determined structures of Rab11 in complex with the effector FIP3 (refs. 40,41) suggested the possibility

of simultaneous binding of FIP3 and Rabin8 to Rab11 (**Supplementary Fig. 3b**). Although a dodecameric Rab11–FIP3–Rabin8 complex is possible in principle, clashes between FIP3 and Rabin8 molecules suggested that a hexameric complex is more likely. We conclude that Rabin8 binds Rab11 at an unusual effector-binding site that would in principle allow for the simultaneous binding of a different effector at the canonical effector–binding site.

Rab11 simultaneously binds Rabin8 and FIP3 effectors
To test the hypothesis of simultaneous binding of Rabin8 and FIP3 effectors to Rab11, we mixed purified human Rab11 with FIP3 Rab-binding domain (FIP3$_{RBD}$) and Rabin8C and carried out SEC (**Fig. 2a**). The minimal FIP3$_{RBD}$ (residues 695–756) was previously reported to bind Rab11 with the same affinity as longer FIP3 constructs[40]. The copurification experiment demonstrated that the Rab11–FIP3$_{RBD}$–Rabin8C complex coeluted in a relatively broad peak separate from the elution peaks of the individual proteins (**Fig. 2a** and **Supplementary Data Set 1**). The apparent excess of Rabin8 in the later fractions on the SDS gel (**Fig. 2a**) is probably a result of overlap with the elution profile for the homodimeric Rabin8C that was added in excess. The Rab11–FIP3$_{RBD}$–Rabin8C complex had an apparent molecular weight (MW) of 81 kDa, which is consistent with a hexameric complex containing two subunits of each protein (calculated MW of 100 kDa). The coelution of Rab11–FIP3$_{RBD}$–Rabin8C as a complex during SEC suggested higher stability of the ternary complex than Rab11–Rabin8C, for which we observed almost-complete dissociation during SEC (**Supplementary Fig. 1a**). To address this increased stability quantitatively, we carried out ITC of Rab11–FIP3$_{RBD}$ with Rabin8C (**Fig. 2c**). The dissociation constant of Rabin8C from the Rab11–FIP3$_{RBD}$ complex was 10.8 ± 2.1 μM, which represents a four-fold increase in binding affinity as compared to the 40.2 μM measured for the Rab11–Rabin8 complex (**Fig. 1e**). The increased affinity is likely to be a result of direct contacts between the two effectors, because FIP3$_{441-C}$ (containing the Arf-binding domain in addition to the C-terminal RBD) was pulled down by affinity-tagged Rabin8$_{144-C}$ (containing the Rab8 GEF domain in addition to the Rab11-binding C-terminal domain) (**Fig. 2b**, lane 6, and **Supplementary Data Set 1**). To test whether longer constructs of Rabin8 and FIP3 also simultaneously associate with Rab11, we performed pulldown experiments. FIP3$_{441-C}$ and Rabin8$_{144-C}$ interacted to form a ternary complex with Rab11 (**Fig. 2b**, lane 7 and **Supplementary Data Set 1**). Additionally, we found that a Rab11–FIP3–Rabin8 complex could also be reconstituted with full-length (fl) proteins (**Supplementary Fig. 3c**). We conclude that Rabin8 and FIP3 effectors simultaneously bind Rab11 and that dual effector–bound complexes are more stable than the single effector–bound Rab11–Rabin8 complex.

Rab8 GEF activity and Arf4 binding by Rab11–FIP3–Rabin8
The reconstituted Rab11–FIP3$_{441-C}$–Rabin8$_{fl}$ or Rab11–FIP3$_{441-C}$–Rabin8$_{144-C}$ complex contains both the binding region for Arf4 and the
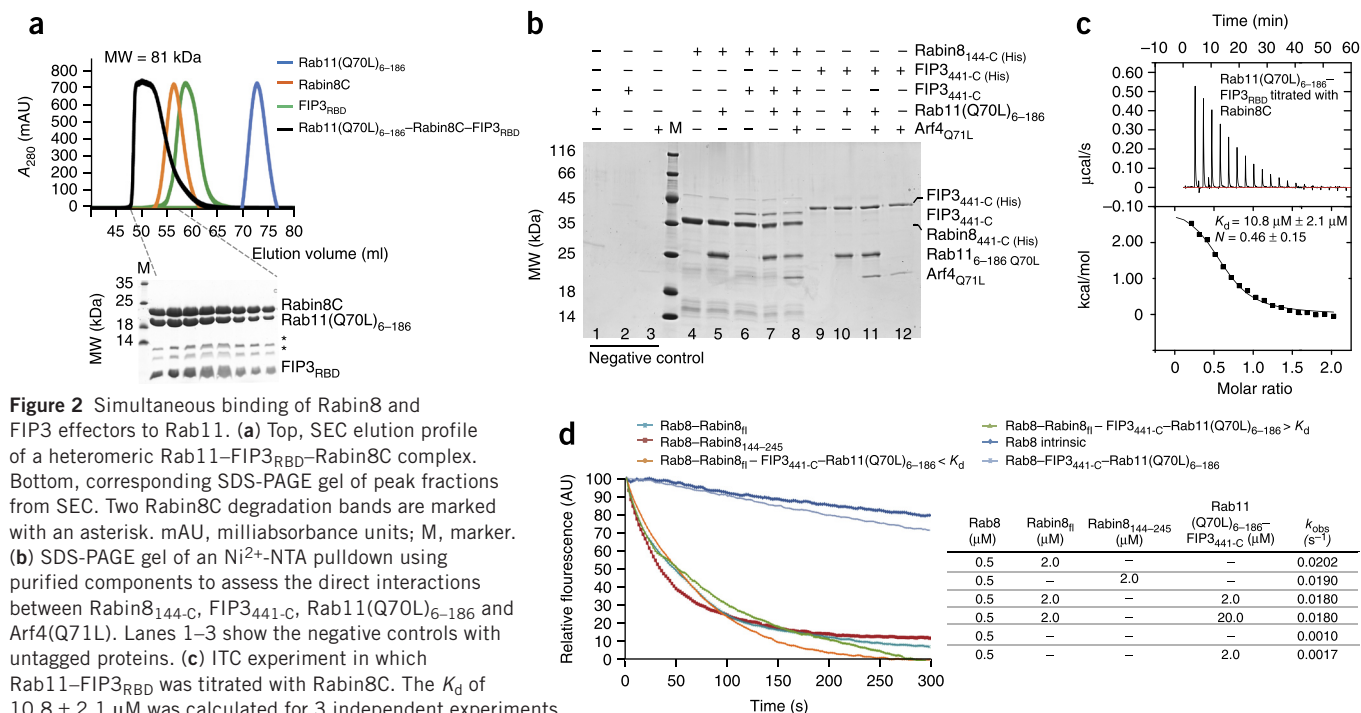
Figure 2 Simultaneous binding of Rabin8 and FIP3 effectors to Rab11. (**a**) Top, SEC elution profile of a heteromeric Rab11–FIP3$_{RBD}$–Rabin8C complex. Bottom, corresponding SDS-PAGE gel of peak fractions from SEC. Two Rabin8C degradation bands are marked with an asterisk. mAU, milliabsorbance units; M, marker. (**b**) SDS-PAGE gel of an Ni^{2+}-NTA pulldown using purified components to assess the direct interactions between Rabin8$_{144-C}$, FIP3$_{441-C}$, Rab11(Q70L)$_{6-186}$ and Arf4(Q71L). Lanes 1–3 show the negative controls with untagged proteins. (**c**) ITC experiment in which Rab11–FIP3$_{RBD}$ was titrated with Rabin8C. The K_d of 10.8 ± 2.1 μM was calculated for 3 independent experiments. (**d**) GEF assay for Rab8 in which the exchange of fluorescently labeled mant-GDP by GTP is followed over time. AU, arbitrary units. The curves are averages of 3 independent experiments. Additional GEF assays were performed with addition of Rab11–FIP3$_{RBD}$ at a concentration either below the K_d (2 μM, orange line) or above the K_d (20 μM, green line) of the Rab11–FIP3–Rabin8C complex. The table to the right of the GEF assay curves shows a quantification of the observed rate constants (k_{obs}) with exponential fitting. Uncropped images are shown in **Supplementary Data Set 1**.

GEF domain for Rab8 (**Fig. 1a**). Pulldown experiments showed that the Rab11–FIP3$_{441-C}$–Rabin8$_{144-C}$ dual effector–bound complex was competent in Arf4 binding (**Fig. 2b**, lane 8). As previously shown[15,27], we verified that Arf4 binds directly to FIP3, because Rab11–FIP3$_{441-C}$ or FIP3$_{441-C}$ was sufficient to pull down Arf4 (**Fig. 2b**, lanes 11 and 12). Rabin8 is a reported GEF that activates Rab8 (refs. 36,42), as is required for the extension of the ciliary membrane[13]. To test whether the dual effector–bound Rab11–FIP3$_{441-C}$–Rabin8$_{fl}$ complex activates Rab8, we carried out GEF assays in which the dissociation of GDP was determined by the release of 2′(3′)-O-(N-methylanthraniloyl)-GDP (mant-GDP) from Rab8 (**Fig. 2d**). The results show that Rab11–FIP3$_{441-C}$–Rabin8$_{fl}$ complex increased the intrinsic GEF activity of Rab8 by ~15-fold. We measured similar GEF activity with Rabin8$_{fl}$ or the Rabin8 GEF domain (**Fig. 2d**). As expected, we did not observe GEF activity for the Rab11–FIP3$_{441-C}$ complex in the absence of Rabin8 (**Fig. 2d**). A previous study reported that Rab11 kinetically stimulates the GEF activity of Rabin8 toward Rab8 (ref. 33). However, we did not observe increased GEF activity of the Rab11–FIP3–Rabin8 complex compared to Rabin8 alone under the conditions of the assay (**Fig. 2d**). We conclude that FIP3 and Rabin8 can simultaneously bind Rab11 to form a functional dual effector–bound complex.
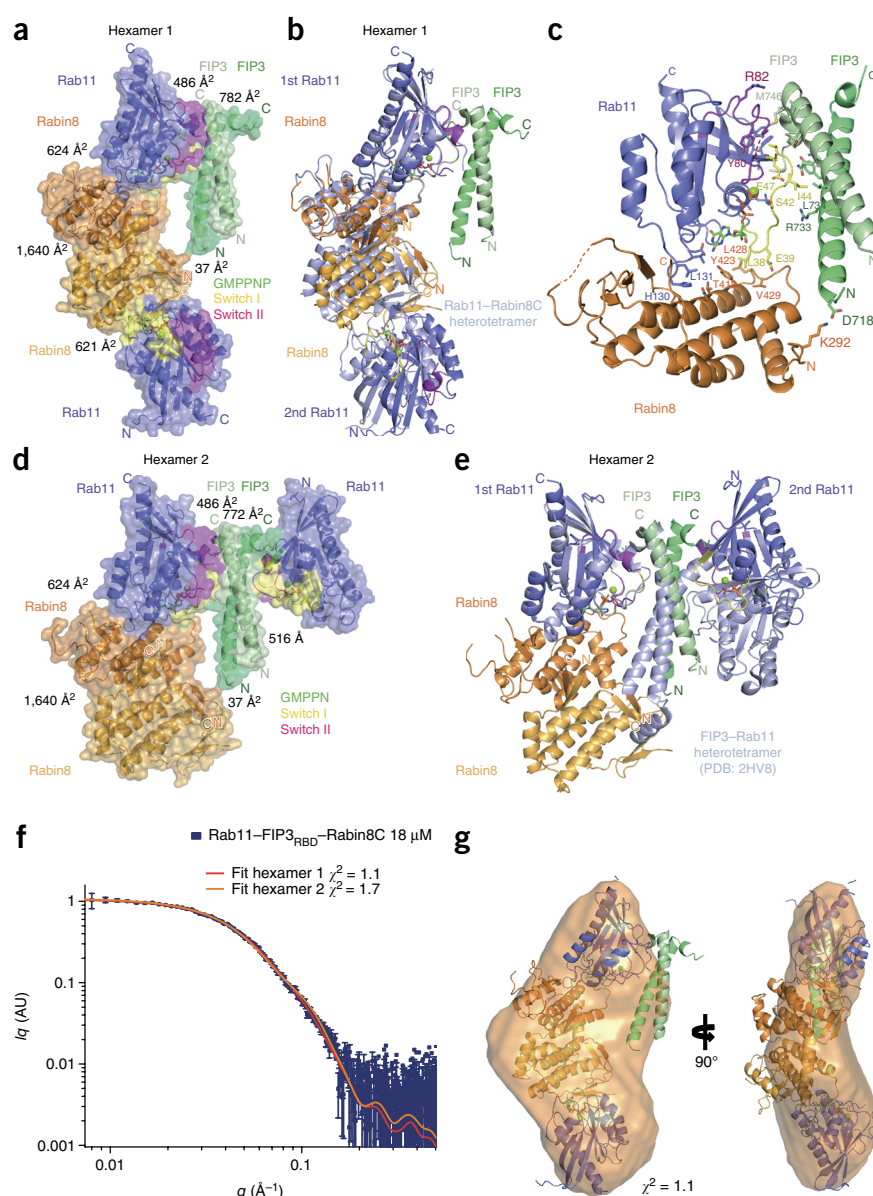
Crystal structure of Rab11–FIP3–Rabin8

To elucidate the molecular basis of how FIP3 and Rabin8 effectors bind Rab11 at the same time, we determined two crystal structures of the Rab11–FIP3$_{RBD}$–Rabin8C complex at 3.0-Å and 4.2-Å resolution (**Fig. 3** and **Table 1**). The two crystal structures are very similar and reveal heterohexameric complexes (**Fig. 3**) that contain two copies of each protein and pack into linear oligomers of dodecamers in the crystals (**Supplementary Fig. 4a**). The dodecamers in the crystals adopt an 'open' conformation that stacks with neighboring dodecamers via crossover FIP3$_{RBD}$ helices (**Supplementary Fig. 4**). From the

packing of protein subunits in the crystals, two different heterohexameric Rab11–FIP3$_{RBD}$–Rabin8C complexes are possible (**Fig. 3a,d**). Hexamer 1 can be thought of as a Rab11–Rabin8C heterotetramer with one FIP3$_{RBD}$ homodimer associated (**Fig. 3a**). Hexamer 2 can be thought of as a Rab11–FIP3$_{RBD}$ heterotetramer with one Rabin8C homodimer associated (**Fig. 3d**). Both hexameric structures have large buried surface areas between subunits (>4,000 Å^2) and are predicted to be stable assemblies in solution by PISA[43]. Either of the hexameric structures can in principle dimerize to form a dodecamer, although molecular clashes between Rabin8C and FIP3$_{RBD}$ at the center of such a complex make a 'closed' dodecameric assembly unfavorable (**Supplementary Fig. 3b**). In the crystals, we observe an 'open' dodecameric arrangement in which the buried surface area between hexamers is limited to 740 Å^2 and thus is not predicted by PISA to be stable in solution (**Supplementary Fig. 4b**). These results are consistent with the SEC experiment in which the Rab11–FIP3$_{RBD}$–Rabin8C complex elutes at a volume consistent with a hexameric structure (**Fig. 2a**). To evaluate which of the two heterohexameric forms is found in solution, we measured experimental small-angle X-ray scattering (SAXS) curves for the Rab11–FIP3$_{RBD}$–Rabin8C complex at 18 μM concentration and did a comparison with the theoretical curves calculated from the coordinates of each of the two different hexameric forms (**Fig. 3f**). Although the back-calculated scattering curves of both hexameric arrangements are quite similar, the straight slope of hexamer 1 provides a better fit to the experimental data (**Fig. 3f**). This is further supported by the lower χ^2 value of 1.1 for hexamer 1 compared to a χ^2 of 1.7 for hexamer 2. The envelope calculated from the SAXS data obtained from the complex at 18 μM fits well to the structure of hexamer 1 obtained by crystallography (**Fig. 3g**).

Simultaneous binding of FIP3$_{RBD}$ and Rabin8C effectors to Rab11 is facilitated through neighboring recognition sites at the switch regions of Rab11 (**Fig. 3c**). The increased stability of the Rab11–FIP3$_{RBD}$–Rabin8C

complex compared to the Rab11–Rabin8C complex was evident from SEC and ITC experiments (**Figs. 1e** and **2a,c**) and is probably a result of close contacts between FIP3 and Rabin8 molecules within the complex (**Fig. 3c**). The contacts between Rab11 and FIP3 in the hexamers occur via residues on switch I and II and are largely similar to those in previously published structures of heterotetrameric Rab11–FIP3 complexes[40,41]. However, in the structure of Rab11–FIP3$_{RBD}$–Rabin8C, the helices of FIP3 undergo a conformational change to accommodate Rabin8 into the complex (**Fig. 3e**). It is possible that this large conformational change lowers the affinity for the second Rab11-binding site on FIP3$_{RBD}$. This conformational change extends to the Rab11 subunit farthest away from the Rabin8 dimer and positions it more than 10 Å from the location of the same Rab11 subunit in the heterotetrameric Rab11–FIP3 complex (**Fig. 3e**). In the Rab11–FIP3$_{RBD}$–Rabin8C complex, Rabin8C binds Rab11 at switch I and the loop connecting β5 with α4 of Rab11, similarly to the binding observed in the heterotetrameric Rab11–Rabin8C structure (**Fig. 1**). However, a large conformational change occurs within the Rab11–FIP3$_{RBD}$–Rabin8C complex compared to the Rab11–Rabin8C heterotetramer (**Fig. 3b**). This conformational change results in a rotation of the Rab11–Rabin8C subunits farthest away from FIP3, which positions the second Rab11 more than 10 Å from the position observed in the Rab11–Rabin8C heterotetramer (**Fig. 3b**).

Figure 3 Crystal structure of Rab11–FIP3–Rabin8. (**a**) Crystal structure of the Rab11–FIP3$_{RBD}$–Rabin8C complex (hexameric composition 1), shown in cartoon representation with a semitransparent surface. Switch regions, GMPPNP and Mg^{2+} are shown as in **Figure 1**. Buried surface areas as calculated by PISA are shown for the different interfaces. (**b**) Superposition of heterotetrameric Rab11–Rabin8C (as in **Fig. 1**) onto hexamer 1, using one Rab11 subunit. (**c**) Cartoon representation of Rab11 bound to both FIP3$_{RBD}$ and Rabin8C. Interacting residues are shown as sticks and are labeled according to residue number. (**d**) Crystal packing, revealing a second possible hexameric arrangement (hexamer 2) of the Rab11–FIP3$_{RBD}$–Rabin8C complex, as shown in cartoon representation with a semitransparent surface. Switch regions, GMPPNP and Mg^{2+} are shown as in **Figure 1**. Buried surface areas as calculated by PISA are shown for the different interfaces. (**e**) Superpositioning of one Rab11 subunit from the heterotetrameric Rab11–FIP3 complex (PDB 2HV8 (ref. 40)) onto one Rab11 subunit from hexamer 2 of the Rab11–FIP3$_{RBD}$–Rabin8C complex. (**f**) SAXS experimental scattering curve for the Rab11–FIP3$_{RBD}$–Rabin8C complex at 18 μM concentration. Both X-ray scattering (y axis, arbitrary units) and resolution (x axis) are on logarithmic scales. A fit between the X-ray scattering data and the back-calculated scattering curves for the crystal structure of hexamers 1 and 2 in crysol is displayed q, scattering vector; Iq, scattering intensity; AU, arbitrary units. (**g**) Two perpendicular views of a SAXS model calculated with the scattering data from the 18 μM Rab11–FIP3$_{RBD}$–Rabin8C sample manually superposed with the atomic coordinates from the Rab11–FIP3$_{RBD}$–Rabin8C crystal structure (hexamer 1 from **Fig. 3a**).

The structural data presented here provide a molecular basis for dual effector binding by a small GTPase and suggest that cooperative binding of effectors may result in stabilized complexes.

Equilibrium of Rab11–FIP3–Rabin8 oligomers revealed by SAXS
To assess the oligomeric state of the Rab11–FIP3$_{RBD}$–Rabin8C complex in solution, we carried out SAXS experiments on the purified complex at different concentrations (**Fig. 4a,b**). At 18 μM concentration, we observed a complex with an MW of 87 kDa, which is in agreement with the SEC data and probably represents a mixture of mainly heterohexameric complexes containing two of each protein subunit, with a minor fraction of dissociated Rabin8C homodimers and Rab11–FIP3$_{RBD}$ heterotetramers (**Fig. 4c**). For highly concentrated complex (296 μM), the observed MW was 202 kDa, which is close to the calculated MW of 200 kDa for a dodecameric complex containing four of each protein subunit. At intermediate concentrations of 30–262 μM, MWs of 104–190 kDa were observed, which probably represent mixtures of hexameric and dodecameric complexes, although octamers and decamers may also be present. Interestingly, the ITC experiment
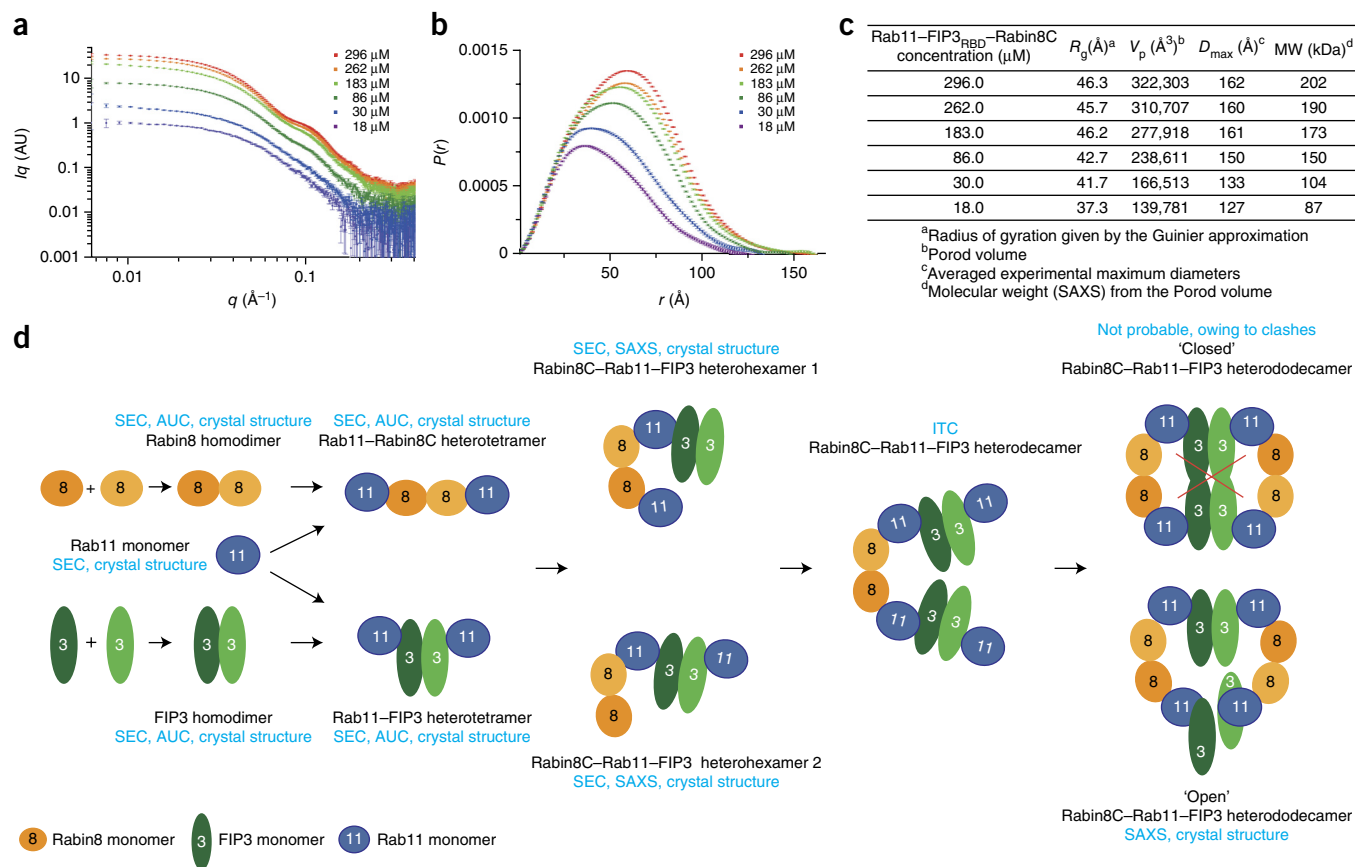
Figure 4 Rab11–FIP3–Rabin8 exists in a concentration-dependent equilibrium between different oligomeric states. (**a**) SAXS curves for different concentrations of the Rab11–FIP3$_{RBD}$–Rabin8C complex. Different complex concentrations are depicted in different colors and are not normalized to concentrations, to facilitate better visualization q, scattering vector; Iq, scattering intensity; AU, arbitrary units. (**b**) Pair distance distribution functions $P(r)$ derived from the experimental SAXS data and normalized to concentrations, showing a concentration-dependent change in molecular dimensions of the complex. (**c**) Tabulation of parameters calculated from the experimental SAXS data. Radius of gyration (R_g) is calculated from the Guinier approximation, and the Porod volume (V_p) and the maximum particle dimension (D_{max}) are calculated with gnom. The MWs are derived from V_p. (**d**) Schematics summarizing the different possible interactions between Rab11, FIP3 and Rabin8. Different homo- and heterodimerization interfaces are indicated. The formation of different oligomeric states is depicted, and the experimental methods by which they were detected are indicated in blue.

(**Fig. 2c**) in which 1,200 µM of Rabin8C was titrated into a solution of 120 µM Rab11–FIP3$_{RBD}$ gave an N value of ~0.5, thus suggesting that each Rabin8C homodimer associates with two Rab11–FIP3$_{RBD}$ heterotetramers to form a decameric complex (**Fig. 4d**). This decameric complex probably assembles only under high-concentration conditions in which Rab11–FIP3 is in large excess to Rabin8. The solution data presented here thus suggest that Rab11–FIP3$_{RBD}$–Rabin8C exists in a concentration-dependent equilibrium between different oligomeric states *in vitro*. This propensity to form a wide range of different oligomeric states is probably a result of the many oligomerization interfaces between Rab11, FIP3 and Rabin8 subunits (homodimeric FIP3 and Rabin8 as well as heterotetrameric Rab11–FIP3 and Rab11–Rabin8; **Fig. 4d**). The larger dodecameric Rab11–FIP3$_{RBD}$–Rabin8C complex has so far been observed only at very high, nonphysiological concentrations *in vitro*. Whether the stability of larger oligomers might be increased by the presence of additional binding partners such as ASAP1 and Arf4 and/or membranes such as endosomes or the TGN, where these targeting complexes assemble, remains to be addressed.

DISCUSSION

Rab GTPases often have multiple effectors, but it has been generally assumed, owing to the limited space at the switch regions of the G site, that effector binding is mutually exclusive. Here we show that Rab11 can simultaneously bind the effectors FIP3 and Rabin8 by using neighboring binding sites on Rab11. Rabin8 is an unusual effector in that it makes only a few contacts with residues from the switch regions, whereas FIP3 binds at the canonical effector–binding site. In the ternary structure of Rab11–FIP3–Rabin8, the two effectors come close together and interact directly, a notion that we confirmed in pulldown experiments. Indeed, Rabin8 has four-times-higher affinity for the Rab11–FIP3 complex than for Rab11 alone, a result in agreement with recently published pulldown experiments[31]. In this respect, Rabin8 should perhaps be thought of as an indirect effector of Rab11 because efficient binding to Rab11 requires the preformation of a complex between Rab11 and the canonical effector FIP3. Dual effector binding may occur for other Rab GTPases such as Rab6, which binds the dimeric GCC185 coiled-coil effector[44] in a similar manner to binding between Rab11 and FIP3 (**Supplementary Fig. 5**) Interestingly, Rab11–FIP3 was shown to tether vesicles to the cytoplasmic dynein motor[45] and, together with dynactin, to activate motor activity[46]. Given this information, it is perhaps not surprising that FIP3 is not required to dissociate from vesicle-bound targeting complexes to allow for Rabin8 binding, because FIP3 dissociation would probably result in vesicles falling off the dynein motor and thus failing to reach their destination.

Ciliary targeting of membrane proteins such as rhodopsin involves cargo recognition at the TGN by active Arf4 and recruitment of
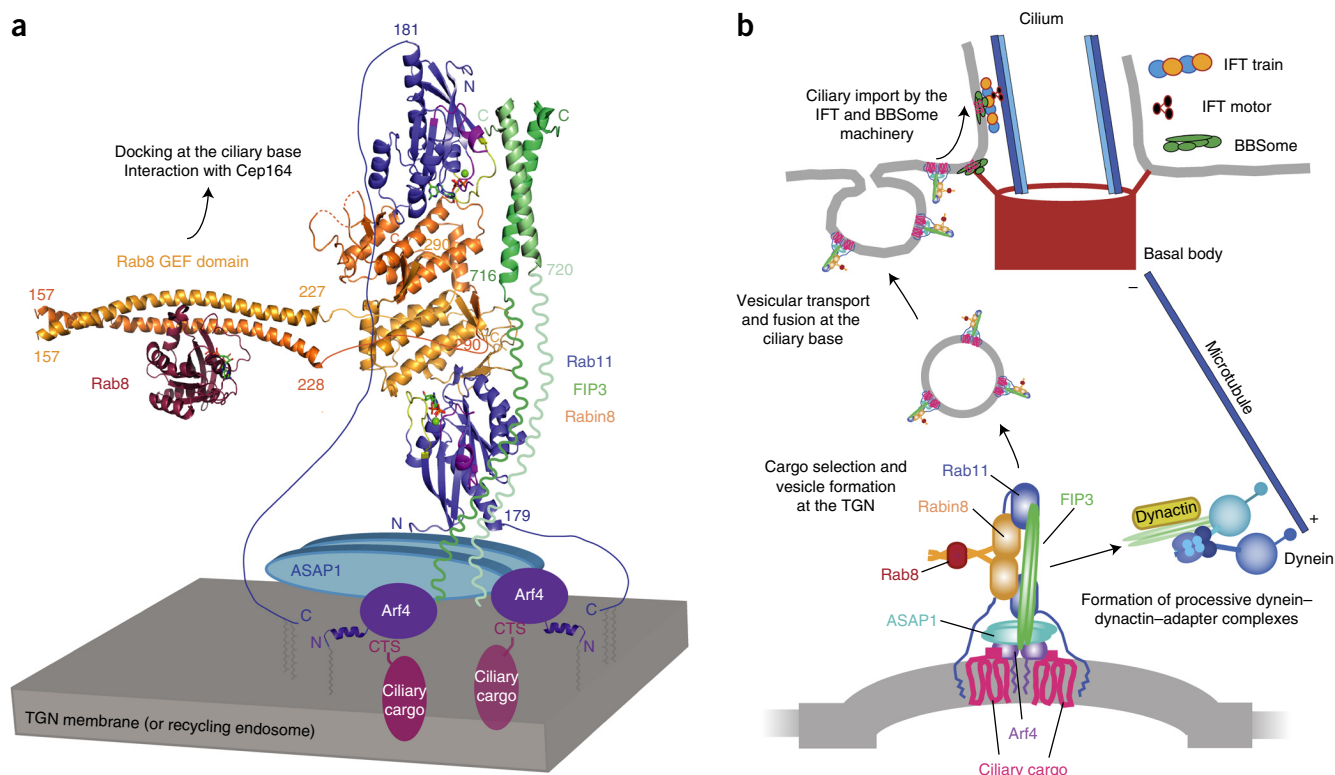
Figure 5 Model of the ciliary-targeting complex at the donor membrane. (**a**) Model of the initial step of cargo sorting by Rab11 complexes at the TGN or endosomes. The Rab11–FIP3–Rabin8 crystal structure presented here is shown as a cartoon representation. (The orientation of the Rab11–FIP3–Rabin8 complex relative to the membrane is currently not known.) GTP-bound Arf4 associates directly with the membrane via an N-terminal amphipathic helix and binds ciliary cargo proteins via their ciliary-targeting sequences (CTS). The region of FIP3 located N terminally to the Rab11-binding site is predicted to be coiled coil and interacts directly with Arf4 (green helices). Rab11 has a prenylated C-terminal extension with membrane affinity. One ASAP1 dimer, which is a GAP for Arf4 and a direct binding partner of FIP3 and Rab11, is shown as a blue oval. ASAP1 has a BAR domain that probably functions in lipid binding and vesicle formation. On the left side of the model, the crystal structure of homodimeric Rabin8 GEF domain bound to one Rab8 (ref. 36) molecule (PDB 4LHY) is shown. The relative orientation between the Rabin8 GEF domain and C-terminal domains is not known. (**b**) Schematic representation of ciliary trafficking of membrane proteins. Cargo selection and vesicle formation at the donor membrane is followed by vesicular transport and fusion with the plasma membrane at the base of the cilium. Translocation into the cilium proper is mediated by the intraflagellar transport (IFT) and BBSome machinery[50–53].

ASAP1, FIP3 and Rab11 (ref. 11). At later stages, Rab11 also recruits Rabin8, thus activating Rab8, which is required for vesicle fusion at the ciliary base. We now show that the effectors FIP3 and Rabin8 can bind active Rab11 simultaneously. Our data thus suggest that FIP3 is not required to dissociate from the ciliary-targeting complex to allow Rabin8 recruitment. Indeed, we find that Rab11–FIP3–Rabin8 binds Arf4 and is active as a GEF toward Rab8 (**Fig. 2b,d**). The formation of ciliary-targeting complexes appears to be mediated by several dimerization events including homodimerization of FIP3 and Rabin8. Additionally, the dimerization of ASAP1 (ref. 47), which binds directly to Rab11 and FIP3 (ref. 11), as well as the potential Arf4-FIP3 heterotetramerization[40,48], probably contributes to formation of the ciliary-targeting complex (**Fig. 5a**). It remains to be explored whether the avidity arising from the many relatively weak interactions supports clustering of targeting complexes, which could in turn result in the creation of a microdomain enriched in ciliary cargo proteins at the donor membrane (**Fig. 5b**).

FIP3 has been reported to bind active Arf5 and Arf6 in addition to Arf4 (refs. 15,27,49), results demonstrating that Arf binding to FIP proteins is promiscuous and suggesting that different membrane-targeting complexes, containing a conserved core but with different Arf proteins, may participate in different intracellular trafficking pathways. Whereas Arf4 has been reported to be involved in ciliary

targeting of membrane proteins[15], Arf5 is involved in ER-to-Golgi transport, and COPI recruitment and Arf6 are required for endocytosis, remodeling of the actin cytoskeleton and recycling of β1 integrins to the plasma membrane[1,12]. It is thus possible that the incorporation of different Arf proteins into otherwise similar membrane-targeting complexes results in different intracellular membrane-trafficking events. The reconstitution and structure solution of larger membrane-targeting assemblies in complex with targeting sequences of cargo proteins will probably be the topic of intense research in the years to come.

METHODS
Methods and any associated references are available in the online version of the paper.

Accession codes. Coordinates and structure factors have been deposited in the Protein Data Bank under accession codes PDB 4UJ3 (HsRab11–GMPPNP–FIP3–Rabin8C complex), PDB 4UJ4 (HsRab11–GMPPNP–FIP3–Rabin8C_2 complex, 4.2-Å resolution) and PDB 4UJ5 (HsRab11–GMPPNP–Rabin8C complex).

Note: Any Supplementary Information and Source Data files are available in the online version of the paper.

ARTICLES

AUTHOR CONTRIBUTIONS

M.V. carried out the protein biochemistry and structural biology under the supervision of E.L. R.S. carried out the SAXS measurements and calculations. C.B. assisted with the ITC measurements. E.L. and M.V. wrote the paper with input from R.S. and C.B.

COMPETING FINANCIAL INTERESTS

The authors declare no competing financial interests.

Reprints and permissions information is available online at http://www.nature.com/reprints/index.html.

1. D'Souza-Schorey, C. & Chavrier, P. ARF proteins: roles in membrane traffic and beyond. *Nat. Rev. Mol. Cell Biol.* **7**, 347–358 (2006).
2. Stenmark, H. Rab GTPases as coordinators of vesicle traffic. *Nat. Rev. Mol. Cell Biol.* **10**, 513–525 (2009).
3. Nachury, M.V., Seeley, E.S. & Jin, H. Trafficking to the ciliary membrane: how to get across the periciliary diffusion barrier? *Annu. Rev. Cell Dev. Biol.* **26**, 59–87 (2010).
4. Ao, X., Zou, L. & Wu, Y. Regulation of autophagy by the Rab GTPase network. *Cell Death Differ.* **21**, 348–358 (2014).
5. Faini, M., Beck, R., Wieland, F.T. & Briggs, J. Vesicle coats: structure, function, and general principles of assembly. *Trends Cell Biol.* **23**, 279–288 (2013).
6. Pfeffer, S.R. Rab GTPases: specifying and deciphering organelle identity and function. *Trends Cell Biol.* **11**, 487–491 (2001).
7. Ullrich, O. Rab11 regulates recycling through the pericentriolar recycling endosome. *J. Cell Biol.* **135**, 913–924 (1996).
8. Chen, W., Feng, Y., Chen, D. & Wandinger-Ness, A. Rab11 Is required for trans-Golgi network–to–plasma membrane transport and a preferential target for GDP dissociation inhibitor. *Mol. Biol. Cell* **9**, 3241–3257 (1998).
9. Ren, M. *et al.* Hydrolysis of GTP on rab11 is required for the direct delivery of transferrin from the pericentriolar recycling compartment to the cell surface but not from sorting endosomes. *Proc. Natl. Acad. Sci. USA* **95**, 6187–6192 (1998).
10. Skop, A.R., Bergmann, D., Mohler, W.A. & White, J.G. Completion of cytokinesis in *C. elegans* requires a brefeldin A-sensitive membrane accumulation at the cleavage furrow apex. *Curr. Biol.* **11**, 735–746 (2001).
11. Deretic, D. Crosstalk of Arf and Rab GTPases en route to cilia. *Small GTPases* **4**, 70–77 (2013).
12. Pellinen, T. Integrin traffic. *J. Cell Sci.* **119**, 3723–3731 (2006).
13. Nachury, M.V. *et al.* A core complex of BBS proteins cooperates with the GTPase Rab8 to promote ciliary membrane biogenesis. *Cell* **129**, 1201–1213 (2007).
14. Westlake, C.J. *et al.* Primary cilia membrane assembly is initiated by Rab11 and transport protein particle II (TRAPPII) complex-dependent trafficking of Rabin8 to the centrosome. *Proc. Natl. Acad. Sci. USA* **108**, 2759–2764 (2011).
15. Mazelova, J. *et al.* Ciliary targeting motif VxPx directs assembly of a trafficking module through Arf4. *EMBO J.* **28**, 183–192 (2009).
16. Sung, C.-H. & Leroux, M.R. The roles of evolutionarily conserved functional modules in cilia-related trafficking. *Nat. Cell Biol.* **15**, 1387–1397 (2013).
17. Wang, J., Morita, Y., Mazelova, J. & Deretic, D. The Arf GAP ASAP1 provides a platform to regulate Arf4- and Rab11–Rab8-mediated ciliary receptor targeting. *EMBO J.* **31**, 4057–4071 (2012).
18. Singla, V. The primary cilium as the cell's antenna: signaling at a sensory organelle. *Science* **313**, 629–633 (2006).
19. Pazour, G.J. *et al. Chlamydomonas* IFT88 and its mouse homologue, polycystic kidney disease gene tg737, are required for assembly of cilia and flagella. *J. Cell Biol.* **151**, 709–718 (2000).
20. Badano, J.L., Mitsuma, N., Beales, P.L. & Katsanis, N. The ciliopathies: an emerging class of human genetic disorders. *Annu. Rev. Genomics Hum. Genet.* **7**, 125–148 (2006).
21. Fliegauf, M., Benzing, T. & Omran, H. When cilia go bad: cilia defects and ciliopathies. *Nat. Rev. Mol. Cell Biol.* **8**, 880–893 (2007).
22. Sharma, N., Berbari, N.F. & Yoder, B.K. Ciliary dysfunction in developmental abnormalities and diseases. *Curr. Top. Dev. Biol.* **85**, 371–427 (2008).
23. Deretic, D. & Papermaster, D.S. Polarized sorting of rhodopsin on post-Golgi membranes in frog retinal photoreceptor cells. *J. Cell Biol.* **113**, 1281–1293 (1991).
24. Follit, J.A. *et al.* Arf4 is required for mammalian development but dispensable for ciliary assembly. *PLoS Genet.* **10**, e1004170 (2014).
25. Deretic, D. *et al.* Rhodopsin C terminus, the site of mutations causing retinal disease, regulates trafficking by binding to ADP-ribosylation factor 4 (ARF4). *Proc. Natl. Acad. Sci. USA* **102**, 3301–3306 (2005).
26. Deretic, D., Schmerl, S., Hargrave, P.A., Arendt, A. & McDowell, J.H. Regulation of sorting and post-Golgi trafficking of rhodopsin by its C-terminal sequence QVS(A)PA. *Proc. Natl. Acad. Sci. USA* **95**, 10620–10625 (1998).
27. Shin, O.H., Ross, A.H., Mihai, I. & Exton, J.H. Identification of arfophilin, a target protein for GTP-bound class II ADP-ribosylation factors. *J. Biol. Chem.* **274**, 36609–36615 (1999).
28. Schonteich, E. *et al.* Molecular characterization of Rab11–FIP3 binding to ARF GTPases. *Eur. J. Cell Biol.* **86**, 417–431 (2007).
29. Hickson, G.R.X. *et al.* Arfophilins are dual Arf/Rab 11 binding proteins that regulate recycling endosome distribution and are related to *Drosophila* nuclear fallout. *Mol. Biol. Cell* **14**, 2908–2920 (2003).
30. Horgan, C.P. *et al.* Rab11–FIP3 is critical for the structural integrity of the endosomal recycling compartment. *Traffic* **8**, 414–430 (2007).
31. Wang, J. & Deretic, D. The Arf/Rab11 effector FIP3 acts synergistically with the Arf GAP ASAP1 to direct Rabin8 in ciliary receptor targeting. *J. Cell Sci.* **128**, 1375–1385 (2015).
32. Inoue, H., Ha, V.L., Prekeris, R. & Randazzo, P.A. Arf GTPase-activating protein ASAP1 interacts with Rab11 effector FIP3 and regulates pericentrosomal localization of transferrin receptor-positive recycling endosome. *Mol. Biol. Cell* **19**, 4224–4237 (2008).
33. Knödler, A. *et al.* Coordination of Rab8 and Rab11 in primary ciliogenesis. *Proc. Natl. Acad. Sci. USA* **107**, 6346–6351 (2010).
34. Moritz, O.L. *et al.* Mutant rab8 impairs docking and fusion of rhodopsin-bearing post-Golgi membranes and causes cell death of transgenic *Xenopus* rods. *Mol. Biol. Cell* **12**, 2341–2351 (2001).
35. Wang, J. & Deretic, D. Molecular complexes that direct rhodopsin transport to primary cilia. *Prog. Retin. Eye Res.* (2014).
36. Guo, Z., Hou, X., Goody, R.S. & Itzen, A. Intermediates in the guanine nucleotide exchange reaction of Rab8 protein catalyzed by guanine nucleotide exchange factors Rabin8 and GRAB. *J. Biol. Chem.* **288**, 32466–32474 (2013).
37. Feng, S. *et al.* A Rab8 guanine nucleotide exchange factor-effector interaction network regulates primary ciliogenesis. *J. Biol. Chem.* **287**, 15602–15609 (2012).
38. Vetter, I.R. & Wittinghofer, A. The guanine nucleotide-binding switch in three dimensions. *Science* **294**, 1299–1304 (2001).
39. Burke, J.E. *et al.* Structures of PI4KIIIβ complexes show simultaneous recruitment of Rab11 and its effectors. *Science* **344**, 1035–1038 (2014).
40. Eathiraj, S., Mishra, A., Prekeris, R. & Lambright, D.G. Structural basis for Rab11-mediated recruitment of FIP3 to recycling endosomes. *J. Mol. Biol.* **364**, 121–135 (2006).
41. Shiba, T. *et al.* Structural basis for Rab11-dependent membrane recruitment of a family of Rab11-interacting protein 3 (FIP3)/Arfophilin-1. *Proc. Natl. Acad. Sci. USA* **103**, 15416–15421 (2006).
42. Hattula, K., Furuhjelm, J., Arffman, A. & Peränen, J.A. Rab8-specific GDP/GTP exchange factor is involved in actin remodeling and polarized membrane transport. *Mol. Biol. Cell* **13**, 3268–3280 (2002).
43. Krissinel, E. & Henrick, K. Inference of macromolecular assemblies from crystalline state. *J. Mol. Biol.* **372**, 774–797 (2007).
44. Burguete, A.S., Fenn, T.D., Brunger, A.T. & Pfeffer, S.R. Rab and Arl GTPase family members cooperate in the localization of the golgin GCC185. *Cell* **132**, 286–298 (2008).
45. Horgan, C.P., Hanscom, S.R., Jolly, R.S., Futter, C.E. & McCaffrey, M.W. Rab11–FIP3 links the Rab11 GTPase and cytoplasmic dynein to mediate transport to the endosomal-recycling compartment. *J. Cell Sci.* **123**, 181–191 (2010).
46. McKenney, R.J., Huynh, W., Tanenbaum, M.E., Bhabha, G. & Vale, R.D. Activation of cytoplasmic dynein motility by dynactin-cargo adapter complexes. *Science* **345**, 337–341 (2014).
47. Nie, Z. *et al.* A BAR domain in the N terminus of the Arf GAP ASAP1 affects membrane structure and trafficking of epidermal growth factor receptor. *Curr. Biol.* **16**, 130–139 (2006).
48. Isabet, T., Montagnac, G. & Regazzoni, K. The structural basis of Arf effector specificity: the crystal structure of ARF6 in a complex with JIP4. *EMBO J.* **28**, 2835–2845 (2009).
49. Fielding, A.B. *et al.* Rab11–FIP3 and FIP4 interact with Arf6 and the exocyst to control membrane traffic in cytokinesis. *EMBO J.* **24**, 3389–3399 (2005).
50. Jin, H. *et al.* The conserved Bardet-Biedl syndrome proteins assemble a coat that traffics membrane proteins to cilia. *Cell* **141**, 1208–1219 (2010).
51. Mourão, A., Nager, A.R., Nachury, M.V. & Lorentzen, E. Structural basis for membrane targeting of the BBSome by ARL6. *Nat. Struct. Mol. Biol.* **21**, 1035–1041 (2014).
52. Taschner, M., Bhogaraju, S. & Lorentzen, E. Architecture and function of IFT complex proteins in ciliogenesis. *Differentiation* **83**, S12–S22 (2012).
53. Bhogaraju, S., Engel, B.D. & Lorentzen, E. Intraflagellar transport complex structure and cargo interactions. *Cilia* **2**, 10 (2013).

ONLINE METHODS

Protein purification and crystallization. Human Rab11a (residues 6–186, Q70L constitutively active mutant), Rabin8C (residues 270–460) and FIP3$_{RBD}$ (residues 695–756) containing tobacco etch virus (TEV)-cleavable N-terminal N-terminal His$_6$ or N-terminal His$_6$-GST tags were expressed in *Escherichia coli* BL21(DE3). Cells were lysed by sonication in a buffer containing 50 mM phosphate, pH 7.5, 150 mM NaCl, 10% glycerol and 5 mM MgCl$_2$. Proteins were purified by Ni-NTA affinity chromatography and, in the case of His-GST-tagged proteins, by an additional GSH affinity-chromatography step. To remove the N-terminal His or His-GST tag, proteins were incubated with TEV protease overnight. Further purification was done by ion-exchange chromatography (Q-Sepharose) and subsequent size-exclusion chromatography (SEC) in a buffer of 10 mM HEPES, pH 7.5, 150 mM NaCl, 5 mM MgCl$_2$ and 2 mM DTT, with a HiLoad Superdex 75 or 200 column. The Rab11–Rabin8C complex was prepared by mixture of equal molar ratios of the two proteins (Rab11 was preloaded with GMPPNP according to the protocol in ref. 54) and subsequent incubation for 1 h at 4 °C. The complex was concentrated to 40 mg/ml and crystallized by the hanging-drop vapor-diffusion method at 18 °C. Crystals of Rab11–Rabin8C appeared in drops containing 1 μl each of the protein mixture and reservoir solution: 0.1 M HEPES, pH 7.0, 0.2 M lithium sulfate and 24% PEG 3350. The Rab11–Rabin8C–FIP3$_{RBD}$ complex was prepared by mixture of equal molar ratios of the three proteins (Rab11 was preloaded with GMPPNP); this was followed by incubation for 1 h at 4 °C and SEC on a HiLoad Superdex 75 column. The Rab11–FIP3$_{RBD}$–Rabin8C complex was concentrated to 30 mg/ml. Crystals of the Rab11–FIP3$_{RBD}$–Rabin8C complex were obtained by the hanging-drop vapor-diffusion method against a reservoir solution at 18 °C. Drops contained 0.3 μl each of the protein mixture and reservoir solutions: 50 mM MES, pH 5.6, 0.2 M ammonium sulfate and 12% PEG 8000 (*P*21 crystals) or 50 mM MES, pH 5.8, 0.2 M ammonium sulfate and 14% PEG 8000 (*P*2$_1$2$_1$2$_1$ crystals).

X-ray diffraction data collection and structure determination. Crystals of the human Rab11–Rabin8C and Rab11–FIP3$_{RBD}$–Rabin8C complex were flash cooled in liquid nitrogen in mother liquor supplemented with 20% glycerol. Diffraction data were collected at the Swiss Light Source and processed with XDS[55]. Phases were obtained for the Rab11–Rabin8C complex by molecular replacement (MR) with the human GppNHp-bound Rab11a structure (PDB 1YZK[56]) in Phaser[57], thus yielding electron density maps into which Rabin8C could be built. Four copies of Rab11 and Rabin8C were located in the asymmetric unit. The model was completed by iterative cycles of model building in COOT[58] and refinement in PHENIX[59] with four-fold NCS restraints. The Rab11–FIP3$_{RBD}$–Rabin8C complex structure was determined by finding eight copies of the heterodimeric Rab11–Rabin8C complex (forming parts of two dodecamers) by MR with the 3.0-Å-resolution data. Eight FIP3$_{RBD}$ helices were built into the resulting map with Coot, and refinement was done in PHENIX with eight-fold NCS restraints. The complete Rab11–FIP3$_{RBD}$–Rabin8C dodecamer was used in MR searches with the 4.2-Å-resolution data locating one dodecamer in the asymmetric unit. The 4.2-Å-resolution structure was refined with rigid-body and overall *B*-factor refinement in PHENIX. Data collection and refinement statistics are summarized in **Table 1**.

Pulldown experiments. Ni^{2+}-NTA beads were preequilibrated with buffer containing PBS, pH 7.5, and 10 mM imidadzole. Purified His-tagged proteins and untagged proteins were mixed at equal molar ratios. Individual proteins and mixtures of the proteins were incubated with Ni^{2+}-NTA beads for 1.5 h at 4 °C. Beads were washed 3× with PBS buffer to remove contaminants. Bound proteins were eluted from the beads with buffer supplemented with 500 mM imidazole. Eluted proteins were analyzed by SDS-PAGE.

Small-angle X-ray scattering (SAXS) experiments. SAXS data were collected from 70-μL samples of purified Rab11–FIP3$_{RBD}$–Rabin8C complex in 10 mM HEPES, pH 7.5, 150 mM NaCl, 5 mM MgCl$_2$ and 2 mM TCEP. SAXS measurements were carried out with a Rigaku BioSAXS1000 system and a microfocus rotating anode (Cu-K$_\alpha$ 0.154 nm, 40 kV, 30 mA). A Pilatus 100k detector was used for image collection, and a built-in photo diode was used for transmission measurements. Silver behenate was used for q calibration. Four frames per sample were measured at 20 °C in a 0.77-mm capillary flow cell. Each frame resulted from a 900-s exposure and showed no radiation damage. The Rigaku SaxsLab software 3.0.1r1 was used for radial averaging, q calibration, and solvent subtraction. The
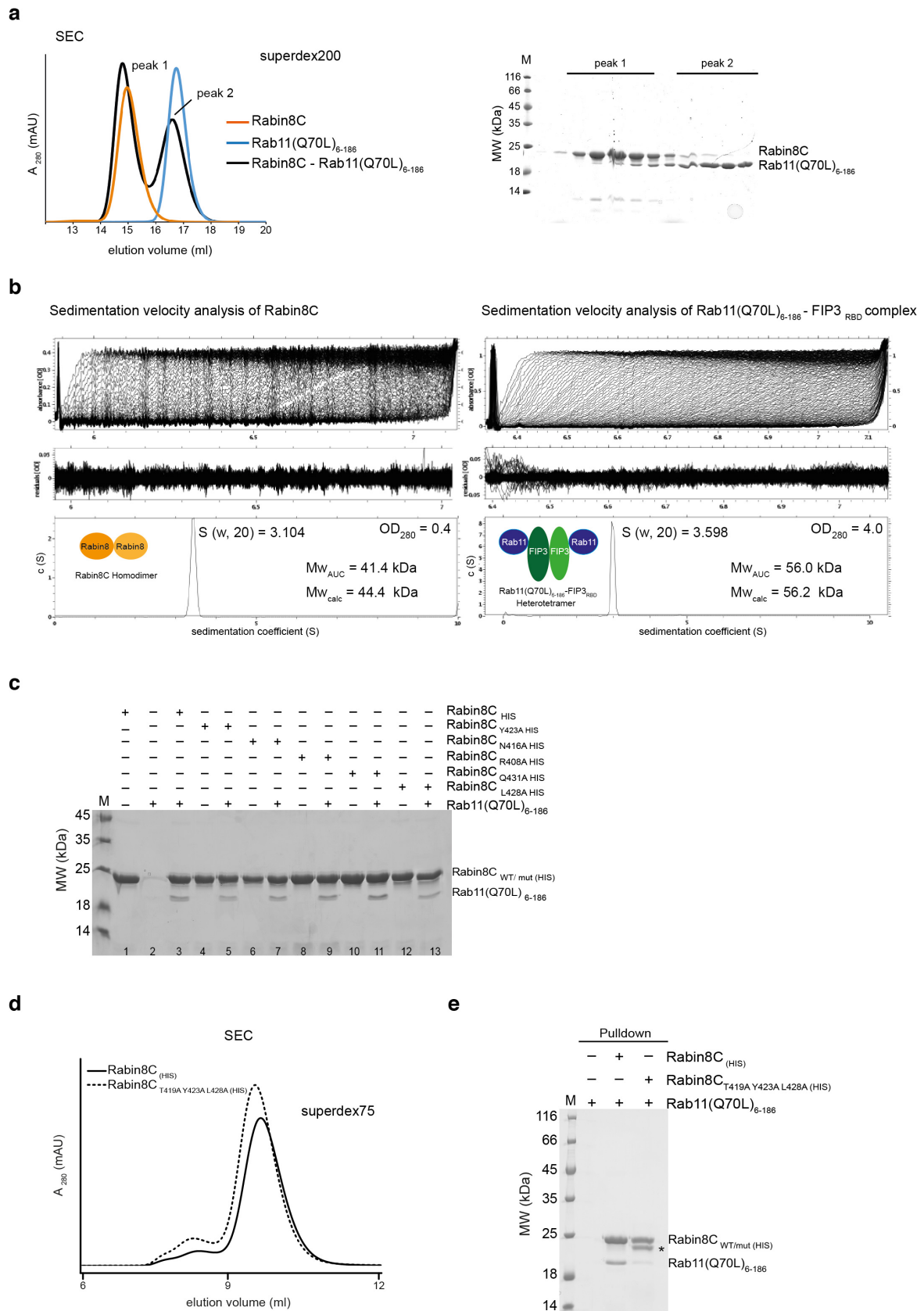
ATSAS package 2.5.0-2 (ref. 60) was used for further data evaluation. P(r) curves and envelopes were calculated with gnom and dammif, respectively. Molecular weights were calculated from Porod volumes according to ref. 60 and have an error of about 20%, and the χ^2 values were calculated with crysol.

Analytical ultracentrifugation. Sedimentation velocity experiments were performed on an Optima XL-I analytical ultracentrifuge (Beckman) with an An-60 Ti rotor and double-sector epon centerpieces. The Rabin8C and Rab11–FIP3$_{RBD}$ proteins were in a buffer containing 10 mM HEPES, pH 7.5, 150 mM NaCl, 5 mM MgCl$_2$, and 2 mM TCEP at concentrations of 0.4 or 4 mg/ml. Buffer density and viscosity was measured with a DMA 5000 densitometer and an AMVn viscosimeter, respectively (both from Anton Paar). Protein concentration distribution was monitored at 280 nm at 54,000 r.p.m. and 20 °C. Time-derivative analysis was computed with the SEDFIT package, version 12.1b (ref. 61), thus resulting in a c(s) distribution and an estimate for the molecular weight Mf from the sedimentation coefficient and the diffusion coefficient, as inferred from the broadening of the sedimentation boundary, assuming that all observed species share the same frictional coefficient f/f$_0$.

Isothermal titration microcalorimetry. ITC was carried out with a VP-ITC MicroCal calorimeter (MicroCal, Malvern). Proteins were buffered with 10 mM HEPES, pH 7.5, 150 mM NaCl, 10 mM MgCl$_2$ and 2 mM TCEP. 18 injections of 2 μl each were added from a computer-controlled microsyringe at intervals of 180 s into the sample solution (300 μL) under constant stirring (800 r.p.m.) at 20 °C. The concentration of the protein in the syringe was in all cases 10× the concentration of protein in the cell. For all ITC curves, a background curve consisting of protein titration into buffer and/or buffer titration into protein was subtracted to account for heat dilution. The ITC data were analyzed with Origin version 7 provided by MicroCal.

Nucleotide exchange reaction (GEF assay). The Rabin8 GEF activity for the GDP-to-GTP exchange reaction for Rab8 was determined according to a method described previously[62]. Purified nucleotide-free (as judged by HPLC) Rab8a$_{1-183}$ was incubated with a 1.5-fold molar excess of 2′(3′)-*O*-(*N*-methylanthraniloyl)-GDP (mant-GDP, Jena Bioscience) for 2 h at room temperature; this was followed by removal of unbound mant-GDP with a Micro Bio-Spin column (Bio-Rad). To measure GEF activity, 0.5 μM mant-GDP–bound Rab8 was incubated for 30 min at 20 °C with 2 μM or 20 μM purified Rabin8$_{fl}$, Rabin8$_{144-245}$ (GEF domain) or Rab11(Q70L)$_{6-186}$–FIP3$_{441-C}$–Rabin8$_{fl}$ complex, diluted to a total volume of 50 μl with GEF buffer (30 mM Tris, pH 7.5, 5 mM MgCl$_2$, 3 mM DTT and 10 mM potassium phosphate, pH 7.4). Because we observed a gradual loss of GEF activity when storing Rabin8 because of the formation of an inactive homotetrameric Rabin8 complex, Rabin8 and Rabin8-containing complexes were always subjected to SEC immediately before GEF activity assays. The nucleotide-exchange reaction was initiated by addition of GTP to a final concentration of 1 mM. The dissociation of mant-GDP from Rab8 was followed in a glass cuvette with a fluorescence spectrometer (PerkinElmer, 366-nm excitation and 450-nm emission). Fluorescence emission was monitored every 2 s for a total of 300 s at 20 °C. The data were fitted to a one-phase exponential-decay equation without constraints with nonlinear regression. The resulting observed rate constants (k_{obs}) were calculated with Prism 6.0.

54. Wu, S., Mehta, S.Q., Pichaud, F., Bellen, H.J. & Quiocho, F.A. Sec15 interacts with Rab11 via a novel domain and affects Rab11 localization *in vivo. Nat. Struct. Mol. Biol.* **12**, 879–885 (2005).
55. Kabsch, W. XDS. *Acta Crystallogr. D Biol. Crystallogr.* **66**, 125–132 (2010).
56. Eathiraj, S., Pan, X., Ritacco, C. & Lambright, D.G. Structural basis of family-wide Rab GTPase recognition by rabenosyn-5. *Nature* **436**, 415–419 (2005).
57. Storoni, L.C., McCoy, A.J. & Read, R.J. Likelihood-enhanced fast rotation functions. *Acta Crystallogr. D Biol. Crystallogr.* **60**, 432–438 (2004).
58. Emsley, P., Lohkamp, B., Scott, W.G. & Cowtan, K. Features and development of Coot. *Acta Crystallogr. D Biol. Crystallogr.* **66**, 486–501 (2010).
59. Adams, P.D. *et al.* PHENIX: a comprehensive Python-based system for macromolecular structure solution. *Acta Crystallogr. D Biol. Crystallogr.* **66**, 213–221 (2010).
60. Petoukhov, M.V. *et al.* New developments in the ATSASprogram package for small-angle scattering data analysis. *J. Appl. Crystallogr.* **45**, 342–350 (2012).
61. Schuck, P. Size-distribution analysis of macromolecules by sedimentation velocity ultracentrifugation and Lamm equation modeling. *Biophys. J.* **78**, 1606–1619 (2000).
62. Eberth, A. & Ahmadian, M.R. *In vitro* GEF and GAP assays. *Curr. Protoc. Cell Biol.* **43**, 14.9 (2009).

a

SEC

superdex200

peak 1

peak 2

Rabin8C
Rab11(Q70L)$_{6-186}$
Rabin8C - Rab11(Q70L)$_{6-186}$

A$_{280}$ (mAU)

elution volume (ml)

M   peak 1   peak 2

116
66
45
35
25   Rabin8C
                            Rab11(Q70L)$_{6-186}$
18

14

MW (kDa)

b

Sedimentation velocity analysis of Rabin8C

Sedimentation velocity analysis of Rab11(Q70L)$_{6-186}$ - FIP3$_{RBD}$ complex

absorbance [OD]

residuals [OD]

c (S)

Rabin8   Rabin8

Rabin8C Homodimer

S (w, 20) = 3.104   OD$_{280}$ = 0.4

Mw$_{AUC}$ = 41.4 kDa

Mw$_{calc}$ = 44.4 kDa

sedimentation coefficient (S)

Rab11   FIP3 FIP3   Rab11

Rab11(Q70L)$_{6-186}$-FIP3$_{RBD}$
Heterotetramer

S (w, 20) = 3.598   OD$_{280}$ = 4.0

Mw$_{AUC}$ = 56.0 kDa

Mw$_{calc}$ = 56.2 kDa

sedimentation coefficient (S)

c

| | | | | | | | | | | | | | |
|+|−|+|−|−|−|−|−|−|−|−|−|−| Rabin8C $_{HIS}$|

Rabin8C $_{HIS}$
Rabin8C $_{Y423A\ HIS}$
Rabin8C $_{N416A\ HIS}$
Rabin8C $_{R408A\ HIS}$
Rabin8C $_{Q431A\ HIS}$
Rabin8C $_{L428A\ HIS}$
Rab11(Q70L)$_{6-186}$

M

45
35
25   Rabin8C $_{WT/\ mut\ (HIS)}$
18   Rab11(Q70L)$_{6-186}$
14

MW (kDa)

1 2 3 4 5 6 7 8 9 10 11 12 13

d

SEC

Rabin8C $_{(HIS)}$
Rabin8C $_{T419A\ Y423A\ L428A\ (HIS)}$

superdex75

A$_{280}$ (mAU)

elution volume (ml)

e

Pulldown

− + −   Rabin8C $_{(HIS)}$
− − +   Rabin8C $_{T419A\ Y423A\ L428A\ (HIS)}$
M + + + Rab11(Q70L)$_{6-186}$

116
66
45
35
25   Rabin8C $_{WT/mut\ (HIS)}$
                            *
18   Rab11(Q70L)$_{6-186}$
14

MW (kDa)

59

Supplementary Figure 1

Size-exclusion chromatography (SEC), ultracentrifugation and interface validation of Rab11–Rabin8C.

(a) (left) SEC elution profile for Rabin8C (orange), Rab11 (blue) and a stoichiometric mixture of Rab11-Rabin8C incubated for 1h prior to loading onto a superdex 200 column. (right) SDS PAGE of the peak fractions from the Rab11-Rabin8C elution. Both the elution profile and the SDS-PAGE gel show that a stable Rab11-Rabin8C complex is not formed during the chromatography step. **(b)** Sedimentation velocity ultracentrifugation experiments for Rabin8C (left) and the Rab11-FIP3$_{RBD}$ complex (right). The determined Mw of Rabin8C was 41kDa, which corresponds to a homo-dimer (Mw$_{calc}$=44kDa) and is consistent with our crystallographic data. The determined Mw for the Rab11-FIP3$_{RBD}$ complex was 56kDa consistent with a hetero-tetramer containing two copies of each protein (Mw$_{calc}$=56kDa). This result is consistent with the crystallographic data previously published. **(c)** Ni-NTA pull-down of constitutively active Rab11(Q70L) using Wild-type (WT) and five different Rab11-interface single point-mutants (mut) of His-tagged Rabin8C. None of the mutations abolish Rab11-Rabin8C complex formation. **(d)** SEC profile of WT and triple-mutant Rabin8C (T419, Y423, L428 to alanine) demonstrating that the mutant Rabin8C elutes in a similarly peak to WT Rabin8C and is thus folded. **(e)** Ni-NTA pull-down of constitutively active Rab11(Q70L) using WT and the Rab11-interface triple point-mutant of His-tagged Rabin8C. The triple mutation substantially reduces complex formation with Rab11. An asterisk marks a band on the SDS-gel that corresponds to Rabin8C with the HIS-tagged cleaved. The cleaved form of Rabin8C nevertheless binds to Ni-NTA resin under PBS pH 7.5 and 10mM imidazole conditions and is pulled down similarly to HIS-tagged Rabin8C.

Crab-fold
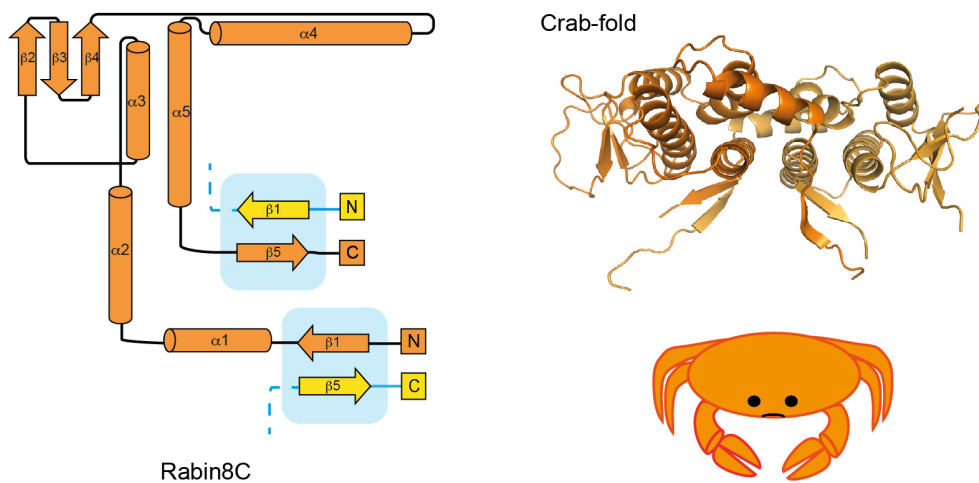
Rabin8C

Supplementary Figure 2
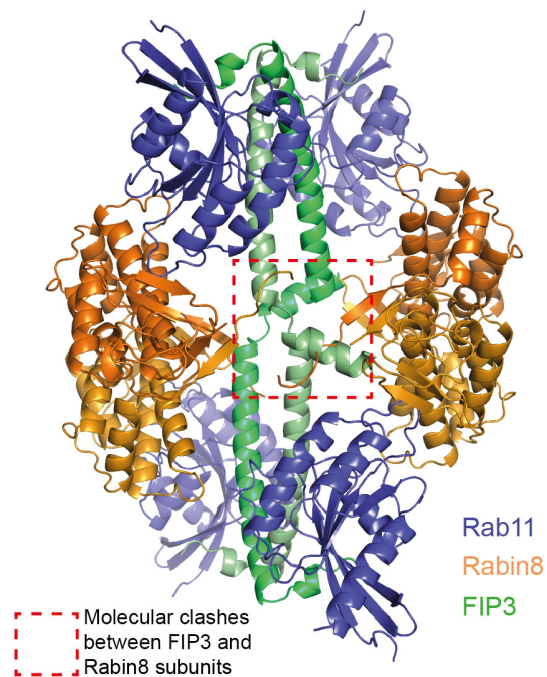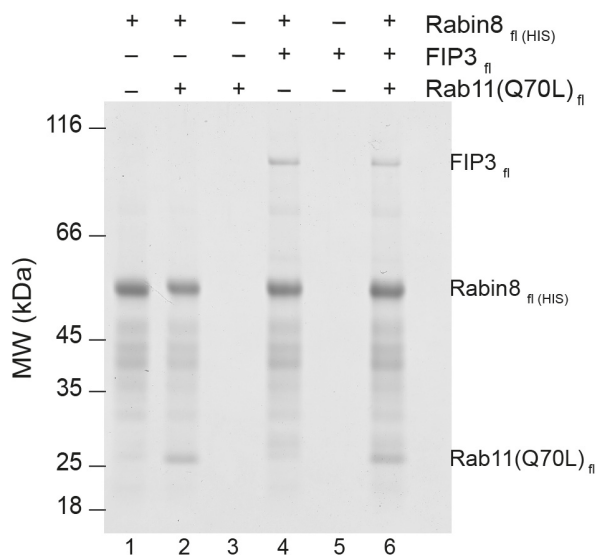
Topology of the Rabin8C domain.

Searches using the DALI server (Holm, L & Rosenström *et al*., *Nucleic Acids Research*. **38**, W545–9, 2010) with the Rabin8C structure did not reveal any previously determined structure of the same fold. The diagram on the left shows the topology of one Rabin8C monomer in orange with the domain-swapped beta-strands of the neighboring subunit in the homo-dimer shown in yellow. The topology diagram was generated using Pro-origami (Stivala, A. *et al*., *Bioinformatics*. **27**, 3315–3316, 2011). The right panel shows the Rabin8C dimer structure. The two subunits are interlinked via the domain-swapped beta-strands to resemble a single pair of crab claws and we thus designate the Rabin8C fold the Crab-fold.

61

a

Superpositioning of Rab11-Rabin8
and Rab11-PIKIIIβ structures

Rab11
Rabin8
PI4KIIIß
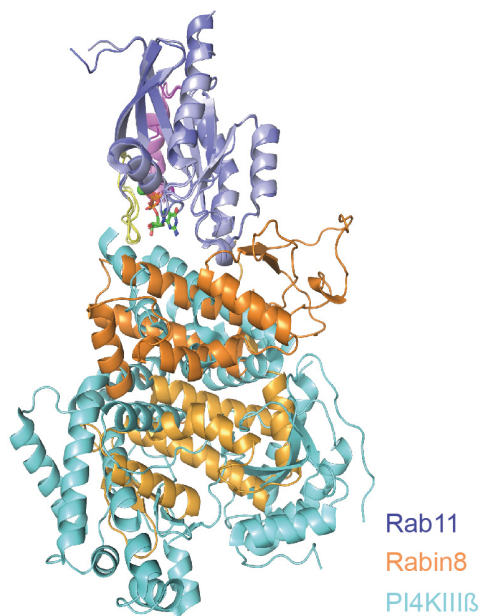
b

Model of the Rab11-FIP3-Rabin8 complex based
on the structures of Rab11-FIP3 and Rab11-Rabin8

Rab11
Rabin8
FIP3

Molecular clashes
between FIP3 and
Rabin8 subunits

c

	+	+	–	+	–	+	Rabin8 fl (HIS)
	–	–	–	+	+	+	FIP3 fl
	–	+	+	–	–	+	Rab11(Q70L) fl

MW (kDa)

116 —

66 —

45 —
35 —

25 —

18 —

1 2 3 4 5 6

FIP3 fl

Rabin8 fl (HIS)

Rab11(Q70L) fl

Supplementary Figure 3

Structural overlay of Rab11–Rabin8C with Rab11–PI4KIIIβ, structural model for Rab11–FIP3–Rabin8C and interactions of ciliary-targeting-complex subunits.

62

(a) Superpositioning of Rab11-Rabin8C and Rab11-PI4KIIIb (PDB code: 4D0L) structures reveal that Rabin8 and PI4KIIIb use similar binding sites on Rab11 despite adopting different folds. **(b)** Modeled dodecameric Rab11-FIP3-Rabin8 complex based on the structural superpositioning of Rab11-FIP3 (PDB code 2HV8) and Rab11-Rabin8 crystal structures. The model shows a closed arrangement of the complex with no unpaired dimerization interfaces. Several clashes, indicated by a red box, occur between FIP3 and Rabin8 at the center of the model suggesting that conformational rearrangements have to take place to accommodate a dodecameric structure. **(c)** Ni-NTA pull-downs of FIP3 and Rab11 with His-tagged Rabin8 demonstrates the formation of dual-effector-bound Rab11 complexes with full-length Rab11, FIP3 and Rabin8 constructs. Rabin8$_{fl}$ is prone to degradation from the N-termini giving rise to a pronounced smear of truncated Rabin8 proteins in the gel.

a

Crystal packing in space group P21

FIP3

Rab11   Rabin8   Rabin8   FIP3   Rotation 90°
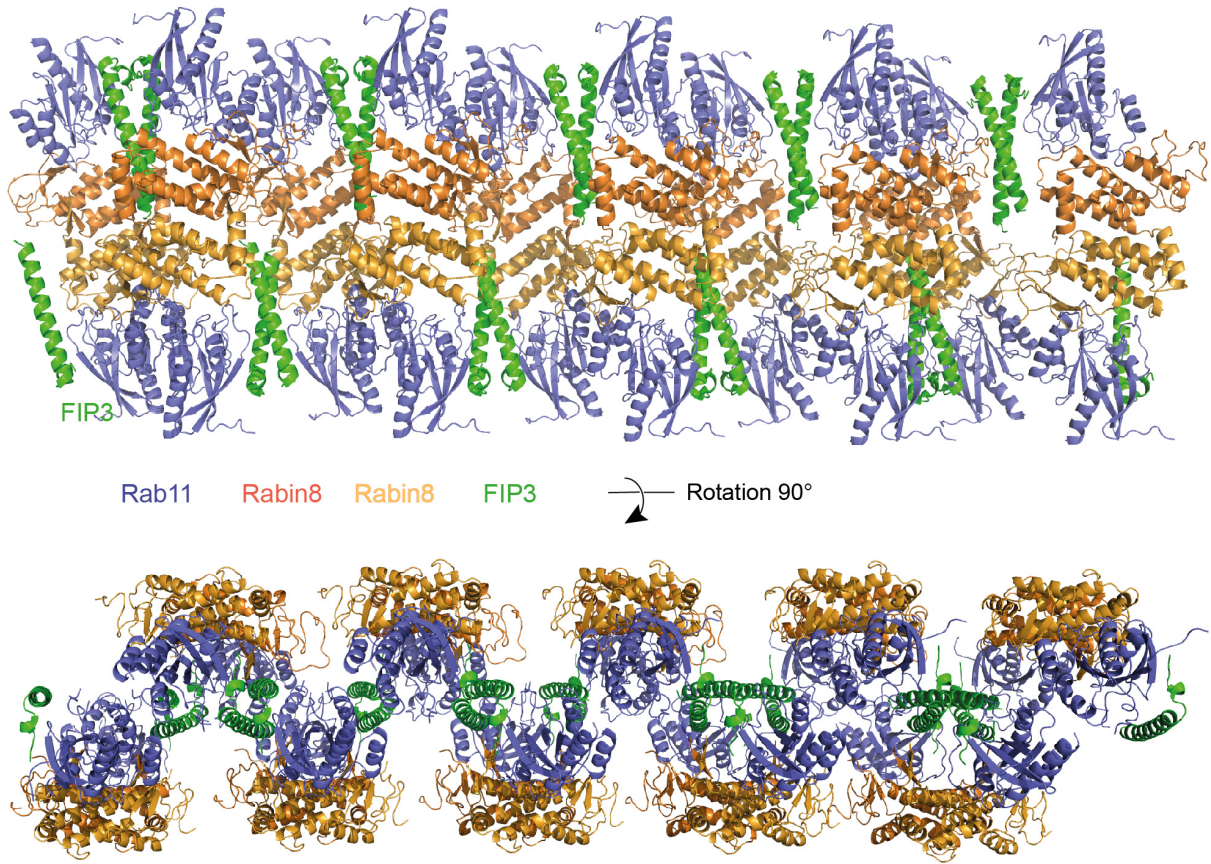
b

'open' dodecamer
740 Å² of buried surface area in between hexamers

2nd Rab11   FIP3 dimer   1st Rab11

1st Rabin8 dimer

~12 Å

~3 Å

2nd Rabin8 dimer

4th Rab11   3rd Rab11

Rotation 90°

FIP3 dimerization interface   FIP3 dimerization interface
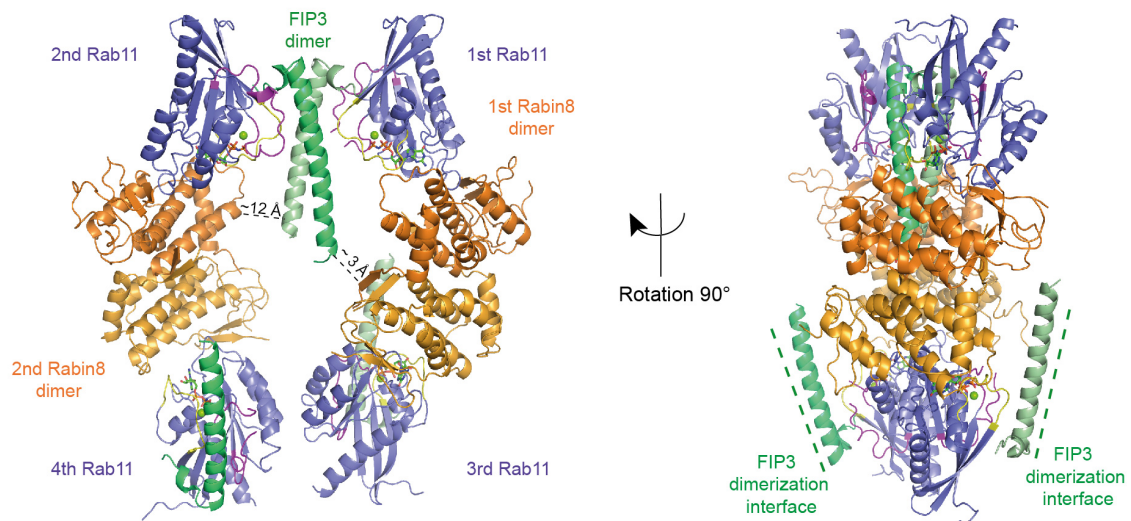
64

Packing of Rab11–FIP3–Rabin8C complexes in the crystals.

(a) Crystal packing for the 3.0Å P21 data reveals oligomerization of Rab11- $FIP3_{RBD}$-Rabin8C dodecamers via the well-characterized $FIP3_{RBD}$ homo-dimerization interface. **(b)** Structure of dodecameric Rab11-$FIP3_{RBD}$-Rabin8C as found in the asymmetric unit of the crystals. In this structure, two central $FIP3_{RBD}$ helices dimerize to form an asymmetric dodecamer with close contacts to only one of the two Rabin8C dimers. The contacts between the central $FIP3_{RBD}$ homo-dimer and the 1st Rabin8C homo-dimer induce a rotation that results in close interactions of the 3rd and 4th Rab11 molecule. This in turn exposes one $FIP3_{RBD}$ helix at each side of the dodecamer as shown in the perpendicular view.
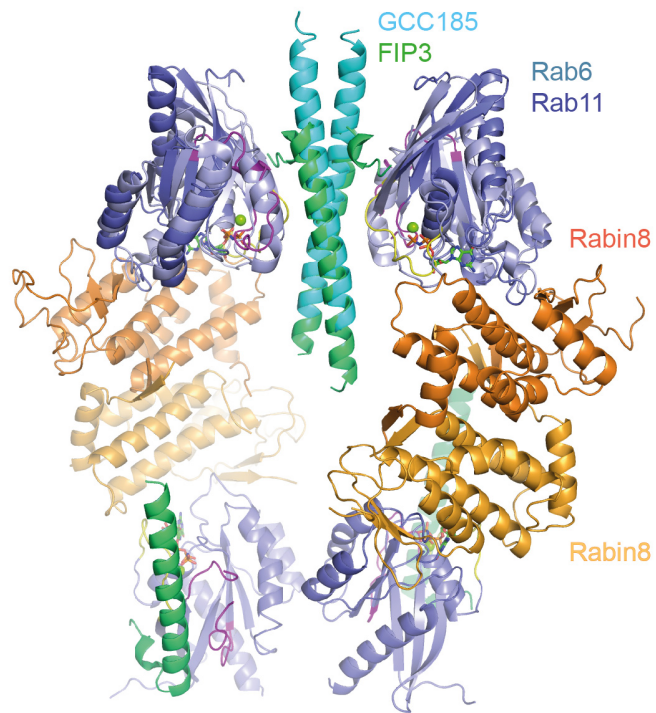
Supplementary Figure 5

Structural comparison with Rab6–GCC185.

Structural overlay of the Rab6-GCC185$_{RBD}$ complex structure (PDB code 3BBP) onto the Rab11-FIP3$_{RBD}$ hetero-tetramer of the Rab11-FIP3$_{RBD}$-Rabin8C dodecameric structure presented here. The two structures superimpose well with an RMSD of 3Å. The binding site of Rabin8 on Rab11 is unoccupied in the Rab6-GCC185 structure.

66

2.2 Atomic resolution structure of human α-tubulin acetyltransferase bound to acetyl-CoA

This research article deals with the structural characterization of the human α-tubulin acetyltransferase (αTAT1) and elucidates the underlying mechanism. As the name implies, αTAT1, is an enzyme that specifically acetylates lysine 40 of α-tubulin inside the microtubule lumen (Shida *et al.*, 2010). Lysine acetylation is a conserved posttranslational modification important to stabilize microtubules of axons and cilia. Depletion of αTAT1 leads to delay in ciliogenesis, suggesting a role for αTAT1 in proper cilia function. In this study, the atomic-resolution protein structure (1.05 Å) of the αTAT1 catalytic GNAT domain bound to its cosubstrate acetyl-CoA, is presented. Acetylation assays combined with structure-based mutational analysis allowed for identification and mapping of residues important for acetyl-Co-A binding, substrate binding and catalysis. The study revealed a conserved basic patch that mediates substrate binding and further identified a conserved glutamine residue (Q58), which appears to be required for catalysis. Analysis of the crystal structure of the catalytically dead Q58A mutant provides further evidence that this glutamine residue plays an important role in catalysis either acting as the general base or in stabilization of the reaction intermediate. Taken together, this article shows that tubulin and histone acetyltransferases use distinct reaction mechanisms.

Methods and supplementary material are attached at the end of the article.

Atomic resolution structure of human α-tubulin acetyltransferase bound to acetyl-CoA

Michael Taschner, Melanie Vetter, and Esben Lorentzen[1]

Department of Structural Cell Biology, Max Planck Institute of Biochemistry, D-82152 Martinsried, Germany

Acetylation of lysine residues is an important posttranslational modification found in all domains of life. α-tubulin is specifically acetylated on lysine 40, a modification that serves to stabilize microtubules of axons and cilia. Whereas histone acetyltransferases have been extensively studied, there is no structural and mechanistic information available on α-tubulin acetyltransferases. Here, we present the structure of the human α-tubulin acetyltransferase catalytic domain bound to its cosubstrate acetyl-CoA at 1.05 Å resolution. Compared with other lysine acetyltransferases of known structure, α-tubulin acetyltransferase displays a relatively well-conserved cosubstrate binding pocket but is unique in its active site and putative α-tubulin binding site. Using acetylation assays with structure-guided mutants, we map residues important for acetyl-CoA binding, substrate binding, and catalysis. This analysis reveals a basic patch implicated in substrate binding and a conserved glutamine residue required for catalysis, demonstrating that the family of α-tubulin acetyltransferases uses a reaction mechanism different from other lysine acetyltransferases characterized to date.

cilium | crystal structure | post-translational modification

Lysine acetylation is an ancient posttranslational protein modification conserved from bacteria to humans. In eukaryotes, protein acetylation regulates many aspects of cellular function including gene expression and neuronal migration and differentiation (1). Although this posttranslational modification has been known for decades (2), it was not until recently that acetylation was shown to be as widespread as phosphorylation, with 3,600 different sites mapped in human cells (3). Proteomics have revealed that acetylation is enriched in macromolecular complexes involved in very different cellular functions including DNA replication, transcription and repair, cell-cycle regulation, and intracellular trafficking (3). The transfer of an acetyl group to the ε-amino group of lysines is a reversible reaction catalyzed by lysine acetyltransferases (KATs) and relies on the coenzyme acetyl-CoA (AcCoA). The reverse reaction, which removes the acetyl group, is carried out by lysine deacetylases (KDACs), a group of enzymes that have attracted a lot of attention because they serve as drug targets in the treatment of cancer and Parkinson's and Alzheimer's diseases (4, 5). The KAT superfamily can be subdivided into several families with different substrate specificities and often limited sequence identity between families (1, 6). The KATs that are best understood at the molecular level are those that target lysine residues in the N-terminal tails of histones (2, 7, 8). Histone acetyltransferases (HATs) are typically divided into four families (GCN5/PCAF, p300/CBP, MYST, and Rtt109), which share a common core domain but have diverged significantly in substrate specificity and catalytic mechanism (3, 9). Another important acetylation is that of lysine-40 (K40) of α-tubulin, a modification found in cilia and neuronal processes that stabilizes polymerized microtubules (MT) (3, 10–13). This modification was shown to predominantly occur in polymerized MT rather than in free αβ-tubulin dimers (4, 5, 14, 15). K40 α-tubulin acetylation was shown to be catalyzed by the α-tubulin acetyltransferase (αTAT1) enzyme (also known as MEC-17) (16, 17), a distant homolog of HATs (18). αTAT1 acetylates α-tubulin

in a wide range of species including humans, and mutations that disrupt its function are known to cause neuromuscular and mechanosensory defects (16, 17). Furthermore, αTAT1 is conserved in all ciliated organisms examined and the depletion of αTAT1 was shown to significantly delay ciliogenesis, suggesting an important function of αTAT1 in stabilization of MT during elongation of the axoneme (16).

Structural studies of members of the four HAT families including GCN5/PCAF (19–22), MYST (23), Rtt109 (24, 25), and p300/CBP (26) have unraveled the molecular basis for substrate recognition and catalysis, demonstrating that different families use different reaction mechanisms. αTAT1 is known to specifically acetylate α-tubulin with no detectable activity toward core histones (16), but the molecular basis for this substrate specificity is unknown. To this end, we have determined the atomic resolution structure of human αTAT1 bound to its cosubstrate AcCoA and have characterized residues important for substrate binding and catalysis.

Results and Discussion

Overall Structure Characterization. Human αTAT1 (residues 1–196) was overexpressed in *Escherichia coli*, purified, and crystallized. The crystallized construct encompasses the catalytic domain (as identified, see ref. 16) and was active in MT acetylation in vitro (Fig. S1). The crystal structure was determined by using single-wavelength anomalous dispersion on selenomethionine substituted protein crystals and yielded electron density of excellent quality (Fig. S2). Optimized native crystals of αTAT1 were highly ordered and diffracted X-rays to atomic resolution (1.05 Å resolution, $R_{free} = 15.7\%$; Table S1). The structure reveals that the αTAT1 catalytic domain is composed of a central six-stranded antiparallel β-sheet flanked on each side by three α-helices (Fig. 1). The central β-sheet has a β-hairpin insertion (β4–β5; Fig. 1) between β3 and β6 that packs against the C-terminal part of the catalytic domain. The N-terminal 35 residues form mostly random coil structure that appears to have an important architectural role keeping cosubstrate-binding helix α2 in a correct position. Several conserved phenylalanine residues near the N terminus (F3, F5, and F11) pack into a hydrophobic pocket created by residues from the N-terminal half of α2 (Q42 and I46; Fig. S3). Although none of these residues are directly involved in cosubstrate binding, this observation provides a rationale for why a small N-terminal deletion renders the enzyme completely inactive (αTAT[10-236]; ref. 16). 3D structure searches
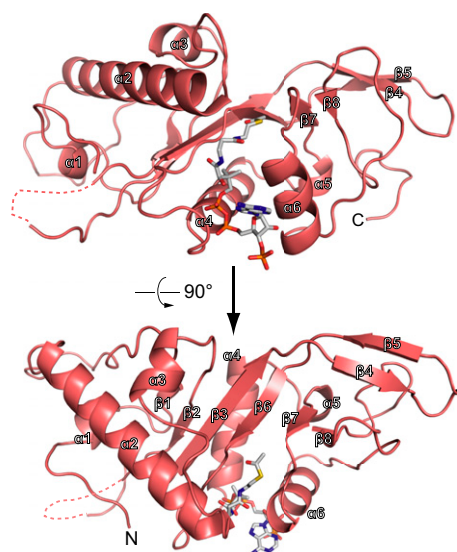

Fig. 1. Cartoon representation of the crystal structure of human αTAT1[1-196] bound to the cosubstrate AcCoA (shown as sticks). Termini and secondary structure elements are labeled. A short disordered loop region (residues 88–91) is indicated with a dashed line.

using the DALI server (27) revealed that the core domain of αTAT1 is similar to that of other KAT families with root-mean-square deviations (rmsd) of approximately 3 Å for more than 50% of all Cα-atoms of αTAT1. The structural conservation is, however, restricted to the very core of the enzyme as the surrounding amino acid sequences adopt different structures in different KATs (Fig. 2A and Fig. S4). This structural comparison confirms that the αTAT1 family of acetyltransferases, despite having low sequence identity in the range of 10–15%, share a common evolutionary origin with HATs (7, 18).

Cosubstrate Binding by αTAT1. Although the cosubstrate was not added before crystallization, the electron density unambiguously revealed the presence of an AcCoA coenzyme molecule in the active site of the protein that likely copurified with the recombinantly expressed protein in *E. coli* (Fig. 2B). The cosubstrate is buried deeply within a groove located at the center of the core domain and makes extensive contacts with αTAT1 mainly via helices α2, α4, and α6 and β-strands β6–7 as well as with the connecting loops (Figs. 1 and 2). Because the structure presented here was determined to atomic resolution, the AcCoA binding geometry can be determined accurately (Fig. 2C). αTAT1 makes more than 20 interactions of both hydrophobic and hydrophilic nature with AcCoA (Fig. 2C). Comparison with members of different HAT families reveals that the overall binding site for AcCoA is conserved among HATs and TATs, although the specific residues involved in cosubstrate recognition have diverged substantially (Fig. 2A and Fig. S5). For example, αTAT1 does not contain the unusually long L1 loop observed to contribute to cosubstrate binding in the p300/CBP and Rtt109 families of KATs (24, 26). The binding mode of AcCoA in different KATs is such that the activated acetyl groups are in similar positions, but the phosphoribose adenine (3′,5′-ADP) moieties occupy different positions (Fig. 2A). In the case of αTAT1, the adenine base of AcCoA has a binding mode not previously observed in members of other KAT families. In αTAT1, the adenine base of AcCoA is sandwiched between the side chains of K162 and R132 (Fig. 2B). R132 serves a dual role as it also forms multiple interactions with the 3′ phosphate group of the ribose ring of the AcCoA molecule (Fig. 2C). As K162 and R132 are well conserved among αTAT1 proteins (Fig. S5), the interactions that hold the adenine moiety in

place are likely to be a structural hallmark of the αTAT1 family. To test for the functional importance of K162 and R132 in binding and positioning of AcCoA, acetylation assays with polymerized MT were carried out by using αTAT1[1-196] R132A and K162A single-point mutants and the R132A/K162A double-point mutant (Fig. 2D). All αTAT1 mutants used in this study are soluble and properly folded as judged by size exclusion chromatography (Fig. S6). Quantifications within the linear range of the enzyme activity show that whereas the single-point mutants have approximately 50% of wild-type (wt) activity, the R132A/K162A double mutant has activity reduced to near background levels (Fig. 2E). As expected for AcCoA-binding mutants, the acetylation activity could be partly restored by adding 20× more cosubstrate (Fig. 2 D and E). The structural and biochemical data are thus consistent with a role for R132 and K162 in AcCoA binding and positioning in the αTAT1 family of KATs.

Substrate Recognition. *Conserved basic patch of αTAT1 is required for the acetylation of α-tubulin K40.* TATs and HATs share a common evolutionary origin reflected by a conserved core fold and AcCoA coenzyme binding site. However, HATs and TATs act on different substrates and are thus expected to have evolved different substrate binding sites specific for histones and α-tubulin, respectively. This assumption is supported by the fact that αTAT1 is specific for MT and does not acetylate core histones in vitro (16). Crystal structures of HATs in complex with histone substrate peptides reveal that the substrate adopts a random coil conformation and binds to an extended groove that runs parallel to the AcCoA cosubstrate binding site (22, 28). αTAT1 acetylates K40 of α-tubulin, a residue that is located in a highly conserved loop region of α-tubulin (α-Loop[K40]) found at the luminal side of MT (29). Comparison of the surface properties of the αTAT1 structure reveals a groove in a similar position to that of the histone peptide-binding groove in HATs (Fig. 3). The residues lining this groove are highly conserved among αTAT1 proteins (Fig. 3B), suggesting that it could be the binding site for the α-Loop[K40]. In agreement with this notion, the position of histone peptide seen in HATs fits the groove of αTAT1 without major clashes (Fig. 3 C and D). However, when Loop[K40] in the conformation observed in the αβ-tubulin structure (30) is superposed onto the HAT histone substrate, only the residues located N-terminally to K40 of α-tubulin share a similar binding mode with the histone peptide (the residues located C-terminally to K40 diverge substantially in structure; Fig. 3C). However, Loop[K40] may adopt a different conformation or be more flexible in the context of polymerized MT compared with Zn²⁺-induced tubulin sheets (which was the basis for the structural analysis in ref. 30). The residues flanking K40 of α-tubulin are mainly acidic, which is in contrasts to histone peptides that are mainly basic (Fig. 3 C and D). Consistently, the predicted α-tubulin binding groove of αTAT1 has a prominent positively charged patch formed by residues R69, H75, and K102 that is well suited to bind a negatively charged substrate. To test the functional importance of these residues, acetylation assays were performed with point-mutated proteins. Mutation of R69, H75, or K102 to glutamates results in a reduction of MT acetylation to background levels, an effect that cannot be significantly rescued by adding 5× more substrate, suggesting that substrate binding is severely impaired in these mutants (Fig. 3 E and F). Because R69, H75, and K102 are all located too far away from the acetyl group of the cosubstrate (>10 Å) to participate directly in catalysis or cosubstrate binding, the lack of activity upon mutation is most consistent with a role for these residues in α-tubulin substrate binding.

Lysine-binding cleft. The active site of αTAT1 harboring the acetyl group of the cosubstrate is located in a cleft into which the substrate target lysine must be inserted to become acetylated. The structure presented here does not have an α-tubulin substrate bound, but examination of crystal packing reveals that a

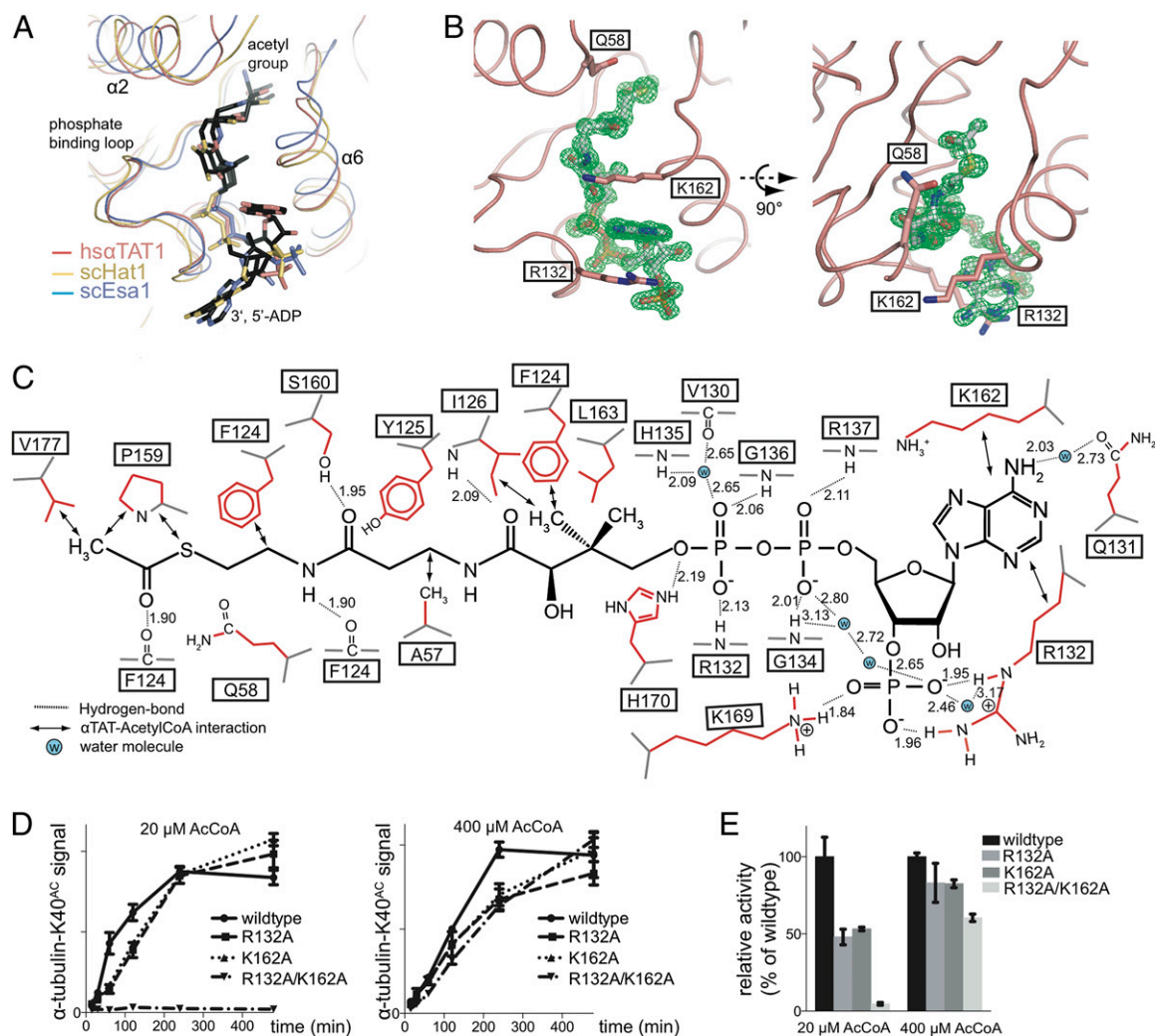Fig. 2. A conserved binding groove for the cosubstrate AcCoA in different KAT families. (A) Superimposed acetyl-CoA binding site of human αTAT1 (salmon), yeast Esa1 HAT (blue), and Hat1 (yellow). Secondary structure elements of αTAT1 and the 3′,5′-ADP and acetyl groups of AcCoA are indicated. (B) Two orthogonal views of AcCoA bound to αTAT1 with an unbiased difference electron density map (Fo-Fc) displayed in green at 5σ level. The adenine group is sandwiched between conserved residues (R132 and K162). (C) Detailed interaction map between αTAT1 and AcCoA. Different types of interactions are indicated. Distances for hydrogen bonds are measured between the hydrogen atom and the electronegative atom. For interactions with water molecules, the distances are measured from the oxygen atom of the solvent to the interacting atom. (D) Results of in vitro acetylation assays of MT with either wt or mutant αTAT1. Various time points (0–480 min) were analyzed by dot blot for K40-acetylated α-tubulin, and the resulting signals were quantified. Whereas the single R132 and K162 point mutants were only affected in the initial phase of the reaction but reached acetylation levels similar to the wt reaction toward the end of the time course with a concentration of 20 μM AcCoA (Left), the R132/K162 double mutant only showed background activity. The defects of both single mutants and the double mutant could be significantly rescued by addition of 20× AcCoA (400 μM), indicating that these residues play a role in cofactor binding (Right). Error bars show the SD from three independent experiments and are smaller than some symbols. (E) Comparison of the activities of αTAT1 proteins within the linear range of the reaction (0–120 min) both at low and high concentrations of AcCoA. The activity of the wt protein in both conditions was set to 100%. Error bars show the SD of three independent experiments.

neighboring αTAT1 molecule inserts the side chain of an arginine residue (R86 from the β2–β3 loop) into the active site (Fig. 4A) resembling the recognition of substrate lysines by HATs (22). This potential lysine-binding cleft is lined by the side chains of the well-conserved residues I64 and R158 (Fig. 4A and Fig. S5). The side chain of I64 and the aliphatic part of the R158 side chain form a hydrophobic cleft that could serve as a binding pocket for the hydrophobic part of the α-tubulin K40 side chain. In addition, the guanidinium group of R158 forms a hydrogen bond with the main-chain carbonyl of the loop from which the arginine pseudosubstrate protrudes, further stabilizing its position (Fig. 4A). To investigate the importance of I64 and R158 in αTAT1 function, single alanine point mutations were tested in MT acetylation assays. These experiments show that the activity

of the I64A mutant is at background levels, and the activity of the R158A mutant is approximately 20% of wt activity (Fig. 4 C and D). Consistent with a role in substrate binding, the activities of the I64A and R158A are partly rescued by the addition of 5× more substrate (Fig. 4 C and D). The structural and mutational data are consistent with a function of I64 and R158 in forming a pocket that binds and positions α-tubulin-K40 for acetylation.

Catalytic Mechanism of αTAT1. Several structures of HATs in complex with cosubstrates, histone-peptide substrates, and products of the acetylation reaction have elucidated that different HAT families operate via different reaction mechanisms. The classical catalytic mechanism described for GCN5/PCAF is relatively well understood and involves a glutamate residue (general base) that
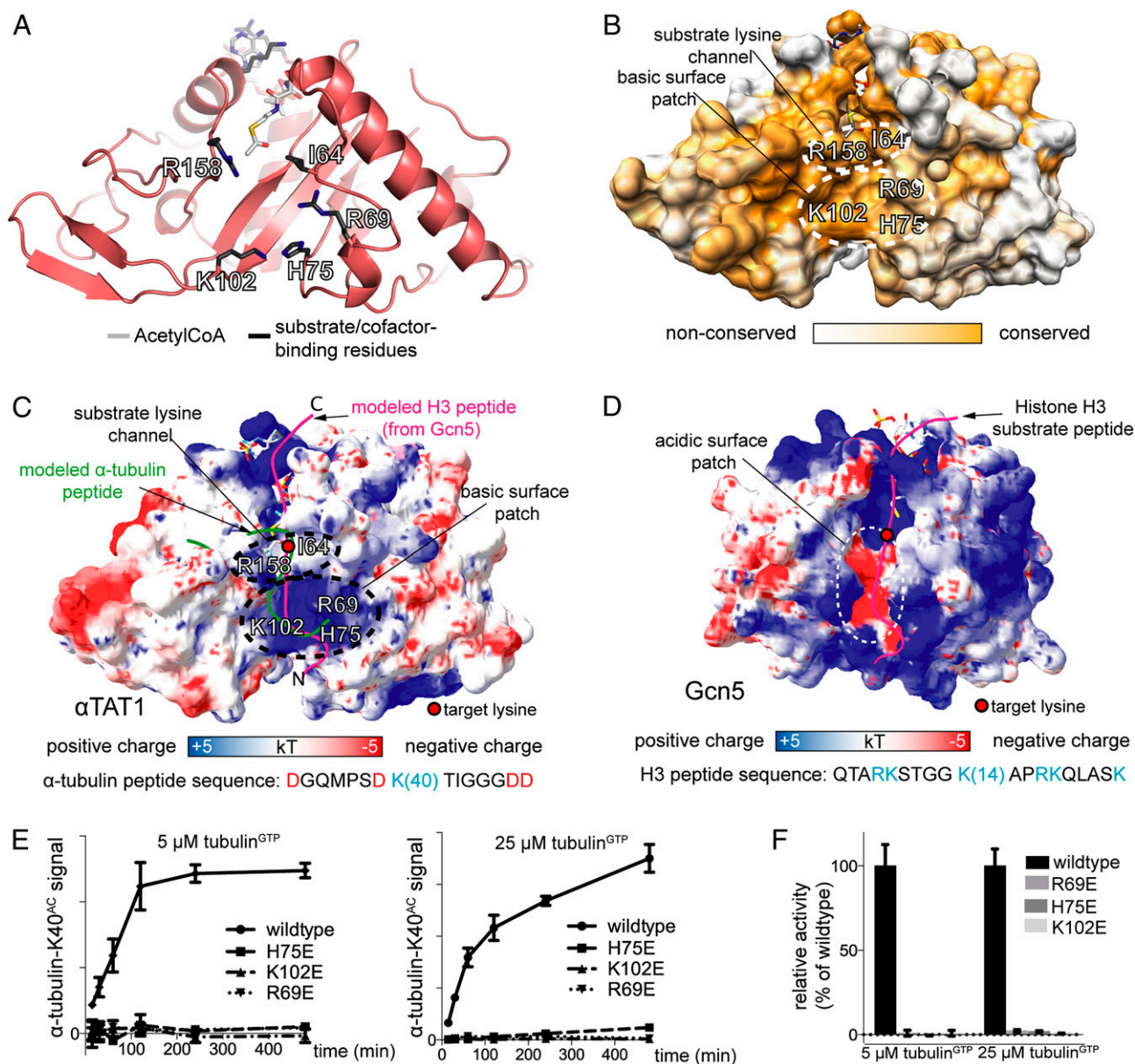
Fig. 3. A conserved basic patch likely mediates α-tubulin substrate binding in αTAT1. (*A*) Cartoon representation of the αTAT1 structure with important residues shown as gray sticks. Residues R158, I64, R69, H75, and K102 are potentially involved in substrate binding. (*B*) Surface representation of the αTAT1 structure colored according to sequence conservation within the αTAT1 family. A highly conserved cleft located close to the acetyl group of the cosubstrate is prime candidate for α-tubulin binding. The positions of conserved amino acids lining the cleft are indicated. (*C*) Electrostatic surface potential of αTAT1 with the cosubstrate shown as sticks and a modeled H3 substrate peptide shown in pink (from the GCN5 structure; PDB ID code 1PU9) and a modeled α-Loop^{K40} peptide (superimposed on the H3 peptide ofGCN5) shown in green (αβ-tubulin structure; PDB ID code 1TUB). Potential substrate binding regions are encircled. α-Loop^{K40} sequence is shown below the image, with basic and acidic residues shown in blue and red, respectively. (*D*) Electrostatic surface potential of the GCN5 HAT bound to H3 histone peptide (PDB ID code 1PU9). A region similar to the positively charged patch in Fig. 3*C* is encircled and shows a distinctively negatively charged area, providing a possible explanation for substrate specificity between histone and tubulin acetyltransferases. The sequence of the bound H3 histone peptide is indicated below the image. Results of in vitro acetylation assays of MT by basic patch αTAT1 mutants (*E*) and quantification of the results (*F*). Acetylation assays were done with either 5 or 25 μM substrate concentration. For further details, see Fig. 2 *D* and *E*.

activates a water molecule to remove a proton from the ε-amino group of the target lysine residue (22). The neutral lysine side chain can then perform a nucleophilic attack on the acetyl group of the cosubstrate, thus releasing the acetylated protein product and the CoA coenzyme. In contrast, the MYST family of HATs uses a ping-pong mechanism that requires a catalytic cysteine and autoacetylation of an active site lysine (23, 31). The Rtt109 family also uses autoacetylation of a buried lysine residue but has a divergent active site configuration compared with other KAT families. Further details of the catalytic mechanism of Rtt109 are not

well understood (24). Another difference of the Rtt109 family is the reliance on either of the two histone chaperones Asf1 or Vps75 for activity. However, another different mechanism was suggested for the P300/CBP family that lacks the catalytic glutamate and appears to use a so-called hit-and-run reaction that does not rely on a general base (26).

Inspection of the active site of the αTAT1 structure presented here reveals a different configuration from that of other KAT families. Both the catalytic glutamate and cysteine residues found in HATs are not present in αTAT1. A cysteine is found at β6 of
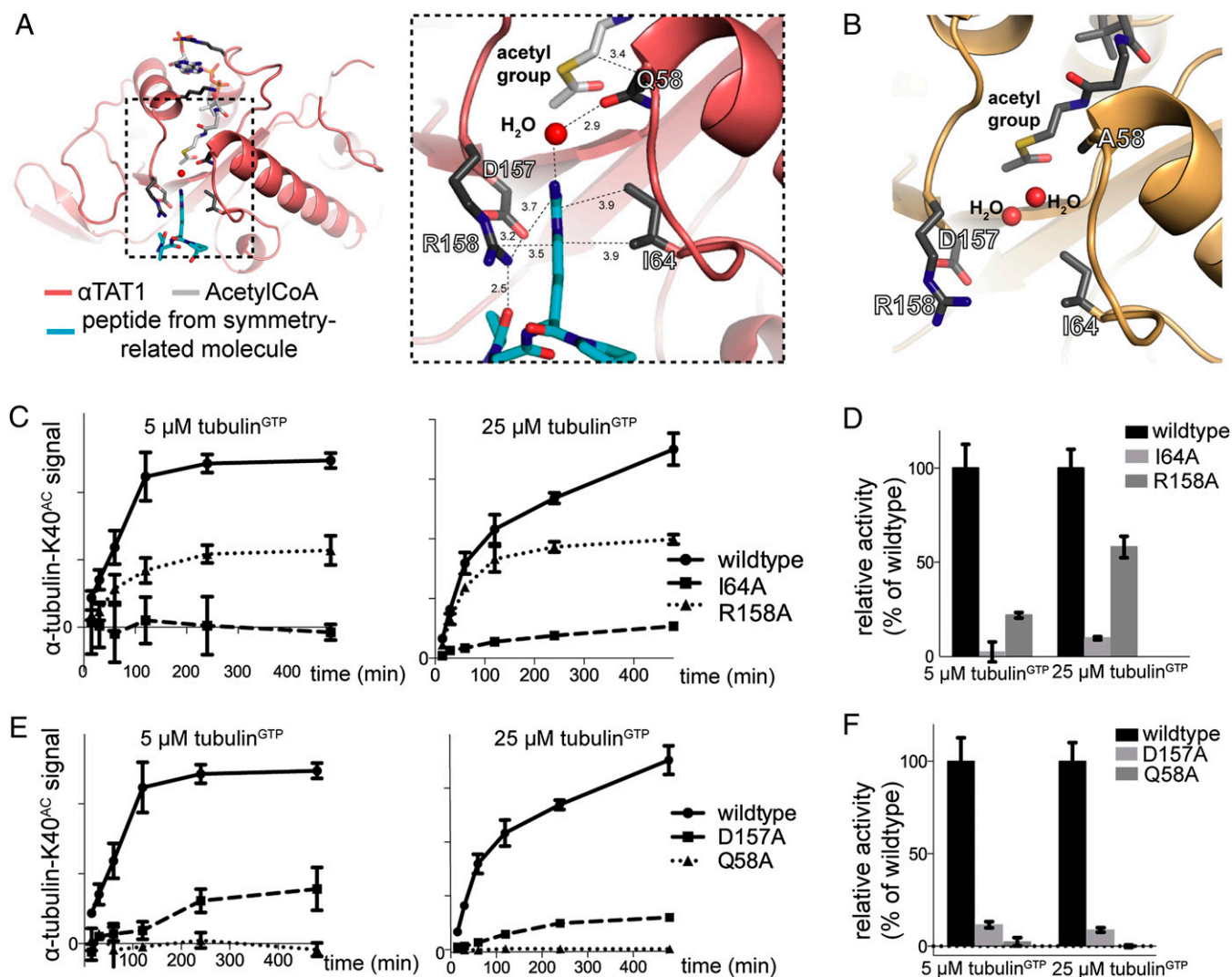
Fig. 4. Substrate lysine binding cleft and catalysis of αTAT1. (*A*) αTAT1 structure is shown as cartoon with AcCoA (white) and active site residues (gray) displayed as sticks. A loop region from a neighboring αTAT1 molecule in the crystal inserts the side chain of an arginine residue (blue) into the active site mimicking the substrate target lysine. A well-ordered water molecule that could participate in catalysis is shown as a red ball. A zoom-in with interaction distances indicated is shown within the dashed box. (*B*) Active site configuration of the Q58A point mutation. Two well-ordered water molecules are observed in the active site of the Q58A mutant structure (each approximately 2 Å away from the water molecule observed in the wt structure). The αTAT1 Q58A mutant crystallized in a different spacegroup where the insertion of a pseudosubstrate into the active site is not observed. (*C* and *E*) Acetylation assays of MT with potential lysine channel and catalytic residue mutants using either 5 or 25 μM substrate concentration. (*D* and *F*) Quantification of the results in *C* and *E*. For further details, see Fig. 2 *D* and *E*.

αTAT1 but is located too far away (11 Å) from the acetyl group of AcCoA to be involved in the catalytic mechanism (Fig. S7). However, a conserved aspartate residue (D157 in Hs-αTAT1) is found at a similar structural position as the catalytic glutamate in GCN5, suggesting that it could serve as the general base. In support of this notion, mutation of D157 to asparagine renders αTAT1 completely inactive (16). In the structure of αTAT1 presented here, D157 is positioned close to where the K40 target lysine is predicted to enter the active site (Fig. 4*A*). Additionally, D157 forms a salt bridge with and positions the side chain of R158, one of the residues suggested to line the α-tubulin K40-binding pocket. The structural data are thus both compatible with a role for D157 in catalysis as the general base and with a role in structuring the active site for substrate binding. To evaluate these possibilities, D157A mutant αTAT1[1-196] was tested in MT acetylation assays, demonstrating that the mutant is not catalytically dead but retains approximately 10% of wt protein acetylation activity (Fig. 4 *E* and *F*). This result is incompatible with D157 as an essential catalytic residue in the reaction mechanism. The

complete lack of activity observed for the D157N mutation (16) is likely a result of R158 occupying a conformation that occludes the substrate in the D157N mutant protein. To test whether the main function of D157 is in substrate binding, assays with 5× the substrate concentration were carried out but were unable to rescue the reduction in activity (Fig. 4 *E* and *F*). Another interesting property of the D157A mutant is that this protein behaves as a mixture of monomers and dimers in size exclusion chromatography (Fig. S6). The data are not consistent with the D157 as the general base in the reaction mechanism and suggest that mutation of this residue leads to significant structural changes resulting in dimerization of the enzyme.

This analysis raises the question of the nature of the potential general base in αTAT1. Examination of the αTAT1 active site reveals that a conserved glutamine (Q58 in hs-αTAT1) occupies a prominent position close to the acetyl group of the cosubstrate and could serve a role in keeping the cosubstrate in a productive conformation for catalysis or in stabilization of the reaction intermediate (Fig. 4*A* and Fig. S5). Additionally, Q58 coordinates

a well-ordered water molecule located at the end of the proposed target lysine-binding cleft (Fig. 4*A*), indicating that Q58 could serve the role as the general base in the reaction mechanism. To test whether Q58 is important for activity, αTAT1[1-196] Q58A mutant protein was purified and assayed for its ability to acetylate MT. The result of this experiment shows that αTAT1[1-196] Q58A is catalytically dead (Fig. 4 *E* and *F*). One possible explanation for the lack of αTAT1[1-196] Q58A activity is that this mutant is unable to bind AcCoA or that AcCoA binds but with the acetyl group positioned in a catalytically unproductive way. To assess this issue, the αTAT1[1-196] Q58A was crystallized and the structure determined at 1.6 Å resolution, demonstrating that AcCoA is still bound in the mutant protein. Wild-type and Q58A αTAT1[1-196] superimpose with an rmsd of 0.4 Å over all Cα atoms and the acetyl groups of the cosubstrate are positioned less than 0.3 Å apart, demonstrating that Q58 is not required for the correct positioning of AcCoA for catalysis (Fig. 4*B*). These results are consistent with a direct role for Q58 in catalysis, either as the general base required for activation of a water molecule or in stabilization of the reaction intermediate. In agreement with this notion, the activity of the Q58A mutant is not restored when increasing the substrate concentration (Fig. 4 *E* and *F*). Additional structural studies of αTAT1 in complex with substrates, reaction intermediates, and products of the reaction will be required for a more complete understanding of the catalytic mechanism of this family of acetyltransferases.

Acetylation of Ciliary MT by αTAT1. The fact that αTAT1 acts on α-tubulin K40 found at the luminal side of polymerized MT presents a logistical problem of how the enzyme gets access to the substrate in vivo. In the case of the cilium, αTAT1 likely enters this organelle via intraflagellar transport and is released inside the

cilium where it has to diffuse into the lumen of MT. Given the dimensions of the αTAT1 catalytic domain of 3–6 nm, diffusion through the 1.7-nm pores between MT protofilaments does not seem possible. The only entry point for αTAT1 into the MT lumen thus appears either to be at the MT plus end openings or through lateral openings created by MT defects (i.e., missing protofilaments). Once inside the MT lumen (inner diameter of 14 nm), αTAT1 can diffuse freely and would have a very high effective substrate concentration, which could contribute toward the higher efficiency toward MT substrates compared with free αβ-tubulin (16). Studies of how αTAT1 is transported into the cilium and into the lumen of MT should be the focus of future studies.

Materials and Methods

Recombinant protein expression in bacteria and subsequent crystallization and X-ray diffraction data collection were carried out as described in *SI Materials and Methods*. Acetyltransferase activity assays on polymerized microtubules were used to assess the effect of various mutations on enzymatic activity. Details about microtubule polymerization, the acetyltransferase assay, and quantification of enzyme activities can also be found in *SI Materials and Methods*.

1. Creppe C, et al. (2009) Elongator controls the migration and differentiation of cortical neurons through acetylation of alpha-tubulin. *Cell* 136(3):551–564.
2. Allfrey VG, Faulkner R, Mirsky AE (1964) Acetylation and methylation of histones and their possible role in the regulation of RNA synthesis. *Proc Natl Acad Sci USA* 51:786–794.
3. Choudhary C, et al. (2009) Lysine acetylation targets protein complexes and co-regulates major cellular functions. *Science* 325(5942):834–840.
4. Bolden JE, Peart MJ, Johnstone RW (2006) Anticancer activities of histone deacetylase inhibitors. *Nat Rev Drug Discov* 5(9):769–784.
5. Kazantsev AG, Thompson LM (2008) Therapeutic application of histone deacetylase inhibitors for central nervous system disorders. *Nat Rev Drug Discov* 7(10):854–868.
6. Aka JA, Kim G-W, Yang X-J (2011) K-acetylation and its enzymes: Overview and new developments. *Handb Exp Pharmacol* 206:1–12.
7. Kuo MH, Allis CD (1998) Roles of histone acetyltransferases and deacetylases in gene regulation. *Bioessays* 20(8):615–626.
8. Marmorstein R, Roth SY (2001) Histone acetyltransferases: Function, structure, and catalysis. *Curr Opin Genet Dev* 11(2):155–161.
9. Marmorstein R, Trievel RC (2009) Histone modifying enzymes: Structures, mechanisms, and specificities. *Biochim Biophys Acta* 1789:58–68.
10. Janke C, Bulinski JC (2011) Post-translational regulation of the microtubule cytoskeleton: Mechanisms and functions. *Nat Rev Mol Cell Biol* 12(12):773–786.
11. Webster DR, Borisy GG (1989) Microtubules are acetylated in domains that turn over slowly. *J Cell Sci* 92(Pt 1):57–65.
12. L'Hernault SW, Rosenbaum JL (1985) Reversal of the posttranslational modification on Chlamydomonas flagellar alpha-tubulin occurs during flagellar resorption. *J Cell Biol* 100(2):457–462.
13. LeDizet M, Piperno G (1987) Identification of an acetylation site of Chlamydomonas alpha-tubulin. *Proc Natl Acad Sci USA* 84(16):5720–5724.
14. Maruta H, Greer K, Rosenbaum JL (1986) The acetylation of alpha-tubulin and its relationship to the assembly and disassembly of microtubules. *J Cell Biol* 103(2):571–579.
15. Piperno G, LeDizet M, Chang XJ (1987) Microtubules containing acetylated alpha-tubulin in mammalian cells in culture. *J Cell Biol* 104(2):289–302.
16. Shida T, Cueva JG, Xu Z, Goodman MB, Nachury MV (2010) The major alpha-tubulin K40 acetyltransferase alphaTAT1 promotes rapid ciliogenesis and efficient mechanosensation. *Proc Natl Acad Sci USA* 107(50):21517–21522.

17. Akella JS, et al. (2010) MEC-17 is an alpha-tubulin acetyltransferase. *Nature* 467(7312):218–222.
18. Steczkiewicz K, Kinch L, Grishin NV, Rychlewski L, Ginalski K (2006) Eukaryotic domain of unknown function DUF738 belongs to Gcn5-related N-acetyltransferase superfamily. *Cell Cycle* 5(24):2927–2930.
19. Dutnall RN, Tafrov ST, Sternglanz R, Ramakrishnan V (1998) Structure of the histone acetyltransferase Hat1: A paradigm for the GCN5-related N-acetyltransferase superfamily. *Cell* 94(4):427–438.
20. Clements A, et al. (1999) Crystal structure of the histone acetyltransferase domain of the human PCAF transcriptional regulator bound to coenzyme A. *EMBO J* 18(13):3521–3532.
21. Lin Y, Fletcher CM, Zhou J, Allis CD, Wagner G (1999) Solution structure of the catalytic domain of GCN5 histone acetyltransferase bound to coenzyme A. *Nature* 400(6739):86–89.
22. Rojas JR, et al. (1999) Structure of Tetrahymena GCN5 bound to coenzyme A and a histone H3 peptide. *Nature* 401(6748):93–98.
23. Yuan H, et al. (2012) MYST protein acetyltransferase activity requires active site lysine autoacetylation. *EMBO J* 31(1):58–70.
24. Tang Y, et al. (2008) Fungal Rtt109 histone acetyltransferase is an unexpected structural homolog of metazoan p300/CBP. *Nat Struct Mol Biol* 15(7):738–745.
25. Tang Y, et al. (2011) Structure of the Rtt109-AcCoA/Vps75 complex and implications for chaperone-mediated histone acetylation. *Structure* 19(2):221–231.
26. Liu X, et al. (2008) The structural basis of protein acetylation by the p300/CBP transcriptional coactivator. *Nature* 451(7180):846–850.
27. Holm L, Rosenström P (2010) Dali server: Conservation mapping in 3D. *Nucleic Acids Res* 38(Web Server issue):W545–549.
28. Poux AN, Marmorstein R (2003) Molecular basis for Gcn5/PCAF histone acetyltransferase selectivity for histone and nonhistone substrates. *Biochemistry* 42(49):14366–14374.
29. Nogales E, Whittaker M, Milligan RA, Downing KH (1999) High-resolution model of the microtubule. *Cell* 96(1):79–88.
30. Nogales E, Wolf SG, Downing KH (1998) Structure of the alpha beta tubulin dimer by electron crystallography. *Nature* 391(6663):199–203.
31. Yan Y, Harper S, Speicher DW, Marmorstein R (2002) The catalytic mechanism of the ESA1 histone acetyltransferase involves a self-acetylated intermediate. *Nat Struct Biol* 9(11):862–869.

Supporting Information

Taschner et al. 10.1073/pnas.1209343109

SI Materials and Methods

Purification and Crystallization of αTAT[1-196]. Isoform 5 of human αTAT1 (323 residues) was cloned from the MegaMan Human transcriptome cDNA library (Agilent) into different pET-based vectors and subsequently used to clone a truncated version of αTAT1 containing only the catalytic domain (residues 1–196). αTAT[1-196] (wild-type and point mutants) was overexpressed with an N-terminal hexa-histidine tag in *Escherichia coli* and purified by Ni-NTA affinity, Q-Sepharose ion-exchange, and Superdex75 size exclusion chromatography (final buffer: 10 mM Tris·HCl at pH 7.5, 150 mM NaCl, and 1 mM DTT). The selenium methionine substituted protein was purified as the native protein but with 5 mM DTT added to buffers used in the Q-Sepharose and size exclusion chromatography steps. For crystallization, wild-type αTAT[1-196] at 45 mg/mL concentration was mixed with an equal volume of precipitant solution containing 50 mM Tris·HCl at pH 8.0, 200 mM NaCl, and 15% (wt/vol) PEG 8000. Crystals grew in 4–6 d at 18 °C to a maximum size of 0.5 mm and were flash cooled (liquid nitrogen) in mother liquor supplemented with 15% glycerol. αTAT[1-196] Q58A mutant protein was crystallized at 74 mg/mL concentration by mixing the protein with an equal volume of 2.8 M Na-acetate at pH 7.0. The mother liquor was supplemented with 20% glycerol before flash-cooling in liquid nitrogen.

X-Ray Diffraction Data Collection and Structure Refinement. Selenomethionine substituted αTAT1 crystals diffracted X-rays to approximately 1.5 Å resolution by using an attenuated beam. A SAD dataset of 720° rotation was collected at the Se peak wavelength at PXIII at the Swiss Light Source (Villigen, Switzerland) and processed by using XDS (1). A strong anomalous signal was detectable, extending to 2 Å resolution. Phase calculation, solvent flattening, and initial automated model building were carried out by using the SHELX package (2). Native crystals diffracted X-rays extremely well, and data were collected and processed to 1.05 Å resolution. Because the mosaicity was estimated as low as 0.1° for the best native crystal, finely sliced data of 4,500 frames (0.05° rotation per frame) were collected and processed by using XDS. The wavelength of the X-rays was reduced to 0.8 Å to capture all high-resolution reflections that would otherwise fall outside the detector space. Refinement was carried out in PHENIX (3) by using the model obtained from the selenomethionine SAD data as a starting point. The final model

resulted from iterative cycles of model building in COOT (4) and refinement in PHENIX. The model contains all residues from 1 to 195 except a small disordered loop between residues 88–91 that could not be modeled. Residues 105–115 were clearly observed to be flexible and were modeled in the two most prominent conformations. After completing the building of the polypeptide, clear electron density remained at the core of the protein and could be unambiguously identified as a bound acetyl-CoA molecule. Because of the atomic resolution of the data, all heavier atoms (C, N, O, S, and P) were refined with anisotropic atomic displacement parameters (ADPs) in PHENIX. Well-ordered parts of the protein and the acetyl-CoA molecule clearly displayed positive electron density peaks at the theoretical positions for hydrogens, which were consequently added to the model (but not to solvent molecules). Hydrogens were refined in riding positions by using isotropic ADPs. αTAT[1-196] Q58A mutant protein crystals diffracted to 1.6 Å resolution and belonged to a different spacegroup than crystals of αTAT[1-196] wild-type protein (Table 1). The structure of αTAT[1-196] Q58A was determined by molecular replacement using the structure of the wild-type protein and refined in PHENIX with isotropic ADPs and hydrogens in a riding position.

MT Acetylation Assay. For assembly of microtubules, 50 μM αβ-tubulin dimers (bovine brain, Cytoskeleton) were incubated at 37 °C for 40 min in the presence of 2 mM GTP and 5% glycerol and used in acetylation reactions with αTAT1. The reaction mix contained either 5 μM or 25 μM polymerized microtubules, 2.5 μM αTAT1 (either wild type or mutant), 80 mM Pipes at pH 6.9, 0.5 mM EGTA, 2 mM MgCl$_2$, 10% glycerol, 1 mM DTT, and either 20 μM or 400 μM acetyl-CoA. Total reaction volumes of 50 μL were set up and incubated at 37 °C. Seven-microliter samples were removed at the indicated time points, mixed with an equal volume of 2× SDS loading dye, and incubated at 95 °C for 5 min to stop the reaction. Three microliters of the obtained sample were spotted on nitrocellulose membranes, and K40-acetylated α-tubulin was subsequently detected by using the 6-11B-1 antibody (Sigma), followed by incubation with Alexa Fluor 647 rabbit anti-mouse antibody. The fluorescent signals were detected by using a Typhoon FLA 7000 scanner (GE Healthcare) and quantified by using the ImageQuant software. The acetylation activity of each mutant was tested in three independent experiments.

1. Kabsch W (2010) XDS. *Acta Crystallogr D Biol Crystallogr* 66(Pt 2):125–132.
2. Sheldrick GM (2008) A short history of SHELX. *Acta Crystallogr A* 64(Pt 1):112–122.
3. Adams PD, et al. (2010) PHENIX: A comprehensive Python-based system for macromolecular structure solution. *Acta Crystallogr D Biol Crystallogr* 66(Pt 2):213–221.
4. Emsley P, Lohkamp B, Scott WG, Cowtan K (2010) Features and development of Coot. *Acta Crystallogr D Biol Crystallogr* 66(Pt 4):486–501.
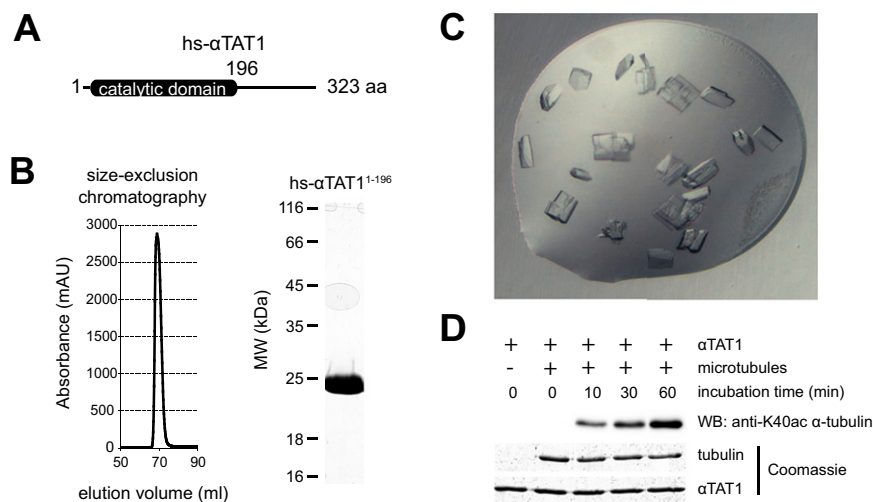
74

Fig. S1. Purification, crystallization, and activity of αTAT1[1-196]. (*A*) Schematic representation of the hs-αTAT1 protein. The 323-aa protein contains the catalytic domain at the N terminus (1–196) and a C-terminal tail predicted to be unstructured. (*B*) Purification of hs-αTAT1[1-196]. The final elution profile from size exclusion chromatography (HiLoad Superdex75) is shown, together with a Comassie stained gel. The protein fragment eluted as a sharp single peak corresponding to monomeric protein and was highly pure. (*C*) Native protein crystals formed by the protein preparation shown in *B* in the initial crystallization screen. (*D*) The purified hs-αTAT1[1-196] is catalytically active toward α-tubulin K40 in microtubules. Five micromolar αTAT1[1-196] was incubated either without microtubules or with 2 μM polymerized α/β-tubulin dimers for the indicated times. K40-acetylated α-tubulin was detected by Western blot using an acetlyation-specific antibody, and the presence of equal amounts of protein (both αTAT1[1-196] and tubulin) was confirmed by Coomassie staining.
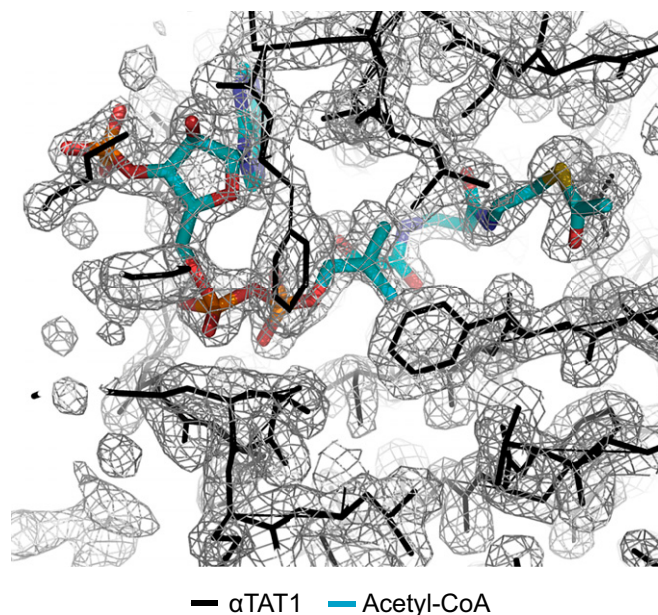

Fig. S2. Experimental electron density map at 1σ displayed around the cofactor binding site. The AcCoA is shown as sticks (carbons in turquoise color), and amino acids of the αTAT1 protein are displayed as black sticks.
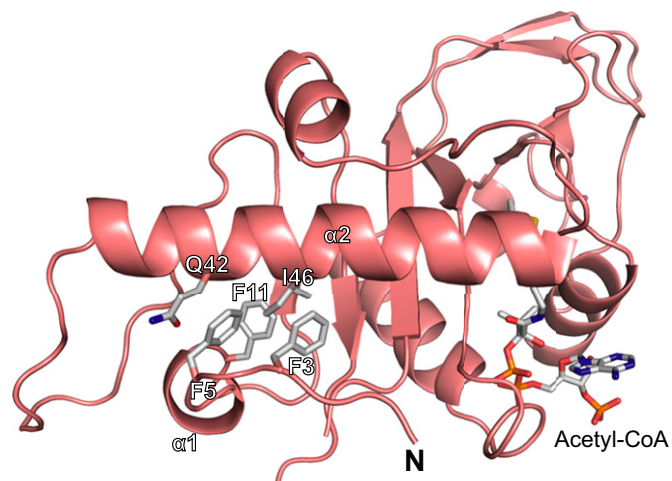
Fig. S3. Cartoon representation of αTAT1[1-196] displaying the N-terminal part of the protein. Three conserved phenylalanines (F3, F5, F11) pack into a hydrophobic pocket created by residues from the N-terminal half of α2 (Q42 and I46), thereby stabilizing this helix. The AcCoA molecule is shown as sticks; the N terminus of αTAT1[1-196] is labeled.
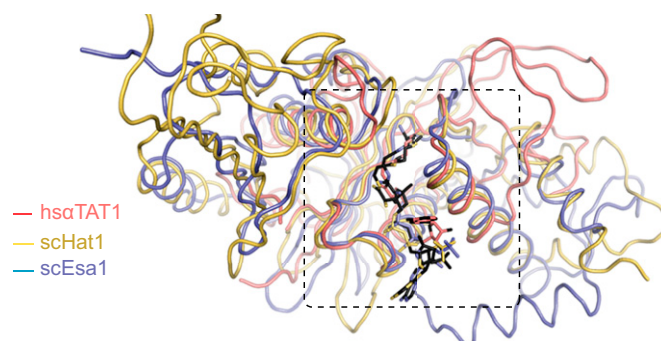

Fig. S4. Superposition of three different families of KATs: αTAT1 is colored salmon, yeast Esa1 HAT (PDB ID code: 3TO7) is shown in blue, and yeast Hat1 (1BOB) in yellow. The cofactors are shown a stick models. The structural conservation between HATs and αTAT1 is restricted to the very core of the enzymes. The boxed region is shown in Fig. 2A.
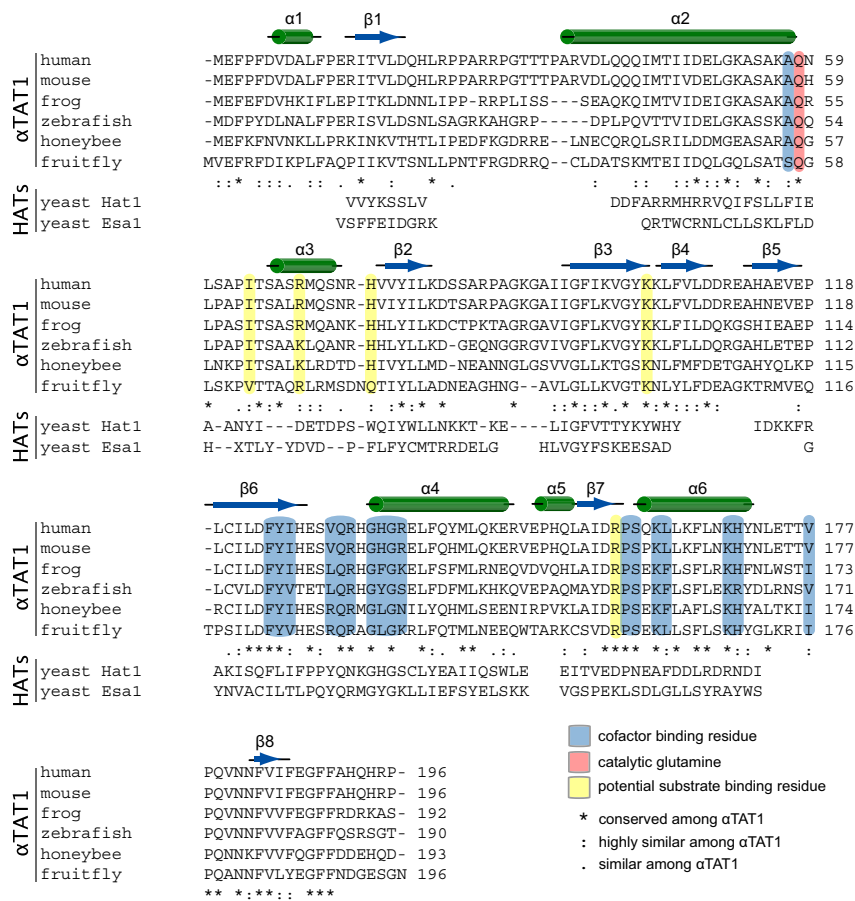
Fig. S5. Sequence alignment of αTAT1 from various species. The positions of secondary structure elements from human αTAT1 are shown above the alignment. Important residues (as determined in this study) are highlighted. AcCoA binding residues are marked in blue, potential substrate-binding residues are marked in yellow, and the glutamine proposed here to function in catalysis marked in red. Sequences from two HATs (ScHat1 and ScEsa1) are also shown at the appropriate positions (as determined by a structure-based alignment using the DALI server).

77

Fig. S6. Size-exclusion chromatograms (Superdex75) of the wild type and all of the mutant versions of αTAT1[1-196] used in this study. With the exception of the D157A mutant, all proteins elute at the same volume as the wild type, indicative of proper folding of the mutants. In the case of D157A, we observe a second peak at a lower elution volume in addition to the peak observed for the wild type, which is most likely caused by dimerization of the mutant protein. We note that these two forms of the D157A mutant protein are in equilibrium and are interconverted after storage for several hours at 4 °C.

Fig. S7. Position of Cys120 relative to the catalytic site. (*A*) Structure of the αTAT1 active site reveals that Cys120 is located approximately 11 Å from the acetyl group of the cosubstrate. Cys120 is part of a hydrophobic pocket together with Leu104 and Phe183 and, thus, unlikely to be a catalytic cysteine in a ping-pong mechanism. (*B*) Acetylation assays of MT with C120A and C120S mutants, both at 2.5 μM and 12.5 μM enzyme concentration. Note that both cysteine mutants displayed a pronounced tendency to aggregate, likely due to a destabilization of the hydrophobic core. (*C*) Quantification of the results shown in (*B*). The C120A αTAT1 mutant protein has approximately 8% of wild-type activity under steady-state conditions and approximately 36% under single turnover conditions. These results further speak against Cys120 as a catalytic residue.

Table S1. Data collection and refinement statistics for Hs αTAT1

Measurement	Native	Q58A point mutant	Se-Met peak
Space group	*P21212*	*P212121*	*P21212*
Data collection			
Wavelength, Å	0.8000	0.9999	0.9786
Unit cell, Å	*a* = 42.20	*a* = 36.76	*a* = 42.22
	b = 121.96	*b* = 110.87	*b* = 121.84
	c = 37.28	*c* = 113.58	*c* = 37.29
Resolution, Å	40–1.05 (1.10–1.05)	40–1.60 (1.70–1.60)	40–1.82 (1.93–1.82)
R_{sym}	0.026 (0.788)	0.035 (0.744)	0.050 (0.277)
$I/\sigma(I)$	29.0 (2.3)	24.7 (2.7)	38.5 (9.6)
Completeness	0.999 (0.993)	0.963 (0.881)	0.997 (0.979)
Multiplicity	7.6 (6.1)	6.6 (6.3)	13.1 (12.8)
Refinement			
Resolution, Å	40–1.05 (1.062–1.050)	40–1.60 (1.64–1.60)	—
No. of unique reflections	86,586	60,072	—
R_{work}	0.131 (0.349)	0.185 (0.331)	—
R_{free}	0.157 (0.354)	0.222 (0.295)	—
Ramachandran plot			
Preferred regions	0.975	0.975	—
Allowed regions	0.025	0.025	—
R.m.s. deviations			
Bond lengths (Å)	0.021	0.016	—
Bond angles (°)	2.1	1.7	—

Highest resolution shell is shown in parentheses.

2.3 Phosphoproteomics reveals that Parkinson's disease kinase LRRK2 regulates a subset of Rab GTPases

Steger, M., Tonelli, F., Ito, G., Davies, P., Trost, M., **Vetter, M.,** Wachter, S., Lorentzen, E., Duddy, G., Wilson, S., Baptista, M., Fiske, B., Fell, M., Morrow, J., Reith, A., Alessi, D., Mann, M. (2016). Phosphoproteomics reveals that Parkinson's disease kinase LRRK2 regulates a subset of Rab GTPases. *eLife* ((5), e12813).

The study identified a subset of Rab GTPases as key targets of the Leucine-rich repeat kinase (LRRK2). Mutations in the Park8 gene that encodes LRRK2 are the most common causes of Parkinson's disease, a degenerative disorder of the nervous system (Khan *et al.*, 2005; West *et al.*, 2005; Jaleel *et al.*, 2007; Simón-Sánchez *et al.*, 2009). It has been demonstrated that amino acid substitutions in LRRK2 activates the kinase two-to-threefold (West *et al.*, 2005; Jaleel *et al.*, 2007), which in turn led to the development of drugs that aim to inhibit kinase activity in order to prevent or delay the progression of the disease (Yao *et al.*, 2013). A phosphoproteomic screening approach using mouse embryonic fibroblasts revealed that several Rab GTPases (3, 8, 10 and 12), important regulators of membrane traffic, are key targets of the LRRK2 kinase. LRRK2 directly phosphorylates these substrates both *in vitro* and *in vivo* on a conserved threonine residue located in the nucleotide-sensitive switch II region. Since switch regions not only mediate GDP/GTP exchange but also interact with effector and regulatory proteins, the functional role of Rab phosphorylation has been further elucidated using non-phosphorylatable T72A-Rab8 and phosphomimetic T72E-Rab8 mutants. Affinity-purification mass spectrometry (AP-MS) revealed that more proteins bind to T72A-Rab8 compared to T72E-Rab8 including Rab GDP dissociation inhibitors α and β (GDI1 and GDI2) and the Rab8 guanine nucleotide exchange factor (GEF) Rabin8. Pulldown experiments and GEF assays using phosphorylated T72Rab8 exhibit not only reduced binding to Rabin8, but also show decreased levels of Rabin8-catalzyed GDP to GTP exchange, thus further substantiated the findings that Rab8 phosphorylation by LRRK2 can limit its activation by Rabin8. The affinities of GDIs for target LRRK2 Rabs are diminished in a manner correlating with phosphorylation levels induced by different LRRK2 pathogenic mutations, demonstrating that interference with Rab-GDI interactions results in an altered subcellular localization of Rabs.

Methods and supplementary material are attached at the end of the article.

Phosphoproteomics reveals that Parkinson's disease kinase LRRK2 regulates a subset of Rab GTPases

Martin Steger[1], Francesca Tonelli[2], Genta Ito[2], Paul Davies[2], Matthias Trost[2], Melanie Vetter[3], Stefanie Wachter[3], Esben Lorentzen[3], Graham Duddy[4†], Stephen Wilson[5], Marco AS Baptista[6], Brian K Fiske[6], Matthew J Fell[7], John A Morrow[8], Alastair D Reith[9], Dario R Alessi[2*], Matthias Mann[1*]

[1]Department of Proteomics and Signal Transduction, Max Planck Institute of Biochemistry, Martinsried, Germany; [2]Medical Research Council Protein Phosphorylation and Ubiquitylation Unit, College of Life Sciences, University of Dundee, Dundee, United Kingdom; [3]Department of Structural Cell Biology, Max Planck Institute of Biochemistry, Martinsried, Germany; [4]Molecular Discovery Research, GlaxoSmithKline Pharmaceuticals R&D, Harlow, United Kingdom; [5]RD Platform Technology and Science, GlaxoSmithKline Pharmaceuticals R&D, Stevenage, United Kingdom; [6]The Michael J. Fox Foundation for Parkinson's Research, New York, United States; [7]Early Discovery Neuroscience, Merck Research Laboratories, Boston, United States; [8]Neuroscience, Merck Research Laboratories, Westpoint, United States; [9]Neurodegeneration Discovery Performance Unit, GlaxoSmithKline Pharmaceuticals R&D, Stevenage, United Kingdom

Abstract Mutations in Park8, encoding for the multidomain Leucine-rich repeat kinase 2 (LRRK2) protein, comprise the predominant genetic cause of Parkinson's disease (PD). G2019S, the most common amino acid substitution activates the kinase two- to threefold. This has motivated the development of LRRK2 kinase inhibitors; however, poor consensus on physiological LRRK2 substrates has hampered clinical development of such therapeutics. We employ a combination of phosphoproteomics, genetics, and pharmacology to unambiguously identify a subset of Rab GTPases as key LRRK2 substrates. LRRK2 directly phosphorylates these both in vivo and in vitro on an evolutionary conserved residue in the switch II domain. Pathogenic LRRK2 variants mapping to different functional domains increase phosphorylation of Rabs and this strongly decreases their affinity to regulatory proteins including Rab GDP dissociation inhibitors (GDIs). Our findings uncover a key class of bona-fide LRRK2 substrates and a novel regulatory mechanism of Rabs that connects them to PD.
DOI: 10.7554/eLife.12813.001

Introduction

Parkinson's disease (PD) is the second most common neurodegenerative disease, affecting 1–2% of the elderly population (*Lees et al., 2009*). Environmental and genetic factors contribute to the development of the disease, but its precise etiology still remains elusive (*Burbulla and Krüger, 2011*). Genome-wide association studies (GWAS) have related 28 genetic risk variants at 24 loci with nonfamilial PD (*Nalls et al., 2014*). Among those, mutations in LRRK2 (Park8) are also found in hereditary forms, pinpointing a shared molecular pathway driving pathogenesis in both familial and non-familial PD and comprising the most common cause of the disease (*Simón-Sánchez et al.,*

eLife digest Parkinson's disease is a degenerative disorder of the nervous system that affects approximately 1% of the elderly population. Mutations in the gene that encodes an enzyme known as LRRK2 are the most common causes of the inherited form of the disease. Such mutations generally increase the activity of LRRK2 and so drug companies have developed drugs that inhibit LRRK2 to prevent or delay the progression of Parkinson's disease. However, it was not known what role LRRK2 plays in cells, and why its over-activation is harmful.

Steger et al. used a 'proteomics' approach to find other proteins that are regulated by LRRK2. The experiments tested a set of newly developed LRRK2 inhibitors in cells and brain tissue from mice. The mice had mutations in the gene encoding LRRK2 that are often found in human patients with Parkinson's disease. The experiments show that LRRK2 targets some proteins belonging to the Rab GTPase family, which are involved in transporting molecules and other 'cargoes' around cells. Several Rab GTPases are less active in the mutant mice, which interferes with the ability of these proteins to correctly direct the movement of cargo around the cell.

Steger et al.'s findings will help to advance the development of new therapies for Parkinson's disease. The next challenges are to identify how altering the activity of Rab GTPases leads to degeneration of the nervous system and how LRRK2 inhibitors may slow down these processes.
DOI: 10.7554/eLife.12813.002

2009; *Satake et al., 2009*). LRRK2 encodes a large protein composed of central kinase and GTPase (ROC-COR) domains that are surrounded by multiple protein-protein interaction regions. PD pathogenic LRRK2 mutations map predominantly to the kinase (G2019S, I2020T) and the ROC-COR domains (R1441C/G/H, Y1699C), implying that these enzymatic activities are crucial for pathogenesis (*Rudenko and Cookson, 2014*). Presently, it is unclear how LRRK2 mutations occurring in different functional domains all predispose to PD. The most common PD-associated LRRK2 mutation is the G2019S amino acid substitution, which activates the kinase two- to threefold (*West et al., 2005*; *Khan, 2005*; *Jaleel et al., 2007*). Since protein kinases are attractive pharmacological targets, this finding has raised hopes that selective LRRK2 inhibition can prevent or delay the onset of PD (*Yao et al., 2013*).

Extensive studies of LRRK2 have associated it with diverse cellular processes such as Wnt signaling, mitochondrial disease, cytoskeleton remodeling, vesicular trafficking, autophagy, and protein translation (*Taymans et al., 2015*; *Cookson, 2015*; *Schapansky et al., 2014*; *Papkovskaia et al., 2012*). Moreover, several LRRK2 substrates have been reported previously; however, evidence that they are phosphorylated by LRRK2 in a physiological context is generally lacking and proofs are confined to in vitro approaches or to cellular systems using overexpressed kinase (*Jaleel et al., 2007*; *Kumar et al., 2010*; *Ohta et al., 2011*; *Kawakami et al., 2012*; *Bailey et al., 2013*; *Martin et al., 2014*; *Qing et al., 2009*; *Chen et al., 2012*; *Gloeckner et al., 2009*; *Imai et al., 2008*; *Gillardon, 2009*; *Kanao et al., 2010*; *Matta et al., 2012*; *Xiong et al., 2012*; *Yun et al., 2013*; *Yun et al., 2015*; *Krumova et al., 2015*). Significant off-target effects for LRRK2 compounds that have been used previously further complicate interpretation of the data (*Schapansky et al., 2015*). Overall, there is little consensus on the cellular roles of LRRK2; thus, identification of definitive and verifiable physiological LRRK2 substrates is considered to be one of the greatest challenges in the field (*Schapansky et al., 2015*).

Besides mutations in LRRK2, other genetic risk variants for PD map to the Park16 locus. Among the five genes within this locus is Rab7L1 (also known as Rab29), which together with LRRK2 increases nonfamilial PD risk. Depletion of Rab7L1 recapitulates the dopaminergic neuron loss observed with LRRK2-G2019S expression and its overexpression rescues mutant LRRK2 phenotypes (*MacLeod et al., 2013*). Rab GTPases comprise ~70 family members in humans, and they are key players in all forms of intracellular vesicular trafficking events (*Stenmark, 2009*; *Rivero-Ríos et al., 2015*). Apart from Rab7L1, several other family members have been associated with PD pathogenesis. For example, mutations in Rab39b (Park21 locus) predispose to PD in humans (*Wilson et al., 2014*; *Mata et al., 2015*). Moreover, overexpression of Rab8a, Rab1, and Rab3a attenuate α-synuclein-induced cytotoxicity in cellular and animal models of PD, suggesting a functional interplay

between Rab GTPases and known PD factors (*Cooper, 2006*; *Gitler et al., 2008*). Recently, another PD-connected protein kinase termed PTEN-Induce Kinase-1 (PINK1) has been reported to indirectly control the phosphorylation of a small group of Rabs including Rab8a at Ser111 (*Lai et al., 2015*). Despite these intriguing links, it is presently unclear whether LRRK2 directly or indirectly modulates Rab GTPases at the molecular level and if so, by which mechanism.

High-resolution quantitative mass spectrometry (MS) has become the method of choice for confident identification of in vitro and in vivo phosphorylation events (*Roux and Thibault, 2013*; *Lemeer and Heck, 2009*; *Olsen et al., 2006*). With current MS instrumentation, proteomics can identify tens of thousands of phosphosites (*Sharma et al., 2014*; *Mallick and Kuster, 2010*). However, challenges in the phosphoproteomic approaches are to determine functionally relevant residues from these large datasets and to establish direct kinase-substrate relationships.

As such, we complement the power of modern phosphoproteomics with parallel genetic, biochemical and pharmacological approaches to establish direct, in vivo LRRK2 substrates. Using fibroblasts derived from two different LRRK2 knock-in mouse lines we identify a subset of Rab GTPases as bona-fide LRRK2 targets. LRRK2 phosphorylates these substrates on an evolutionarily conserved residue situated in their switch II domain both in human and murine cells and in mouse brain. The phosphorylation of Rabs by LRRK2 is direct and strikingly all LRRK2 missense mutations that contribute to PD pathogenesis increase the phosphorylation of at least three Rab GTPases. Further, we establish that different PD pathogenic mutations modulate the interaction with a number of regulatory proteins including guanine dissociation inhibitors (GDI1/2). In this way, LRRK2 regulates the specific insertion of Rab GTPases into target membranes thereby altering their membrane-cytosol equilibrium.

Results

Identification of LRRK2 substrates in mouse embryonic fibroblasts (MEFs)

To search for bona-fide physiological LRRK2 substrates, we performed a dual-phosphoproteomic screening approach using knock-in lines harboring either hyperactive LRRK2 or a LRRK2 variant with wild-type activity but insensitive to a highly selective, newly developed LRRK2 compound. For our first screen (PS1), we generated a mouse model harboring the LRRK2-G2019S substitution that increases kinase activity two- to threefold (*Figure 1B*). We derived fibroblasts from these animals and treated them with two structurally different LRRK2 inhibitors, GSK2578215A (*Reith et al., 2012*) or HG-10-102-01 (*Choi et al., 2012*) (*Figure 1A* and *Figure 1—figure supplement 1A*). This screening modality offers three major advantages; first, increased activity of the G2019S-LRRK2 kinase amplifies the chance of finding bona-fide substrates, second, using an isogenic system excludes that measured phosphoproteome changes are due to differences in the genetic background and third, considering only the overlapping population of significantly modulated phosphopeptides of two structurally distinct inhibitors constitutes a very stringent criterion for specifically pinpointing LRRK2 substrates.

The second screen (PS2) added another layer of specificity by combining phosphoproteomics with genetics and chemical biology. For this, we used fibroblasts derived from either wt or A2016T-LRRK2 knock-in mice and treated them with the newly developed, highly potent and selective LRRK2 compound MLI-2 (*Fell et al., 2015*) The A2016T substitution does not change basal LRRK2 activity but decreases sensitivity to MLI-2 ~10-fold (*Figure 1C,D* and *Figure 1—figure supplement 1B*). At a dose of 10 nM, we observed a substantial decrease in phosphorylation of LRRK2-pS935, which is associated with LRRK2 kinase activity (*Dzamko et al., 2010*), in wt but not in A2016T cells (*Figure 1E* and *Figure 1—figure supplement 1C*). Under these conditions, the phosphoproteome of wt MEFs includes both LRRK2-specific and off-target sites, whereas A2016T (which is resistant to MLI-2) only includes off-targets. Therefore, direct quantitative comparison should reveal true LRRK2 substrates (*Figure 1C*).

Using a state-of-the-art workflow for phosphopeptide enrichment, label-free LC-MS/MS and the MaxQuant environment for stringent statistical data evaluation (*Humphrey et al., 2015*; *Cox and Mann, 2008*; *Cox et al., 2011*), we quantified over 9000 high-confidence phosphosites in each replicate in both screens (median R=0.80 and 0.89 in PS1 and PS2, respectively), (*Figure 1—figure*
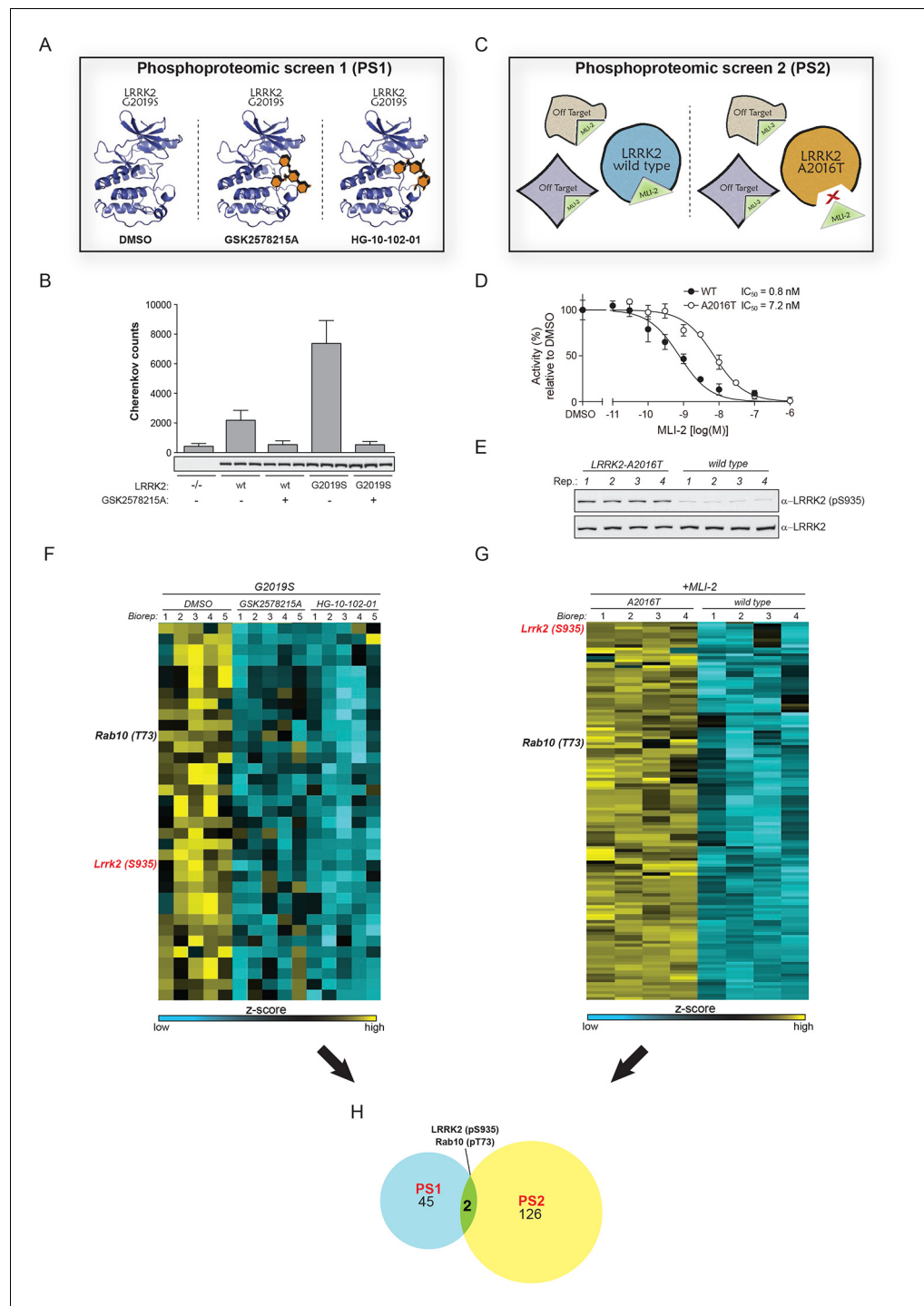
Figure 1. Two unbiased phosphoproteomic screens identify physiological LRRK2 targets. (**A**) Experimental setup of PS1. LRRK2-G2019S[GSK] mouse embryonic fibroblasts (MEFs, n=5) were treated with DMSO or each of two structurally distinct LRRK2 inhibitors GSK2578215A or HG-10-102-01 (1 μM for 90 min). (**B**) LRRK2 immunoprecipitated from either knockout (-/-), wild-type (wt) or LRRK2-G2019S[GSK] (G2019S) knock-in MEFs was assessed for phosphorylation of Nictide (*Nichols et al., 2009*) peptide substrate in absence or presence of GSK2578215A (2 μM). Western blot below shows that similar levels of LRRK2 were immunoprecipitated. Error bars are mean ± SD (n=3). (**C**) Scheme of PS2. The higher affinity of MLI-2 toward wt-LRRK2 allows specific pinpointing of LRRK2 substrates when comparing the phosphoproteomes of wt and A2016T MEFs. (**D**) Kinase activities of wt (closed circles) and A2016T (open circles) GST-LRRK2 [1326-2527] purified from HEK293 cells were assayed in the presence of the indicated concentration of MLI-2 (n=3). (**E**) Decreased levels of pS935-LRRK2 in wt MEFs after

Figure 1 continued on next page

Figure 1 continued

treatment with 10 nM MLI-2. (**F**) Heat map cluster of phosphopeptides in PS1 (p<0.005) which are downregulated after treatment with both GSK2578215A and HG-10-102-01. (**G**) Heat map cluster of downregulated (FDR=0.01, S0=0.2) phosphopeptides in PS2. (**H**) Venn diagram of overlapping downregulated phosphosites in PS1 and PS2. (Biorep= biological replicate). SD, standard deviation.
DOI: 10.7554/eLife.12813.003

The following figure supplements are available for figure 1:

Figure supplement 1. Two unbiased phosphoproteomic screens identify physiological LRRK2 targets.
DOI: 10.7554/eLife.12813.004

Figure supplement 2. Two unbiased phosphoproteomic screens identify physiological LRRK2 targets.
DOI: 10.7554/eLife.12813.005

supplement 1D–G and *Supplementary file 1*). Independently acquired proteome measurements verified that the detected phosphorylation changes in PS2 were not due to altered protein abundances (changes as determined by label-free quantification in MaxQuant (*Cox et al., 2014*) were less than twofold [*Supplementary file 2*]).

Next, we determined how many of the identified sites were significantly and robustly modulated. As we were interested in capturing the most strongly regulated sites, we required that the fold change had to be at least as strong as pS935-LRRK2. In PS1, we thus found 234 significantly regulated sites after treatment with each of the two LRRK2 compounds GSK2578215A and HG-10-102-01 (ANOVA, p<0.005), with 78 sites regulated by both (*Figure 1—figure supplement 2A*). Hierarchical clustering divided them into several subgroups (*Figure 1—figure supplement 2B–C* and *Supplementary file 3A*). Besides revealing potential off-target sites of the two LRRK2 inhibitors, this identified a particularly interesting cluster containing 47 sites that were downregulated after treatment with both compounds (*Figure 1—figure supplement 2C*, cluster 5).

In PS2, we identified 204 significantly regulated sites (two sample t-test, FDR=0.01, S0=0.3), when comparing wild-type and inhibitor-resistant LRRK2 fibroblasts, with 128 sites specifically downregulated in the wild type, thus excluding off-target effects (*Figure 1G*, *Figure 1—figure supplement 2D* and *Supplementary file 3B*).

Finally, to stringently define LRRK2 substrates, we overlapped the results of the two orthogonal screens. Remarkably, only two phosphosites passed these stringent filtering criteria, our positive control pS935-LRRK2 and the conserved T73 residue of the small GTPase Rab10 (*Figure 1H*).

Direct in vitro phosphorylation of Rab isoforms by LRRK2

Rab10 belongs to the Ras family of small GTPases that regulate intracellular vesicular transport, with ~70 members in human. They function as molecular switches in the tethering, docking, fusion, and motion of intracellular membranes (*Stenmark, 2009*; *Wandinger-Ness and Zerial, 2014*). The T73 residue of Rab10 is located in the switch II domain, which is characteristic of Rab GTPases (*Figure 2A*). This region changes conformation upon nucleotide binding and regulates the interaction with multiple regulatory proteins (*Pfeffer, 2005*). Sequence alignment revealed that the equivalent site to T73-Rab10 is highly conserved in more than 40 human Rab-family members, indicating strong functional relevance (*Figure 2B*). Moreover, superposing the crystal structures of multiple Rab GTPases localizes the equivalent residues to T73-Rab10 in nearly the same position (*Figure 2— figure supplement 1A*). To investigate whether the phosphorylation of Rab10 by LRRK2 is direct, we performed an in vitro kinase assay using recombinant components. Notably, we found that both wt and LRRK2-G2019S, but neither kinase inactive D1994A mutant nor small molecule-inhibited LRRK2, efficiently phosphorylated Rab10, proving a direct kinase-substrate relationship (*Figure 2C*). Furthermore, incubation of Rab10 with LRRK2 followed by tryptic digestion and MS analysis unambiguously identified T73 as the major phosphorylation site (*Figure 2—figure supplement 1B*). Given the high conservation of T73-Rab10, we investigated whether other Rab GTPases were also phosphorylated by LRRK2 in vitro. Therefore, we first measured LRRK2-mediated phosphorylation of Rab8a, Rab1a, and Rab1b, all of which contain a Thr at the site equivalent to T73-Rab10, by MS or ^{32}P incorporation followed by Edman sequencing. Remarkably, all proteins were rapidly phosphorylated on the predicted LRRK2 phosphorylation site in the switch II domain (*Figure 2D–F* and *Figure 2—figure supplement 1C–E*). Next, we compared Rab family members containing Thr sites in
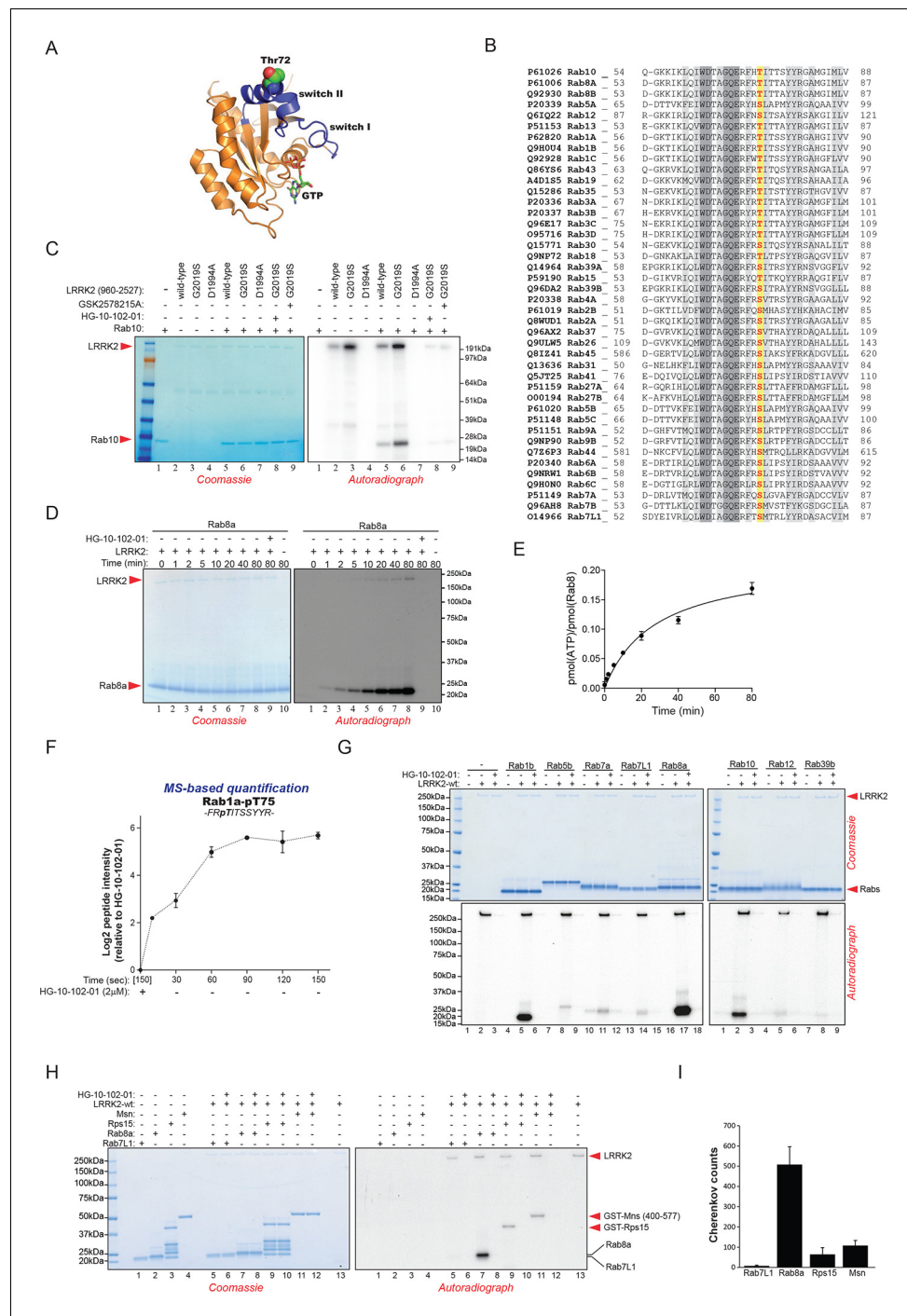
Figure 2. Phosphorylation of Rab GTPases by LRRK2 in vitro. (**A**) Position of threonine 72 in the switch II region of Rab8a (PDB: 4HLY). (**B**) Sequence alignment of Rab10 and other indicated Rab-family members. (**C**) Phosphorylation of Rab10 (1 µM) by wt-, G2019S- or kinase inactive LRRK2-D1994A. Inhibition of LRRK2-G2019S by GSK2578215A or HG-10-102-01 prevents phosphorylation. (**D**) Time course of LRRK2 (wt) mediated Rab8a (4 µM) phosphorylation and (**E**) quantification of phosphorylation stoichiometry (n=3). (**F**) Time course of LRRK2-wt-mediated pT75-Rab1a phosphorylation and MS-based label-free quantification (n=3). (**G**) In vitro phosphorylation of recombinant Rab proteins (4 µM) by LRRK2-wt. (**H**) Phosphorylation of recombinant Rab7L1, Rab8a, moesin, and Rps15 by LRRK2 and (**I**) quantification of the signals. For all reactions LRRK2 inhibitors= 2 µM and LRRK2= 100 ng. Error bars indicate mean ± SEM of replicates. MS, mass spectrometry; SEM, standard error of the mean; wt, wild type.

DOI: 10.7554/eLife.12813.006

Figure 2 continued on next page

the switch II region with those containing a Ser in the equivalent position. Interestingly, while Rabs with threonines (Rab1b, Rab8a, and Rab10) were efficiently phosphorylated, those with the equivalent serine sites (Rab5b, Rab7a, Rab7L1, Rab12, and Rab39b) were phosphorylated to a drastically lower extent (*Figure 2G*). This confirms the previously reported in vitro preference for threonines by LRRK2 (*Nichols et al., 2009*). Finally, we performed a side by side comparison of the phosphorylation efficiencies of recombinant Rab8a and Rab7L1 against two previously reported substrates, moesin (Msn) and Rps15 (*Jaleel et al., 2007*; *Martin et al., 2014*). Msn is a cytoskeletal protein and a well-known in vitro LRRK2 substrate, whereas Rps15 is part of the 40S ribosomal subunit and its phosphorylation on Thr136 has been reported to regulate protein translation in *D. melanogaster* (*Martin et al., 2014*). In accordance with our previous observations (*Figure 2G*), phosphorylation levels of RAB7L1 were barely detectable, and even lower than those of Msn and Rps15. Strikingly, levels of pRab8a were about ten times higher as compared to Rps15 and Msn, two of the best in vitro LRRK2 substrates known to date, demonstrating that Rabs with Thr sites in the switch II domain are primary LRRK2 targets (*Figure 2H,I*).

A subset of Rabs are physiological LRRK2 substrates

Because of the high conservation of T73-Rab10 (*Figure 2B*) and the ability of LRRK2 to phosphorylate multiple Rabs in vitro, we inspected our quantitative MS data further to determine whether all sequence and structurally equivalent sites are targets of LRRK2. This turned out not to be the case as pS72-Rab7a was not regulated in either of our screens. LRRK2 thus phosphorylates only a subset of Rab GTPases in mouse fibroblasts. Surprisingly, we noticed that pS105-Rab12, which is not phosphorylated by LRRK2 in vitro (*Figure 2G*), was among the significantly modulated sites in PS1 and also downregulated upon MLI-2 treatment in wt cells as compared to the inhibitor-resistant A2016T mutant in PS2 (*Figure 3A,B*). However, because of elevated intergroup variability and stringent FDR cut-offs, it was not selected in our first analysis. LRRK2 is found also in lower eukaryotes such as *C. elegans* and *D. melanogaster* (*Liu et al., 2011*) and T73-Rab10 is conserved in these organisms as well. Also, S105-Rab12 is present throughout the vertebrates (*Figure 3A,B*). We identified both pT73-Rab10 and pS105-Rab12 multiple times with high identification and phosphosite localization scores (*Supplementary file 1*) and the MS/MS fragmentation spectra of the corresponding synthetic peptides independently validated the MS results (*Figure 3—figure supplement 1A,B*). Total protein levels of Rab10 and Rab12 did not change appreciably in the A2016T knock-in model as judged by quantitative MS analysis, ruling out that that the observed phospho-level changes are due to differential protein expression (*Figure 3—figure supplement 2A*).

To extend the analysis of LRRK2-mediated phosphorylation of Rab10, we used human embryonic kidney cells harboring doxycycline-dependent gene expression of LRRK2-G2019S (HEK293-t-rex-flpIn). Expression of the kinase, treatment with either GSK2578215A or HG-10-102-01 and enrichment of Rab10 by immunoprecipitation followed by quantitative MS analysis confirmed a strong, LRRK2-dependent decrease of pT73-Rab10 peptide levels (*Figure 3—figure supplement 2B*). Polyclonal antibodies recognizing pT73-Rab10 and pS106-Rab12 (note that the equivalent site is S105 in mouse) independently verified LRRK2-dependent phosphorylation of both Rab isoforms in HEK293 cells (*Figure 3C,D*).

Next, we evaluated whether more Rab isoforms can be phosphorylated in a LRRK2-dependent manner in human cells, focusing on Rab1a, Rab3a, and Rab8a, all of which contain Thr as predicted LRRK2 phosphorylation site (*Figure 2B*). Therefore, we first ectopically expressed LRRK2 along with either Rab1a or Rab3a, in presence or absence of HG-10-102-01 and quantified pT75-Rab1a and pT86-Rab3a peptide levels by MS. Whereas T86-Rab3a is clearly a LRRK2 target, Rab1a is not, indicating that overexpression of LRRK2 is not sufficient to phosphorylate all Rabs in cells (*Figure 3—figure supplement 2C,D*). Next, we inhibited LRRK2 in HEK293-t-rex-flpIn cells expressing LRRK2-G2019S and quantified pT72-Rab8. Again, we found a strong decrease of pT72 peptide levels upon
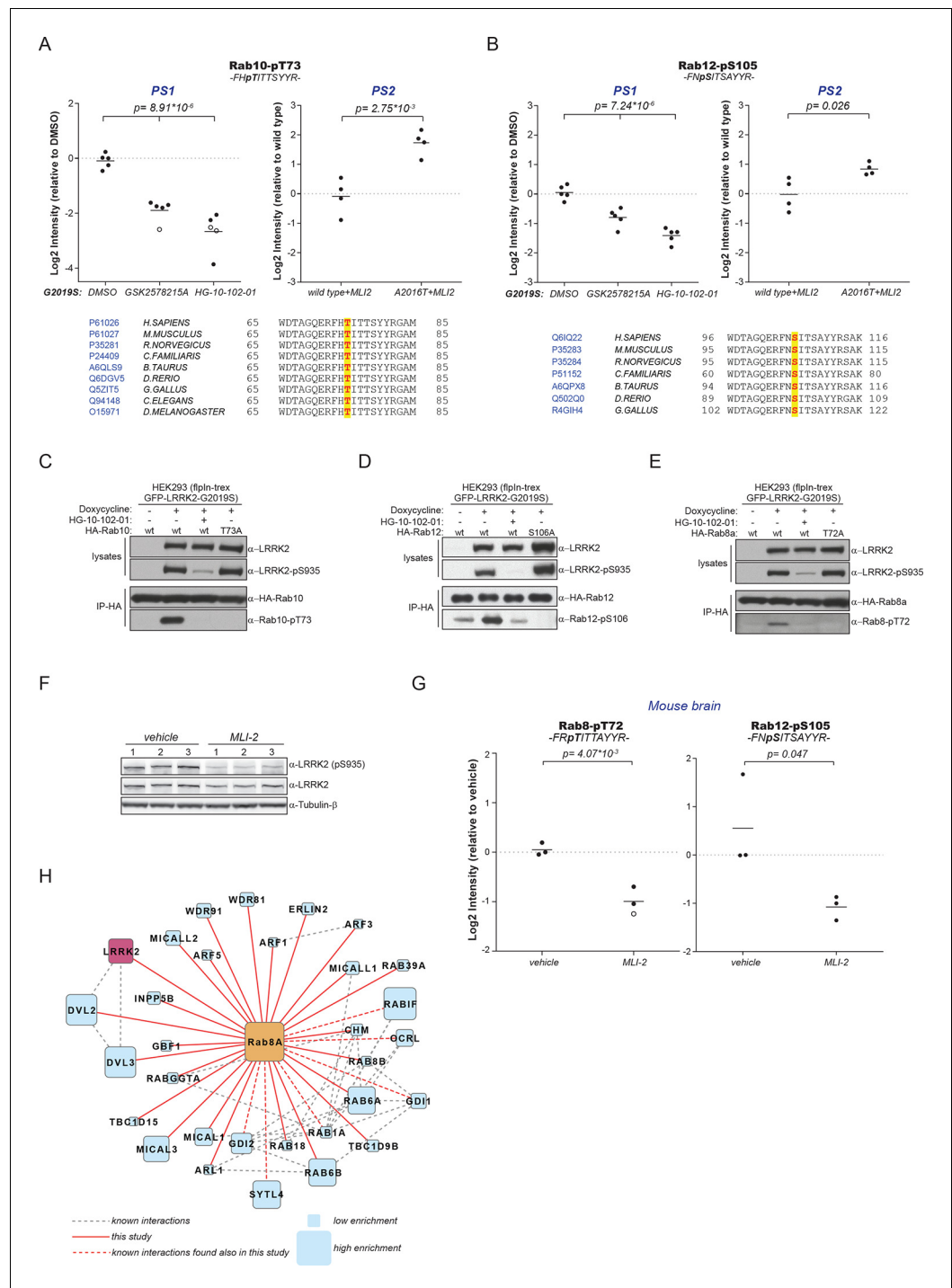
Figure 3. A number of Rab GTPases are physiological LRRK2 substrates. (**A**) MS-quantified pT73-Rab10 peptide intensities in PS1 and PS2. Sequence alignment of the T73-Rab10 region is shown below. (**B**) Same as (**A**) with pS106-Rab12. Western blots illustrating phosphorylation of T73-HA-Rab10 (**C**), S106-HA-Rab12 (**D**), and T72-Rab8 (**E**) after induction of LRRK2 expression by doxycycline (1 μg/ml). HG-10-102-01 (1 μM) was added prior to lysis. (**F**) Western blot of homogenized brain lysates from LRRK2-G2019S[Lilly] mice injected with vehicle (40% HPβCD) or with 3 mg/kg MLI-2 (Biorep= biological replicate) and (**G**) MS-based quantification of pT72-Rab8 and pS105-Rab12 peptides. (**H**) Cytoscape network analysis of Rab8a interacting proteins determined by affinity-purification mass spectrometry (AP-MS). LRRK2 is in purple and dashed lines in grey show experimentally determined interactions from string database (http://string-db.org/).

DOI: 10.7554/eLife.12813.008

Figure 3 continued on next page

LRRK2 inhibition with both GSK2578215A and HG-10-102-01 (*Figure 3—figure supplement 2E*). An antibody raised for specific detection for pT72-Rab8 confirmed these results further (*Figure 2E*).

To analyze LRRK2-dependent phosphorylation of Rabs in an endogenous context, we quantified pT72-Rab8 and pT73-Rab10 peptide levels in MEFs derived from LRRK2 knockout, wt, or G2019S[GSK] animals. In the knock-out, the decrease was only about twofold compared to wt, implying a very low intrinsic LRRK2 activity in cells. Consistent with the two- to threefold increased in vitro activity of MEFs-extracted LRRK2-G2019S[GSK] (*Figure 1B*), our quantitative MS analysis revealed a threefold increase in both pT72-Rab8 and pT73-Rab10, which was restored to near wt levels by selective LRRK2 kinase inhibition (*Figure 3—figure supplement 2F–I*). Finally, we globally measured the brain phosphoproteome of LRRK2-G2019S[Lilly] mice injected with vehicle (40% HPβCD) or with MLI-2 (3 mg/kg). Levels of pT72-Rab8 and pS105-Rab12 were decreased more than twofold upon LRRK2 inhibition, validating our findings in the context of a LRRK2 pathogenic mouse model (*Figure 3F,G*).

Having identified Rabs as physiological substrates of LRRK2, we next asked if kinase and substrate also stably interact. Indeed, affinity-purification mass-spectrometry (AP-MS) showed that transiently expressed epitope-tagged LRRK2 and Rab8a efficiently associated with each other, demonstrating that LRRK2 is able to form stable complexes with Rab GTPases in cells (*Figure 3H* and *Figure 3—figure supplement 3A,B*). Similarly, Rab10 as well as Rab12 associate with LRRK2 when transiently overexpressed in HEK293 cells (*Figure 3—figure supplement 3C–E*).

Parkinson's disease-associated pathogenic mutations modulate Rab GTPase phosphorylation levels

Pathogenic PD LRRK2 mutations predominantly map to the kinase and the ROC-COR (GTPase) domains and a PD risk factor coding mutation is also found in the WD-40 domain (*Martin et al., 2014*; *Farrer et al., 2007*) (*Figure 4A*). Because it is presently unclear how mutations occurring in distinct LRRK2 functional domains lead to similar disease phenotypes, we decided to investigate if different LRRK2 pathogenic mutations might impact on the phosphorylation status of Rab GTPases. For this, we expressed different disease causing LRRK2 variants along with either Rab8a or Rab10 in HEK293 cells. This revealed that besides PD-associated mutations located in the kinase domain that augment LRRK2 kinase activity, those occurring in the GTPase (ROC-COR) or the WD-40 domains also increased pT72-Rab8a and pT73-Rab10 levels in cells (*Figure 4B–E*).

To determine whether this interplay between different functional domains was direct, we next tested whether pathogenic LRRK2 mutations which lie outside the kinase domain also increase Rab phosphorylation in vitro. As expected, compared to wt, the G2019S mutation resulted in a two- to threefold increase in Rab8a phosphorylation. However, the ROC-COR domain R1441C mutation failed to do so, which is consistent with previous data suggesting that these mutations do not directly enhance LRRK2 kinase activity (*Nichols et al., 2010*), indicating that its effect on Rab8a phosphorylation levels is mediated by accessory factors in cells (*Figure 4F,G*).

LRRK2 controls the interaction of Rabs with regulatory proteins

Rab GTPases consist of a similar core structure comprising highly conserved P-loop, switch I and switch II regions (*Pfeffer, 2005*). They cycle between the cytosol, in which they are GDP bound and inactive and specific membrane compartments, where they are activated by GDP/GTP exchange (*Hutagalung and Novick, 2011*). In the crystal structure of Rab8a (*Guo et al., 2013*), the LRRK2-mediated phosphorylation site is in the switch II region (*Figure 2A*), which regulates hydrolysis of GTP and coordinates the binding to various regulatory proteins (*Pfeffer, 2005*). We therefore tested
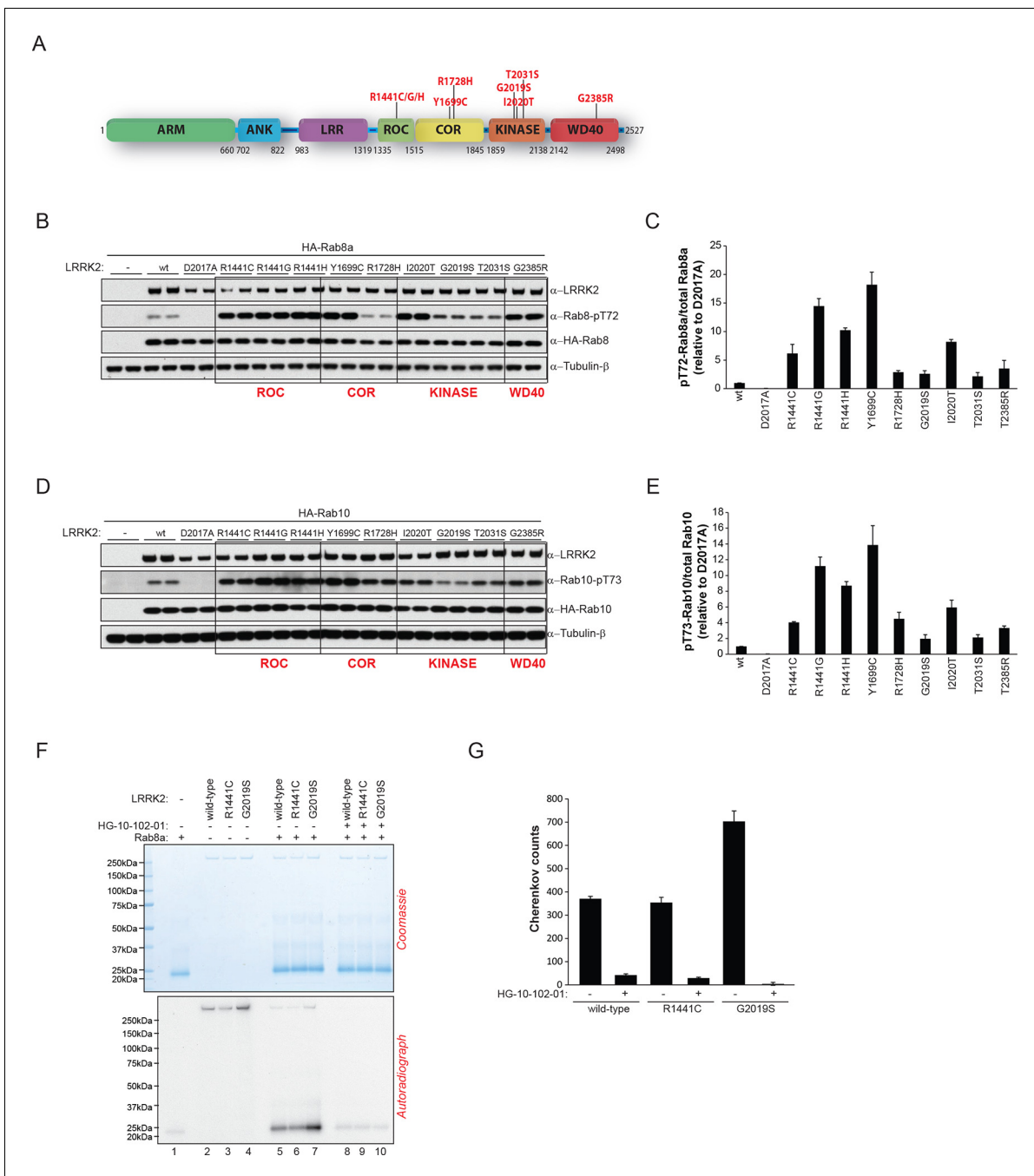
Figure 4. LRRK2 pathogenic variants increase phosphorylation of Rab GTPases. (A) Scheme of LRRK2 and common PD-associated amino acid substitutions (in red). (B) Different LRRK2 versions were co-expressed with Rab8a in HEK293 cells, lysates subjected to immunoblot analysis and (C) indicated signals quantified. (D) and (E) Same as (B) but HA-Rab10 was used. (F) In vitro phosphorylation of recombinant Rab8a (4 μM) by indicated LRRK2 variants (100 ng) and (G) quantification of the signals. HG-10-102-01= 2 μM. Error bars indicate mean ± SEM of replicates (n=3). PD, Parkinson's disease; SEM, standard error of the mean.

DOI: 10.7554/eLife.12813.012

whether the phosphomimetic T72E substitution would modulate GDP/GTP binding or interfere with Rab8a protein interactions. Binding affinities of wt and the TE mutant, determined with fluorescently labeled (N-Methylanthraniloyl, mant) GDP and non-hydrolysable GTP analogue GMPPNP, did not differ (*Figure 5—figure supplement 1*). In contrast, AP-MS revealed that a number of proteins preferentially bind to non-phosphorylatable T72A-Rab8a compared to the T72E
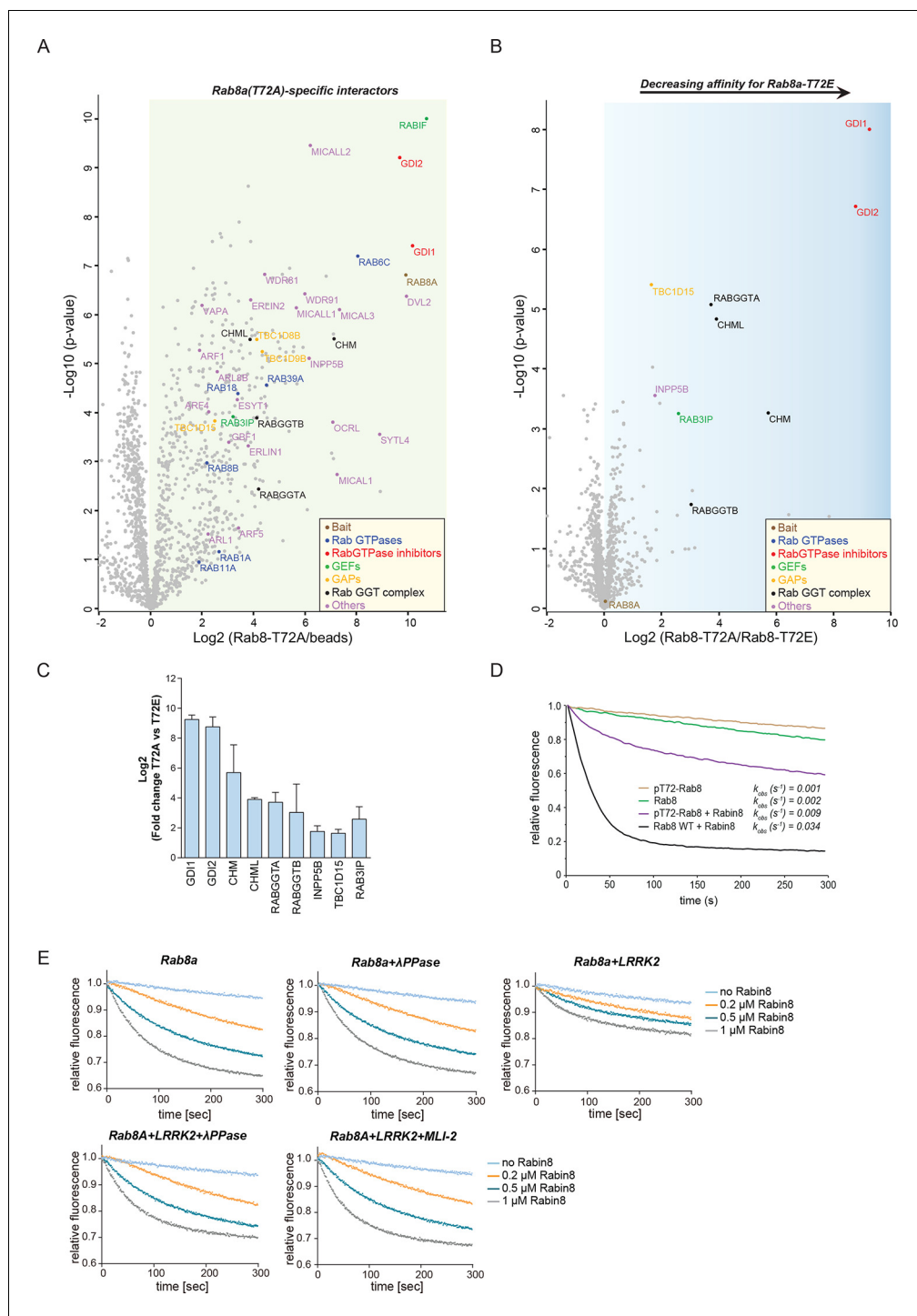
Figure 5. LRRK2 controls the interaction of Rabs with regulatory proteins. (**A**) Volcano plots showing interactors of GFP-Rab8a (T72A) transiently expressed in HEK293 cells and (**B**) Proteins differentially binding to T72A as compared to T72E. (**C**) Fold changes (T72A/T72E, n=4) of regulated proteins shown in (**B**). (**D**) Kinetic measurements of the dissociation of mant-GDP from non-phosphorylated and T72 phosphorylated Rab8a by Rabin8. Observed rate constants (k_{obs}) are indicated for each reaction and data points represent mean (n=3). (**E**) Measurements of mant-GDP dissociation from LRRK2 phosphorylated Rab8a by Rabin8 in absence or presence of λ-phosphatase (λ-PPase) or MLI-2 (1 μM). Error bars are mean ± SD of replicates.
DOI: 10.7554/eLife.12813.013

The following figure supplements are available for figure 5:

Figure 5 continued on next page

phosphomimetic protein (*Figure 5A,B*). These were Rab GDP dissociation inhibitors α and β (GDI1 and GDI2), Rab geranyltransferase complex members (CHM, CHML, and RabGGTA/RabGGTB), the Rab8a guanine nucleotide exchange factor (GEF) Rabin8 (Rab3IP), a guanine nucleotide activating protein TBC1D15 and the inositol phosphatase INPP5B (*Figure 5C*).

Rabin8 interacts with membrane-bound Rab8a and activates it by catalyzing the exchange of GDP to GTP (*Westlake et al., 2011*). This in turn triggers retention of Rab effector proteins that mediate downstream vesicular trafficking events. Rabin8 binds to the switch II domain of Rab8a and contacts the conserved, phosphorylatable T72 residue (*Figure 5—figure supplement 2A*) (*Guo et al., 2013*). We found that compared to wt, the T72E phosphomimetic substitution decreased the level of Rabin8-catalyzed mant-GDP displacement from a Rab8-GDP complex (*Figure 5—figure supplement 2B–D*). To further substantiate this finding, we phosphorylated purified Rab8a using LRRK2, which resulted in ~60% of T72-phosphorylated protein as determined by total protein MS and LC-MS/MS after tryptic digestion (*Figure 5—figure supplement 2E,F*). Further enrichment by ion-exchange chromatography yielded a highly enriched (~100%) fraction of pT72-Rab8a (*Figure 5—figure supplement 2E*). Loading of non-phosphorylated and phosphorylated Rab8a with mant-GDP following incubation with Rabin8 revealed that LRRK2-induced phosphorylation of T72-Rab8a inhibits rates of Rabin8-catalyzed GDP exchange fourfold and decreases Rab8a-Rabin8 interaction (*Figures 5D* and *Figure 5—figure supplement 2G*). Both λ-phosphatase treatment of LRRK2-phosphorylated Rab8a and pharmacological inhibition of LRRK2 prevented the decreased GEF activity of Rabin8 toward pT72-Rab8a (*Figure 5E* and *Figure 5—figure supplement 2H*). Thus, phosphorylation of Rab8a by LRRK2 can limit its activation by Rabin8.

PD pathogenic LRRK2 mutations interfere with Rab-GDI1/2 association

GDI1 and GDI2, along with CHM and CHML (also known as Rab escorting proteins REP1 and REP2) form the GDI superfamily and are essential regulators of the Rab cycle. GDIs extract inactive, prenylated Rabs from membranes and bind them with high affinity in the cytosol (*Pylypenko et al., 2003*). The regulatory mechanism by which Rabs are displaced from GDIs to facilitate their insertion into specific target membranes is unknown. The co-crystal structure of GDI1 with the yeast Rab homologue Ypt1 shows that GDIs closely contact the switch II region (*Rak, 2003*), which explains why phosphorylation in this domain interferes with the Rab-GDI interaction. Since GDIs are not specific to one Rab isoform (*Seabra and Wasmeier, 2004*), we reasoned that phosphorylation of the switch II domain could be a general mechanism of Rab-GDI dissociation. We therefore substituted S106-Rab12 and T73-Rab10 with non-phosphorylatable Ala or phosphomimetic Glu residues and tested their capacity to form complexes with GDIs by immunoprecipitation followed by MS or western blotting. As compared to non-phosphorylatable Rab10 and Rab12, neither S106E-Rab12 nor T73E-Rab10 was able to bind GDIs, demonstrating the functional importance of these residues (*Figure 6A,B* and *Figure 6—figure supplement 1A,B*).

To further analyze the effect of Rab phosphorylation and GDI dissociation in the context of PD, we expressed LRRK2 variants harboring various pathogenic mutations along with Rab8a in cells and assessed Rab-GDI complex formation by immunoprecipitation. Strikingly, the level of Rab8a-GDI interaction closely correlated with the degree of T72-Rab8a phosphorylation (*Figure 6C,D*). Similarly, LRRK2-mediated phosphorylation of S106-Rab12 diminished the interaction with GDIs, confirming that the effect is not specific to one Rab isoform (*Figure 6E,F*). All tested LRRK2 pathogenic mutations that affect kinase activity thus control the interaction of Rabs with GDIs. Finally, to directly test whether disruption of the Rab-GDI interaction results in an altered subcellular distribution of Rabs, we quantitatively determined T72A-Rab8 and T72E-Rab8 protein abundances in SILAC (*Ong, 2002*) labeled HEK293 cells. This revealed a twofold increase of non-phosphorylatable T72A mutant in the cytosol. Consistently, we detected a significant ($p= 2.58*10^{-3}$) increase of T72E-Rab8 protein levels
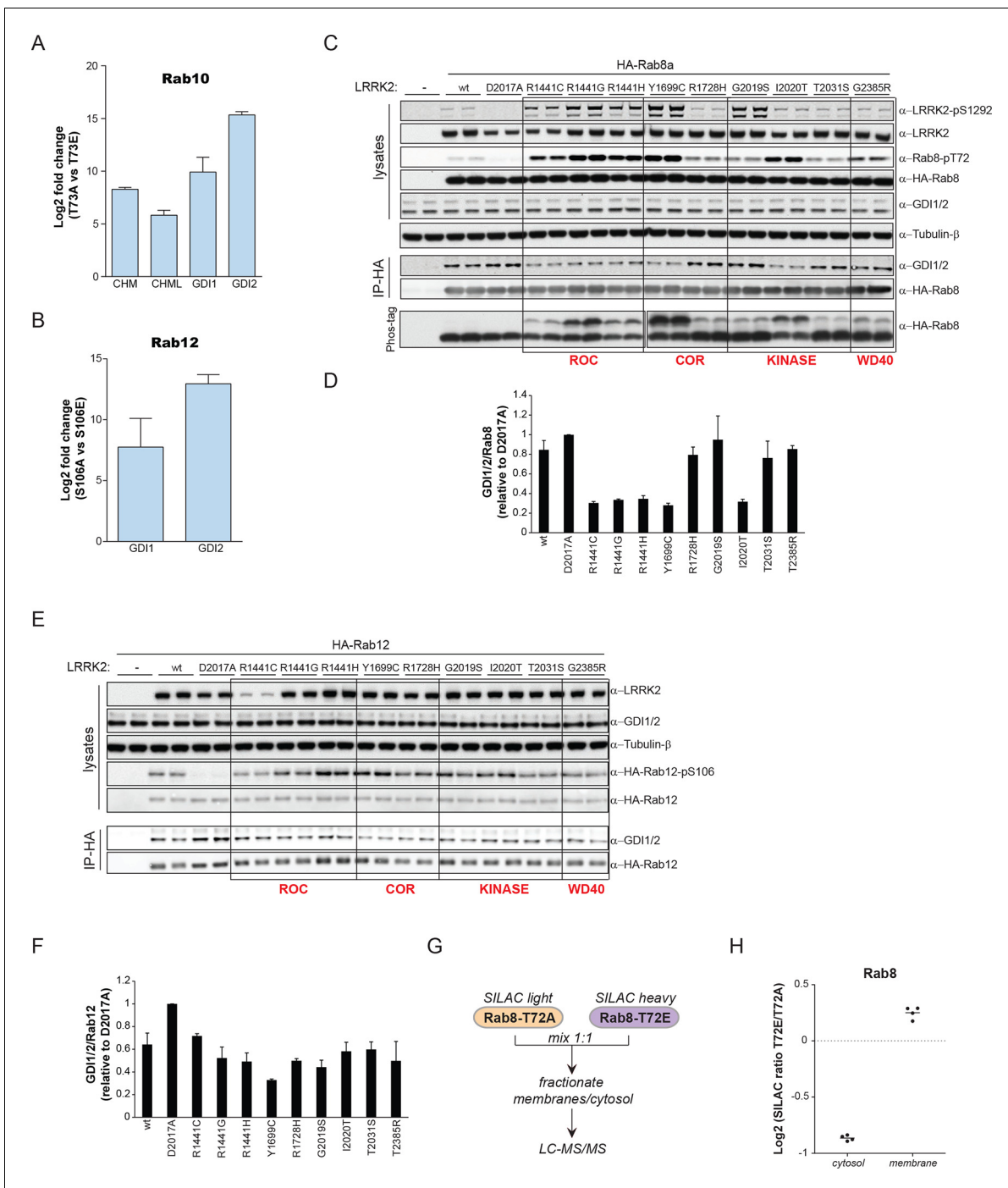
Figure 6. PD pathogenic LRRK2 mutations interfere with Rab-GDI1/2 association. (**A**) Fold changes (T73A/T73E, n=3) of indicated MS-quantified Rab10 interactors. (**B**) Same as (**A**) but S106A-Rab12 and S106E-Rab12 (n=4). (**C**) Different LRRK2 versions were co-expressed with Rab8a in HEK293 cells, lysates subjected to immunoblot analysis or immunoprecipitation using α-HA antibodies and indicated signals quantified (**D**). (**E**) and (**F**) Same as (**C**) with Rab12 expression. (**G**) Scheme for analyzing T72A-Rab8a and T72E-Rab8a subcellular protein distributions in a SILAC experiment. (**H**) SILAC ratios (Log2) of T72E-Rab8a/T72A-Rab8a proteins in the cytosolic and membrane fraction of HEK293 cells. PD, Parkinson's disease.
DOI: 10.7554/eLife.12813.016

The following figure supplement is available for figure 6:

Figure supplement 1. Rab10/12-GDI interactions.
DOI: 10.7554/eLife.12813.017

in the membrane fraction, demonstrating that interference with the Rab-GDI interaction results in an unbalanced membrane-cytosol distribution of Rabs (*Figure 6G,H*).

Discussion

Here, we used a state of art MS-based phosphoproteomics workflow in combination with cells of two genetically engineered mouse models as well as a mixture of selective LRRK2 compounds to define LRRK2 targets with high stringency. Starting with almost 30,000 identified phosphosites, our screens rapidly narrowed down the candidates to a small number that were consistently and strongly regulated with all tested compounds and genetic models. Only the known phosphorylation site pS935 on LRRK2 itself and a specific residue in the Rab10 GTPase (T73) fulfilled our most specific criteria. LRRK2 kinase is conserved also in flies and worms and this is true of the T73-Rab10 substrate site as well. Further experiments with diverse model systems and techniques all verified the T73-Rab10 site as well as the equivalent sites on many but not all other Rab family members. These include the threonine sites on Rab8a and Rab3a (T72 and T86, respectively), as well as S106-Rab12. Rab7a is an important component of the endocytic pathway (*Wandinger-Ness and Zerial, 2014*) and phosphorylation on S72 has recently been shown to play a functional role in B-cell signaling (*Satpathy et al., 2015*). While our data clearly show that this site is not regulated by LRRK2 in mouse fibroblasts, its regulation by LRRK2 in B cells remains possible, given the high expression levels of LRRK2 in those cell types (*Gardet et al., 2010*). In vitro experiments proved that LRRK2 directly phosphorylates Thr but not the Ser sites in Rab isoforms, in line with its well-established in vitro preference (*Jaleel et al., 2007*; *Martin et al., 2014*; *Nichols et al., 2009*). We found that Ser sites on Rabs were hardly phosphorylated in vitro but S105-Rab12 (S106 in human) was clearly regulated in cells and brain tissue, establishing that accessory factors are required in this case. Consistent with this finding, the major characterized in vivo LRRK2 autophosphorylation site is a Ser residue (Ser1292) (*Sheng et al., 2012*). Our observation of residual Thr72-Rab8 phosphorylation in LRRK2$^{-/-}$ mice implies that one or more other kinase(s) are able to act upon this residue.

Besides defining Rab GTPases as LRRK2 targets, our screens identified a number of phosphosites as potential LRRK2 targets. However, these were validated by only one of the screens, their regulation was weaker and for many of them regulation may reflect indirect modulation by the LRRK2 kinase. This is likely to account for the difficulty in identifying substrates of this kinase. In a direct comparison of threonine Rab phosphorylation it was much stronger than the known in vitro LRRK2 targets we tested. Overall, the relatively small number of regulated sites in our screens, suggest that LRRK2 is a very specific or low activity kinase. LRRK2 is ubiquitously expressed, but highly abundant in the kidney, lungs, pancreas, and certain cell types of the immune system (*Schapansky et al., 2015*). Therefore, it is possible that different LRRK2 substrates, including Rab isoforms, are phosphorylated in a cell- or tissue-specific manner. Further phosphoproteomic research should shed more light on this open question. We conclude that the threonine sites on Rab family members identified here may not be the only functional ones in the context of LRRK2, but that they are the most prominent ones.

In searching for a functional role for LRRK2-mediated Rab phosphorylation, we noted that it maps onto the switch II region, which is known to mediate GDP/GTP exchange as well as interaction with regulatory proteins. Results from nucleotide affinity measurements make the former mechanism unlikely but AP-MS established phosphorylation-dependent binding of several proteins involved in regulating their cycling between cytosol and membrane compartments. This indicates that direct phosphorylation of Rabs on a conserved residue situated in the switch II domain regulates their movement by controlling the interaction with numerous regulatory proteins. The affinities of GDIs for Rabs are vastly decreased in a manner correlating with the phosphorylation levels induced by different LRRK2 pathogenic variants. Our data thus establish that LRRK2 is an important regulator of Rab homeostasis which is likely contributing to PD development (*Figure 7A*). Overactive LRRK2, which results in increased Rab phosphorylation, promotes dissociation from GDIs in the cytosol with concomitant membrane insertion (*Figure 7B*). In this way, the relative pool of membrane bound and cytosolic Rab is altered, disturbing intracellular trafficking. In particular, PD-associated LRRK2 mutations would shift the membrane-cytosol balance of Rabs toward the membrane compartment, thereby causing accumulation of inactive Rabs in the membranes (*Figure 7B*). The subtle increase in
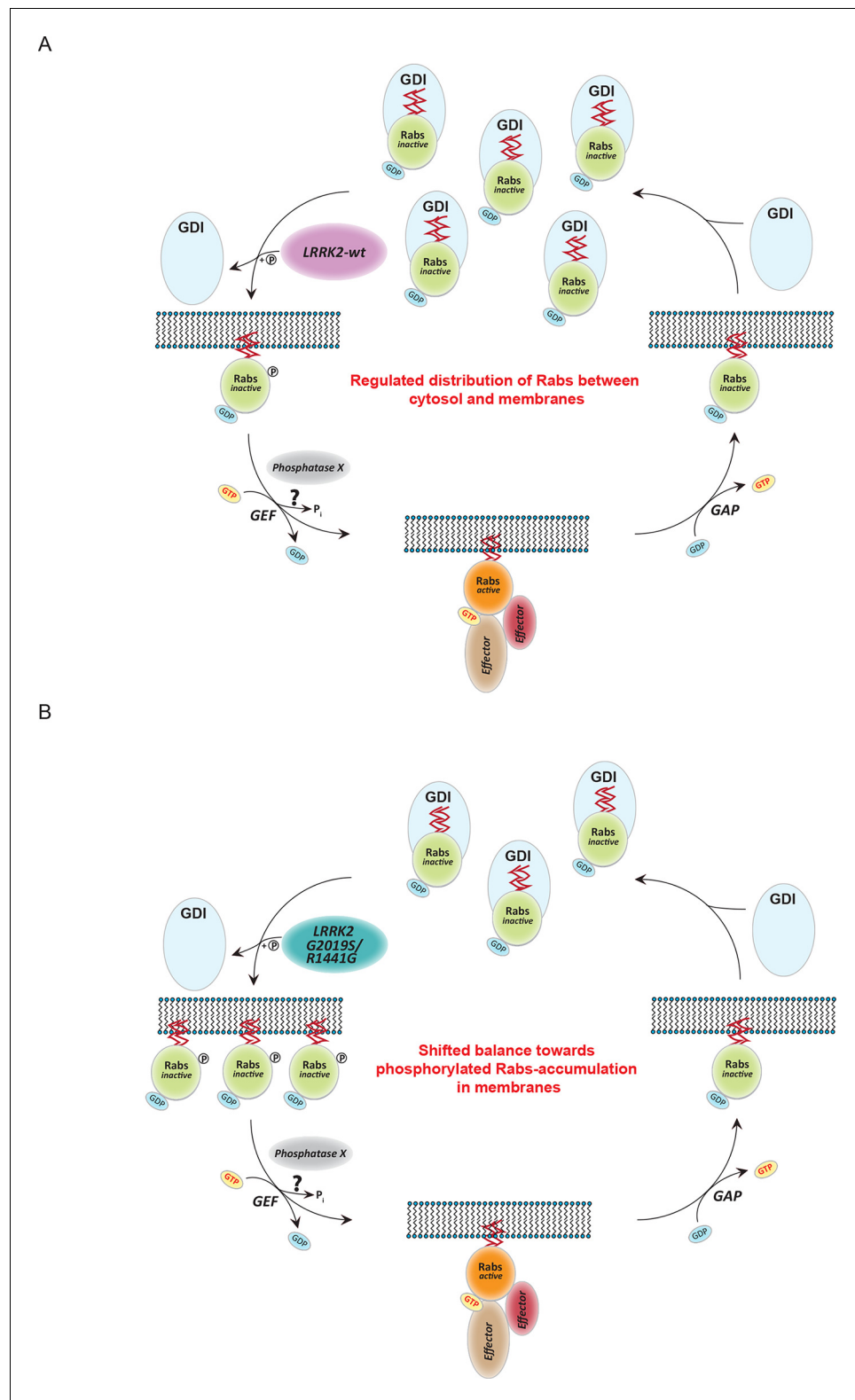
Figure 7. Model of Rab GTPase phosphorylation by LRRK2 and its outcome. (**A**) Rab GTPases (Rabs) cycle between an inactive (GDP-bound) and an active state (GTP-bound) between cytosol and membranes, respectively. Geranyl-geranyl-modified Rab GTPases in their GDP-bound state are tightly bound by guanine dissociation inhibitors (GDIs) in the cytosol. LRRK2 aids the insertion of Rabs in their specific target membrane. After removal of the LRRK2 phosphorylation site, guanine exchange factors (GEFs) facilitate exchange of GDP to GTP. This in

Figure 7 continued on next page

Figure 7 continued

turn allows binding to effector proteins and membrane trafficking events. Next, a Rab-specific GTPase-activating protein (GAP) assists in the hydrolysis of GTP followed by removal of the Rab GTPase from the target membrane by GDIs. (**B**) In pathogenic conditions, in which LRRK2 is hyperactive, RabGTPases have strongly diminished affinities for GDIs. As a result, the equilibrium between membrane-bound and cytosolic Rabs is disturbed, which may contribute to LRRK2 mutant carrier disease phenotypes. Model adapted and modified from (*Hutagalung and Novick, 2011*).

DOI: 10.7554/eLife.12813.018

Rab phosphorylation in cells derived from LRRK2-G2019S knock-in mice is consistent with the long time needed for PD to manifest in humans.

Intriguingly, our results show that pathogenic LRRK2 mutations outside the kinase domain can also increase Rab phosphorylation. Although our in vitro data clearly shows that this mechanism is indirect, they will still act on the same pathway as kinase domain mutants. Therefore, the same model would also be applicable in this case.

Independent evidence that Rabs are likely to be primary LRRK2 substrates comes from LRRK2 knockout animal studies. LRRK2$^{-/-}$ mice and rats have deformed kidneys and lungs, indicative of defects in the autophagosome/lysosome pathway, which depend on properly tuned Rab activity (*Herzig et al., 2011*; *Hinkle et al., 2012*; *Baptista et al., 2013*). Moreover, it was recently reported that LRRK2 and Rab2a regulate Paneth cell function, which is compromised in Crohn's disease (*Zhang et al., 2015*). In this context, it is interesting that we found pS70-Rab2a/b to be regulated in our second screen, although it's very low abundance impedes meaningful statistical interpretation. Taken together these observations make it plausible that LRRK2 regulates Rab2a by direct phosphorylation of S70 in specialized cell types.

In conclusion, we prove that LRRK2 induces phosphorylation of Rabs and provide evidence that it deregulates cycling between cytosol and target membrane compartments. It will be interesting to investigate whether the Rab regulatory mechanism uncovered here is of key importance in vesicular trafficking in general. Discovery of a key physiological LRRK2 substrate should inform and accelerate research into PD, including monitoring the efficacy of therapeutic intervention.

Materials and methods

Reagents

MLI-2 (*Fell et al., 2015*) was obtained from Merck, GSK2578215A (*Reith et al., 2012*) from Tocris or GlaxoSmithKline. HG-10-102-01 was custom synthesized by Natalia Shapiro (University of Dundee) as described previously (*Choi et al., 2012*). Doxycycline, ATP, and trypsin were from Sigma. LysC was obtained from Wako. ^{32}P-γATP was from PerkinElmer. GST-LRRK2 (residues 960-2527 wild type, G2019S, D1994A), full-length wild type flag-LRRK2 from Invitrogen and MANT-GDP (2'-(or-3')-O-(N-Methylanthraniloyl) Guanosine 5'-Diphosphate, Disodium Salt) and MANT-GMPPNP from Jena Bioscience. GFP beads for affinity purification were from Chromotek. Recombinant Rab10 and Rab1a (*Figure 3A and 3C*) were purchased from mybiosource.

Antibodies

Anti-Rab10 and Rab8 were from Cell Signaling Technologies, anti-GFP from Invitrogen, anti-HA high affinity from Roche, anti-GDI1/2 from Sigma, and anti-pS1292-LRRK2 from Abcam. Rabbit monoclonal antibodies for total LRRK2 and pS935-LRRK2 were purified at the University of Dundee (*Dzamko et al., 2012*). Antibodies against Rab8a phospho-Thr72 (S874D), Rab10 phospho-Thr73 (S873D) and Rab12 phospho-Ser106 (S876D) were generated by injection of the KLH (keyhole limpet hemocyanin)-conjugated phospho-peptides AGQERFRpTITTAYYR (Rab8a), AGQERFHpTITTSYYR (Rab10), AGQERFNpSITSAYYR (Rab12) and IAGQERFpTSMTRLYYR (where pS/T is phospho-serine/threonine) into sheep and affinity purified using the phosphopeptides. Antibodies were used at final concentrations of 1 µg/ml in the presence of 10 µg/ml of non-phosphorylated peptide.

Plasmids

The following constructs were used: 6His-SUMO-Rab8a wt/T72A/T72E (DU47363, DU47433, DU47436), HA-Rab8 wt/T72A/T72E (DU35414, DU47360), 6His-SUMO-Rab5b (DU26116), 6-His-SUMO-Rab7a (DU24781), 6-His-SUMO-Rab7L1 (DU50261). 6-HIS-SUMO-Rab10 (DU51062), HA-Rab10 wt/T73A/T73E (DU44250, DU51006, DU51007), 6-His-SUMO-Rab12 (DU52221), HA-Rab12 wt/S106A/S106E (DU48963, DU48966, DU48967), and 6-His-SUMO-Rab39b (DU43869). Full datasheets are available on https://mrcppureagents.dundee.ac.uk/.

Protein purification

Purification of Rabs and Rabin8 (*Figures 2D, 2G*, and *5E*)

Buffer A: 50 mM HEPES pH 8.0, 500 mM LiCl, 1 mM $MgCl_2$, 10 µM GDP, 2 mM beta-mercaptoethanol; Elution buffer: buffer A + 500 mM imidazole; Lysis buffer: buffer A + 1 mM PMSF and Roche Complete protease inhibitor cocktail (EDTA-free); Gel-filtration buffer: 20 mM HEPES pH 8.0, 50 mM NaCl, 1 mM $MgCl_2$, 10 µM GDP, 25 µM ATP, 2 mM DTT.

Rab isoforms and Rabin8 (153-237) were expressed as N-terminal His-Sumo fusion proteins in *E. coli* as described previously (*Bleimling et al., 2009*). The His-Sumo tag was removed using SENP1 protease (*Chaugule et al., 2011*). Transformed BL21 (DE3) harboring the GroEL/S plasmid (*Bleimling et al., 2009*) were grown at 37°C to an OD 600 of 0.8, then shifted to 19°C and protein expression induced with Isopropyl β-D-1-thiogalactopyranoside (0.5 mM) for 16 hr. Cells were pelleted at 5000 g (4°C for 20 min) and lysed by sonication (45% amplitude, 20 s pulse, 1 min pause, total of 10 min pulse) in lysis buffer. Lysates were clarified by centrifugation at 30,000 g for 20 min at 4°C followed by incubation with 1 ml of Nickel-NTA agarose/l culture for 1 hr at 4°C. The resin was equilibrated on an AKTA FPLC with buffer A, and bound proteins eluted with imidazole gradient (25 mM-500 mM). Fractions containing the protein of interest were identified by SDS-PAGE and pooled; 10 µg/ml His-SENP1 catalytic domain (residues 415–643) was used to cleave the His tag (16 hr at 4 °C). Imidazole was removed by buffer exchange gel filtration on a G25 column equilibrated in Buffer A plus 20 mM Imidazole. His-SENP1 protease was removed using Nickel-NTA agarose. Proteins were concentrated to a maximum of 10 mg/ml using a Vivaspin 10 kDa cut centricon and 0.5 ml samples were resolved on a high-resolution Superdex 200, 24 ml gel-filtration column equilibrated with gel filtration buffer and 0.2 ml fractions were collected. Peak fractions containing recombinant protein were pooled. Identity and purity of proteins were assessed by Maldi-TOF MS and SDS-PAGE.

Purification of Rab8a and Rabin8 (*Figures 5D*)

Human Rab8a (wt, T72E, T72A, residues 1-183) and human Rabin8 constructs (144-460 and 144-245) containing tobacco etch virus (TEV) cleavable N-terminal 6-HIS tag were expressed in *E. coli* BL21 (DE3). Cells were lysed by sonication in a buffer containing 50 mM phosphate pH 7.5, 150 mM NaCl, 10% glycerol. For Rab8a proteins 5 mM $MgCl_2$ was added. Proteins were purified by Ni-NTA affinity chromatography. To remove the N-terminal HIS tag, proteins were incubated with TEV protease overnight. Further purification was done by ion-exchange chromatography (Q-Sepharose) followed by size exclusion chromatography (SEC) in a buffer of 10 mM HEPES pH 7.5, 150 mM NaCl, and 2 mM DTT using a HiLoad Superdex 75 column. For Rab8a proteins 5 mM $MgCl_2$ was added to the SEC buffer.

Mice

Mice were maintained under specific pathogen-free conditions at the University of Dundee (UK). All animal studies were ethically reviewed and carried out in accordance with Animals (Scientific Procedures) Act 1986, the GSK Policy on the Care, Welfare and Treatment of Animals, regulations set by the University of Dundee and the U.K. Home Office. Animal studies and breeding were approved by the University of Dundee ethical committee and performed under a U.K. Home Office project license.

The LRRK2-G2019S[GSK] knock-in mouse line was generated by a targeting strategy devised to introduce the point mutation G2019S into exon 41 of the LRRK2 gene by homologous recombination in mouse embryonic stem (ES) cells. 5' and 3' homology arms (approximately 4.8 and 3.8 kb, respectively) flanking exon 41 were generated using Phusion High-Fidelity DNA Polymerase (New England BioLabs) on a C57BL/6J genomic DNA template. Similarly a 739 bp fragment carrying exon

41 lying between these two homology arms was isolated and subjected to site-directed mutagenesis with the QuickChangeII site-directed mutagenesis kit (Stratagene) to introduce the appropriate point mutation (GG to TC mutation at bps 107/8). The 5' and 3' homology arms and the mutated exon 41 fragments were subcloned into a parental targeting vector to achieve the positioning of the loxP and FRT sites and PGKneo cassette. Gene targeting was performed in de novo generated C57BL/6J-derived ES cells. The targeting construct was linearized and electroporated into ES cells according to standard methods. ES cells correctly targeted at the 3' end were identified by Southern blot analysis of EcoRV digested genomic DNA using a PCR-derived external probe. Correct gene targeting at the 5' end and presence of the point mutation was confirmed by sequencing of a ~6 kb PCR product. High-fidelity PCR of ES cell clone-derived genomic DNA using primers spanning the 5' homology arm generated the latter. Correctly targeted ES cell clones were injected into BALB/c blastocysts and implanted into foster mothers according to standard procedures. Male chimaeras resulting from the G2019S targeted ES cells were bred with C57BL/6J female mice, and germline transmission of the targeted allele was confirmed by PCR. The PGKneo cassette was subsequently removed by breeding germline mice to FLPeR (*Farley et al., 2000*) mice expressing Flp recombinase from the Rosa26 locus (C57BL/6J genetic background). Absence of the PGKneo cassette in offspring was confirmed by PCR and subsequent breeding to C57BL/6J mice removed the Flper locus (confirmed by PCR). The line was maintained by breeding with C57BL/6J, and crossing mice heterozygous for the point mutation generated homozygous mice. Standard genotyping which distinguishes wild type from point mutation knock-in alleles was used throughout. Requests for LRRK2 G2019SGSK mice should be directed to: alastair.d.reith@gsk.com.

The Michael J. Fox Foundation for Parkinson's Research generated the A2016T knock-in mice. A targeting vector was designed to introduce an alanine to threonine (A2016T) substitution at codon 2016 in exon 41 of the endogenous locus. In addition, an FRT-flanked neomycin resistance (neo) cassette was introduced 400 bp downstream of exon 41. The construct was electroporated into C57BL/6N-derived JM8 ES cells. Correctly targeted ES cells were injected into blastocysts and chimeric mice were bred to B6.Cg-Tg (ACTFLPe)9205Dym/J (JAX stock No. 005703) to remove the neo cassette and leave a silent FRT site. The resulting animals were crossed to C57BL/6NJ inbred mice (JAX stock No. 005304) for one generation. These mice are available from The Jackson Laboratory and for further information see http://jaxmice.jax.org/strain/021828.html. The LRRK2-G2019S[Lilly] were generated by Ely Lilly and maintained on a C57BL/6J background.

Genotyping of mice was performed by PCR using genomic DNA isolated from ear biopsies. For LRRK2-G2019S[GSK] knock-in mice, Primer 1 (5'-CCGAGCCAAAAACTAAGCTC -3') and Primer 2 (5'-C-CATCTTGGGTACTTGACC-3') were used to detect the wild-type and knock-in alleles. For LRRK2-G2019S[Lilly] knock-in mice Primer 1 (5'-CATTGCGAAGATTGCGGACTACTCAATT-3') and Primer 2 (5'-AAACAGTAACTATTTCCGTCGTGATCCG-3') were used to detect the wild-type and knock-in alleles. For LRRK2-A2016T Primer 1 (5'-TTGCCTGTGAGTGTCTCTGG-3') and Primer 2 (5'-AGGAAA-TGTGGTTCCGACAC-3') were used to detect the wild-type and knock-in alleles. The PCR program consisted of 5 min at 95°C, then 35 cycles of 30 s at 95°C, 30 s at 60°C and 30 s at 72°C, and 5 min at 72°C. DNA sequencing was used to confirm the knock-in mutation and performed by DNA Sequencing & Services (MRC–PPU; http://www.dnaseq.co.uk) using Applied Biosystems Big-Dye version 3.1 chemistry on an Applied Biosystems model 3730 automated capillary DNA sequencer.

For experiments shown in *Figure 3F–G*, homozygous LRRK2-G2019S[Lilly] mice (3 months of age) were injected subcutaneously with vehicle (40% Hydroxypropyl-β-Cyclodextran) or MLI-2 (3 mg/kg of body mass dissolved in 40% Hydroxypropyl-β-Cyclodextran) and euthanized by cervical dislocation 1 hr after treatment. Brains were rapidly isolated and snap frozen in liquid nitrogen. No specific randomization method or blinding was applied to experiments.

Generation of MEFs

Littermate matched wild type and homozygous LRRK2-A2016T mouse embryonic fibroblasts (MEFs) were isolated from mouse embryos at day E12.5 resulting from crosses between heterozygous LRRK2-A2016T/WT mice using a previously described protocol (*Wiggin et al., 2002*). Cells were genotyped as described above for mice and wild type and homozygous A2016T knock-in cells generated from the same littermate selected for subsequent experiments. Cells cultured in parallel at passage 4 were used for MS and immunoblotting experiments.

Littermate matched wild type and homozygous LRRK2-G2019S[GSK] MEFs were isolated from mouse embryos at day E12.5 resulting from crosses between heterozygous LRRK2-G2019S[GSK]/WT mice as described previously (*Wiggin et al., 2002*). Wild-type and homozygous LRRK2-G2019S[GSK]/ G2019S[GSK] MEFs were continuously passaged in parallel for at least 15 passages before being used for MS and immunoblotting experiments. All cells were cultured in DMEM containing 10% FBS, 2 mM L-glutamine, 50 units/ml penicillin, 50 µg/ml streptomycin, and non-essential amino acids (Life Technologies). Littermate matched wild type and homozygous knock-out MEFs were isolated from LRRK2 knock-out mice (*Dzamko et al., 2012*) as described previously (*Davies et al., 2013*). All knock-in and knock-out cell lines were verified by allelic sequencing.

Culture and transfection of cells

HEK293 were purchased from ATCC and cultured in Dulbecco's modified Eagle medium (Glutamax, Gibco) supplemented with 10% fetal calf serum, 100 U/ml penicillin, and 100 µg/ml streptomycin. The HEK293-t-rex-flpIn stable cell lines with doxycycline-inducible wild type and mutant forms of LRRK2 have been described previously (*Nichols et al., 2010*). Transient transfections were performed 36-48 hr prior to cell lysis using Lipofectamine 2000 (Life Technologies) or FuGene HD (Promega). LRRK2 expression in HEK293-t-rex-flpIn was induced by doxycycline (1 µg/ml, 24 hr). All cells were tested for mycoplasma contamination and overexpressing lines were verified by Western blot analysis.

Immunoprecipitations, pull-downs, and subcellular fractionation

For HA-Rab immunoprecipitations, HA-agarose (Sigma) was washed 3 times with PBS and incubated with lysates at a concentration of 25 µl of resin/mg lysate for 1 hr. Beads were then washed twice with 1 ml PBS and samples eluted in 2 x LDS (50 µl per 25 µl of resin) and centrifuged through a 0.22 µm Spinex filter, 2-mercpatoethanol added to 2% (v/v) and heated to 70°C for 5 min prior to SDS-PAGE. For GFP pulldowns and immunoprecipitations, cells were lysed in ice-cold NP-40 extraction buffer (50 mM Tris-HCl, pH 7.5, 120 mM NaCl, 1 mM EDTA, 6 mM EGTA, 15 mM sodium pyrophosphate and 1% NP-40 supplemented with protease and phosphatase inhibitors (Roche) and clarified by centrifugation at 14,000 rpm. Supernatants were incubated over night with Rab8 or Rab10 antibodies and bound complexes recovered using agarose protein A/G beads (Pierce). For GFP pull-downs, lysates were incubated with GFP beads for 2 hr (Chromotek). On bead digestion of protein complexes used for MS analysis was performed as described previously (*Hubner et al., 2010*).

For subcellular fractionation, SILAC (*Ong, 2002*) labeled HEK293 cells were counted and mixed in a 1:1 ratio after harvesting in PBS, spun at 1000 rpm at 4°C for 5 min and then resuspended in subcellular fractionation buffer (250 mM sucrose, 20 mM HEPES pH 7.4, 10 mM KCl, 1.5 mM MgCl$_2$, 1 mM EDTA, 1 mM EGTA and protease/phosphatase inhibitor cocktail [Roche]). Cells were then Dounce homogenized, left on ice for 20 min and spun at 750 g for 5 min. The supernatant spun in an ultracentrifuge (100,000 *g*) for 45 min to obtain cytosolic (supernatant) and membrane (pellet) fractions.

Phos-tag SDS-PAGE

Phos-tag acrylamide and MnCl$_2$ were added to a standard gel solution at a final concentration of 50 µM and 100 µM, respectively. After degassing for 10 min, gels were polymerized by ammonium persulfate and TEMED. Cell lysates used for Phos-tag SDS-PAGE were supplemented with MnCl$_2$ at 10 mM to mask the effect of EDTA in the lysates. After SDS-PAGE, gels were washed 3 times with transfer buffer containing 10 mM EDTA followed by a wash with transfer buffer (10 min each). Blotting to nitrocellulose membranes was carried out according to a standard protocol.

Total proteome and phosphoproteome sample preparation and MS analyses

All samples were lysed in SDS lysis buffer (4% SDS, 10 mM DTT, 10 mM Tris pH 7.5), boiled and sonicated, and precipitated overnight using ice-cold acetone (v/v= 80%). After centrifugation (4000 g), the pellet was washed at least twice with 80% ice-cold acetone before air drying and resuspension (sonication) in either urea (6 M urea, 2 M thiorurea, 50 mM Tris pH 8) or TFE buffer (10% 2-2-2-

trifluorethanol, 100 mM ammonium bicarbonate [ABC]). Proteins were digested using LysC and trypsin (1:100), overnight at 37°C. Peptides for total proteome measurements were desalted on C18 StageTips and phosphopeptides were enriched as described previously (*Humphrey et al., 2015*).

LC-MS/MS measurements

Peptides were loaded on a 50 cm reversed phase column (75 µm inner diameter, packed in-house with ReproSil-Pur C18-AQ 1.9 µm resin [Dr. Maisch GmbH]). Column temperature was maintained at 50°C using a homemade column oven. An EASY-nLC 1000 system (Thermo Fisher Scientific) was directly coupled online with a mass spectrometer (Q Exactive, Q Exactive Plus, Q Exactive HF, LTQ Orbitrap, Thermo Fisher Scientific) via a nano-electrospray source, and peptides were separated with a binary buffer system of buffer A (0.1% formic acid [FA]) and buffer B (80% acetonitrile plus 0.1% FA), at a flow rate of 250nl/min. Peptides were eluted with a gradient of 5-30% buffer B over 30, 95, 155, or 240 min followed by 30-95% buffer B over 10 min, resulting in approximately 1, 2, 3, or 4 hr gradients, respectively. The mass spectrometer was programmed to acquire in a data-dependent mode (Top5–Top15) using a fixed ion injection time strategy. Full scans were acquired in the Orbitrap mass analyzer with resolution 60,000 at 200 m/z (3E6 ions were accumulated with a maximum injection time of 25 ms). The top intense ions (N for TopN) with charge states $\geq$2 were sequentially isolated to a target value of 1E5 (maximum injection time of 120 ms, 20% underfill), fragmented by HCD (NCE 25%, Q Exactive) or CID (NCE 35%, LTQ Orbitrap) and detected in the Orbitrap (Q Exactive, R= 15,000 at m/z 200) or the Ion trap detector (LTQ Orbitrap).

Data processing and analysis

Raw MS data were processed using MaxQuant version 1.5.1.6 or 1.5.3.15 (*Cox and Mann, 2008*; *Cox et al., 2011*) with an FDR < 0.01 at the level of proteins, peptides and modifications. Searches were performed against the Mouse or Human UniProt FASTA database (September 2014). Enzyme specificity was set to trypsin, and the search included cysteine carbamidomethylation as a fixed modification and N-acetylation of protein, oxidation of methionine, and/or phosphorylation of Ser, Thr, Tyr residue (PhosphoSTY) as variable modifications. Up to two missed cleavages were allowed for protease digestion, and peptides had to be fully tryptic. Quantification was performed by MaxQuant, 'match between runs' was enabled, with a matching time window of 0.5-0.7 min. Bioinformatic analyses were performed with Perseus (www.perseus-framework.org) and Microsoft Excel and data visualized using Graph Prism (GraphPad Software) or R studio (https://www.rstudio.com/). Hierarchical clustering of phosphosites was performed on logarithmized (Log2) intensities. Significance was assessed using one sample t-test, two-sample student's t-test, and ANOVA analysis, for which replicates were grouped, and statistical tests performed with permutation-based FDR correction for multiple hypothesis testing. Missing data points were replaced by data imputation after filtering for valid values (all valid values in at least one experimental group). Error bars are mean ± SEM or mean ± SD. Proteomics raw data have been deposited to the ProteomeXchange Consortium (http://proteomecentral.proteomexchange.org) via the PRIDE partner repository with the data set identifier PXD003071.

LRRK2 inhibitor IC50 LRRK2 kinase assay

LRRK2 kinase activity was assessed in an in vitro kinase reaction performed as described previously (*Nichols et al., 2009*). For IC$_{50}$ determination of LRRK2 inhibitor, peptide kinase assays were set up in a total volume of 30 µl with recombinant wild type GST-LRRK2-(1326-2527) or mutant GST-LRRK2 [A2016T]-(1326-2527) (6 nM) in 50 mM Tris-HCl pH 7.5, 0.1 mM EGTA, 10 mM MgCl$_2$, 0.1 mM [γ-32P]ATP (~300-600 cpm/pmol), and 20 µM Nictide LRRK2 substrate peptide substrate, in the presence of indicated concentration of MLI-2. After incubation for 20 min at 30°C, reactions were terminated by applying 25 µl of the reaction mixture onto P81 phosphocellulose papers and immersion in 50 mM phosphoric acid. After extensive washing, reaction products were quantified by Cerenkov counting. IC50 values were calculated using non-linear regression analysis using GraphPad Prism (GraphPad Software). The IC$_{50}$s for GSK2578215A (*Reith et al., 2012*) against wild type GST-LRRK2-(1326-2527) or mutant GST-LRRK2[A2016T]-(1326-2527) are 10.9 nM and 81.1 nM, respectively, and the IC50s for HG-10-102-01 (*Choi et al., 2012*) vs LRRK2 WT and A2016T are 20.3 nM and 153.7 nM, respectively. The IC$_{50}$ of MLI-2 against wild type GST-LRRK2-(1326-2527) or mutant GST-LRRK2

[A2016T]-(1326-2527) are 0.8 nM and 7.2 nM (see Extended Data *Figure 1A*). As MLI-2 displayed greater potency as well as a higher degree of resistance between wild type and A2016T mutation (9-fold compared to 7.4-fold for GSK2578215A and 7.6-fold for HG-10-102-01), we used MLI-2 for MS studies employing LRRK2[A2016T] knock-in MEFs.

In vitro kinase assays

Phosphorylation of Rab isoforms (*Figures 2D, 2G, 2H* and *4F*)

LRRK2 kinase assays were performed using purified recombinant GST-tagged LRRK2 (960-2527, wt, D1994A, G2019S, Invitrogen) incubated with recombinant Rab isoform (1 µM). Proteins were incubated in kinase assay buffer (20 mM Tris pH 7.5, 1 mM EGTA, 5 mM β-glycerophosphate, 5 mM NaF, 10 mM MgCl$_2$, 2 mM DTT, 10 µM ATP, and 0.5 µCi of γ-32P-ATP) at a combined volume of 30 µL. The reaction mixture was incubated at 30°C for 30 min, or as indicated. Reactions were quenched by the addition of SDS-sample loading buffer, heated to 70°C for 10 min and then separated on SDS-PAGE. Following electrophoresis, gels were fixed (50% (v/v) methanol, 10% (v/v) acetic acid), stained in Coomassie brilliant blue, dried and exposed to a phospho-imaging screen for assessing radioactive ^{32}P incorporation. For MS analysis, 100 µM of ATP was used and the reaction was stopped by addition of 2 M urea buffer (2 M urea in 50 mM Tris pH 7.5) containing LRRK2 inhibitor HG-10-102-01 (2 µM).

Phosphorylation of Rab isoforms (*Figures 2C and 2F*)

Assays were set up in a total volume of 25 µl with recombinant full-length Flag-LRRK2 (100 ng, Invitrogen) in 50 mM Tris-HCl pH 7.5, 0.1 mM EGTA, 10 mM MgCl$_2$, 0.1 mM [γ-^{32}P]ATP (~300-600 cpm/pmol), with recombinant Rab isoform (1.5 µg) in the presence or absence of the LRRK2 inhibitor HG-10-102-01 (2 µM). After incubation for 30 min at 30°C, reactions were stopped by the addition of Laemmli sample buffer and reaction products resolved on SDS-PAGE. The incorporation of phosphate into protein substrates was determined by autoradiography. For phosphorylation of Rab8a or Nictide (*Figure 1B*) LRRK2 was immunoprecipitated from MEFs and kinase activity was assessed in an in vitro kinase reaction as described previously (*Davies et al., 2013*).

Phosphosite identification by MS and Edman sequencing (*Figure 2—figure supplement 1*)

Purified Rab1b and Rab8a (5 µg) were phosphorylated using recombinant full-length wild type Flag-LRRK2 (0.2 µg; Invitrogen) in a buffer containing 50 mM Tris-HCl pH 7.5, 0.1 mM EGTA, 10 mM MgCl2, 0.1 mM [γ-32P]ATP (~3000 Ci/pmol) for 1 hr at 30°C. The reactions were stopped by the addition of SDS sample buffer, and reaction products were resolved by electrophoresis on SDS-PAGE gels that were stained with Coomassie blue. The band corresponding to Rab1b/Rab8a was excised and digested overnight with trypsin at 30°C, and the peptides were separated on a reverse-phase HPLC Vydac C18 column (Separations Group) equilibrated in 0.1% (v/v) trifluoroacetic acid, and the column developed with a linear acetonitrile gradient at a flow rate of 0.2 ml/min. Fractions (0.1 ml each) were collected and analyzed for ^{32}P radioactivity by Cerenkov counting. Phosphopeptides were analyzed by liquid chromatography (LC)-MS/MS using a Thermo U3000 RSLC nano liquid chromatography system (Thermo Fisher Scientific) coupled to a Thermo LTQ-Orbitrap Velos mass spectrometer (Thermo Fisher Scientific). Data files were searched using Mascot (www.matrixscience.com) run on an in-house system against a database containing the appropriate Rab sequences, with a 10 ppm mass accuracy for precursor ions, a 0.6 Da tolerance for fragment ions, and allowing for Phospho (ST), Phospho (Y), Oxidation (M), and Dioxidation (M) as variable modifications. Individual MS/MS spectra were inspected using Xcalibur 2.2 (Thermo Fisher Scientific), and Proteome Discoverer with phosphoRS 3.1 (Thermo Fisher Scientific) was used to assist with phosphosite assignment. The site of phosphorylation of 32P-labeled peptides was determined by solid-phase Edman degradation on a Shimadzu PPSQ33A Sequencer of the peptide coupled to Sequelon-AA membrane (Applied Biosystems) as described previously (*Campbell and Morrice, 2002*).

Phosphorylation of Rab8a (*Figure 5D*)

Rab8a was phosphorylated using LRRK2-G2019S (see 'in vitro kinase assays' section). Non-phosphorylated and phosphorylated Rab8a proteins were separated using ion-exchange chromatography

(Mono S 4.6/100; GE Healthcare) with a linear salt gradient from buffer A (20 mM Tris/HCl pH 7.5, 50 mM NaCl, 10% (v/v) glycerol) to buffer B (as buffer A, but with 1000 mM NaCl). The successful enrichment of phosphorylated Rab8a was confirmed by ESI-TOF MS.

Rab8a nucleotide binding experiments

Rab8a (1-183, wt and T72E) were subjected to HPLC revealing that the purified proteins were (>90%) in the nucleotide-free form. To determine affinities for G-nucleotides, fluorescence measurements were carried out at 20°C in a buffer containing 50 mM Tris pH 7.5, 100 mM NaCl, and 5 mM MgCl$_2$. Spectra were measured with a PerkinElmer LS50B fluorescence spectrophotometer; 1 µM of methylanthraniloyl (mant) labeled GMPPNP and GDP was incubated with increasing concentrations of wild type and T72E Rab8a in 60 µl volumes. Fluorescence of mant-nucleotides was excited at 355 nm and emission spectra monitored from 400 to 500 nm, with emission maxima detected at 448 nm. Intrinsic protein fluorescence and mant-nucleotide background fluorescence was subtracted from the curves. Data collection was performed with the program FL WinLab (PerkinElmer), while further analysis, curve fitting and dissociation constant (K$_d$) determination was done using GraphPad Prism (GraphPad Software).

Guanine exchange factor (GEF) assays

Figure 5E: Purified Rab8a (100 µg) was phosphorylated using LRRK2 G2019S (1.5 µg) in a buffer containing 50 mM Tris-HCl pH 7.5, 0.1 mM EGTA, 10 mM MgCl$_2$, 2 mM DTT, 1 mM ATP (18 hr, room temperature [RT]) in a Dispo-Biodialyzer MWCO 1 kDa (Sigma-Aldrich) and incubated in 2 l of the same Buffer to allow for ADP exchange. The buffer was subsequently exchanged to a GDP dissociation assay buffer containing 20 mM HEPES-NaOH pH 7.5, 50 mM NaCl, 2 mM DTT, 1 mM MnCl$_2$, 0.01% (w/v) Brij-35 using Zeba Spin desalting columns (Invitrogen). Phosphorylated Rab8a (50 µg) was treated with lambda phosphatase (5 µg) for 30 min at 30°C where indicated. To load mant-GDP, Rab8a was incubated with 40 µM mant-GDP in the presence of 5 mM EDTA at 30°C for 30 min. After adding MgCl$_2$ at 10 mM, in order to remove unbound mant-GDP, the buffer was exchanged to a buffer containing 10 mM HEPES-NaOH pH 7.5, 50 mM NaCl, 5 mM DTT, 1 mM MgCl$_2$ using Zeba Spin desalting columns. GDP dissociation reactions were set up in a total volume of 50 µl with 1 µM Rab8a:mant-GDP in 20 mM HEPES-NaOH pH 7.5, 50 mM NaCl, 2 mM DTT, 1 mM MgCl$_2$, and 0.1 mM GDP, and the reaction was started by adding the indicated concentration of Rabin8 (residues 153-237) (*Guo et al., 2013*). Kinetic measurement of the mant fluorescence was carried out in a black half-area 96-well plate with PHERAStar FS (BMG Labtech) at RT using a set of filters (excitation: 350 nm, emission: 460 nm). The observed rate constant (k$_{obs}$) and the catalytic efficiency (k$_{cat}$/K$_m$) were calculated as described previously (*Delprato et al., 2004*). Phosphorylation stoichiometry (63%) was calculated by digestion of the protein with trypsin and analyzing the fragments by Orbitrap MS.

Figure 5D: Phosphorylated Rab8a was obtained as described in section 'Phosphorylation of Rab8a'. GEF assays were performed as described previously (*Eberth and Ahmadian, 2009*). Loading of purified nucleotide-free (both phosphorylated and non-phosphorylated) Rab8a (1-183) with 2'(3')-O-(N-methylanthraniloyl)-GDP (mantGDP) was achieved by incubation with an 1.5 molar excess of mantGDP for 2 hr at RT. Unbound mantGDP was removed using a size-exclusion chromatography column. (Micro Bio-Spin column, Bio-RAD). The nucleotide exchange reactions were set up in a total volume of 50 µl in a quartz-glass cuvette (Hellma Analytics) with 0.5 µM mantGDP-bound Rab8a (non-phosphorylated or phosphorylated) using a GEF buffer containing 30 mM Tris pH 7.5, 5 mM MgCl$_2$, 3 mM DTT and 10 mM KH$_2$PO$_4$, pH 7.4. Purified Rabin8 (144-245, GEF domain) was subjected to size exclusion chromatography prior to GEF activity assay to ensure no loss of GEF activity due to storage. Rabin8 was added to a final concentration of 2 µM and incubated for 30 min at 20°C. The reactions were initiated by addition of GTP (1 mM c$_f$). The dissociation of mant-GDP from Rab8a was monitored every 2 s for a total of 300 s at 20°C using a fluorescence spectrometer (PerkinElmer, 366 nm excitation and 450 nm emission). The observed rate constants (k$_{obs}$) were calculated by fitting the data into a one-phase exponential decay equation without constraints using nonlinear regression in GraphPad Prism (GraphPad Software Inc).

Ni²⁺-NTA Rabin8 pull-down

Ni²⁺-NTA beads were pre-equilibrated with buffer containing PBS pH 7.4, 30 mM imidazole and 5 mM MgCl$_2$. Purified HIS-tagged Rabin8 (residues 144-460) and untagged Rab8a (1-183) WT or quantitatively phosphorylated pT72 were mixed at equal molar ratios. Individual proteins and a mixture of the proteins were incubated with Ni²⁺-NTA beads for 1.5 hr at 4°C. Beads were washed 3 times with PBS, bound proteins eluted with 500 mM imidazole followed by SDS–PAGE and western blot analysis.

Acknowledgements

Additional information

Competing interests

SWi: Employee of GlaxoSmithKline, a global healthcare company that may conceivably benefit financially through this publication. MJF: Employee of Merck Research Laboratories. JAM: Employee of GlaxoSmithKline, a global healthcare company that may conceivably benefit financially through this publication. ADR: Employee of Merck Research Laboratories, Contributed unpublished essential data or reagents. The other authors declare that no competing interests exist.

Funding

Author contributions

MS, Designed the experiments, Performed the experiments, Conducted all global MS experiments and bioinformatic analyses of MS data and discovered the regulated Rab phosphorylation, Conception and design, Acquisition of data, Analysis and interpretation of data, Drafting or revising the article; FT, GI, Designed the experiments, Performed the experiments, Discussed the results and

approved the manuscript, Acquisition of data, Analysis and interpretation of data; PD, Designed the experiments, Discussed the results and approved the manuscript, Analysis and interpretation of data, Drafting or revising the article; MT, Performed the experiments, Discussed the results and approved the manuscript, Analysis and interpretation of data; MV, SWa, Performed the experiments, Discussed the results and approved the manuscript, Acquisition of data, Analysis and interpretation of data; EL, Designed the experiments, Discussed the results and approved the manuscript, Conception and design, Analysis and interpretation of data; GD, SWi, Contributed essential reagents, Generated the G2019SGSK knock-in mouse line, Discussed the results and approved the manuscript, Contributed unpublished essential data or reagents; MASB, BKF, Generated A2016T knock-in mice and supported the project, Discussed the results and approved the manuscript, Conception and design, Contributed unpublished essential data or reagents; MJF, Employees of Merck Research Laboratories, Contributed unpublished essential data or reagents; JAM, Contributed essential reagents, Provided MLI-2, Discussed the results and approved the manuscript, Contributed unpublished essential data or reagents; ADR, Contributed essential reagents, Generated the G2019SGSK knock-in mouse line, Provided GSK2578215A and supported the project from conception, Discussed the results and approved the manuscript, Contributed unpublished essential data or reagents; DRA, Designed the experiments, Wrote the manuscript, Discussed the results and approved the manuscript, Conception and design, Analysis and interpretation of data, Drafting or revising the article; MM, Conception and design, Analysis and interpretation of data, Drafting or revising the article

Ethics

Animal experimentation: All animal studies were ethically reviewed and carried out in accordance with Animals (Scientific Procedures) Act 1986, the GSK Policy on the Care, Welfare and Treatment of Animals, regulations set by the University of Dundee and the U.K. Home Office. Animal studies and breeding were approved by the University of Dundee ethical committee and performed under a U.K. Home Office project license.

Additional files

Supplementary files

• Supplementary file 1. All phosphosites quantified in the phosphoproteomic screens one (PS1, LRRK2-G2019S^{GSK} MEFs and two (PS2, wt and LRRK2-A2016T MEFs).
DOI: 10.7554/eLife.12813.019

• Supplementary file 2. All quantified proteins of wt and LRRK2-A2016T MEFs.
DOI: 10.7554/eLife.12813.020

• Supplementary file 3. (A) Significantly modulated sites of PS1. (B) Significantly modulated sites of PS2.
DOI: 10.7554/eLife.12813.021

References

Bailey RM, Covy JP, Melrose HL, Rousseau L, Watkinson R, Knight J, Miles S, Farrer MJ, Dickson DW, Giasson BI, Lewis J. 2013. LRRK2 phosphorylates novel tau epitopes and promotes tauopathy. *Acta Neuropathologica* **126**: 809–827. doi: 10.1007/s00401-013-1188-4

Baptista MAS, Dave KD, Frasier MA, Sherer TB, Greeley M, Beck MJ, Varsho JS, Parker GA, Moore C, Churchill MJ, Meshul CK, Fiske BK. 2013. Loss of leucine-rich repeat kinase 2 (LRRK2) in rats leads to progressive abnormal phenotypes in peripheral organs. *PLoS One* **8**:e80705. doi: 10.1371/journal.pone.0080705

Bleimling N, Alexandrov K, Goody R, Itzen A. 2009. Chaperone-assisted production of active human Rab8A GTPase in escherichia coli. *Protein Expression and Purification* **65**:190–195. doi: 10.1016/j.pep.2008.12.002

Burbulla LF, Krüger R. 2011. Converging environmental and genetic pathways in the pathogenesis of parkinson's disease. *Journal of the Neurological Sciences* **306**:1–8. doi: 10.1016/j.jns.2011.04.005

Campbell DG, Morrice NA. 2002. Identification of protein phosphorylation sites by a combination of mass spectrometry and solid phase edman sequencing. *Journal of Biomolecular Techniques* **13**:119–130.

Chaugule VK, Burchell L, Barber KR, Sidhu A, Leslie SJ, Shaw GS, Walden H. 2011. Autoregulation of parkin activity through its ubiquitin-like domain. *The EMBO Journal* **30**:2853–2867. doi: 10.1038/emboj.2011.204

Chen C-Y, Weng Y-H, Chien K-Y, Lin K-J, Yeh T-H, Cheng Y-P, Lu C-S, Wang H-L. 2012. (G2019S) LRRK2 activates MKK4-JNK pathway and causes degeneration of SN dopaminergic neurons in a transgenic mouse model of PD. *Cell Death and Differentiation* **19**:1623–1633. doi: 10.1038/cdd.2012.42

Choi HG, Zhang J, Deng X, Hatcher JM, Patricelli MP, Zhao Z, Alessi DR, Gray NS. 2012. Brain penetrant LRRK2 inhibitor. *ACS Medicinal Chemistry Letters* **3**:658–662. doi: 10.1021/ml300123a

Cookson MR. 2015. LRRK2 pathways leading to neurodegeneration. *Current Neurology and Neuroscience Reports* **15**:42. doi: 10.1007/s11910-015-0564-y

Cooper AA, Gitler AD, Cashikar A, Haynes CM, Hill KJ, Bhullar B, Liu K, Xu K, Strathearn KE, Liu F, Cao S, Caldwell KA, Caldwell GA, Marsischky G, Kolodner RD, Labaer J, Rochet JC, Bonini NM, Lindquist S. 2006. Alpha-synuclein blocks ER-golgi traffic and Rab1 rescues neuron loss in parkinson's models. *Science* **313**:324–328. doi: 10.1126/science.1129462

Cox J, Hein MY, Luber CA, Paron I, Nagaraj N, Mann M. 2014. Accurate proteome-wide label-free quantification by delayed normalization and maximal peptide ratio extraction, termed MaxLFQ. *Molecular & Cellular Proteomics* **13**:2513–2526. doi: 10.1074/mcp.M113.031591

Cox J, Mann M. 2008. MaxQuant enables high peptide identification rates, individualized p.p.b.-range mass accuracies and proteome-wide protein quantification. *Nature Biotechnology* **26**:1367–1372. doi: 10.1038/nbt.1511

Cox J, Neuhauser N, Michalski A, Scheltema RA, Olsen JV, Mann M. 2011. Andromeda: a peptide search engine integrated into the MaxQuant environment. *Journal of Proteome Research* **10**:1794–1805. doi: 10.1021/pr101065j

Davies P, Hinkle KM, Sukar NN, Sepulveda B, Mesias R, Serrano G, Alessi DR, Beach TG, Benson DL, White CL, Cowell RM, Das SS, West AB, Melrose HL. 2013. Comprehensive characterization and optimization of anti-LRRK2 (leucine-rich repeat kinase 2) monoclonal antibodies. *Biochemical Journal* **453**:101–113. doi: 10.1042/BJ20121742

Delprato A, Merithew E, Lambright DG. 2004. Structure, exchange determinants, and family-wide rab specificity of the tandem helical bundle and Vps9 domains of rabex-5. *Cell* **118**:607–617. doi: 10.1016/j.cell.2004.08.009

Dzamko N, Deak M, Hentati F, Reith AD, Prescott AR, Alessi DR, Nichols RJ. 2010. Inhibition of LRRK2 kinase activity leads to dephosphorylation of Ser^{910}/Ser^{935}, disruption of 14-3-3 binding and altered cytoplasmic localization. *Biochemical Journal* **430**:405–413. doi: 10.1042/BJ20100784

Dzamko N, Inesta-Vaquera F, Zhang J, Xie C, Cai H, Arthur S, Tan L, Choi H, Gray N, Cohen P, Pedrioli P, Clark K, Alessi DR. 2012. The IkappaB kinase family phosphorylates the parkinson's disease kinase LRRK2 at Ser935 and Ser910 during toll-like receptor signaling. *PLoS One* **7**:e39132. doi: 10.1371/journal.pone.0039132

Eberth A, Ahmadian MR. 2009. In vitro GEF and GAP assays. *Current Protocols in Cell Biology / Editorial Board, Juan S Bonifacino [Et Al]* **14**. doi: 10.1002/0471143030.cb1409s43

Farley FW, Soriano P, Steffen LS, Dymecki SM. 2000. Widespread recombinase expression using FLPeR (flipper) mice. *Genesis* **28**:106–110. doi: 10.1002/1526-968X(200011/12)28:3/4<106::AID-GENE30>3.0.CO;2-T

Farrer MJ, Stone JT, Lin C-H, Dächsel JC, Hulihan MM, Haugarvoll K, Ross OA, Wu R-M. 2007. Lrrk2 G2385R is an ancestral risk factor for parkinson's disease in asia. *Parkinsonism & Related Disorders* **13**:89–92. doi: 10.1016/j.parkreldis.2006.12.001

Fell MJ, Mirescu C, Basu K, Cheewatrakoolpong B, DeMong DE, Ellis JM, Hyde LA, Lin Y, Markgraf CG, Mei H, Miller M, Poulet FM, Scott JD, Smith MD, Yin Z, Zhou X, Parker EM, Kennedy ME, Morrow JA. 2015. MLi-2, a potent, selective, and centrally active compound for exploring the therapeutic potential and safety of LRRK2 kinase inhibition. *Journal of Pharmacology and Experimental Therapeutics* **355**:397–409. doi: 10.1124/jpet.115.227587

Gardet A, Benita Y, Li C, Sands BE, Ballester I, Stevens C, Korzenik JR, Rioux JD, Daly MJ, Xavier RJ, Podolsky DK. 2010. LRRK2 is involved in the IFN- response and host response to pathogens. *The Journal of Immunology* **185**:5577–5585. doi: 10.4049/jimmunol.1000548

Gillardon F. 2009. Leucine-rich repeat kinase 2 phosphorylates brain tubulin-beta isoforms and modulates microtubule stability - a point of convergence in parkinsonian neurodegeneration? *Journal of Neurochemistry* **110**:1514–1522. doi: 10.1111/j.1471-4159.2009.06235.x

Gitler AD, Bevis BJ, Shorter J, Strathearn KE, Hamamichi S, Su LJ, Caldwell KA, Caldwell GA, Rochet J-C, McCaffery JM, Barlowe C, Lindquist S. 2008. The parkinson's disease protein -synuclein disrupts cellular rab homeostasis. *Proceedings of the National Academy of Sciences of the United States of America* **105**:145–150. doi: 10.1073/pnas.0710685105

Gloeckner CJ, Schumacher A, Boldt K, Ueffing M. 2009. The parkinson disease-associated protein kinase LRRK2 exhibits MAPKKK activity and phosphorylates MKK3/6 and MKK4/7, *in vitro*. *Journal of Neurochemistry* **109**:959–968. doi: 10.1111/j.1471-4159.2009.06024.x

Guo Z, Hou X, Goody RS, Itzen A. 2013. Intermediates in the guanine nucleotide exchange reaction of Rab8 protein catalyzed by guanine nucleotide exchange factors Rabin8 and GRAB. *Journal of Biological Chemistry* **288**:32466–32474. doi: 10.1074/jbc.M113.498329

Herzig MC, Kolly C, Persohn E, Theil D, Schweizer T, Hafner T, Stemmelen C, Troxler TJ, Schmid P, Danner S, Schnell CR, Mueller M, Kinzel B, Grevot A, Bolognani F, Stirn M, Kuhn RR, Kaupmann K, van der Putten PH, Rovelli G, Shimshek DR. 2011. LRRK2 protein levels are determined by kinase function and are crucial for kidney and lung homeostasis in mice. *Human Molecular Genetics* **20**:4209–4223. doi: 10.1093/hmg/ddr348

Hinkle KM, Yue M, Behrouz B, Dächsel JC, Lincoln SJ, Bowles EE, Beevers JE, Dugger B, Winner B, Prots I, Kent CB, Nishioka K, Lin W-L, Dickson DW, Janus CJ, Farrer MJ, Melrose HL. 2012. LRRK2 knockout mice have an

intact dopaminergic system but display alterations in exploratory and motor co-ordination behaviors. *Molecular Neurodegeneration* **7**:25. doi: 10.1186/1750-1326-7-25

Hubner NC, Bird AW, Cox J, Splettstoesser B, Bandilla P, Poser I, Hyman A, Mann M. 2010. Quantitative proteomics combined with BAC TransgeneOmics reveals in vivo protein interactions. *The Journal of Cell Biology* **189**:739–754. doi: 10.1083/jcb.200911091

Humphrey SJ, Azimifar SB, Mann M. 2015. High-throughput phosphoproteomics reveals in vivo insulin signaling dynamics. *Nature Biotechnology* **33**:990–995. doi: 10.1038/nbt.3327

Hutagalung AH, Novick PJ. 2011. Role of rab GTPases in membrane traffic and cell physiology. *Physiological Reviews* **91**:119–149. doi: 10.1152/physrev.00059.2009

Imai Y, Gehrke S, Wang H-Q, Takahashi R, Hasegawa K, Oota E, Lu B. 2008. Phosphorylation of 4E-BP by LRRK2 affects the maintenance of dopaminergic neurons in drosophila. *The EMBO Journal* **27**:2432–2443. doi: 10.1038/emboj.2008.163

Jaleel M, Nichols RJ, Deak M, Campbell DG, Gillardon F, Knebel A, Alessi DR. 2007. LRRK2 phosphorylates moesin at threonine-558: characterization of how parkinson's disease mutants affect kinase activity. *Biochemical Journal* **405**:307–317. doi: 10.1042/BJ20070209

Kanao T, Venderova K, Park DS, Unterman T, Lu B, Imai Y. 2010. Activation of FoxO by LRRK2 induces expression of proapoptotic proteins and alters survival of postmitotic dopaminergic neuron in drosophila. *Human Molecular Genetics* **19**:3747–3758. doi: 10.1093/hmg/ddq289

Kawakami F, Yabata T, Ohta E, Maekawa T, Shimada N, Suzuki M, Maruyama H, Ichikawa T, Obata F. 2012. LRRK2 phosphorylates tubulin-associated tau but not the free molecule: LRRK2-mediated regulation of the tau-tubulin association and neurite outgrowth. *PLoS ONE* **7**:e30834. doi: 10.1371/journal.pone.0030834

Khan NL, Jain S, Lynch JM, Pavese N, Abou-Sleiman P, Holton JL, Healy DG, Gilks WP, Sweeney MG, Ganguly M, Gibbons V, Gandhi S, Vaughan J, Eunson LH, Katzenschlager R, Gayton J, Lennox G, Revesz T, Nicholl D, Bhatia KP, Quinn N, Brooks D, Lees AJ, Davis MB, Piccini P, Singleton AB, Wood NW. 2005. Mutations in the gene LRRK2 encoding dardarin (pARK8) cause familial parkinson's disease: clinical, pathological, olfactory and functional imaging and genetic data. *Brain* **128**:2786–2796. doi: 10.1093/brain/awh667

Krumova P, Reyniers L, Meyer M, Lobbestael E, Stauffer D, Gerrits B, Muller L, Hoving S, Kaupmann K, Voshol J, Fabbro D, Bauer A, Rovelli G, Taymans J-M, Bouwmeester T, Baekelandt V. 2015. Chemical genetic approach identifies microtubule affinity-regulating kinase 1 as a leucine-rich repeat kinase 2 substrate. *The FASEB Journal* **29**:2980–2992. doi: 10.1096/fj.14-262329

Kumar A, Greggio E, Beilina A, Kaganovich A, Chan D, Taymans J-M, Wolozin B, Cookson MR. 2010. The parkinson's disease associated LRRK2 exhibits weaker in vitro phosphorylation of 4E-BP compared to autophosphorylation. *PLoS One* **5**:e8730. doi: 10.1371/journal.pone.0008730

Lai Y-C, Kondapalli C, Lehneck R, Procter JB, Dill BD, Woodroof HI, Gourlay R, Peggie M, Macartney TJ, Corti O, Corvol J-C, Campbell DG, Itzen A, Trost M, Muqit MM. 2015. Phosphoproteomic screening identifies rab GTPases as novel downstream targets of PINK1. *The EMBO Journal* **34**:2840–2861. doi: 10.15252/embj.201591593

Lees AJ, Hardy J, Revesz T. 2009. Parkinson's disease. *The Lancet* **373**:2055–2066. doi: 10.1016/S0140-6736(09)60492-X

Lemeer S, Heck AJR. 2009. The phosphoproteomics data explosion. *Current Opinion in Chemical Biology* **13**:414–420. doi: 10.1016/j.cbpa.2009.06.022

Liu Z, Hamamichi S, Dae Lee B, Yang D, Ray A, Caldwell GA, Caldwell KA, Dawson TM, Smith WW, Dawson VL. 2011. Inhibitors of LRRK2 kinase attenuate neurodegeneration and parkinson-like phenotypes in caenorhabditis elegans and drosophila parkinson's disease models. *Human Molecular Genetics* **20**:3933–3942. doi: 10.1093/hmg/ddr312

MacLeod DA, Rhinn H, Kuwahara T, Zolin A, Di Paolo G, McCabe BD, MacCabe BD, Marder KS, Honig LS, Clark LN, Small SA, Abeliovich A. 2013. RAB7L1 interacts with LRRK2 to modify intraneuronal protein sorting and parkinson's disease risk. *Neuron* **77**:425–439. doi: 10.1016/j.neuron.2012.11.033

Mallick P, Kuster B. 2010. Proteomics: a pragmatic perspective. *Nature Biotechnology* **28**:695–709. doi: 10.1038/nbt.1658

Martin I, Kim JW, Dawson VL, Dawson TM. 2014. LRRK2 pathobiology in parkinson's disease. *Journal of Neurochemistry* **131**:554–565. doi: 10.1111/jnc.12949

Martin I, Kim JW, Lee BD, Kang HC, Xu J-C, Jia H, Stankowski J, Kim M-S, Zhong J, Kumar M, Andrabi SA, Xiong Y, Dickson DW, Wszolek ZK, Pandey A, Dawson TM, Dawson VL. 2014. Ribosomal protein s15 phosphorylation mediates LRRK2 neurodegeneration in parkinson's disease. *Cell* **157**:472–485. doi: 10.1016/j.cell.2014.01.064

Mata IF, Jang Y, Kim C-H, Hanna DS, Dorschner MO, Samii A, Agarwal P, Roberts JW, Klepitskaya O, Shprecher DR, Chung KA, Factor SA, Espay AJ, Revilla FJ, Higgins DS, Litvan I, Leverenz JB, Yearout D, Inca-Martinez M, Martinez E, Thompson TR, Cholerton BA, Hu S-C, Edwards KL, Kim K-S, Zabetian CP. 2015. The RAB39B p.G192R mutation causes x-linked dominant parkinson's disease. *Molecular Neurodegeneration* **10**:50. doi: 10.1186/s13024-015-0045-4

Matta S, Van Kolen K, da Cunha R, van den Bogaart G, Mandemakers W, Miskiewicz K, De Bock P-J, Morais VA, Vilain S, Haddad D, Delbroek L, Swerts J, Chávez-Gutiérrez L, Esposito G, Daneels G, Karran E, Holt M, Gevaert K, Moechars DW, De Strooper B, Verstreken P. 2012. LRRK2 controls an EndoA phosphorylation cycle in synaptic endocytosis. *Neuron* **75**:1008–1021. doi: 10.1016/j.neuron.2012.08.022

Nalls MA, Pankratz N, Lill CM, Do CB, Hernandez DG, Saad M, DeStefano AL, Kara E, Bras J, Sharma M, Schulte C, Keller MF, Arepalli S, Letson C, Edsall C, Stefansson H, Liu X, Pliner H, Lee JH, Cheng R, Ikram MA, Ioannidis JP, Hadjigeorgiou GM, Bis JC, Martinez M, Perlmutter JS, Goate A, Marder K, Fiske B, Sutherland M,

Xiromerisiou G, Myers RH, Clark LN, Stefansson K, Hardy JA, Heutink P, Chen H, Wood NW, Houlden H, Payami H, Brice A, Scott WK, Gasser T, Bertram L, Eriksson N, Foroud T, Singleton AB. International Parkinson's Disease Genomics Consortium (IPDGC); Parkinson's Study Group (PSG) Parkinson's Research: The Organized GENetics Initiative (PROGENI); 23andMe; GenePD; NeuroGenetics Research Consortium (NGRC); Hussman Institute of Human Genomics (HIHG); Ashkenazi Jewish Dataset Investigator; Cohorts for Health and Aging Research in Genetic Epidemiology (CHARGE); North American Brain Expression Consortium (NABEC); United Kingdom Brain Expression Consortium (UKBEC); Greek Parkinson's Disease Consortium; Alzheimer Genetic Analysis Group. 2014. Large-scale meta-analysis of genome-wide association data identifies six new risk loci for parkinson's disease. *Nature Genetics* **46**:989–993. doi: 10.1038/ng.3043

Nichols RJ, Dzamko N, Hutti JE, Cantley LC, Deak M, Moran J, Bamborough P, Reith AD, Alessi DR. 2009. Substrate specificity and inhibitors of LRRK2, a protein kinase mutated in parkinson's disease. *Biochemical Journal* **424**:47–60. doi: 10.1042/BJ20091035

Nichols RJ, Dzamko N, Morrice NA, Campbell DG, Deak M, Ordureau A, Macartney T, Tong Y, Shen J, Prescott AR, Alessi DR. 2010. 14-3-3 binding to LRRK2 is disrupted by multiple parkinson's disease-associated mutations and regulates cytoplasmic localization. *Biochemical Journal* **430**:393–404. doi: 10.1042/BJ20100483

Ohta E, Kawakami F, Kubo M, Obata F. 2011. LRRK2 directly phosphorylates Akt1 as a possible physiological substrate: impairment of the kinase activity by parkinson's disease-associated mutations. *FEBS Letters* **585**:2165–2170. doi: 10.1016/j.febslet.2011.05.044

Olsen JV, Blagoev B, Gnad F, Macek B, Kumar C, Mortensen P, Mann M. 2006. Global, in vivo, and site-specific phosphorylation dynamics in signaling networks. *Cell* **127**:635–648. doi: 10.1016/j.cell.2006.09.026

Ong SE, Blagoev B, Kratchmarova I, Kristensen DB, Steen H, Pandey A, Mann M. 2002. Stable isotope labeling by amino acids in cell culture, SILAC, as a simple and accurate approach to expression proteomics. *Molecular & Cellular Proteomics* **1**:376–386. doi: 10.1074/mcp.M200025-MCP200

Papkovskaia TD, Chau K-Y, Inesta-Vaquera F, Papkovsky DB, Healy DG, Nishio K, Staddon J, Duchen MR, Hardy J, Schapira AHV, Cooper JM. 2012. G2019S leucine-rich repeat kinase 2 causes uncoupling protein-mediated mitochondrial depolarization. *Human Molecular Genetics* **21**:4201–4213. doi: 10.1093/hmg/dds244

Pfeffer SR. 2005. Structural clues to rab GTPase functional diversity. *Journal of Biological Chemistry* **280**:15485–15488. doi: 10.1074/jbc.R500003200

Pylypenko O, Rak A, Reents R, Niculae A, Sidorovitch V, Cioaca M-D, Bessolitsyna E, Thomä NH, Waldmann H, Schlichting I, Goody RS, Alexandrov K. 2003. Structure of rab escort protein-1 in complex with rab geranylgeranyltransferase. *Molecular Cell* **11**:483–494. doi: 10.1016/S1097-2765(03)00044-3

Qing H, Wong W, McGeer EG, McGeer PL. 2009. Lrrk2 phosphorylates alpha synuclein at serine 129: parkinson disease implications. *Biochemical and Biophysical Research Communications* **387**:149–152. doi: 10.1016/j.bbrc.2009.06.142

Rak A, Pylypenko O, Durek T, Watzke A, Kushnir S, Brunsveld L, Waldmann H, Goody RS, Alexandrov K. 2003. Structure of rab GDP-dissociation inhibitor in complex with prenylated YPT1 GTPase. *Science* **302**:646–650. doi: 10.1126/science.1087761

Reith AD, Bamborough P, Jandu K, Andreotti D, Mensah L, Dossang P, Choi HG, Deng X, Zhang J, Alessi DR, Gray NS. 2012. GSK2578215A; a potent and highly selective 2-arylmethyloxy-5-substitutent-n-arylbenzamide LRRK2 kinase inhibitor. *Bioorganic & Medicinal Chemistry Letters* **22**:5625–5629. doi: 10.1016/j.bmcl.2012.06.104

Rivero-Ríos P, Gómez-Suaga P, Fernández B, Madero-Pérez J, Schwab AJ, Ebert AD, Hilfiker S. 2015. Alterations in late endocytic trafficking related to the pathobiology of LRRK2-linked parkinson's disease. *Biochemical Society Transactions* **43**:390–395. doi: 10.1042/BST20140301

Roux PP, Thibault P. 2013. The coming of age of phosphoproteomics—from large data sets to inference of protein functions. *Molecular & Cellular Proteomics* **12**:3453–3464. doi: 10.1074/mcp.R113.032862

Rudenko IN, Cookson MR. 2014. Heterogeneity of leucine-rich repeat kinase 2 mutations: genetics, mechanisms and therapeutic implications. *Neurotherapeutics* **11**:738–750. doi: 10.1007/s13311-014-0284-z

Satake W, Nakabayashi Y, Mizuta I, Hirota Y, Ito C, Kubo M, Kawaguchi T, Tsunoda T, Watanabe M, Takeda A, Tomiyama H, Nakashima K, Hasegawa K, Obata F, Yoshikawa T, Kawakami H, Sakoda S, Yamamoto M, Hattori N, Murata M, Nakamura Y, Toda T. 2009. Genome-wide association study identifies common variants at four loci as genetic risk factors for parkinson's disease. *Nature Genetics* **41**:1303–1307. doi: 10.1038/ng.485

Satpathy S, Wagner SA, Beli P, Gupta R, Kristiansen TA, Malinova D, Francavilla C, Tolar P, Bishop GA, Hostager BS, Choudhary C. 2015. Systems-wide analysis of BCR signalosomes and downstream phosphorylation and ubiquitylation. *Molecular Systems Biology* **11**:810. doi: 10.15252/msb.20145880

Schapansky J, Nardozzi JD, Felizia F, LaVoie MJ. 2014. Membrane recruitment of endogenous LRRK2 precedes its potent regulation of autophagy. *Human Molecular Genetics* **23**:4201–4214. doi: 10.1093/hmg/ddu138

Schapansky J, Nardozzi JD, LaVoie MJ. 2015. The complex relationships between microglia, alpha-synuclein, and LRRK2 in parkinson's disease. *Neuroscience* **302**:74–88. doi: 10.1016/j.neuroscience.2014.09.049

Seabra MC, Wasmeier C. 2004. Controlling the location and activation of rab GTPases. *Current Opinion in Cell Biology* **16**:451–457. doi: 10.1016/j.ceb.2004.06.014

Sharma K, D'Souza RCJ, Tyanova S, Schaab C, Wiśniewski JR, Cox J, Mann M. 2014. Ultradeep human phosphoproteome reveals a distinct regulatory nature of tyr and Ser/Thr-based signaling. *Cell Reports* **8**:1583–1594. doi: 10.1016/j.celrep.2014.07.036

Sheng Z, Zhang S, Bustos D, Kleinheinz T, Le Pichon CE, Dominguez SL, Solanoy HO, Drummond J, Zhang X, Ding X, Cai F, Song Q, Li X, Yue Z, van der Brug MP, Burdick DJ, Gunzner-Toste J, Chen H, Liu X, Estrada AA, Sweeney ZK, Scearce-Levie K, Moffat JG, Kirkpatrick DS, Zhu H. 2012. Ser1292 autophosphorylation is an

indicator of LRRK2 kinase activity and contributes to the cellular effects of PD mutations. *Science Translational Medicine* **4**:164ra161. doi: 10.1126/scitranslmed.3004485

Simón-Sánchez J, Schulte C, Bras JM, Sharma M, Gibbs JR, Berg D, Paisan-Ruiz C, Lichtner P, Scholz SW, Hernandez DG, Krüger R, Federoff M, Klein C, Goate A, Perlmutter J, Bonin M, Nalls MA, Illig T, Gieger C, Houlden H, Steffens M, Okun MS, Racette BA, Cookson MR, Foote KD, Fernandez HH, Traynor BJ, Schreiber S, Arepalli S, Zonozi R, Gwinn K, van der Brug M, Lopez G, Chanock SJ, Schatzkin A, Park Y, Hollenbeck A, Gao J, Huang X, Wood NW, Lorenz D, Deuschl G, Chen H, Riess O, Hardy JA, Singleton AB, Gasser T. 2009. Genome-wide association study reveals genetic risk underlying parkinson's disease. *Nature Genetics* **41**:1308–1312. doi: 10.1038/ng.487

Stenmark H. 2009. Rab GTPases as coordinators of vesicle traffic. *Nature Reviews Molecular Cell Biology* **10**: 513–525. doi: 10.1038/nrm2728

Taymans J-M, Nkiliza A, Chartier-Harlin M-C. 2015. Deregulation of protein translation control, a potential game-changing hypothesis for parkinson's disease pathogenesis. *Trends in Molecular Medicine* **21**:466–472. doi: 10.1016/j.molmed.2015.05.004

Vizcaíno JA, Deutsch EW, Wang R, Csordas A, Reisinger F, Ríos D, Dianes JA, Sun Z, Farrah T, Bandeira N, Binz P-A, Xenarios I, Eisenacher M, Mayer G, Gatto L, Campos A, Chalkley RJ, Kraus H-J, Albar JP, Martinez-Bartolomé S, Apweiler R, Omenn GS, Martens L, Jones AR, Hermjakob H. 2014. ProteomeXchange provides globally coordinated proteomics data submission and dissemination. *Nature Biotechnology* **32**:223–226. doi: 10.1038/nbt.2839

Wandinger-Ness A, Zerial M. 2014. Rab proteins and the compartmentalization of the endosomal system. *Cold Spring Harbor Perspectives in Biology* **6**:a022616–:a022616 doi: 10.1101/cshperspect.a022616

West AB, Moore DJ, Biskup S, Bugayenko A, Smith WW, Ross CA, Dawson VL, Dawson TM. 2005. From the cover: parkinson's disease-associated mutations in leucine-rich repeat kinase 2 augment kinase activity. *Proceedings of the National Academy of Sciences of the United States of America* **102**:16842–16847. doi: 10.1073/pnas.0507360102

Westlake CJ, Baye LM, Nachury MV, Wright KJ, Ervin KE, Phu L, Chalouni C, Beck JS, Kirkpatrick DS, Slusarski DC, Sheffield VC, Scheller RH, Jackson PK. 2011. Primary cilia membrane assembly is initiated by Rab11 and transport protein particle II (tRAPPII) complex-dependent trafficking of Rabin8 to the centrosome. *Proceedings of the National Academy of Sciences of the United States of America* **108**:2759–2764. doi: 10.1073/pnas.1018823108

Wiggin GR, Soloaga A, Foster JM, Murray-Tait V, Cohen P, Arthur JSC. 2002. MSK1 and MSK2 are required for the mitogen- and stress-induced phosphorylation of CREB and ATF1 in fibroblasts. *Molecular and Cellular Biology* **22**:2871–2881. doi: 10.1128/MCB.22.8.2871-2881.2002

Wilson GR, Sim JCH, McLean C, Giannandrea M, Galea CA, Riseley JR, Stephenson SEM, Fitzpatrick E, Haas SA, Pope K, Hogan KJ, Gregg RG, Bromhead CJ, Wargowski DS, Lawrence CH, James PA, Churchyard A, Gao Y, Phelan DG, Gillies G, Salce N, Stanford L, Marsh APL, Mignogna ML, Hayflick SJ, Leventer RJ, Delatycki MB, Mellick GD, Kalscheuer VM, D'Adamo P, Bahlo M, Amor DJ, Lockhart PJ. 2014. Mutations in RAB39B cause x-linked intellectual disability and early-onset parkinson disease with α-synuclein pathology. *The American Journal of Human Genetics* **95**:729–735. doi: 10.1016/j.ajhg.2014.10.015

Xiong Y, Yuan C, Chen R, Dawson TM, Dawson VL. 2012. ArfGAP1 is a GTPase activating protein for LRRK2: reciprocal regulation of ArfGAP1 by LRRK2. *Journal of Neuroscience* **32**:3877–3886. doi: 10.1523/JNEUROSCI.4566-11.2012

Yao C, Johnson WM, Gao Y, Wang W, Zhang J, Deak M, Alessi DR, Zhu X, Mieyal JJ, Roder H, Wilson-Delfosse AL, Chen SG. 2013. Kinase inhibitors arrest neurodegeneration in cell and c. elegans models of LRRK2 toxicity. *Human Molecular Genetics* **22**:328–344. doi: 10.1093/hmg/dds431

Yun HJ, Kim H, Ga I, Oh H, Ho DH, Kim J, Seo H, Son I, Seol W. 2015. An early endosome regulator, Rab5b, is an LRRK2 kinase substrate. *Journal of Biochemistry* **157**:485–495. doi: 10.1093/jb/mvv005

Yun HJ, Park J, Ho DH, Kim H, Kim C-H, Oh H, Ga I, Seo H, Chang S, Son I, Seol W. 2013. LRRK2 phosphorylates snapin and inhibits interaction of snapin with SNAP-25. *Experimental & Molecular Medicine* **45**:e36. doi: 10.1038/emm.2013.68

Zhang Q, Pan Y, Yan R, Zeng B, Wang H, Zhang X, Li W, Wei H, Liu Z. 2015. Commensal bacteria direct selective cargo sorting to promote symbiosis. *Nature Immunology* **16**:918–926. doi: 10.1038/ni.3233

Figure supplements

Phosphoproteomics reveals that Parkinson's disease kinase LRRK2 regulates a subset of Rab GTPases

Martin Steger et *al*
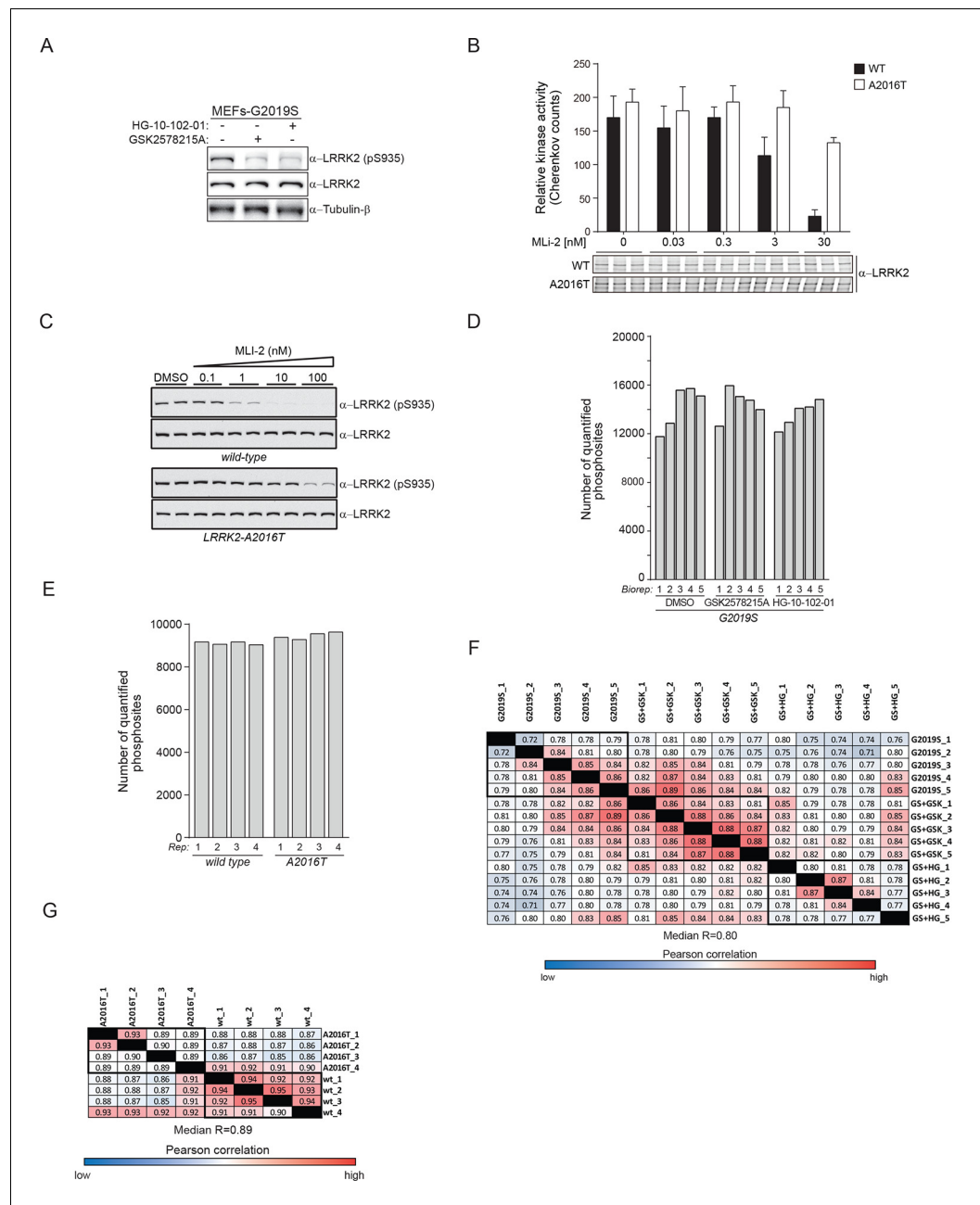
Figure 1—figure supplement 1. Two unbiased phosphoproteomic screens identify physiological LRRK2 targets. (A) Western blot analysis of wild type (wt) and LRRK2-G2019S[GSK] (G2019S) mouse embryonic fibroblasts (MEFs), treated with DMSO (-) or 1 μM of GSK2578215A or HG-10-102-01 for 90 min. (B) In vitro kinase assay using LRRK2 immunoprecipitated from MEFs (wt and A2016T) in the presence of various concentrations of MLi-2. Phosphorylation of Nictide was quantified by liquid scintillation counting. The western blot below shows that similar levels of LRRK2 were used. Error bars are mean ± SD (n=3). (C) Western blot analysis of pS935-LRRK2 and total LRRK2 levels in wt-LRRK2 MEFs and A2016T-LRRK2 MEFs treated for 60 min with the indicated concentrations of MLi-2. (D) Number of quantified class I phosphorylation sites of PS1 in five biological replicates (Biorep) per phenotype analyzed. (E) More than 9000 phosphorylation sites are identified in each of the four biological replicates (Biorep) of wild type and A2016T MEFs (PS2). (F) Pearson correlations for the phosphoproteomes of PS1 and PS2 (G). SD, standard deviation.
DOI: 10.7554/eLife.12813.004
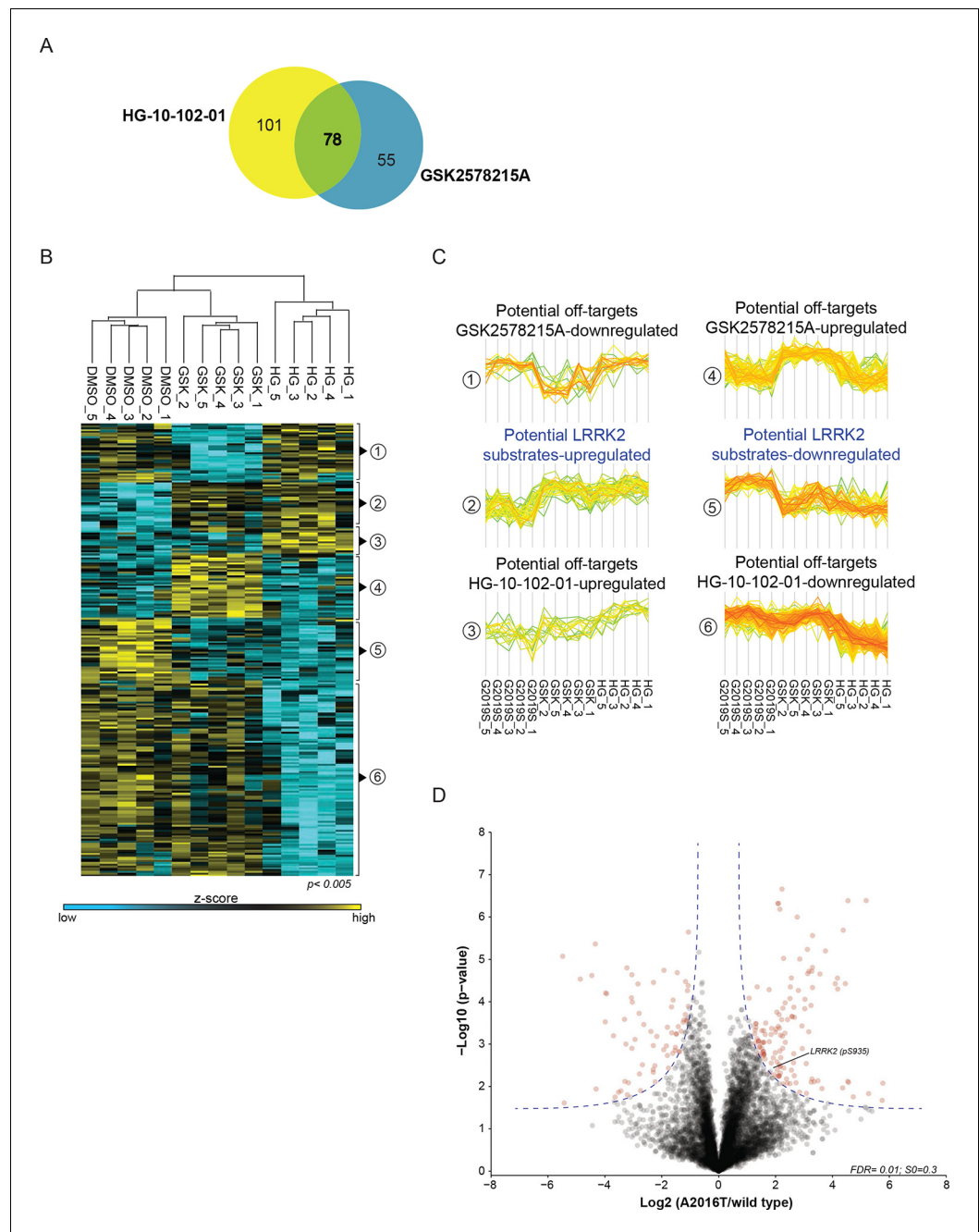
Figure 1—figure supplement 2. Two unbiased phosphoproteomic screens identify physiological LRRK2 targets. (**A**) Venn diagram of significantly regulated (ANOVA, p<0.005) sites with GSK2578215A and HG-10-102-01 in PS1. (**B**) Heat map of regulated phosphosites identified in five biological replicates of MEFs (LRRK2-G2019S^{GSK} (DMSO), LRRK2-G2019S^{GSK}+ GSK2578215A. and LRRK2-G2019S^{GSK} + HG-10-102-01). (**C**) Clusters identified in (**B**). (**D**) Volcano plot of all phosphosites of PS2. Significant sites are in blue and pS935 is indicated. ANOVA, analysis of variance.
DOI: 10.7554/eLife.12813.005
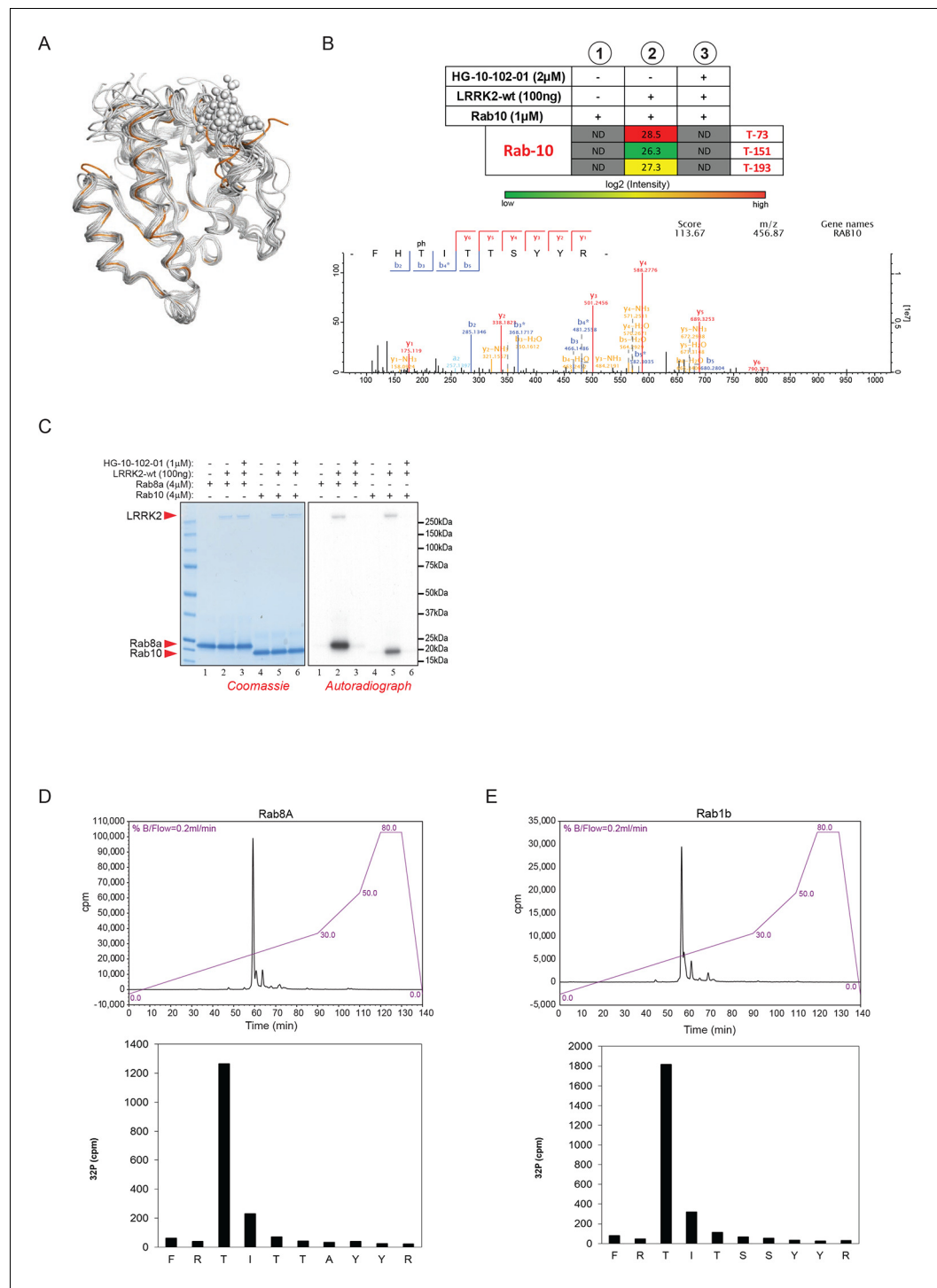
Figure 2—figure supplement 1. Phosphorylation of Rab GTPases by LRRK2 in vitro. (**A**) Superposition of the crystal structures of 14 Rab isoforms (Rab1a, 1b, 2, 3, 4, 6, 7, 9, 12, 18, 27, 30, 31, 43). All potential LRRK2 phosphorylation sites (in grey) cluster in the same region. (**B**) MS analysis of in vitro phosphorylated Rab10 identified three LRRK2-specific sites (note that phosphorylation is prevented completely by HG-10-102-01) and pT73 as the one with the highest intensity. The collosion-induced dissociation (CID) fragmentation spectrum and the Andromeda score (score) (**Cox et al., 2011**) for the tryptic pT73-Rab10 peptide are shown. (**C**) Phosphorylation of Rab8a and Rab1b by LRRK2-wt. Inhibition of LRRK2 by HG-10-102-01 prevents phosphorylation. (**D**) HPLC trace of tryptic peptides of Rab8a and Rab1b (**E**) after in vitro phosphorylation by LRRK2-wt and

Figure 2—figure supplement 1 continued on next page

Figure 2—figure supplement 1 continued

sequence analysis of tryptic peptides. Y axis units are relative Cherenkov counts per minute. MS, mass spectrometry; wt, wild type.
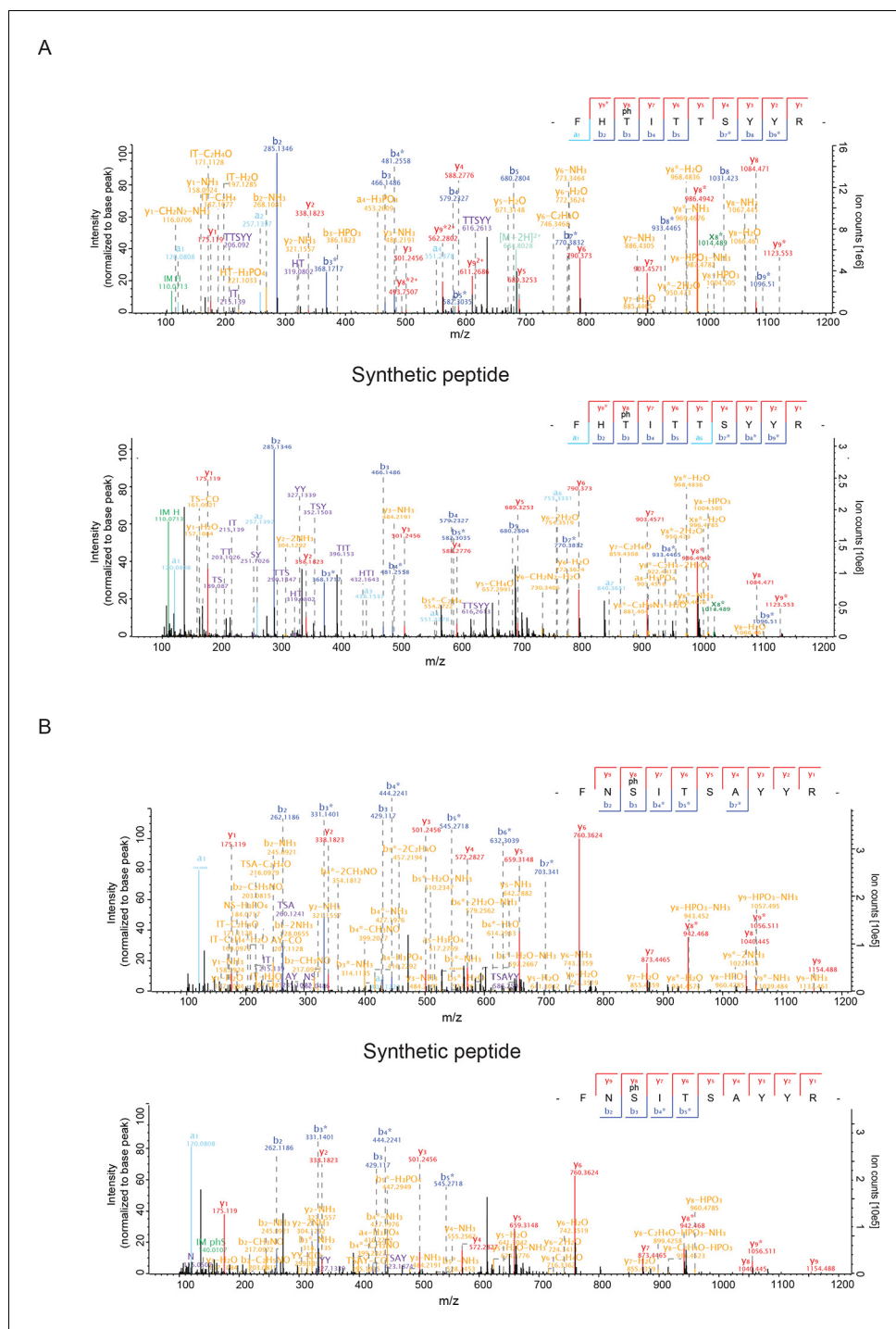
Figure 3—figure supplement 1. HCD MS/MS spectra of synthetic Rab peptides (**A**) Higher energy collision-induced dissociation (HCD) MS/MS spectra of the pT73-Rab10 peptide identified in PS2. The spectrum of the corresponding synthetic peptide is shown below. (**B**) Same as (**A**) but pS105-Rab12.
DOI: 10.7554/eLife.12813.009
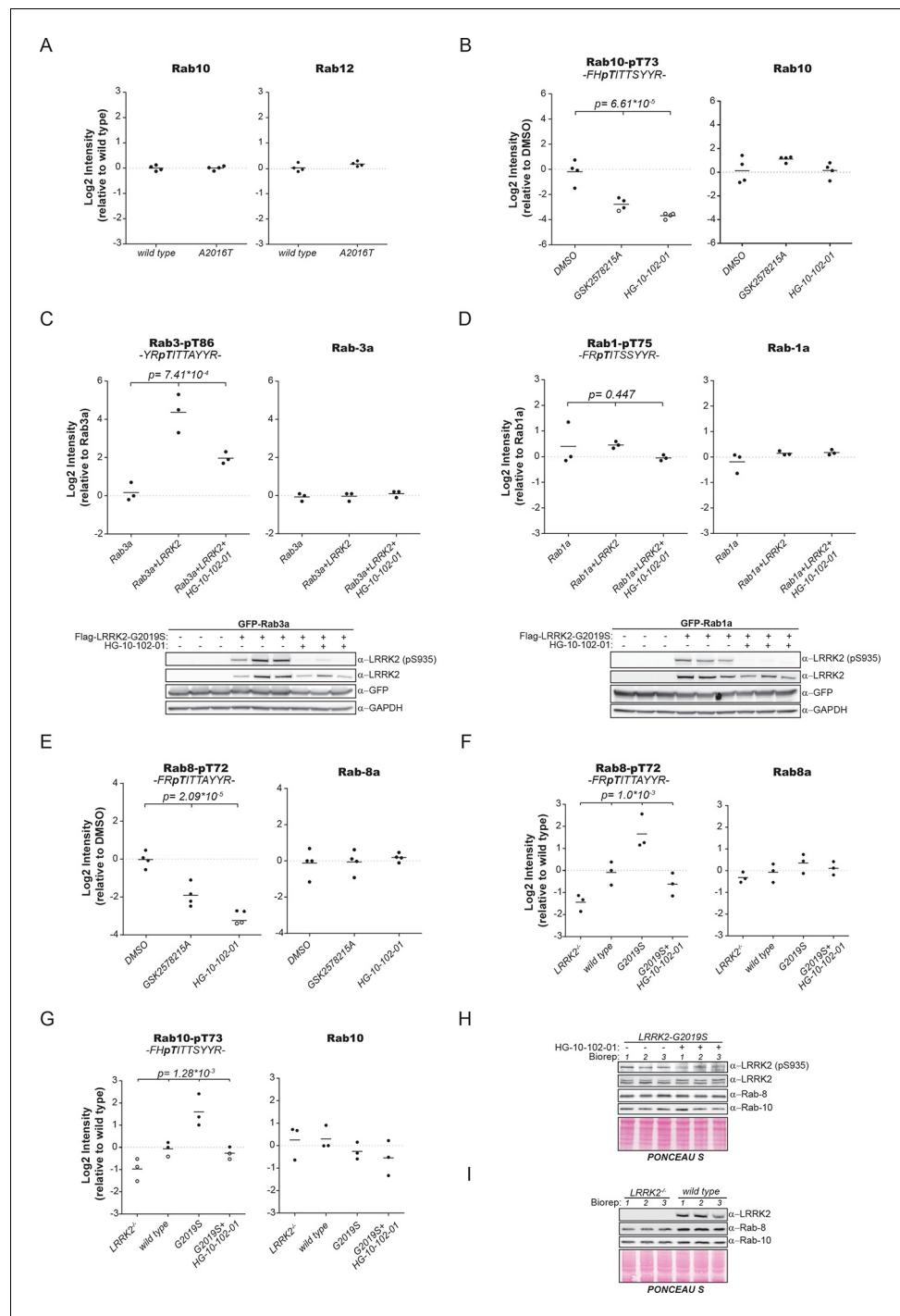
Figure 3—figure supplement 2. Quantification of Rab phosphorylation by mass spectrometry (MS). (**A**) MS-based label-free quantification (MaxLFQ, *Cox et al., 2014*) of the Rab10 and Rab12 protein intensities in PS2. (**B**) MS-based quantification of pT73-Rab10 (left) and total Rab10 (right) derived from HEK293 (trex flpIn) cells expressing GFP-LRRK2-G2019S after LRRK2 inhibition (n=4). (**C**) MS-quantified Rab3-pT86 peptide levels of ectopically expressed Rab3a alone or in combination with LRRK2-G2019S, in presence or absence of HG-10-102-01 (3 μM, 3 hr, n=3). A western blot of the same samples is shown below. (**D**) Same as (**C**) but Rab1a was expressed and pT75-Rab1a quantified. (**E**) Same as (**B**) with pT72-Rab8 (left) and total Rab8a (right). (**F**) Label-free quantification of pT73-Rab10 and (**G**) pT72-Rab8a from knockout, wt, G2019S, or G2019S treated with HG-10-102-01 (3 μM, 3 hr) MEFs. Total Rab10 and Rab8 protein levels were also quantified (n=3). (**H**) and (**I**) Western blot analyses of samples used in (**F**) and (**G**). Open circles indicate imputed values. MEFs, mouse embryonic fibroblasts; wt, wild type.

DOI: 10.7554/eLife.12813.010
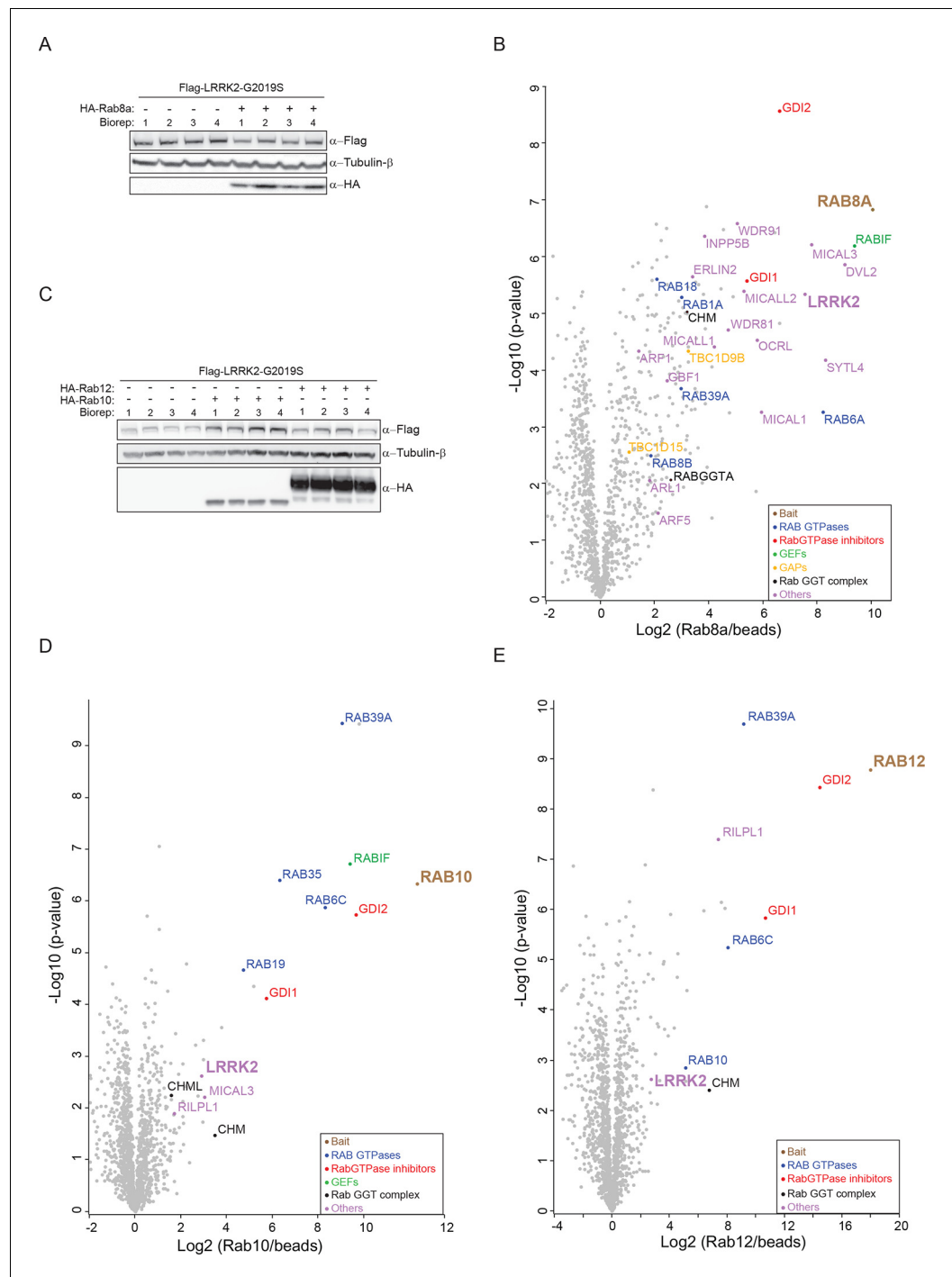
Figure 3—figure supplement 3. Several Rabs stably associate with LRRK2 in cells. (**A**) Western blot of HEK293 cells expressing flag-LRRK2-G2019S, either alone or in combination with HA-Rab8a. (**B**) Volcano plot of MS-quantified Rab8a interactors (n=4). (**C**) Same as (**A**) with HA-Rab10 or HA-Rab12. (**D**) and (**E**) Volcano plots of MS-quantified Rab10 and Rab12 interactors. MS, mass spectrometry.

DOI: 10.7554/eLife.12813.011
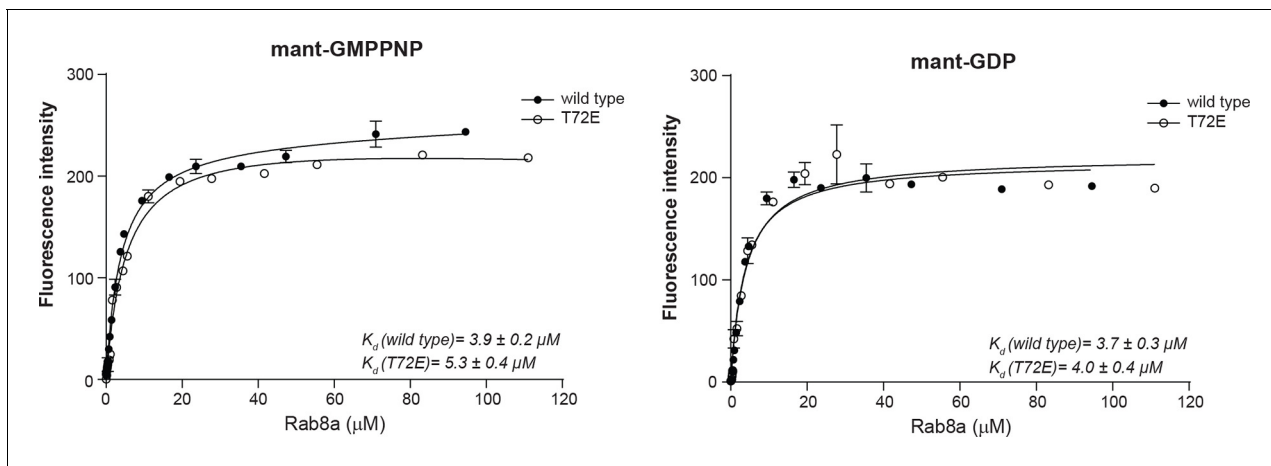
Figure 5—figure supplement 1. Rab8a nucleotide binding experiments. Titration experiment using Rab8a (wt and T72E) and fluorescently labeled non-hydrolysable GTP analog (mant-GMPPNP) or GDP (mant-GDP). The fluorescence signal is plotted as a function of Rab8a concentration. The dissociation constants (K_d) ± SD are indicated. Error bars are mean ± SD (n=3). SD, standard deviation; wt, wild type.
DOI: 10.7554/eLife.12813.014
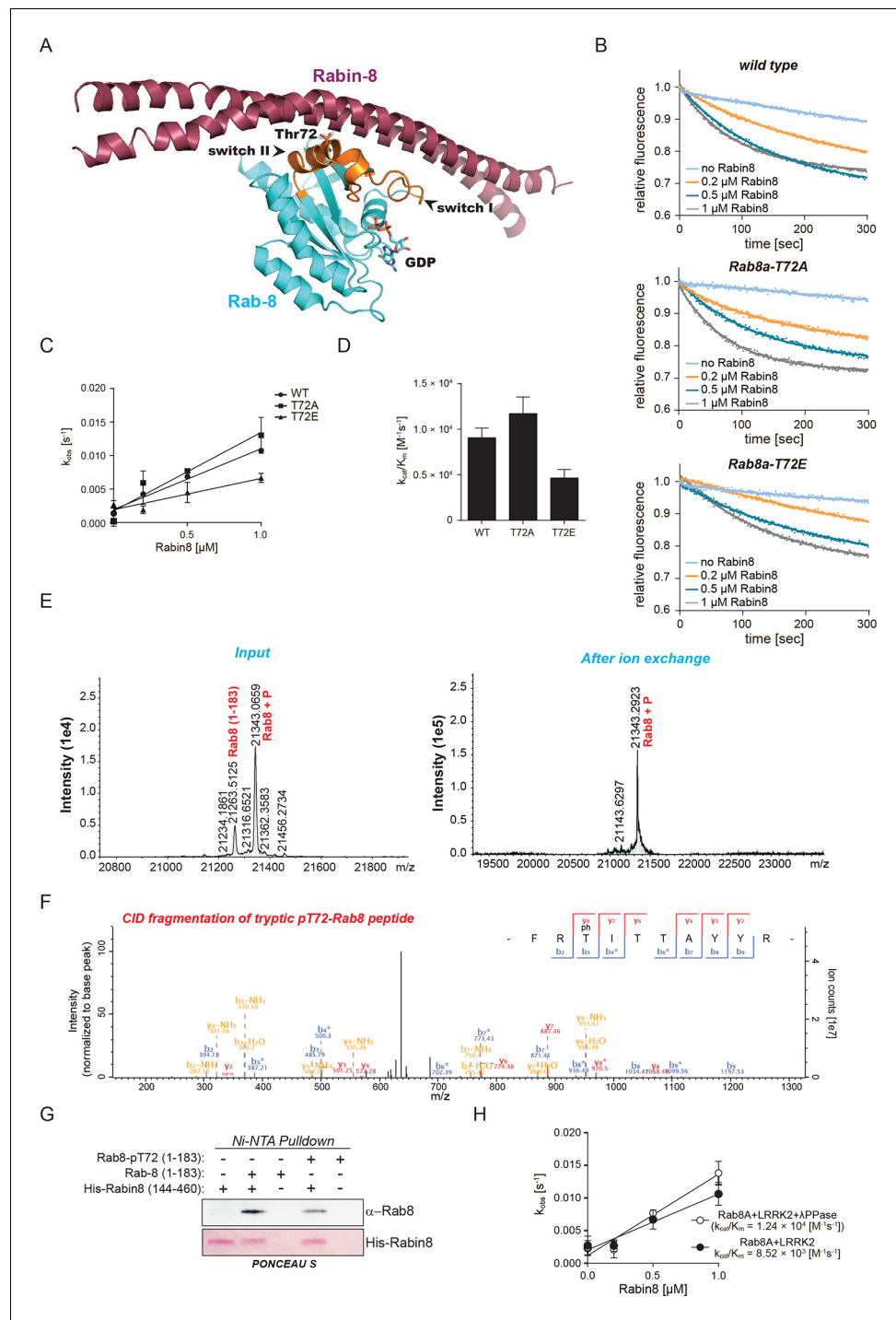
Figure 5—figure supplement 2. Rab8a guanine nucleotide exchange assays. (**A**) Ribbon structure of Rab8a in complex with Rabin8 (PDB: 4LHY). The LRRK2 phosphorylation site (T72) situated in the switch II region and forming close contact with Rabin8 is indicated. (**B**) Kinetics of mant-GDP dissociation from Rab8a (wt, T72A, and T72E) by Rabin8. (**C**) and (**D**) Representation of the observed rate constants (k_{obs}) and catalytic efficiencies (k_{cat}/K_m) for the same reactions. (**E**) ESI-TOF mass determination of Rab8a after in vitro phosphorylation by LRRK2-G2019S (left) and after enrichment of phosphorylated Rab8a by ion-exchange chromatography (right). (**F**) Collision-induced dissociation (CID) fragmentation spectrum of the tryptic pT72-Rab8a peptide, which was identified after phosphorylation of Rab8a by LRRK2 followed by enrichment of the phosphorylated form by ion exchange chromatography. (**G**) Ni^{2+}-NTA pull-down of Rab8a (non-phosphorylated or phosphorylated on T72) by HIS-

Figure 5—figure supplement 2 continued on next page

Figure 5—figure supplement 2 continued

tagged Rabin8 using purified components. (**H**) Representation of the observed rate constants (k_{obs}) and catalytic efficiencies (k_{cat}/K_m) for the indicated reactions. Error bars are mean ± SD (n=3).
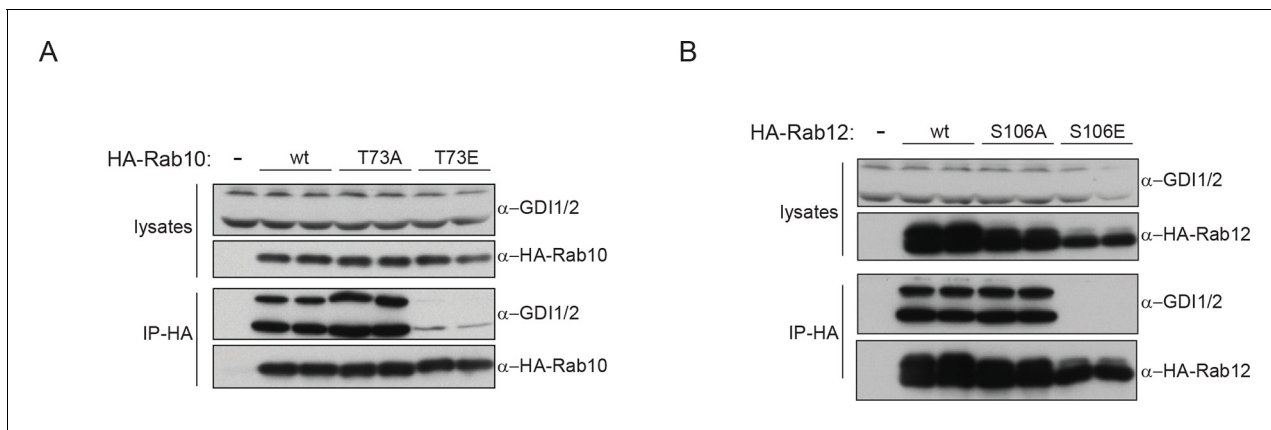
Figure 6—figure supplement 1. Rab10/12-GDI interactions. (**A**) HA-Rab10 constructs (wt, T73A, T73E) were expressed in HEK293 cells and lysates subjected to α-HA immunoprecipitation before western blotting. (**B**) Same as (**A**) using HA-Rab12 (wt, S106A, S106E). wt, wild type.

DOI: 10.7554/eLife.12813.017

3 Discussion

Small GTPases are versatile temporal and spatial regulators of cellular processes including signal transduction, cytoskeleton dynamics and membrane trafficking. They act as molecular switches, aided by a multitude of regulatory and effector proteins that link them into functional networks. Members of Rab and Arf subfamilies regulate multiple stages of membrane traffic including transport of membrane proteins from the Golgi to the cilium. At least three macromolecular complexes have been implicated in ciliary targeting, which are controlled by small GTPases: IFT complex, the BBSome and the Arf4-based ciliary targeting complex. Ciliary targeting complexes, which assemble at the TGN, are the major focus of this thesis. Gained structural und biochemical insights are presented in the result section (subchapter 2.1) and comprise crystal structures of human Rab11–Rabin8 and Rab11–FIP3–Rabin8 complexes. The latter complex structure revealed simultaneous binding of FIP3 and Rabin8 effectors to Rab11. The following subchapters discuss structural and functional aspects of the Rab11–Rabin8 and the Rab11-FIP3-Rabin8 dual effector complexes in greater detail and shed light on their role in ciliary targeting of membrane proteins. Dysfunction of this transport process causes cilia defects underlying human disorders known as ciliopathies. Major parts of the discussion have been published in the journal *Small GTPases* as a review: Vetter, M., Wang,J., Lorentzen, E., & Deretic, D. (2015) 'Novel topography of the Rab11-effector interaction network within a ciliary membrane targeting complex'. In addition, to ensure controlled intracellular membrane trafficking and effector binding in a spatial and temporal manner, regulation of small GTPases by GEFs and GAPs is required. Thus, the last section focuses on activation of Rab11 by GEF(s) to illustrate the important roles of GEFs and GAPs as critical elements in the control of small GTPases.

3.1   The Rab11-FIP3- Rabin8 dual effector complex

Whereas Rabin8 functions as a Rab11 effector at the final stages of ciliary trafficking, FIP3 interacts with Rab11a early in the ciliary pathway (Mazelova *et al.*, 2009a). FIP3 also functions as a Rab11 effector in cytokinesis (Fielding *et al.*, 2005; Wilson *et al.*, 2005; Eathiraj *et al.*, 2006; Schiel *et al.*, 2012) and in the maintenance of the recycling compartment (Horgan *et al.*, 2007; Inoue *et al.*, 2008). The function of FIP3 as a Rab11 effector within the ciliary targeting complex was less clear until now. Given the known sequential interactions within the ciliary targeting complex, the model for its assembly suggested an initial recruitment of FIP3 that is subsequently replaced by Rabin8 to activate Rab8 and facilitate fusion of transport carriers with the plasma membrane (Deretic, 2013; Wang and Deretic, 2013). In this context, by serving as a Rab11 effector upstream of the conserved ciliogenesis cascade, FIP3 could provide a safety valve to block the premature assembly of the Rab11-Rabin8-Rab8 complex. However, recent structural and functional studies including results presented in this thesis (subchapter 2.1) reveal that this is not the case because the two Rab11a effectors cooperate in carrying out Rab11a-related functions (Wang and Deretic, 2015; Vetter *et al.*, 2015a). The first surprise came from the study showing that FIP3 shapes the Rabin8 binding site within the ciliary targeting complex by significantly increasing Rabin8 interactions with both Rab11a and ASAP1 (Wang and Deretic, 2015). Furthermore, FIP3 and Rab11a bind Rabin8 separately, indicating that the two Rab11 effectors directly interact (Wang and Deretic, 2015). In a concurrent study (presented in subchapter 2.1), the crystal structure of the Rab11-GMPPNP-FIP3-Rabin8 complex revealed simultaneous binding of FIP3 and Rabin8 effectors to activated Rab11 (Vetter *et al.*, 2015a). Direct interaction between Rabin8 and FIP3 effectors within the dual effector bound complex likely functions to stabilize the transient complexes and create a high avidity hub for cross talk of Arf and Rab GTPases in ciliary trafficking (Fig. 11).
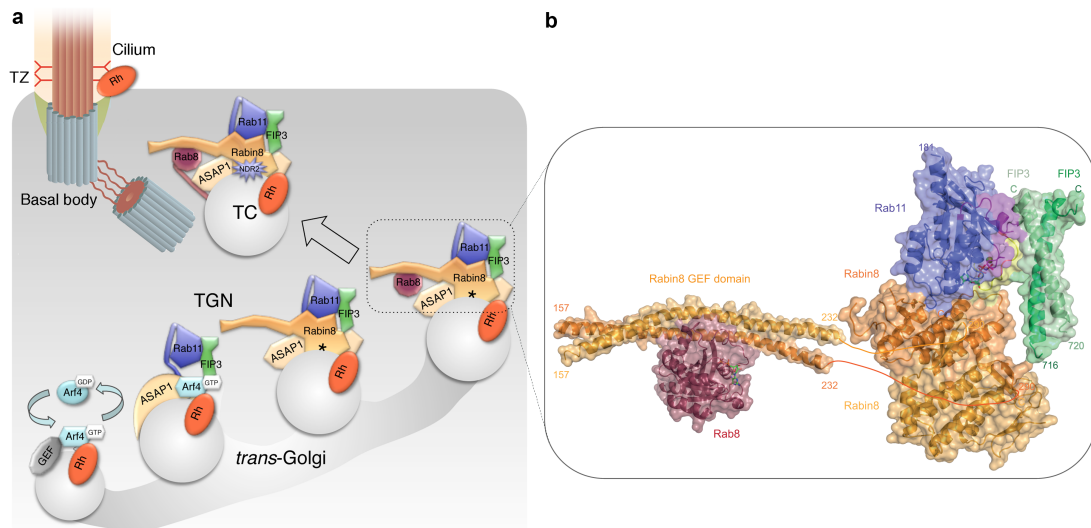
Figure 11: Golgi to cilia transport via ciliary targeting complexes. a) Schematic representation of ciliary membrane trafficking in the photoreceptor cell via ciliary targeting complexes. Rh, rhodopsin, a ciliary sensory receptor. TC, transport carriers. At the TGN, the Arf GAP ASAP1 serves as a platform for the stepwise assembly of the Rab11-FIP3-Rabin8 complex. Although the majority of the components that constitute the complex act as dimers, multiple complexes are omitted form the scheme for clarity. Asterisks indicate the potential site where the Rabin8$^{250-290}$ linker region could approach the membrane to recognize phosphatidylserine (PS). By phosphorylating S272 within this region, NDR2 switches the specificity of Rabin8 binding from PS to Sec15, in preparation for TC fusion with the periciliary plasma membrane. (b) Crystal structure of the human Rab11-FIP3$_{RBD}$-Rabin8C complex (PDB code: 4UJ3) (Vetter et al., 2015a) and Rabin8 GEF domain in complex with Rab8 (PDB code: 4LHY) (Guo et al., 2013) are shown in a cartoon representation with a semi-transparent surface. Switch regions are indicated. GMPPNP, GDP and Mg^{2+} ions are shown as balls-and-sticks (Figure and description from (Vetter et al., 2015b).

3.2   Simultaneous binding of FIP3 and Rabin8 effectors to active Rab11

A hallmark of small GTPases is the nucleotide dependent conformational change of the switch regions that allows effectors to discriminate between the active GTP-bound and the inactive GDP-bound states (Vetter and Wittinghofer, 2001). Small GTPases often have multiple effectors, but because of the limited accessible surface area shaped by the switch regions at the G-site, the binding of different effectors is thought to be sequential and mutually exclusive. Numerous effectors have been described for Rab11 including FIPs, Rabin8, Sec15 and Rab11BP/WDR44 (Zeng *et al.*, 1999; Junutula *et al.*, 2004; Zhang *et al.*, 2004; Wu *et al.*, 2005; Knödler *et al.*,

2010). Two of these effectors, FIP3 and Rabin8, have been implicated in ciliogenesis and in the trafficking of membrane proteins from the TGN to the cilium (Knödler *et al.*, 2010; Wang *et al.*, 2012; Wang and Deretic, 2015). However, recent new data demonstrate that FIP3 and Rabin8 can associate with Rab11 at the same time (subchapter 2.1) (Wang and Deretic, 2015; Vetter *et al.*, 2015a). Pull-down experiments, size exclusion chromatography (SEC) and isothermal titration calorimetry (ITC) experiments revealed that the C-terminal Rab11-effector domain of Rabin8 (Rabin8C) binds a preformed Rab11-FIP3 complex to form a ternary Rab11*GMPPNP-FIP3-Rabin8C complex (Wang and Deretic, 2015; Vetter *et al.*, 2015a). Interestingly, Rabin8C has ~4-fold higher affinity for Rab11-FIP3 than for Rab11 alone, suggesting that FIP3 and Rabin8 either interact directly, or that the binding of FIP3 to Rab11 induces a conformational change in Rab11 that strengthens the Rabin8 association. Pull-down experiments suggested that the former possibility is most likely correct, as a direct interaction between FIP3 and Rabin8 was observed (Wang and Deretic, 2015; Vetter *et al.*, 2015a). Moreover, the regions of Rab11 that interact with Rabin8 do not undergo conformational changes upon FIP3 effector binding (Eathiraj *et al.*, 2005; 2006; Shiba *et al.*, 2006). These results are in agreement with a model where FIP3 and Rabin8 effectors simultaneously associate with Rab11 (Fig. 11).

3.3   Rabin8 C-terminal domain is a novel low-affinity Rab effector

The fact that FIP3 and Rabin8 are able to bind Rab11 at the same time raises the question of how this is achieved structurally. Previously published crystal structures of Rab11 bound to FIP2 or FIP3 revealed a canonical effector-binding site with extensive contacts with switch I and II regions, which leave little space for simultaneous Rabin8 binding at the G-site (Fig. 16) (Eathiraj *et al.*, 2006; Jagoe *et al.*, 2006; Shiba *et al.*, 2006). However, although Rabin8 as an effector does have a preference for GTP- vs. GDP-bound Rab11, the K_D of 40µM demonstrates weak affinity that could be the result of a relatively small Rabin8-binding-surface on Rab11*GTP (Vetter *et al.*, 2015a). Indeed, the crystal structure of the Rab11-Rabin8 complex revealed a relatively small (~600Å2) binding interface utilizing mostly non-switch region residues (Fig. 12). The C-terminal domain of Rabin8 adopts a novel fold that interacts with Rab11 via a non-canonical effector-binding site through contacts with two residues of switch I (L38 and E39), four residues of a non-switch-region loop connecting β5 and α4 of Rab11 (L128, R129, H130 and L131), and no contacts with switch II. Additionally, several main-chain hydrogen bonds are

facilitated by beta strand β2 of Rabin8 and residues 129-134 of Rab11 (Fig. 12). The Rabin8 binding-site on Rab11 is thus neighboring the canonical effector-binding site suggesting how dual effector binding to Rab11 may be achieved. The Rab11*GMPPNP-FIP3-Rabin8 crystal structure revealed how the two FIP3/Rabin8 effectors bind Rab11 at neighboring sites closely approaching and interacting with each other (Fig. 11b) (Vetter *et al.*, 2015a). FIP3 binds GTP-bound Rab11 with a K_D of ~0.3μM (Eathiraj *et al.*, 2006), which is 2 orders of magnitude higher than the affinity of Rabin8 for Rab11 (Vetter *et al.*, 2015a). It is thus conceivable that Rab11 first binds FIP3 to form a Rab11-FIP3 complex that subsequently recruits Rabin8 to form the Rab11-FIP3-Rabin8 complex. This notion is supported by the fact that Rab11-FIP3 has 4-5 fold higher affinity for Rabin8 than Rab11 (Wang and Deretic, 2015; Vetter *et al.*, 2015a). In this respect, part of the preference of Rabin8 for GTP-bound Rab11 is indirectly assured via binding of the canonical FIP3 effector. The Rabin8 C-terminal domain thus represents an unusual Rab11 effector that binds at an unconventional effector-binding site with low affinity.
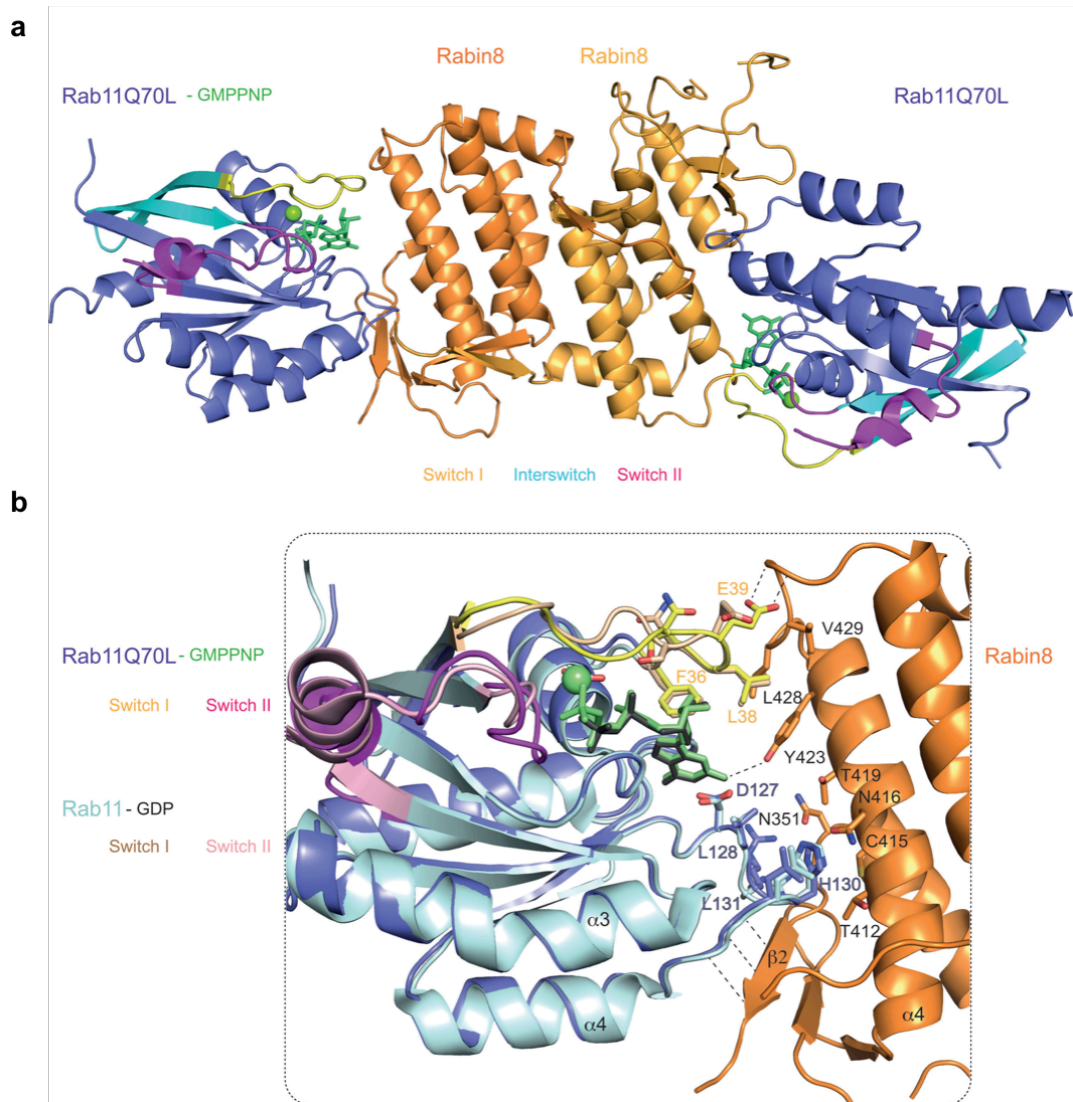
Figure 12: Structural overlay of Rab11-GMPPNP-Rabin8C with Rab11-GDP. *a)
Crystal structure of the heterotetrameric Rab11-GMPPNP-Rabin8C complex (PDB
code: 4UJ5) (Vetter et al., 2015a) shown as a cartoon representation, switch regions
are indicated as in Fig. 11. (b) Superimposition of the Rab11-GMPPNP-Rabin8
complex structure onto the Rab11-GDP structure (PDB code: 1OIV) (Pasqualato et
al., 2004). Interacting residues are shown as sticks and labeled according to residue
number. Backbone interactions between the γ-carboxyl group of E39 of Rab11 and
residues 430–431 of Rabin8, the hydroxyl of Y423 with the guanine base of
GMPPNP of Rab11 and hydrogen bonds between β2 of Rabin8C and the loop β5-α4
of Rab11 are indicated with dashed lines. (Figure and description from (Vetter et al.,
2015b).*

3.4 Rabin8C and PI4KIIIβ utilize the same binding surface on Rab11

Comparison of the Rab11*GMPPNP-Rabin8 structure to previously determined structure of Rab11 complexes revealed that Rabin8 binds Rab11 at a similar site to that of the phosphatidylinositol 4-kinase IIIβ (PI4KIIIβ) (Burke *et al.*, 2014; Vetter *et al.*, 2015a) (Fig 13). PI4KIIIβ catalyzes the phosphorylation of phosphatidylinositol to generate phosphatidylinositol4-phosphate (PI4P), a reaction important for the formation and function of the Golgi where PI4KIIIβ is localized and where it interacts with Rab11 (de Graaf *et al.*, 2004). Despite different folds of PI4KIIIβ and Rabin8, both proteins contact a similar set of Rab11 residues including L38, E39, L128, H130 and L131 (Fig. 13). Interestingly, PI4KIIIβ was reported not to be an effector for Rab11 as the binding affinity for Rab11*GTP was only 3-4 fold higher than for Rab11*GDP in agreement with the fact that most contacts are with non-switch-region residues (Burke *et al.*, 2014). This relatively small but significant preference of PI4KIIIβ for GTP- vs. GDP-bound forms of Rab11 is likely a result of contacts with L38 and E39 of switch I. Given the fact that Rabin8 and PI4KIIIβ bind to similar sites on Rab11 with contacts to L38 and E39 of switch 1 an interesting question is to which degree Rabin8 prefers GTP- vs. GDP-bound Rab11.
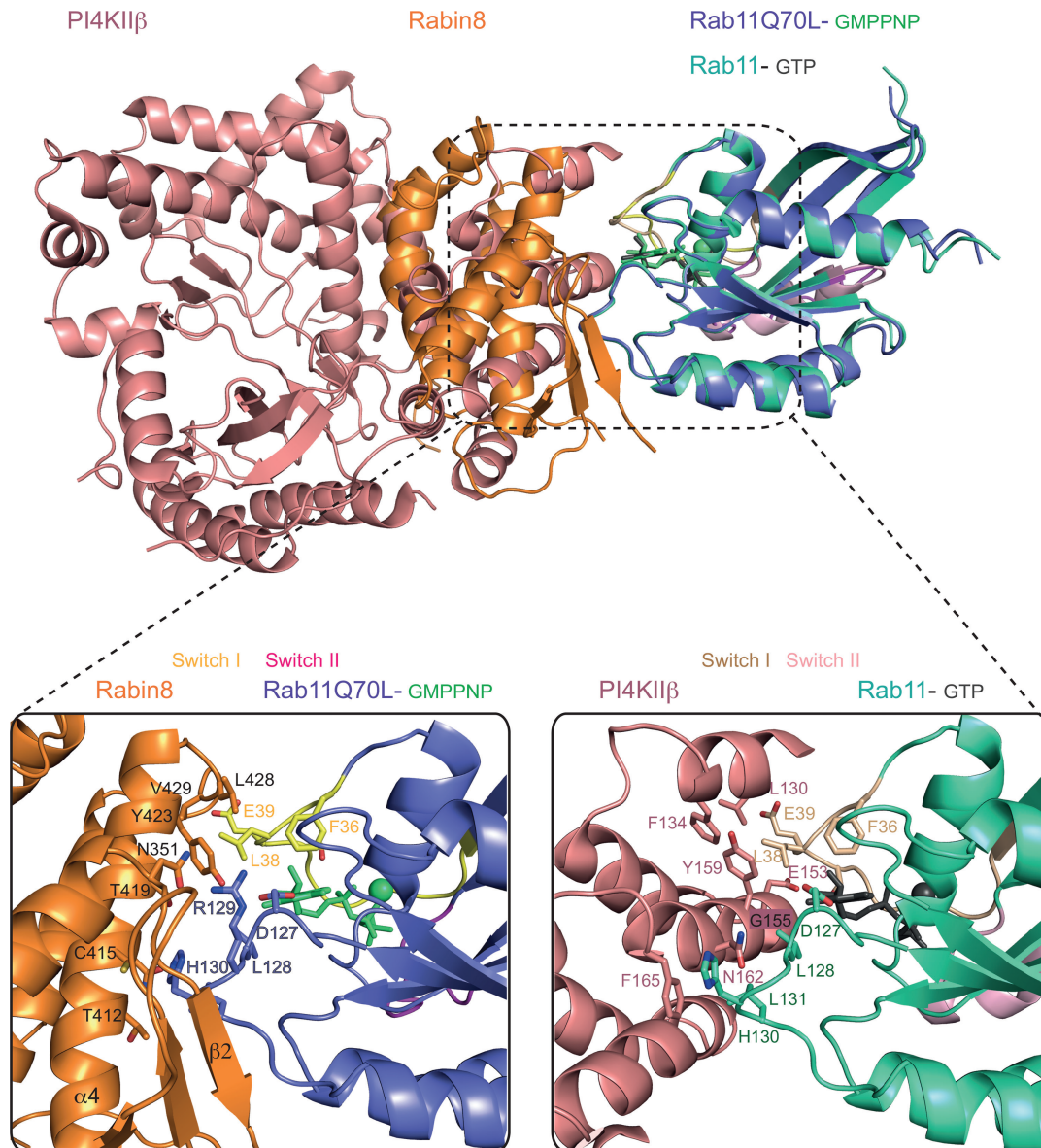
***Figure 13: Comparison of the Rab11-Rabin8C and the Rab11-PI4KIIIb interface.**
Structural overlay of Rab11-GMPPNP-Rabin8C and Rab11-GTP-PI4KIIIb (PDB
code: 4D0L) (Burke et al., 2014). Rab11 molecules superimpose well and use the
same interface to bind the structurally different Rabin8 and PI4KIIIb molecules. The
boxed-in region represents a zoom-in on the interaction interfaces between Rab11
and Rabin8 (left) and Rab11 and PI4KIIIb (right). Switch regions are indicated,
GMPPNP, GTP and Mg2+ are shown as balls-and-sticks. Interacting residues are
shown as sticks and labeled according to residue number. (Figure and description
from (Vetter et al., 2015b).*

3.5 Specificity of Rabin8 for GTP-bound vs. GDP-bound Rab11

Rabin8 was reported to be an effector of Rab11 as it recognizes the GTP-bound
and not the GDP-bound state of the small GTPase in pull-down experiments (Knödler

et al., 2010; Vetter *et al.*, 2015a). A K_D value for the Rab11*GDP-Rabin8 complex has not been published but is, based on pull-down experiments, clearly much higher than the K_D of 40µM measured for the Rab11*GMPNP-Rabin8 complex (Vetter *et al.*, 2015a). Although it is hard to measure the low affinity of Rabin8 for Rab11*GDP accurately, ITC experiments suggest a Kd for the Rab11*GDP- Rabin8 complex in the 200-400µM range (M. Vetter and E. Lorentzen, unpublished data). This indicates that the affinity of Rabin8 for Rab11*GTP is 5-10 fold higher than for Rab11*GDP. The specificity of effectors for the GTP-bound state of small GTPases arises from the unique conformation adopted by the switch regions when bound to GTP, which shape the binding surface to engage different effectors in a specific manner. Although the GDP-bound state often results in disordered switch regions (Lee *et al.*, 2009), some small GTPases adopt well-ordered but different conformations of the switch regions depending on nucleotide state. One such case is Arl6 where only the GTP-bound conformation can recruit the BBSome to membranes via the BBS1 effector protein because the GDP-bound conformation prevents BBS1-binding due to molecular clashes (Jin *et al.*, 2010; Mourão *et al.*, 2014). Importantly, the switch regions are also ordered in crystal structures of both GDP- and GTP-bound Rab11 (Pasqualato *et al.*, 2004; Eathiraj *et al.*, 2005). The conformational differences in switch regions between different nucleotide states of Rab11 are relatively modest with a root-mean-square-deviation (rmsd) between cα-atoms of maximum 5Å (Fig 12). Given the fact that Rabin8 does not contact switch 2 of Rab11, the preference for GTP-bound Rab11 is likely attributed to the contacts with L38/E39 of switch 1 (Fig. 12). By comparing the conformation of L38/E39 between GDP- and GTP-bound Rab11, it is striking that only the side-chain of E39 but not the side-chain of L38 displays a nucleotide dependent conformational change (Fig. 12). In the GTP-bound form of Rab11, the side-chain of E39 points towards residues 430-431 of Rabin8 and makes two hydrogen bonds of 3Å in length with backbone NH groups. In the GDP-bound form of Rab11, E39 adopts a different rotameric conformation that points away from Rabin8 and would increase the hydrogen bonding distances to 5-6Å (Fig 12). Notably, the Rabin8-binding competent conformation of E39 is not induced by Rabin8-binding as it adopts the same rotamer in Rab11*GTP not bound to any effectors (Eathiraj *et al.*, 2005). It appears likely that E39 of Rab11 is important for the nucleotide dependent association with Rabin8.

3.6 Rabin8 effector binding is specific for Rab11

Yeast-2-hybrid analysis of Rabin8 binding to a host of different Rab proteins revealed a strong specificity for Rab11 (Westlake *et al.*, 2011). To address the molecular basis of this specificity we superimposed the structure of Rab11-Rabin8 with known structures of different Rab family members in the GTP-bound state (Fig. 14a). The result reveals that there are no major clashes between Rabin8 and other members of the Rab superfamily such as Rab4, Rab6, Rab8, Rab14 or Rab25 suggesting that complex formation with Rabin8 is in principle possible (Fig. 14a). However, the residues utilized by Rab11 to bind Rabin8 are not well conserved in other Rab families (Fig. 14b). In particular the Rabin8-interacting switch 1 residues of Rab11 (L398 and E39) are poorly conserved (Fig. 14b). E39 is often replaced by an aspartic acid that is not well positioned to make tight hydrogen bonds with residues 430-431 of Rabin8. L38 of Rab11 engages in hydrophobic contacts with residues from Rabin8 but is replaced by a hydrophilic residue in most other Rabs. Additionally, sequence alignment of different Rabs demonstrates that the Rabin8/PI4KIIIβ binding residues are only conserved in Rab11 orthologous and not in Rabs from different families, which suggests that the Rabin8/PI4KIIIβ binding site is unique to Rab11. Interestingly, the Rabin8-binding residues of Rab11 are well conserved in Ypt32, which is the yeast homolog of Rab11 (Fig. 14c). This indicates that the molecular mechanism of Sec2 (yeast homolog of Rabin8)-recruitment by Ypt32 to activate Sec4 (yeast homolog of Rab8) is evolutionarily conserved. Surprisingly, the Rabin8 binding residues of Rab11 are also conserved in organisms like *Chlamydomonas reinhardtii* and *Arabidopsis thaliana* that do not appear to have a Rabin8 homolog. The genomes of *Chlamydomonas reinhardtii* and *Arabidopsis thaliana* do however encode putative PI4KIIIβ homologs with the Rab11-binding helical domain conserved. Given that Rab11 utilized the same residues for Rabin8 and PI4KIIIβ binding it appears likely that the binding site in *Chlamydomonas reinhardtii* and *Arabidopsis thaliana* Rab11 is conserved to bind PI4KIIIβ. Collectively, Y2H and bioinformatics analyses suggest that Rabin8 binding is specific to Rab11 and that the recruitment of Rabin8 by Rab11 to activate Rab8 is an evolutionarily ancient pathway in exocytosis.
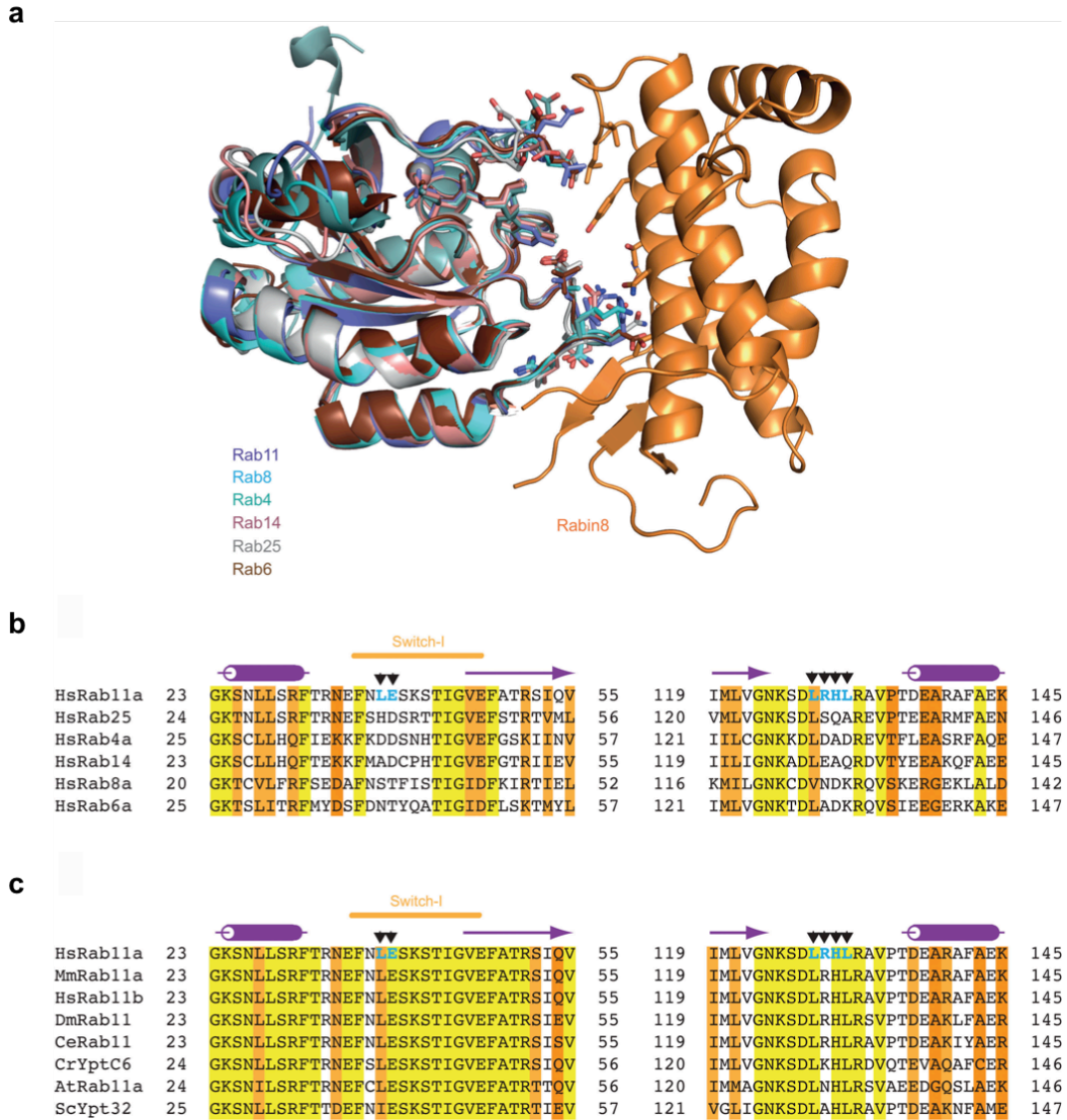
Figure 14: The Rabin8-binding interface is unique to Rab11. *a) Structural overlay of different active Rab GTPases onto the Rab11-GMPPNP-Rabin8 crystal structure shown as a cartoon representation. Rab4 (PDB code: 1YU9), Rab6 (PDB code: 1YZQ), Rab8 (PDB code: 4LHW), Rab14 (PDB code: 4D0G) and Rab25 (PDB code: 3TSO) are cartooned in different colors. Residues utilized by Rab11 to bind Rabin8 and the corresponding residues in different Rab GTPases are shown as sticks. b) Sequence alignment of Rabin8-interacting regions in human Rab11a with other human Rab GTPases. Rab11a residues that interact with Rabin8 are indicated with black arrows and labeled in bold blue color. Highly conserved residues are highlighted in yellow, similar residues in lighter and darker orange, respectively. Secondary structure derived from human Rab11a is indicated above the sequence. c) Multiple sequence alignment of Rab11a protein from different species. Rab11a residues that interact with Rabin8 are indicated as shown in Fig 14b. Secondary structure elements from Rab11a structure are indicated above the sequence. Hs: Homo sapiens, Mm: Mus musculus, Dm: Drosophila melanogaster, Ce: Caenorhabditis elegans, Cr: Chlamydomonas reinhardtii, At: Arabidopsis thaliana, Sc: Saccharomyces cerevisiae. (Figure and description from (Vetter et al., 2015b)*

3.7   Regulation of Rabin8

Rabin8 is recruited to the membrane by Rab11a and interacts with specific phospholipids such as phosphatidylserine (PS, strong interaction) and phosphatidic acid (PA, weak interaction) (Chiba *et al.*, 2013). The amino acids 251–460 were suggested to encompass a minimum PS-binding domain of Rabin8 based on binding experiments with truncated protein constructs (Chiba *et al.*, 2013). PS recognition is typically mediated by Ca^{2+}-dependent C2 domains or by basic stretches of residues (Caberoy *et al.*, 2009). Given that the structure of the C-terminal Rabin8 domain (residues 290-460) does not display a PS-binding domain, residues 250-290 likely encompass the PS-binding region. Rabin8 250-290 is a part of the linker region (predicted to be disordered) that connects the central GEF domain to the C-terminal Rab11-effector domain (Fig. 15). The flexible nature of Rabin8 250-290 probably allows this region to approach the membrane to recognize PS. Examination of the Rabin8 250-290 sequence reveals a basic stretch of residues rich in lysines (260-KTPFKKGHTNKS-272, human Rabin8 numbering) that could serve as the PS-recognition motif (Fig. 15).

Remarkably, NDR2-mediated phosphorylation of Rabin8 regulates the switch in binding specificity of Rabin8 from PS to the Sec15 component of the exocyst complex that mediates carrier tethering at the periciliary plasma membrane (Mazelova *et al.*, 2009b; Feng *et al.*, 2012; Chiba *et al.*, 2013). NDR2 (also known as STK38L) was identified as a canine retinal degeneration gene corresponding to human ciliopathy Leber congenital amaurosis (LCA) characterized by early-onset blindness (Goldstein *et al.*, 2010; Berta *et al.*, 2011), indicating that the switch in binding partners of Rabin8 has a crucial role in ciliary membrane trafficking. The site of NDR2 phosphorylation, S272, lies close to the polybasic stretch of residues within the structurally disordered region of Rabin8 (Fig. 15), suggesting that NDR2 phosphorylation directly regulates PS-binding through the introduction of negative charges. Both S272 and the polybasic residues are well conserved in Rabin8 proteins from different organisms (but not in the Sec2 yeast homolog that instead of PS binds PI4P via its C-terminal residues 258-450 (Mizuno-Yamasaki *et al.*, 2010) suggesting an evolutionary conserved mechanism of regulation in higher eukaryotes (Fig. 15). Ypt32 and Sec15 compete for binding to Sec2 and phosphorylation of Sec2 within the linker region directs a switch in binding from Ypt32 to Sec15 (Mizuno-Yamasaki *et al.*, 2010; Stalder *et al.*, 2013). This mode of action is not conserved, as Sec15 is a common effector for Rab11 and Rab8 (Zhang *et al.*, 2004; Wu *et al.*,

2005), which differs from Ypt32 that does not associate with the exocyst complex. Interestingly, phosphorylation of both Rabin8 and Sec2 acts as a switch in binding to Sec15, but, unlike in yeast, in higher eukaryotes Sec15, Rab11a and Rabin8 diversify to cooperate in ciliary membrane trafficking.


```
                                              *   **   * *▼
HsRabin8  250  SPTQEPLPGGKTPFKKGHTRNKSTSSAMSGSHQDLSVIQPI  290
BtRabin8  250  SPTQEPLPGGKAHFKKGHTRNKSTSSAMSGSHQDLSVIQPI  290
MmRabin8  250  SPTQEPLAAAKTPFKRGHTRNKSTSSAMGGSHQDLSVIQPI  290
MvRabin8  258  SPTKEFQSGGKTPFKKGHARNKSTSSAMGGSHQDLTMMQPI  298
XtRabin8  247  SPTKELQPAGKAPFRKGHVRNKSTSSAMGGGTLDLSVLPPI  287
DrRabin8  215  SPCKEMPPGPKAPFKKGHVRNKSTSSAMLGSQQEVAVTQPI  255
ScSec2p   470  QPTTNIQRAWLQLCKLRCILHWTHIGIWAVDDSISSKIGPL  510
```

* basic (positvely-charged) residues, potentially involved in phosphatidylserine (PS)-binding

▼ serine residue phosphorylated by NDR-2

Figure 15: Putative phosphatidylserine (PS) binding motif in Rabin8. (top) Schematics of the domain architecture of Rabin8 with numbering from the human sequence. (Bottom) Multiple sequence alignment of the flexible linker region (reside 250–290) of Rabin8 located between the Rab8 GEF domain and the Rab11-binding domain. Serine 272 that is phosphorylated by NDR-2 is colored magenta and the positively charged residues that form a potential PS-binding motif are colored blue. Consensus motif of NDR substrates (HxRxxS/T) is absent from Sec2, nevertheless S186 and S188 in the linker region are also phosphorylated by another kinase (Stalder et al., 2013). Clustal2w was used for the alignment. Abbreviations used are: Hs: Homo sapiens, Bt: Bos Taurus, Mm: Mus musculus, Mv: Manacus vitellinus, Xt: Xenopus tropicalis, Dr: Danio rerio, Sc: Saccharomyces cerevisiae. (Figure and description from (Vetter et al., 2015b).

3.8 Activation of Rab11 – What is the specific GEF for Rab11?

Rab11 is a master regulator of intracellular membrane trafficking routes, required for ciliogenesis, recycling of internalized receptors and essential for completion of cytokinesis (Ullrich *et al.*, 1996; Wilson *et al.*, 2005; Stenmark, 2009; Mazelova *et al.*, 2009a; Horgan *et al.*, 2010; Nachury *et al.*, 2010). It is noteworthy that Rab11 has an extensive protein-protein interaction network including a growing cast of effectors such as FIPs, Rabin8, Sec15, Rab11BP/WDR44 and myosin V (Fig. 16) (Zeng *et al.*, 1999; Lapierre *et al.*, 2001; Junutula *et al.*, 2004; Zhang *et al.*, 2004; Knödler *et al.*, 2010; Kelly *et al.*, 2012). Members of the Rab11 subfamily (Rab11a, Rab11b and

Rab25/Rab11c) and their interactors have been implicated in a number of human disorders that include neurodegenerative diseases such as Alzheimer's and Huntington's disease, diabetes and cancer (Kelly *et al.*, 2012; Udayar *et al.*, 2013; Bhuin and Roy, 2014). To carry out its various regulatory functions, Rab11, like other small GTPases, acts as a molecular switch altering between an active and inactive guanine nucleotide state, which is facilitated by GEFs and GAPs (Fig. 16) (Vetter and Wittinghofer, 2001; Bos *et al.*, 2007). However, a GEF for Rab11, which mediates exchange from GDP to GTP to allow for effector binding, is not known at present.

Active Rab11 acts upstream of a conserved ciliogenesis cascade by recruiting the Rab8 GEF Rabin8, which subsequently activates Rab8, but shows no GEF activity towards Rab11 (Knödler *et al.*, 2010; Westlake *et al.*, 2011). A similar regulatory GEF cascade mechanism might apply for Rab11. In the yeast exocytic pathway, Ypt31p and Yp32p (Rab11 orthologs), act downstream of Ypt1p (Rab1 ortholog) suggesting that a putative GEF for Ypt31p/Ypt32p is an effector of Ypt1 (Jones *et al.*, 1995; 2000; Wang and Ferro-Novick, 2002; Mizuno-Yamasaki *et al.*, 2012). Yet, there is no mammalian Rab1 effector identified that shows GEF activity towards Rab11. Furthermore, it was demonstrated that the TRAPP (transport protein particle) complex, a large conserved modular protein complex implicated in the secretory pathway, has not only nucleotide exchange activity towards Ypt1p and its mammalian homologue Rab1, but also towards Ypt31/32p (Wang *et al.*, 2000; Sacher *et al.*, 2001; Morozova *et al.*, 2006). Bet3, Trs120 and Trs130, the conserved subunits of the yeast TRAPPII complex, are suggested to be required for switching the GEF specificity of TRAPP from Ypt1 to Ypt31 to ensure sequential activation of various Ypt proteins (Morozova *et al.*, 2006). On the other hand, structural investigations of the TRAPPI complex bound to Ypt1p, implied that TRAPPII activates Ypt1p by an identical mechanism (Cai *et al.*, 2008). The same study demonstrated that TRAPPII stimulates nucleotide exchange on Ypt1p, but not on Ypt31/Ypt32p, resulting in conflicting reports (Cai *et al.*, 2008; Barrowman *et al.*, 2010; Yip *et al.*, 2010).

Recently, a study using the fungi *Aspergillus nidulans* demonstrated that the physiological target of TRAPPII is RabE, the *Aspergillus* Ypt31 ortholog (Pinar *et al.*, 2015). The same study also suggested that the TRAPPII complex contains two independent bindings sites for RabE and RabO, the Ypt1 and Ypt31/32 orthologs, respectively (Pinar *et al.*, 2015). Interestingly, the N-terminal domain of Rabin8 associates with subunits of the TRAPPII complex in vertebrates (Westlake *et al.*, 2011). Interaction of TRAPPII with centrosomal Rabin8 is required for Rabin8 preciliary targeting and ciliogenesis (Westlake *et al.*, 2011). Thus, TRAPPII (via

Rabin8) might act as a GEF for Rab11. However, experimental support for this hypothesis is currently missing.

Recently, the *Drosophila* Crag protein (known as calmodulin-binding protein related to a Rab3 GDP/GTP exchange protein), required for trafficking of rhodopsin from the TGN to rhabdomere membranes in photoreceptor cells, has been suggested to act as a Rab11 GEF (Xiong *et al.*, 2012). Crag possesses several domains including the tripartite DENN (differentially expressed in neoplastic and normal cells) domain, which appears to be required for GEF activity towards Rab11 (Xiong *et al.*, 2012). In consistency with these results, a recent study revealed that DENN family proteins show GEF activity for a subset of human Rab proteins (Yoshimura *et al.*, 2010). In addition to the DENN domains, Crag possesses a calmodulin-binding site and interacts with calmodulin in a calcium-dependent manner (Xu *et al.*, 1998; Denef *et al.*, 2008). The presence of calmodulin and calcium increases exchange activity towards Rab11 indicating that Crag activity is mediated by calcium signaling (Xiong *et al.*, 2012). An interesting notion is that Rab11 effectors myosins Vb bind calmodulin and class II FIPs encode EF-hand calcium binding motifs (Welz *et al.*, 2014). Since DENN domain proteins are widely conserved in metazoans and protozoans but absent in the budding yeast, one may speculate that the putative GEF function of *Drosophila* Crag protein is conserved (Yoshimura *et al.*, 2010). In mammals, three homologs of the Crag protein have been identified with DENND4A showing the highest homology to Crag (Welz *et al.*, 2014). However, a study of Yoshimura and colleagues showed that DENND4 proteins are targeted to a tubular membrane compartment adjacent to the Golgi, to act as a GEF for Rab10, instead of Rab11 (Yoshimura *et al.*, 2010). Whether DENN domain proteins play a role in Rab11 activation has to be further investigated. Very recently, REI-1 (Rab11 interacting protein 1) was identified as a GEF for Rab11 in *C. elegans*, which regulates Rab11 localization and function in early embryos (Sakaguchi *et al.*, 2015). The human homolog of REI-1 is SH3BP5 that also exhibits GEF activity to Rab11 *in vitro* indicating that Rab11 GEF activity is conserved among the REI-1 protein family (Sakaguchi *et al.*, 2015). Interestingly, REI-1 family members lack known Rab GEF domains such as DENN and Vps9 domains, but have long helical structures (Bos *et al.*, 2007; Barr and Lambright, 2010) similar to the Rab8 specific GEF domain of Rabin8, which folds into a parallel dimeric coiled-coil structure (Dong *et al.*, 2007; Sato *et al.*, 2007; Guo *et al.*, 2013).
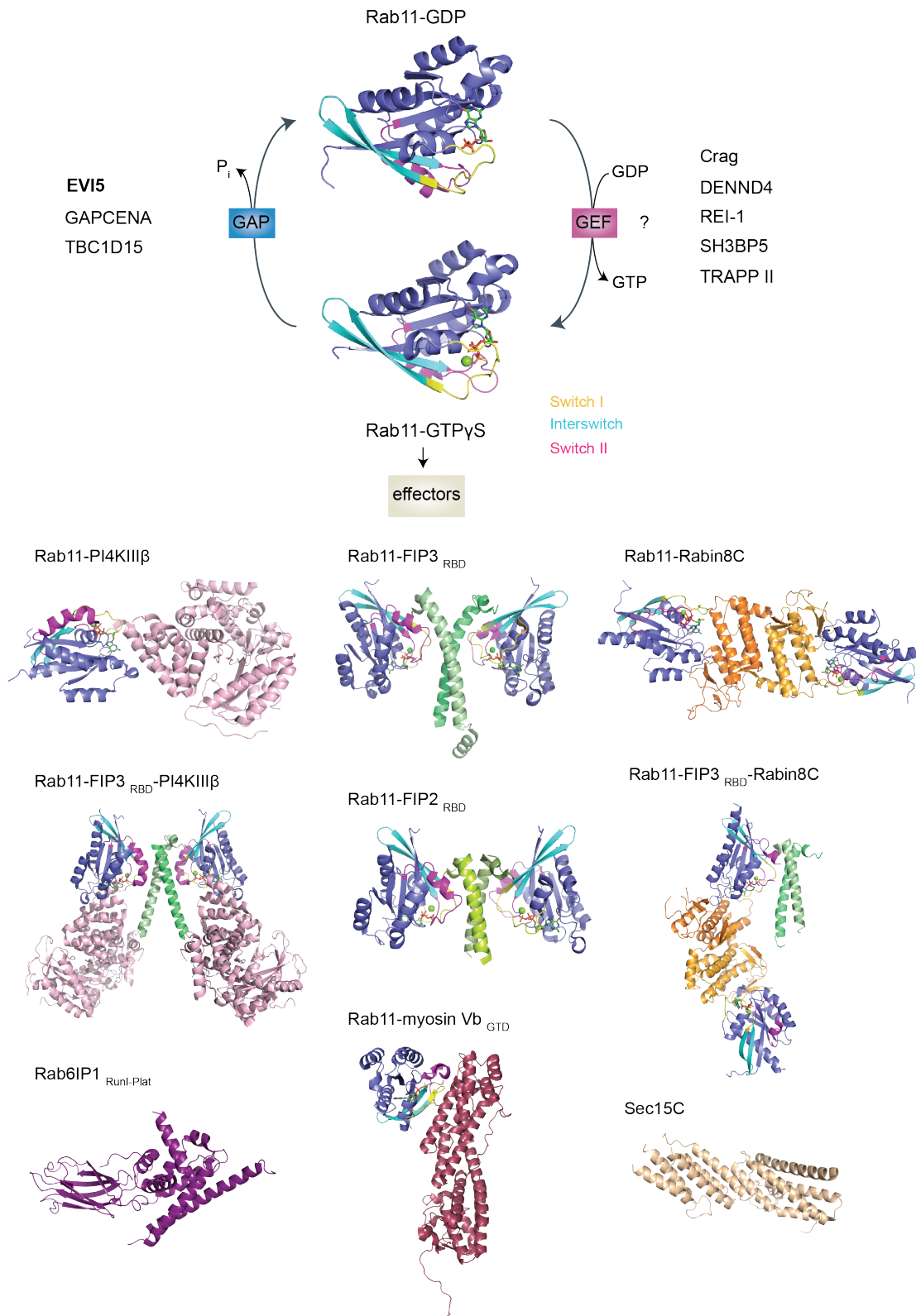
Figure 16: Regulation of Rab11 and Rab11 effector binding. *Rab11 alters between an active GTPγS-bound (pdb: 1OIV (Pasqualato et al., 2004)) and an inactive GDP-bound (pdb: 1OIW (Pasqualato et al., 2004)) state. Three putative Rab11 GAPs, EVI5 (ecotropic viral integration site 5 protein homolog), GAPCENA (TBC1D11) and TBC1D15 have been identified (Zhang et al., 2005; Dabbeekeh et al., 2007; Fuchs et al., 2007; Laflamme et al., 2012; Welz et al., 2014). All Rab11 GAPs possess TBC domains (after Tre-2, BUB2p, Cdc16p), which are known to*

accelerate GTP hydrolysis for Rab GTPases (Pan et al., 2006). The GDP-GTP exchange of Rab11 is catalyzed by various putative GEFs, which show GEF activity in vitro and/or in vivo (discussed in the text). Since Rab11, in its active form, binds a number of different effectors, regulation of Rab11 activity represents an important process. Crystal structures of putative Rab11 effector domains (Sec15 C-terminal domain, pdb: 2A2F (Wu et al., 2005); Rab6IP6 Run I-Plat domain, pdb: 3CWZ (Recacha et al., 2009)) and active Rab11 bound to its effectors (Rab11-FIP3$_{RBD}$, pdb: 2HV8 (Eathiraj et al., 2006); Rab11-FIP2$_{RBD}$, pdb: 2GZD (Jagoe et al., 2006); Rab11-Rabin8C, pdb: 4UJ5 (Vetter et al., 2015a); Rab11- PI4KIIIß, pdb: 4D0L (Burke et al., 2014); Rab11-myosin Vb$_{GTD}$, pdb: 4LX0 (Pylypenko et al., 2013); Rab11-FIP3$_{RBD}$-Rabin8C, pdb: 4UJ3 (Vetter et al., 2015a); Rab11-PI4KIIIß-Rabin8C, pdb: 4D0M (Burke et al., 2014)) are illustrated.

Activation of Rab11 is essential to carry out its various downstream functions. Despite extensive studies, the identification and characterization of a specific Rab11 GEF have not successfully completed. A number of candidates (Fig. 16) identified in different species show GEF activity towards Rab11 and/or Rab11 orthologs. There is only few structural information available of Rab GEF domains, alone or in complex with their specific target Rabs (Barr and Lambright, 2010). However, analysis of solved crystal structures revealed that Rab GEF domains are structurally diverse and suggest largely distinct structural mechanism of catalysis between various Rab GEFs towards their target Rabs (Lee *et al.*, 2009). The fact that Rab11 is a conserved versatile small GTPase, implicated in diverse mechanisms, gives rise to the possibility that different GEFs at precise positions and timings, regulate Rab11 activity. The exact molecular details of Rab11 regulation, in particular upstream activation of Rab11, require clarification.

4 Outlook

Reconstitution and characterization of complexes involved in targeting of membrane proteins to the cilium represent a great challenge due to multiple weak and transient interactions between various members of ciliary targeting complexes and their putative cargos.

The crystal structures of Rab11-Rabin8 and Rab11-FIP3-Rabin8 presented in this thesis provide initial structural insights into formation of ciliary targeting complexes. Analysis of the Rab11-Rabin8 complex revealed that Rabin8 adopts a previously undescribed fold that interacts with the Rab11 GTPase at an unusual effector binding site, to allow for complex assembly of Rab11 with both Rabin8 and FIP3 effectors, simultaneously. These findings will pave the way for reconstruction and structural characterization of larger ciliary targeting assemblies, which might include ASAP1 and Arf4 in complex with ciliary membrane proteins such as rhodopsin. Assembly of the Arf4-based ciliary targeting complex at the TGN (donor membrane) and subsequent delivery to the ciliary base facilitated by vesicular transport involves both membrane association and dissociation, an interesting aspect to take into account for design of future experiments. Structural insights of reconstituted ciliary targeting modules in complex with cargo, associated to vesicles and/or membranes will not only disclose a molecular understanding of ciliary targeting mechanisms but also provide general aspects of intracellular membrane traffic. Recent advances in cryo-electron microscopy in combination with X-ray crystallography represent likely techniques of choice for the described purposes.

Biophysical methods including size exclusion chromatography (SEC), small-angle X-ray scattering (SAXS), analytical ultracentrifugation (AUC) and isothermal titration calorimetry (ITC) demonstrated that not only single components (e.g. Rabin8, FIP3 and ASAP1) but also assembled ciliary targeting complexes form higher oligomers in solution. Based on these observations, I speculate that recruitment of ciliary targeting complexes to the TGN might results in clustering events, which in turn may lead to the creation of a microdomain enriched with cargo proteins destined for the cilium. However, experimental support for this hypothesis is required. Initial approaches that will provide clarification in greater detail might include electron and fluorescence microscopy techniques in combination with live cell-imaging technologies.

The dual effector bound Rab11-FIP3-Rabin8 complex provides a new mechanism that links GTPases into regulatory circuits to control membrane trafficking. One interesting point to address is the level of conservation of dual effector bound complexes. Do other Rab GTPases or even members of other small GTPase subfamilies form dual effector bound complexes that might act as signaling junctions to regulate various steps of membrane trafficking? Further studies are required to answer this interesting question.

Given the pivotal role of Rab11 and Rab11 subfamily members in fundamental intracellular trafficking pathways, it is not surprising that these versatile small Rab GTPases have been implicated in the progression of a number of human diseases. In order to carry out their various functions, GEFs and GAPs are required, which are critical elements in the control of small GTPases. Uncertainties about a specific Rab11 GEF raise several important questions. What is the precise molecular mechanism of upstream activation of Rab11 and Rab11 subfamily members? Does one specific GEF or do multiple GEFs at precise positions and timings catalyze the exchange from GDP to GTP? Identification of Rab11 activator(s) and understanding the precise mechanism of Rab11 regulation are key to uncover its functional role within the cell. A more complete picture of Rab11 will reveal additional regulators and effectors of physiological processes that might unravel the molecular basis for many of the diseases in which Rab11 and subfamily members are implicated. In addition, a growing number of diseases including infectious and congenital disorders as well as cancer were shown to originate from defects in small GTPase regulation, demonstrating the fundamental role of GEFs and GAPs in various basic cellular processes. Due to recent evidence that small GTPase regulators (GEF and GAPs) are potential therapeutic targets (Bos *et al.*, 2007; Vigil *et al.*, 2010), development of drugs to treat various diseases in which small GTPases are implicated, may represent pivotal long-term objectives.

Abbreviations

Å	Angstrom, $1\text{Å} = 1^{-10}$ m = 0.1 nm
AC	adenylyl cyclase
APC	adenomatous polyposis coli
APC/C	anaphase-promoting complex/cyclosome
Arf	ADP-ribosylation factor
αTAT1	α-tubulin acetyltransferase
BB	basal body
BBS	Bardet-Biedl syndrome
Ca^{2+}	calcium ions
CC	connecting cilium
CCPs	clathrin-coated pits
CNG	cyclic nucleotide-gated
CiPo	ciliary pocket
CPC	ciliary pore complex
CPS	ciliary partitioning system
CTS	ciliary targeting sequence
DENN	differentially expressed in neoplastic versus normal cells
DIC	differential interference contrast
Dsh/DSH	dishevelled
EB1	end-binding protein 1
ER	endoplasmic reticulum
ERK	extracellular signal-regulated kinase
ET	electron tomography
EVI5	ecotropic viral integration site 5 protein homolog
GAP	GTPase activating protein

GDF	GDI-displacement factor
GDI	guanine nucleotide dissociation inhibitor
GDP	guanosine diphosphate
GEF	guanine nucleotide exchange factor
Gli	glioma
GliA	glioma activator
GliR	glioma repressor form
GPCR	G protein-coupled receptor
GPI	glycosylphosphatidylinositol
GSK3β	glycogen synthase kinase-3β
GTP	guanosine triphosphate
Hh	hedgehog
IFT	intraflagellar transport
IDA	inner dynein arm
Inv	inversin
IS	inner segment
ITC	isothermal titration calorimetry
K_D	dissociation constant
LRRK2	Leucine-rich repeat kinase 2
MEK	mitogen-activated protein kinase kinase
Mg^{2+}	magnesium ions
MKS	Meckel-Gruber syndrome
MKSR	Meckel Syndrome
MT	microtubule
NPC	nuclear pore complex
NPHP	nephronophthisis
ODA	outer dynein arm

Oprk	Oak Ridge Polycystic Kidney
OS	outer segment
PA	phosphatidic acid
PC1/PKD1/Pkd1	polycystin-1
PC2/PKD2/Pkd2	polycystin-2
PI4KIIIβ	phosphatidylinositol 4-kinase III beta
PDGF	platelet-derived growth factor
PDGFRα	platelet-derived growth factor receptor α
PKD	polycystic kidney disease
PM	plasma membrane
PS	phosphatidylserine
Rab	Ras-like proteins in brain A
REP	Rab escort protein
SAXS	small-angle X-ray scattering
SEC	size-exclusion chromatography
SEM	scanning electron micrograph
Shh	sonic hedgehog
Smo	Smoothened
SNARE	N-ethylmaleimide-sensitive factor attachment protein receptor
Sufu	suppressor of fused
TBC	Tre-2, BUB2p, Cdc16p
TGN	trans-Golgi network
TF	transitional fiber
TRAPP	transport protein particle
TZ	transition zone

References

Absalon, S., Blisnick, T., Bonhivers, M., Kohl, L., Cayet, N., Toutirais, G., Buisson, J., Robinson, D., and Bastin, P. (2008a). Flagellum elongation is required for correct structure, orientation and function of the flagellar pocket in Trypanosoma brucei. J. Cell. Sci. 121, 3704–3716.

Absalon, S., Blisnick, T., Kohl, L., Toutirais, G., Doré, G., Julkowska, D., Tavenet, A., and Bastin, P. (2008b). Intraflagellar transport and functional analysis of genes required for flagellum formation in trypanosomes. Mol. Biol. Cell 19, 929–944.

Adato, A., Lefevre, G., Delprat, B., Michel, V., Michalski, N., Chardenoux, S., Weil, D., El-Amraoui, A., and Petit, C. (2005). Usherin, the defective protein in Usher syndrome type IIA, is likely to be a component of interstereocilia ankle links in the inner ear sensory cells. Hum. Mol. Genet. 14, 3921–3932.

Afzelius, B. A. (1976). A human syndrome caused by immotile cilia. Science 193, 317–319.

Afzelius, B. A. (2004). Cilia-related diseases. J. Pathol. 204, 470–477.

Afzelius, B. A., and Eliasson, R. (1982). Male and female infertility problems in the immotile-cilia syndrome. Eur J Respir Dis Suppl 127, 144–147.

Alberts, B., Johnson, A., Lewis, J., Walter, P., Raff, M., and Roberts, K. (2002). Molecular Biology of the Cell 4th Edition, Garland Science.

ALEXANDROV, K., HORIUCHI, H., STEELEMORTIMER, O., Seabra, M. C., and Zerial, M. (1994). Rab Escort Protein-1 Is a Multifunctional Protein That Accompanies Newly Prenylated Rab Proteins to Their Target Membranes. Embo J. 13, 5262–5273.

Allen, C. L., Goulding, D., and Field, M. C. (2003). Clathrin-mediated endocytosis is essential in Trypanosoma brucei. Embo J. 22, 4991–5002.

Anant, J. S., Desnoyers, L., Machius, M., Demeler, B., Hansen, J. C., Westover, K. D., Deisenhofer, J., and Seabra, M. C. (1998). Mechanism of Rab geranylgeranylation: formation of the catalytic ternary complex. Biochemistry 37, 12559–12568.

Anderson, R. G. (1972). The three-dimensional structure of the basal body from the rhesus monkey oviduct. J. Cell Biol. 54, 246–265.

Andrae, J., Gallini, R., and Betsholtz, C. (2008). Role of platelet-derived growth factors in physiology and medicine. Genes Dev. 22, 1276–1312.

ANDREWS, P. M. (1975). Scanning Electron-Microscopy of Human and Rhesus-Monkey Kidneys. Lab. Invest. 32, 610–618.

Antonny, B., Beraud-Dufour, S., Chardin, P., and Chabre, M. (1997). N-terminal hydrophobic residues of the G-protein ADP-ribosylation factor-1 insert into membrane phospholipids upon GDP to GTP exchange. Biochemistry 36, 4675–4684.

Axelrod, J. D. (2008). Basal bodies, kinocilia and planar cell polarity. Nat. Genet. 40, 10–11.

Badano, J. L., Mitsuma, N., Beales, P. L., and Katsanis, N. (2006). The ciliopathies: an emerging class of human genetic disorders. Annu Rev Genomics Hum Genet 7, 125–148.

Banizs, B., Pike, M. M., Millican, C. L., Ferguson, W. B., Komlosi, P., Sheetz, J., Bell, P. D., Schwiebert, E. M., and Yoder, B. K. (2005). Dysfunctional cilia lead to altered ependyma and choroid plexus function, and result in the formation of hydrocephalus. Development 132, 5329–5339.

Barr, F., and Lambright, D. G. (2010). Rab GEFs and GAPs. Curr. Opin. Cell Biol. 22, 461–470.

Barral, Y. P., Mermall, V., Mooseker, M., and Snyder, M. (2000). Compartmentalization of the cell cortex by septins is required for maintenance of cell polarity in yeast. Mol. Biol. Cell 11, 101A–101A.

Barrowman, J., Bhandari, D., Reinisch, K., and Ferro-Novick, S. (2010). TRAPP complexes in membrane traffic: convergence through a common Rab. Nat. Rev. Mol. Cell Biol. 11, 759–763.

Beisson, J., and Wright, M. (2003). Basal body/centriole assembly and continuity. Curr. Opin. Cell Biol. 15, 96–104.

Benmerah, A. (2013). The ciliary pocket. Curr. Opin. Cell Biol. 25, 78–84.

Benton, R., Sachse, S., Michnick, S. W., and Vosshall, L. B. (2006). Atypical membrane topology and heteromeric function of Drosophila odorant receptors in vivo. PLoS Biol. 4, e20.

Berbari, N. F., Johnson, A. D., Lewis, J. S., Askwith, C. C., and Mykytyn, K. (2008). Identification of ciliary localization sequences within the third intracellular loop of G protein-coupled receptors. Mol. Biol. Cell 19, 1540–1547.

Berbari, N. F., O'Connor, A. K., Haycraft, C. J., and Yoder, B. K. (2009). The primary cilium as a complex signaling center. Curr. Biol. 19, R526–R535.

Berta, Á. I., Boesze-Battaglia, K., Genini, S., Goldstein, O., O'Brien, P. J., Szél, Á., Acland, G. M., Beltran, W. A., and Aguirre, G. D. (2011). Photoreceptor cell death, proliferation and formation of hybrid rod/S-cone photoreceptors in the degenerating STK38L mutant retina. PLoS ONE 6, e24074.

Besharse, J. C., Hollyfield, J. G., and Rayborn, M. E. (1977). Turnover of rod photoreceptor outer segments. II. Membrane addition and loss in relationship to light. J. Cell Biol. 75, 507–527.

Betleja, E., and Cole, D. G. (2010). Ciliary trafficking: CEP290 guards a gated community. Curr. Biol. 20, R928–R931.

Bhogaraju, S. et al. (2013). Molecular Basis of Tubulin Transport Within the Cilium by IFT74 and IFT81. Science 341, 1009–1012.

Bhuin, T., and Roy, J. K. (2014). Rab11 in disease progression. Int J Mol Cell Med 4, 1–8.

Blümer, J., Rey, J., Dehmelt, L., Mazel, T., Wu, Y.-W., Bastiaens, P., Goody, R. S.,

and Itzen, A. (2013). RabGEFs are a major determinant for specific Rab membrane targeting. J. Cell Biol. 200, 287–300.

Boekhoff, I., Tareilus, E., Strotmann, J., and Breer, H. (1990). Rapid activation of alternative second messenger pathways in olfactory cilia from rats by different odorants. Embo J. 9, 2453–2458.

Bonifacino, J. S., and Glick, B. S. (2004). The mechanisms of vesicle budding and fusion. Cell 116, 153–166.

Bonifacino, J. S., and Lippincott-Schwartz, J. (2003). Coat proteins: shaping membrane transport. Nat. Rev. Mol. Cell Biol. 4, 409–414.

Bos, J. L., Rehmann, H., and Wittinghofer, A. (2007). GEFs and GAPs: critical elements in the control of small G proteins. Cell 129, 865–877.

Bourne, H. R., Sanders, D. A., and McCormick, F. (1991). The GTPase superfamily: conserved structure and molecular mechanism. Nature 349, 117–127.

Brazelton, W. J., Amundsen, C. D., Silflow, C. D., and Lefebvre, P. A. (2001). The bld1 mutation identifies the Chlamydomonas osm-6 homolog as a gene required for flagellar assembly. Curr. Biol. 11, 1591–1594.

Breslow, D. K., Koslover, E. F., Seydel, F., Spakowitz, A. J., and Nachury, M. V. (2013). An in vitro assay for entry into cilia reveals unique properties of the soluble diffusion barrier. J. Cell Biol. 203, 129–147.

Brown, M. T., Andrade, J., Radhakrishna, H., Donaldson, J. G., Cooper, J. A., and Randazzo, P. A. (1998). ASAP1, a phospholipid-dependent arf GTPase-activating protein that associates with and is phosphorylated by Src. Mol. Cell. Biol. 18, 7038–7051.

Bröcker, C., Engelbrecht-Vandré, S., and Ungermann, C. (2010). Multisubunit tethering complexes and their role in membrane fusion. Curr. Biol. 20, R943–R952.

Bryant, D. M., Datta, A., Rodríguez-Fraticelli, A. E., Peränen, J., Martín-Belmonte, F., and Mostov, K. E. (2010). A molecular network for de novo generation of the apical surface and lumen. Nat. Cell Biol. 12, 1035–1045.

Buck, L., and Axel, R. (1991). A novel multigene family may encode odorant receptors: a molecular basis for odor recognition. Cell 65, 175–187.

Burke, J. E., Inglis, A. J., Perisic, O., Masson, G. R., McLaughlin, S. H., Rutaganira, F., Shokat, K. M., and Williams, R. L. (2014). Structures of PI4KIIIβ complexes show simultaneous recruitment of Rab11 and its effectors. Science 344, 1035–1038.

Caberoy, N. B., Zhou, Y., Alvarado, G., Fan, X., and Li, W. (2009). Efficient identification of phosphatidylserine-binding proteins by ORF phage display. Biochem. Biophys. Res. Commun. 386, 197–201.

Cai, Y. et al. (2008). The structural basis for activation of the Rab Ypt1p by the TRAPP membrane-tethering complexes. Cell 133, 1202–1213.

Calvert, P. D., Schiesser, W. E., and Pugh, E. N. (2010). Diffusion of a soluble protein, photoactivatable GFP, through a sensory cilium. J. Gen. Physiol. 135, 173–196.

Cano, D. A., Murcia, N. S., Pazour, G. J., and Hebrok, M. (2004). orpk mouse model of polycystic kidney disease reveals essential role of primary cilia in pancreatic tissue organization. Development 131, 3457–3467.

CESARIO, M. M., and BARTLES, J. R. (1994). Compartmentalization, Processing and Redistribution of the Plasma-Membrane Protein Ce9 on Rodent Spermatozoa - Relationship of the Annulus to Domain Boundaries in the Plasma-Membrane of the Tail. J. Cell. Sci. 107, 561–570.

Chavrier, P., and Menetrey, J. (2010). Toward a structural understanding of arf family:effector specificity. Structure 18, 1552–1558.

CHAVRIER, P., Gorvel, J. P., Stelzer, E., Simons, K., Gruenberg, J., and Zerial, M. (1991). Hypervariable C-terminal domain of rab proteins acts as a targeting signal. Nature 353, 769–772.

CHAVRIER, P., Parton, R. G., HAURI, H. P., Simons, K., and Zerial, M. (1990). Localization of Low-Molecular-Weight Gtp Binding-Proteins to Exocytic and Endocytic Compartments. Cell 62, 317–329.

Chen, W., Feng, Y., Chen, D., and Wandinger-Ness, A. (1998). Rab11 is required for trans-golgi network-to-plasma membrane transport and a preferential target for GDP dissociation inhibitor. Mol. Biol. Cell 9, 3241–3257.

Cherfils, J., and Zeghouf, M. (2013). Regulation of small GTPases by GEFs, GAPs, and GDIs. Physiol. Rev. 93, 269–309.

Chiba, S., Amagai, Y., Homma, Y., Fukuda, M., and Mizuno, K. (2013). NDR2-mediated Rabin8 phosphorylation is crucial for ciliogenesis by switching binding specificity from phosphatidylserine to Sec15. Embo J. 32, 874–885.

Chih, B., Liu, P., Chinn, Y., Chalouni, C., Komuves, L. G., Hass, P. E., Sandoval, W., and Peterson, A. S. (2012). A ciliopathy complex at the transition zone protects the cilia as a privileged membrane domain. Nat. Cell Biol. 14, 61–U97.

Chilvers, M. A., Rutman, A., and O'Callaghan, C. (2003). Ciliary beat pattern is associated with specific ultrastructural defects in primary ciliary dyskinesia. J. Allergy Clin. Immunol. 112, 518–524.

Christensen, S. T., Pedersen, L. B., Schneider, L., and Satir, P. (2007). Sensory cilia and integration of signal transduction in human health and disease. Traffic 8, 97–109.

Christensen, S. T., Pedersen, S. F., Satir, P., Veland, I. R., and Schneider, L. (2008). The primary cilium coordinates signaling pathways in cell cycle control and migration during development and tissue repair. Curr. Top. Dev. Biol. 85, 261–301.

Clement, C. A. et al. (2013). TGF-β signaling is associated with endocytosis at the pocket region of the primary cilium. Cell Rep 3, 1806–1814.

Clevers, H. (2006). Wnt/beta-catenin signaling in development and disease. Cell 127, 469–480.

Cole, D. G., Diener, D. R., Himelblau, A. L., Beech, P. L., Fuster, J. C., and Rosenbaum, J. L. (1998). Chlamydomonas kinesin-II-dependent intraflagellar transport (IFT): IFT particles contain proteins required for ciliary assembly in Caenorhabditis elegans sensory neurons. J. Cell Biol. 141, 993–1008.

Concepcion, F., Mendez, A., and Chen, J. (2002). The carboxyl-terminal domain is essential for rhodopsin transport in rod photoreceptors. Vision Res. 42, 417–426.

Cooper, G. M. (2000). The Mechanism of Vesicular Transport.

Corbit, K. C., Aanstad, P., Singla, V., Norman, A. R., Stainier, D. Y. R., and Reiter, J. F. (2005). Vertebrate Smoothened functions at the primary cilium. Nature 437, 1018–1021.

Corbit, K. C., Shyer, A. E., Dowdle, W. E., Gaulden, J., Singla, V., Chen, M.-H., Chuang, P.-T., and Reiter, J. F. (2008). Kif3a constrains beta-catenin-dependent Wnt signalling through dual ciliary and non-ciliary mechanisms. Nat. Cell Biol. 10, 70–76.

Craige, B., Tsao, C.-C., Diener, D. R., Hou, Y., Lechtreck, K.-F., Rosenbaum, J. L., and Witman, G. B. (2010). CEP290 tethers flagellar transition zone microtubules to the membrane and regulates flagellar protein content. J. Cell Biol. 190, 927–940.

Dabbeekeh, J. T. S., Faitar, S. L., Dufresne, C. P., and Cowell, J. K. (2007). The EVI5 TBC domain provides the GTPase-activating protein motif for RAB11. Oncogene 26, 2804–2808.

Dabdoub, A., and Kelley, M. W. (2005). Planar cell polarity and a potential role for a Wnt morphogen gradient in stereociliary bundle orientation in the mammalian inner ear. J. Neurobiol. 64, 446–457.

Danilov, A. I., Gomes-Leal, W., Ahlenius, H., Kokaia, Z., Carlemalm, E., and Lindvall, O. (2009). Ultrastructural and Antigenic Properties of Neural Stem Cells and Their Progeny in Adult Rat Subventricular Zone. Glia 57, 136–152.

Das, A., and Guo, W. (2011). Rabs and the exocyst in ciliogenesis, tubulogenesis and beyond. Trends Cell Biol. 21, 383–386.

de Graaf, P. et al. (2004). Phosphatidylinositol 4-kinasebeta is critical for functional association of rab11 with the Golgi complex. Mol. Biol. Cell 15, 2038–2047.

Deane, J. A., Cole, D. G., Seeley, E. S., Diener, D. R., and Rosenbaum, J. L. (2001). Localization of intraflagellar transport protein IFT52 identifies basal body transitional fibers as the docking site for IFT particles. Curr. Biol. 11, 1586–1590.

DeCaen, P. G., Delling, M., Vien, T. N., and Clapham, D. E. (2013). Direct recording and molecular identification of the calcium channel of primary cilia. Nature 504, 315–318.

Delling, M., DeCaen, P. G., Doerner, J. F., Febvay, S., and Clapham, D. E. (2013). Primary cilia are specialized calcium signalling organelles. Nature 504, 311–314.

Denef, N., Chen, Y., Weeks, S. D., Barcelo, G., and Schüpbach, T. (2008). Crag regulates epithelial architecture and polarized deposition of basement membrane proteins in Drosophila. Dev. Cell 14, 354–364.

Dentler, W. (2005). Intraflagellar transport (IFT) during assembly and disassembly of Chlamydomonas flagella. J. Cell Biol. 170, 649–659.

Deretic, D. (1998). Post-Golgi trafficking of rhodopsin in retinal photoreceptors. Eye (Lond) 12 (Pt 3b), 526–530.

Deretic, D. (2013). Crosstalk of Arf and Rab GTPases en route to cilia. Small GTPases 4, 70–77.

Deretic, D., Huber, L. A., Ransom, N., Mancini, M., Simons, K., and Papermaster, D. S. (1995). rab8 in retinal photoreceptors may participate in rhodopsin transport and in rod outer segment disk morphogenesis. J. Cell. Sci. 108 (Pt 1), 215–224.

Deretic, D., Williams, A. H., Ransom, N., Morel, V., Hargrave, P. A., and Arendt, A. (2005). Rhodopsin C terminus, the site of mutations causing retinal disease, regulates trafficking by binding to ADP-ribosylation factor 4 (ARF4). Proc. Natl. Acad. Sci. U.S.a. 102, 3301–3306.

di Magliano, M. P., and Hebrok, M. (2003). Hedgehog signalling in cancer formation and maintenance. Nat. Rev. Cancer 3, 903–911.

Dishinger, J. F., Kee, H. L., Jenkins, P. M., Fan, S., Hurd, T. W., Hammond, J. W., Truong, Y. N.-T., Margolis, B., Martens, J. R., and Verhey, K. J. (2010). Ciliary entry of the kinesin-2 motor KIF17 is regulated by importin-beta2 and RanGTP. Nat. Cell Biol. 12, 703–710.

Donaldson, J. G., and Jackson, C. L. (2011). ARF family G proteins and their regulators: roles in membrane transport, development and disease. Nat. Rev. Mol. Cell Biol. 12, 362–375.

Dong, G., Medkova, M., Novick, P., and Reinisch, K. M. (2007). A catalytic coiled coil: structural insights into the activation of the Rab GTPase Sec4p by Sec2p. Mol. Cell 25, 455–462.

Duchateau, G. S., Graamans, K., Zuidema, J., and Merkus, F. W. (1985). Correlation between nasal ciliary beat frequency and mucus transport rate in volunteers. Laryngoscope 95, 854–859.

Duchen, M. R., and Szabadkai, G. (2010). Roles of mitochondria in human disease. Essays in Biochemistry: Mitochondrial Function 47, 115–137.

Eathiraj, S., Mishra, A., Prekeris, R., and Lambright, D. G. (2006). Structural basis for Rab11-mediated recruitment of FIP3 to recycling endosomes. J. Mol. Biol. 364, 121–135.

Eathiraj, S., Pan, X., Ritacco, C., and Lambright, D. G. (2005). Structural basis of family-wide Rab GTPase recognition by rabenosyn-5. Nature 436, 415–419.

Efimenko, E., Blacque, O. E., Ou, G., Haycraft, C. J., Yoder, B. K., Scholey, J. M., Leroux, M. R., and Swoboda, P. (2006). Caenorhabditis elegans DYF-2, an orthologue of human WDR19, is a component of the intraflagellar transport machinery in sensory cilia. Mol. Biol. Cell 17, 4801–4811.

Eggenschwiler, J. T., and Anderson, K. V. (2007). Cilia and developmental signaling. Annu. Rev. Cell Dev. Biol. 23, 345–373.

Elias, R., Sezate, S., Cao, W., and McGinnis, J. (2004). Temporal kinetics of the light/dark translocation and compartmentation of arrestin and alpha-transducin in mouse photoreceptor cells. Mol. Vis. 10, 672–681.

Eliasson, R., Mossberg, B., Camner, P., and Afzelius, B. A. (1977). The immotile-cilia syndrome. A congenital ciliary abnormality as an etiologic factor in chronic airway infections and male sterility. N. Engl. J. Med. 297, 1–6.

Engstler, M., Thilo, L., Weise, F., Grünfelder, C. G., Schwarz, H., Boshart, M., and Overath, P. (2004). Kinetics of endocytosis and recycling of the GPI

-anchored variant surface glycoprotein in Trypanosoma brucei. J. Cell. Sci. 117, 1105–1115.

Fahrenkrog, B., and Aebi, U. (2003). The nuclear pore complex: Nucleocytoplasmic transport and beyond. Nat. Rev. Mol. Cell Biol. 4, 757–766.

Fan, S., Whiteman, E. L., Hurd, T. W., McIntyre, J. C., Dishinger, J. F., Liu, C.-J., Martens, J. R., Verhey, K. J., Sajjan, U., and Margolis, B. (2011). Induction of Ran GTP drives ciliogenesis. Mol. Biol. Cell 22, 4539–4548.

Fan, Z.-C., Behal, R. H., Geimer, S., Wang, Z., Williamson, S. M., Zhang, H., Cole, D. G., and Qin, H. (2010). Chlamydomonas IFT70/CrDYF-1 is a core component of IFT particle complex B and is required for flagellar assembly. Mol. Biol. Cell 21, 2696–2706.

Feng, S., Knödler, A., Ren, J., Zhang, J., Zhang, X., Hong, Y., Huang, S., Peränen, J., and Guo, W. (2012). A Rab8 guanine nucleotide exchange factor-effector interaction network regulates primary ciliogenesis. J. Biol. Chem. 287, 15602–15609.

Field, M. C., and Carrington, M. (2009). The trypanosome flagellar pocket. Nat. Rev. Microbiol. 7, 775–786.

Fielding, A. B., Schonteich, E., Matheson, J., Wilson, G., Yu, X., Hickson, G. R. X., Srivastava, S., Baldwin, S. A., Prekeris, R., and Gould, G. W. (2005). Rab11-FIP3 and FIP4 interact with Arf6 and the exocyst to control membrane traffic in cytokinesis. Embo J. 24, 3389–3399.

Fisch, C., and Dupuis-Williams, P. (2011). Ultrastructure of cilia and flagella - back to the future! Biol Cell 103, 249–270.

Fliegauf, M., Benzing, T., and Omran, H. (2007). When cilia go bad: cilia defects and ciliopathies. Nat. Rev. Mol. Cell Biol. 8, 880–893.

Follit, J. A., Agustin, J. T. S., Jonassen, J. A., Huang, T., Rivera-Perez, J. A., Tremblay, K. D., and Pazour, G. J. (2014). Arf4 is required for Mammalian development but dispensable for ciliary assembly. PLoS Genet 10, e1004170–e1004170.

Follit, J. A., Li, L., Vucica, Y., and Pazour, G. J. (2010). The cytoplasmic tail of fibrocystin contains a ciliary targeting sequence. J. Cell Biol. 188, 21–28.

Follit, J. A., Tuft, R. A., Fogarty, K. E., and Pazour, G. J. (2006). The intraflagellar transport protein IFT20 is associated with the Golgi complex and is required for cilia assembly. Mol. Biol. Cell 17, 3781–3792.

Fredriksson, L., Li, H., and Eriksson, U. (2004). The PDGF family: four gene products form five dimeric isoforms. Cytokine Growth Factor Rev. 15, 197–204.

Fuchs, E., Haas, A. K., Spooner, R. A., Yoshimura, S.-I., Lord, J. M., and Barr, F. A. (2007). Specific Rab GTPase-activating proteins define the Shiga toxin and epidermal growth factor uptake pathways. J. Cell Biol. 177, 1133–1143.

Fujiwara, M., Ishihara, T., and Katsura, I. (1999). A novel WD40 protein, CHE-2, acts cell-autonomously in the formation of C. elegans sensory cilia. Development 126, 4839–4848.

Fukuda, T., Kominami, K., Wang, S., Togashi, H., Hirata, K.-I., Mizoguchi, A., Rikitake, Y., and Takai, Y. (2014). Aberrant cochlear hair cell attachments caused by Nectin-3 deficiency result in hair bundle abnormalities. Development 141, 399–409.

Gadelha, C., Rothery, S., Morphew, M., McIntosh, J. R., Severs, N. J., and Gull, K. (2009). Membrane domains and flagellar pocket boundaries are influenced by the cytoskeleton in African trypanosomes. Proc. Natl. Acad. Sci. U.S.a. 106, 17425–17430.

Garcia-Gonzalo, F. R. et al. (2011). A transition zone complex regulates mammalian ciliogenesis and ciliary membrane composition. Nat. Genet. 43, 776–784.

Geng, L., Okuhara, D., Yu, Z., Tian, X., Cai, Y., Shibazaki, S., and Somlo, S. (2006). Polycystin-2 traffics to cilia independently of polycystin-1 by using an N-terminal RVxP motif. J. Cell. Sci. 119, 1383–1395.

Gerdes, J. M. et al. (2007). Disruption of the basal body compromises proteasomal function and perturbs intracellular Wnt response. Nat. Genet. 39, 1350–1360.

Gerdes, J. M., Davis, E. E., and Katsanis, N. (2009). The Vertebrate Primary Cilium in Development, Homeostasis, and Disease. Cell 137, 32–45.

Gherman, A., Davis, E. E., and Katsanis, N. (2006). The ciliary proteome database: an integrated community resource for the genetic and functional dissection of cilia. Nat. Genet. 38, 961–962.

Ghossoub, R., Molla-Herman, A., Bastin, P., and Benmerah, A. (2011). The ciliary pocket: a once-forgotten membrane domain at the base of cilia. Biol Cell 103, 131–144.

Gibbons, I. R., and Rowe, A. J. (1965). Dynein: A Protein with Adenosine Triphosphatase Activity from Cilia. Science 149, 424–426.

Gillingham, A. K., and Munro, S. (2007). The small G proteins of the Arf family and their regulators. Annu. Rev. Cell Dev. Biol. 23, 579–611.

Gillingham, A. K., Tong, A. H. Y., Boone, C., and Munro, S. (2004). The GTPase Arf1p and the ER to Golgi cargo receptor Erv14p cooperate to recruit the golgin Rud3p to the cis-Golgi. J. Cell Biol. 167, 281–292.

Gilula, N. B., and Satir, P. (1972). The ciliary necklace. A ciliary membrane specialization. J. Cell Biol. 53, 494–509.

Goetz, S. C., and Anderson, K. V. (2010). The primary cilium: a signalling centre

during vertebrate development. Nat. Rev. Genet. 11, 331–344.

Goldberg, J. (1998). Structural basis for activation of ARF GTPase: mechanisms of guanine nucleotide exchange and GTP-myristoyl switching. Cell 95, 237–248.

Goldfarb, D. S., Gariépy, J., Schoolnik, G., and Kornberg, R. D. (1986). Synthetic peptides as nuclear localization signals. Nature 322, 641–644.

Goldstein, O., Kukekova, A. V., Aguirre, G. D., and Acland, G. M. (2010). Exonic SINE insertion in STK38L causes canine early retinal degeneration (erd). Genomics 96, 362–368.

Grati, M. et al. (2015). A missense mutation in DCDC2 causes human recessive deafness DFNB66, likely by interfering with sensory hair cell and supporting cell cilia length regulation. Hum. Mol. Genet. 24, 2482–2491.

Guo, W., Roth, D., Walch-Solimena, C., and Novick, P. (1999). The exocyst is an effector for Sec4p, targeting secretory vesicles to sites of exocytosis. Embo J. 18, 1071–1080.

Guo, Z., Hou, X., Goody, R. S., and Itzen, A. (2013). Intermediates in the guanine nucleotide exchange reaction of Rab8 protein catalyzed by guanine nucleotide exchange factors Rabin8 and GRAB. J. Biol. Chem. 288, 32466–32474.

Hales, C. M., Griner, R., Hobdy-Henderson, K. C., Dorn, M. C., Hardy, D., Kumar, R., Navarre, J., Chan, E. K., Lapierre, L. A., and Goldenring, J. R. (2001). Identification and characterization of a family of Rab11-interacting proteins. J. Biol. Chem. 276, 39067–39075.

Hao, L., and Scholey, J. M. (2009). Intraflagellar transport at a glance. J. Cell. Sci. 122, 889–892.

Hattula, K., Furuhjelm, J., Arffman, A., and Peränen, J. (2002). A Rab8-specific GDP/GTP exchange factor is involved in actin remodeling and polarized membrane transport. Mol. Biol. Cell 13, 3268–3280.

Haycraft, C. J., Banizs, B., Aydin-Son, Y., Zhang, Q. H., Michaud, E. J., and Yoder, B. K. (2005). Gli2 and Gli3 localize to cilia and require the intra-flagellar transport protein polaris for processing and function. PLoS Genet 1, 480–488.

Haycraft, C. J., Schafer, J. C., Zhang, Q., Taulman, P. D., and Yoder, B. K. (2003). Identification of CHE-13, a novel intraflagellar transport protein required for cilia formation. Exp. Cell Res. 284, 251–263.

He, X. (2008). Cilia put a brake on Wnt signalling. Nat. Cell Biol. 10, 11–13.

Heldin, C. H., and Westermark, B. (1999). Mechanism of action and in vivo role of platelet-derived growth factor. Physiol. Rev. 79, 1283–1316.

Hirokawa, N., Tanaka, Y., Okada, Y., and Takeda, S. (2006). Nodal flow and the generation of left-right asymmetry. Cell 125, 33–45.

Horgan, C. P., Hanscom, S. R., Jolly, R. S., Futter, C. E., and McCaffrey, M. W. (2010). Rab11-FIP3 links the Rab11 GTPase and cytoplasmic dynein to mediate transport to the endosomal-recycling compartment. J. Cell. Sci. 123, 181–191.

Horgan, C. P., Oleksy, A., Zhdanov, A. V., Lall, P. Y., White, I. J., Khan, A. R., Futter, C. E., McCaffrey, J. G., and McCaffrey, M. W. (2007). Rab11-FIP3 is critical for the structural integrity of the endosomal recycling compartment. Traffic 8, 414–430.

Hornef, N. et al. (2006). DNAH5 mutations are a common cause of primary ciliary dyskinesia with outer dynein arm defects. Am. J. Respir. Crit. Care Med. 174, 120–126.

Horst, C. J., Johnson, L. V., and Besharse, J. C. (1990). Transmembrane assemblage of the photoreceptor connecting cilium and motile cilium transition zone contain a common immunologic epitope. Cell Motil. Cytoskeleton 17, 329–344.

Hou, Y., Pazour, G. J., and Witman, G. B. (2004). A dynein light intermediate chain, D1bLIC, is required for retrograde intraflagellar transport. Mol. Biol. Cell 15, 4382–4394.

Hou, Y., Qin, H., Follit, J. A., Pazour, G. J., Rosenbaum, J. L., and Witman, G. B. (2007). Functional analysis of an individual IFT protein: IFT46 is required for transport of outer dynein arms into flagella. J. Cell Biol. 176, 653–665.

Hsu, S.-C., TerBush, D., Abraham, M., and Guo, W. (2004). The exocyst complex in polarized exocytosis. Int. Rev. Cytol. 233, 243–265.

Hu, Q., and Nelson, W. J. (2011). Ciliary diffusion barrier: the gatekeeper for the primary cilium compartment. Cytoskeleton (Hoboken) 68, 313–324.

Hu, Q., Milenkovic, L., Jin, H., Scott, M. P., Nachury, M. V., Spiliotis, E. T., and Nelson, W. J. (2010). A Septin Diffusion Barrier at the Base of the Primary Cilium Maintains Ciliary Membrane Protein Distribution. Science 329, 436–439.

Huangfu, D., Liu, A., Rakeman, A. S., Murcia, N. S., Niswander, L., and Anderson, K. V. (2003). Hedgehog signalling in the mouse requires intraflagellar transport proteins. Nature 426, 83–87.

HUDSPETH, A. J. (1985). The Cellular Basis of Hearing - the Biophysics of Hair-Cells. Science 230, 745–752.

Hunnicutt, G. R., Kosfiszer, M. G., and Snell, W. J. (1990). Cell body and flagellar agglutinins in Chlamydomonas reinhardtii: the cell body plasma membrane is a reservoir for agglutinins whose migration to the flagella is regulated by a functional barrier. J. Cell Biol. 111, 1605–1616.

Hurd, T. W., Fan, S., and Margolis, B. L. (2011). Localization of retinitis pigmentosa 2 to cilia is regulated by Importin beta2. J. Cell. Sci. 124, 718–726.

Hutagalung, A. H., and Novick, P. J. (2011). Role of Rab GTPases in membrane traffic and cell physiology. Physiol. Rev. 91, 119–149.

Iannaccone, A., Mykytyn, K., Persico, A. M., Searby, C. C., Baldi, A., Jablonski, M. M., and Sheffield, V. C. (2005). Clinical evidence of decreased olfaction in Bardet-Biedl syndrome caused by a deletion in the BBS4 gene. Am. J. Med. Genet. A 132A, 343–346.

Ibanez-Tallon, I., Gorokhova, S., and Heintz, N. (2002). Loss of function of axonemal dynein Mdnah5 causes primary ciliary dyskinesia and hydrocephalus. Hum. Mol.

Genet. 11, 715–721.

Ibanez-Tallon, I., Pagenstecher, A., Fliegauf, M., Olbrich, H., Kispert, A., Ketelsen, U. P., North, A., Heintz, N., and Omran, H. (2004). Dysfunction of axonemal dynein heavy chain Mdnah5 inhibits ependymal flow and reveals a novel mechanism for hydrocephalus formation. Hum. Mol. Genet. 13, 2133–2141.

Ibañez-Tallon, I., Heintz, N., and Omran, H. (2003). To beat or not to beat: roles of cilia in development and disease. Hum. Mol. Genet. 12 Spec No 1, R27–R35.

Inoue, H., and Randazzo, P. A. (2007). Arf GAPs and their interacting proteins. Traffic 8, 1465–1475.

Inoue, H., Ha, V. L., Prekeris, R., and Randazzo, P. A. (2008). Arf GTPase-activating protein ASAP1 interacts with Rab11 effector FIP3 and regulates pericentrosomal localization of transferrin receptor-positive recycling endosome. Mol. Biol. Cell 19, 4224–4237.

Iomini, C., Babaev-Khaimov, V., Sassaroli, M., and Piperno, G. (2001). Protein particles in Chlamydomonas flagella undergo a transport cycle consisting of four phases. J. Cell Biol. 153, 13–24.

Ishikawa, H. et al. (2014). TTC26/DYF13 is an intraflagellar transport protein required for transport of motility-related proteins into flagella. Elife 3, e01566.

Jagoe, W. N., Lindsay, A. J., Read, R. J., McCoy, A. J., McCaffrey, M. W., and Khan, A. R. (2006). Crystal structure of rab11 in complex with rab11 family interacting protein 2. Structure 14, 1273–1283.

Jaleel, M., Nichols, R. J., Deak, M., Campbell, D. G., Gillardon, F., Knebel, A., and Alessi, D. R. (2007). LRRK2 phosphorylates moesin at threonine-558: characterization of how Parkinson's disease mutants affect kinase activity. Biochem. J. 405, 307–317.

Jékely, G., and Arendt, D. (2006). Evolution of intraflagellar transport from coated vesicles and autogenous origin of the eukaryotic cilium. Bioessays 28, 191–198.

Jian, X. et al. (2015). Molecular Basis for Cooperative Binding of Anionic Phospholipids to the PH Domain of the Arf GAP ASAP1. Structure 23, 1977–1988.

Jian, X., Brown, P., Schuck, P., Gruschus, J. M., Balbo, A., Hinshaw, J. E., and Randazzo, P. A. (2009). Autoinhibition of Arf GTPase-activating protein activity by the BAR domain in ASAP1. J. Biol. Chem. 284, 1652–1663.

Jin, H., White, S. R., Shida, T., Schulz, S., Aguiar, M., Gygi, S. P., Bazan, J. F., and Nachury, M. V. (2010). The Conserved Bardet-Biedl Syndrome Proteins Assemble a Coat that Traffics Membrane Proteins to Cilia. Cell 141, 1208–U198.

JL, R., and CHILD, F. M. (1967). Flagellar Regeneration in Protozoan Flagellates. J. Cell Biol. 34, 345–&.

Jones, C., Roper, V. C., Foucher, I., Qian, D., Banizs, B., Petit, C., Yoder, B. K., and Chen, P. (2008). Ciliary proteins link basal body polarization to planar cell polarity regulation. Nat. Genet. 40, 69–77.

Jones, S., Litt, R. J., Richardson, C. J., and Segev, N. (1995). Requirement of nucleotide exchange factor for Ypt1 GTPase mediated protein transport. J. Cell Biol. 130, 1051–1061.

Jones, S., Newman, C., Liu, F., and Segev, N. (2000). The TRAPP complex is a nucleotide exchanger for Ypt1 and Ypt31/32. Mol. Biol. Cell 11, 4403–4411.

Junutula, J. R., Schonteich, E., Wilson, G. M., Peden, A. A., Scheller, R. H., and Prekeris, R. (2004). Molecular characterization of Rab11 interactions with members of the family of Rab11-interacting proteins. J. Biol. Chem. 279, 33430–33437.

Kahn, R. A., Cherfils, J., Elias, M., Lovering, R. C., Munro, S., and Schurmann, A. (2006). Nomenclature for the human Arf family of GTP-binding proteins: ARF, ARL, and SAR proteins. J. Cell Biol. 172, 645–650.

Kee, H. L., Dishinger, J. F., Blasius, T. L., Liu, C.-J., Margolis, B., and Verhey, K. J. (2012). A size-exclusion permeability barrier and nucleoporins characterize a ciliary pore complex that regulates transport into cilia. Nat. Cell Biol. 14, 431–.

Kelly, E. E., Horgan, C. P., and McCaffrey, M. W. (2012). Rab11 proteins in health and disease. Biochemical Society Transactions 40, 1360–1367.

Kennedy, M. P. et al. (2007). Congenital heart disease and other heterotaxic defects in a large cohort of patients with primary ciliary dyskinesia. Circulation 115, 2814–2821.

Khan, N. L. et al. (2005). Mutations in the gene LRRK2 encoding dardarin (PARK8) cause familial Parkinson's disease: clinical, pathological, olfactory and functional imaging and genetic data. Brain 128, 2786–2796.

Kim, S. K. et al. (2010). Planar Cell Polarity Acts Through Septins to Control Collective Cell Movement and Ciliogenesis. Science 329, 1337–1340.

Kindt, K. S., Finch, G., and Nicolson, T. (2012). Kinocilia Mediate Mechanosensitivity in Developing Zebrafish Hair Cells. Dev. Cell 23, 329–341.

Kirchhausen, T. (2000). Three ways to make a vesicle. Nat. Rev. Mol. Cell Biol. 1, 187–198.

Knödler, A., Feng, S., Zhang, J., Zhang, X., Das, A., Peränen, J., and Guo, W. (2010). Coordination of Rab8 and Rab11 in primary ciliogenesis. Proc. Natl. Acad. Sci. U.S.a. 107, 6346–6351.

Koulen, P., Cai, Y., Geng, L., Maeda, Y., Nishimura, S., Witzgall, R., Ehrlich, B. E., and Somlo, S. (2002). Polycystin-2 is an intracellular calcium release channel. Nat. Cell Biol. 4, 191–197.

Kozminski, K. G., Beech, P. L., and Rosenbaum, J. L. (1995). The Chlamydomonas kinesin-like protein FLA10 is involved in motility associated with the flagellar membrane. J. Cell Biol. 131, 1517–1527.

Kozminski, K. G., Johnson, K. A., Forscher, P., and Rosenbaum, J. L. (1993). A motility in the eukaryotic flagellum unrelated to flagellar beating. Proc. Natl. Acad. Sci. U.S.a. 90, 5519–5523.

Kulaga, H. M., Leitch, C. C., Eichers, E. R., Badano, J. L., Lesemann, A., Hoskins, B. E., Lupski, J. R., Beales, P. L., Reed, R. R., and Katsanis, N. (2004). Loss of BBS proteins causes anosmia in humans and defects in olfactory cilia structure and function in the mouse. Nat. Genet. 36, 994–998.

Laflamme, C., Assaker, G., Ramel, D., Dorn, J. F., She, D., Maddox, P. S., and Emery, G. (2012). Evi5 promotes collective cell migration through its Rab-GAP activity. J. Cell Biol. 198, 57–67.

Lapierre, L. A., Kumar, R., Hales, C. M., Navarre, J., Bhartur, S. G., Burnette, J. O., Provance, D. W., Mercer, J. A., Bähler, M., and Goldenring, J. R. (2001). Myosin vb is associated with plasma membrane recycling systems. Mol. Biol. Cell 12, 1843–1857.

Lee, M. C. S., Miller, E. A., Goldberg, J., Orci, L., and Schekman, R. (2004). Bi-directional protein transport between the ER and Golgi. Annu. Rev. Cell Dev. Biol. 20, 87–123.

Lee, M.-T. G., Mishra, A., and Lambright, D. G. (2009). Structural Mechanisms for Regulation of Membrane Traffic by Rab GTPases. Traffic 10, 1377–1389.

Li, T., Snyder, W. K., Olsson, J. E., and Dryja, T. P. (1996). Transgenic mice carrying the dominant rhodopsin mutation P347S: evidence for defective vectorial transport of rhodopsin to the outer segments. Proc. Natl. Acad. Sci. U.S.a. 93, 14176–14181.

Ligeti, E., Welti, S., and Scheffzek, K. (2012). Inhibition and termination of physiological responses by GTPase activating proteins. Physiol. Rev. 92, 237–272.

Lindemann, C. B., and Lesich, K. A. (2010). Flagellar and ciliary beating: the proven and the possible. J. Cell. Sci. 123, 519–528.

Lodowski, K. H., Lee, R., Ropelewski, P., Nemet, I., Tian, G., and Imanishi, Y. (2013). Signals governing the trafficking and mistrafficking of a ciliary GPCR, rhodopsin. J. Neurosci. 33, 13621–13638.

Logan, C. Y., and Nusse, R. (2004). The Wnt signaling pathway in development and disease. Annu. Rev. Cell Dev. Biol. 20, 781–810.

Lowery, J., Szul, T., Styers, M., Holloway, Z., Oorschot, V., Klumperman, J., and Sztul, E. (2013). The Sec7 guanine nucleotide exchange factor GBF1 regulates membrane recruitment of BIG1 and BIG2 guanine nucleotide exchange factors to the trans-Golgi network (TGN). J. Biol. Chem. 288, 11532–11545.

Lynn, D. H. (2008). The Ciliated Protozoa, Springer Science & Business Media.

Lyons, R. A., Saridogan, E., and Djahanbakhch, O. (2006). The reproductive significance of human Fallopian tube cilia.

Marshall, W. F., and Rosenbaum, J. L. (2001). Intraflagellar transport balances continuous turnover of outer doublet microtubules: implications for flagellar length control. J. Cell Biol. 155, 405–414.

Marszalek, J. R., Liu, X., Roberts, E. A., Chui, D., Marth, J. D., Williams, D. S., and Goldstein, L. S. (2000). Genetic evidence for selective transport of opsin and arrestin by kinesin-II in mammalian photoreceptors. Cell 102, 175–187.

Marszalek, J. R., Ruiz-Lozano, P., Roberts, E., Chien, K. R., and Goldstein, L. (1999). Situs inversus and embryonic ciliary morphogenesis defects in mouse mutants lacking the KIF3A subunit of kinesin-II. Proc. Natl. Acad. Sci. U.S.a. 96, 5043–5048.

Martens, S., and McMahon, H. T. (2008). Mechanisms of membrane fusion: disparate players and common principles. Nat. Rev. Mol. Cell Biol. 9, 543–556.

Martin, V., and Shaw-Smith, C. (2010). Review of genetic factors in intestinal malrotation. Pediatr. Surg. Int. 26, 769–781.

Masyuk, A. I., Masyuk, T. V., Splinter, P. L., Huang, B. Q., Stroope, A. J., and LaRusso, N. F. (2006). Cholangiocyte cilia detect changes in luminal fluid flow and transmit them into intracellular Ca2+ and cAMP signaling. Gastroenterology 131, 911–920.

Matsui, Y., Kikuchi, A., Araki, S., Hata, Y., Kondo, J., Teranishi, Y., and Takai, Y. (1990). Molecular cloning and characterization of a novel type of regulatory protein (GDI) for smg p25A, a ras p21-like GTP-binding protein. Mol. Cell. Biol. 10, 4116–4122.

Mazelova, J., Astuto-Gribble, L., Inoue, H., Tam, B. M., Schonteich, E., Prekeris, R., Moritz, O. L., Randazzo, P. A., and Deretic, D. (2009a). Ciliary targeting motif VxPx directs assembly of a trafficking module through Arf4. Embo J. 28, 183–192.

Mazelova, J., Ransom, N., Astuto-Gribble, L., Wilson, M. C., and Deretic, D. (2009b). Syntaxin 3 and SNAP-25 pairing, regulated by omega-3 docosahexaenoic acid, controls the delivery of rhodopsin for the biogenesis of cilia-derived sensory organelles, the rod outer segments. J. Cell. Sci. 122, 2003–2013.

McEwen, D. P., Jenkins, P. M., and Martens, J. R. (2007). Chapter 12 Olfactory Cilia: Our Direct Neuronal Connection to the External World. Curr. Top. Dev. Biol. 85, 333–370.

McGrath, J., Somlo, S., Makova, S., Tian, X., and Brueckner, M. (2003). Two populations of node monocilia initiate left-right asymmetry in the mouse. Cell 114, 61–73.

McMahon, A. P., Ingham, P. W., and Tabin, C. J. (2003). Developmental roles and clinical significance of hedgehog signaling. Curr. Top. Dev. Biol. 53, 1–114.

McMurray, M. A., Bertin, A., Garcia, G. I., Lam, L., Nogales, E., and Thorner, J. (2011). Septin Filament Formation Is Essential in Budding Yeast. Dev. Cell 20, 540–549.

Medkova, M., France, Y. E., Coleman, J., and Novick, P. (2006). The rab exchange factor Sec2p reversibly associates with the exocyst. Mol. Biol. Cell 17, 2757–2769.

Menco, B., and Morrison, E. E. (2003). Morphology of the mammalian olfactory epithelium: form, fine structure, function, and pathology. Neurological Disease and ….

Milburn, M. V., Tong, L., deVos, A. M., Brünger, A., Yamaizumi, Z., Nishimura, S., and Kim, S. H. (1990). Molecular switch for signal transduction: structural differences between active and inactive forms of protooncogenic ras proteins. Science 247, 939–945.

Mizuno-Yamasaki, E., Medkova, M., Coleman, J., and Novick, P. (2010). Phosphatidylinositol 4-phosphate controls both membrane recruitment and a regulatory switch of the Rab GEF Sec2p. Dev. Cell 18, 828–840.

Mizuno-Yamasaki, E., Rivera-Molina, F., and Novick, P. (2012). GTPase networks in membrane traffic. Annu. Rev. Biochem. 81, 637–659.

Molla-Herman, A. et al. (2010). The ciliary pocket: an endocytic membrane domain at the base of primary and motile cilia. J. Cell. Sci. 123, 1785–1795.

MONTESANO, R. (1979). Inhomogeneous Distribution of Filipin-Sterol Complexes in Smooth-Muscle Cell Plasma-Membrane. Nature 280, 328–329.

Morgan, D., Eley, L., Sayer, J., Strachan, T., Yates, L. M., Craighead, A. S., and Goodship, J. A. (2002a). Expression analyses and interaction with the anaphase promoting complex protein Apc2 suggest a role for inversin in primary cilia and involvement in the cell cycle. Hum. Mol. Genet. 11, 3345–3350.

Morgan, G. W., Hall, B. S., Denny, P. W., Carrington, M., and Field, M. C. (2002b). The kinetoplastida endocytic apparatus. Part I: a dynamic system for nutrition and evasion of host defences. Trends Parasitol. 18, 491–496.

Morgan, G. W., Hall, B. S., Denny, P. W., Field, M. C., and Carrington, M. (2002c). The endocytic apparatus of the kinetoplastida. Part II: machinery and components of the system. Trends Parasitol. 18, 540–546.

Moritz, O. L., Tam, B. M., Hurd, L. L., Peränen, J., Deretic, D., and Papermaster, D. S. (2001). Mutant rab8 Impairs docking and fusion of rhodopsin-bearing post-Golgi membranes and causes cell death of transgenic Xenopus rods. Mol. Biol. Cell 12, 2341–2351.

Morozova, N., Liang, Y., Tokarev, A. A., Chen, S. H., Cox, R., Andrejic, J., Lipatova, Z., Sciorra, V. A., Emr, S. D., and Segev, N. (2006). TRAPPII subunits are required for the specificity switch of a Ypt-Rab GEF. Nat. Cell Biol. 8, 1263–1269.

Mourão, A., Nager, A. R., and Nachury, M. V. (2014). Structural basis for membrane targeting of the BBSome by ARL6. Nature Structural & ….

Mukhopadhyay, S., Lu, Y., Shaham, S., and Sengupta, P. (2008). Sensory signaling-dependent remodeling of olfactory cilia architecture in C. elegans. Dev. Cell 14, 762–774.

Munro, N. C., Currie, D. C., Lindsay, K. S., Ryder, T. A., Rutman, A., Dewar, A., Greenstone, M. A., Hendry, W. F., and Cole, P. J. (1994). Fertility in men with primary ciliary dyskinesia presenting with respiratory infection. Thorax 49, 684–687.

Musgrave, A., de Wildt, P., van Etten, I., Pijst, H., Scholma, C., Kooyman, R., Homan, W., and van den Ende, H. (1986). Evidence for a functional membrane barrier in the transition zone between the flagellum and cell body of Chlamydomonas eugametos gametes. Planta 167, 544–553.

MYLES, D. G., PRIMAKOFF, P., and KOPPEL, D. E. (1984). A Localized Surface Protein of Guinea-Pig Sperm Exhibits Free Diffusion in Its Domain. J. Cell Biol. 98, 1905–1909.

Nachury, M. V. et al. (2007). A core complex of BBS proteins cooperates with the GTPase Rab8 to promote ciliary membrane biogenesis. Cell 129, 1201–1213.

Nachury, M. V., Seeley, E. S., and Jin, H. (2010). Trafficking to the ciliary membrane: how to get across the periciliary diffusion barrier? Annu. Rev. Cell Dev. Biol. 26, 59–87.

Nagao, S., Nishii, K., Yoshihara, D., Kurahashi, H., Nagaoka, K., Yamashita, T., Takahashi, H., Yamaguchi, T., Calvet, J. P., and Wallace, D. P. (2008). Calcium channel inhibition accelerates polycystic kidney disease progression in the Cy/+ rat. Kidney Int. 73, 269–277.

Najafi, M., Maza, N. A., and Calvert, P. D. (2012). Steric volume exclusion sets soluble protein concentrations in photoreceptor sensory cilia. Proc. Natl. Acad. Sci. U.S.a. 109, 203–208.

Nakamura, T., and Gold, G. H. (1987). A cyclic nucleotide-gated conductance in olfactory receptor cilia. Nature 325, 442–444.

Nauli, S. M. et al. (2003). Polycystins 1 and 2 mediate mechanosensation in the primary cilium of kidney cells. Nat. Genet. 33, 129–137.

Neu, M., Brachvogel, V., Oschkinat, H., Zerial, M., and Metcalf, P. (1997). Rab7: NMR and kinetics analysis of intact and C-terminal truncated constructs. Proteins 27, 204–209.

Nie, Z. et al. (2006). A BAR domain in the N terminus of the Arf GAP ASAP1 affects membrane structure and trafficking of epidermal growth factor receptor. Curr. Biol. 16, 130–139.

Nonaka, S., Shiratori, H., Saijoh, Y., and Hamada, H. (2002). Determination of left-right patterning of the mouse embryo by artificial nodal flow. Nature 418, 96–99.

Nonaka, S., Tanaka, Y., Okada, Y., Takeda, S., Harada, A., Kanai, Y., Kido, M., and Hirokawa, N. (1998). Randomization of left-right asymmetry due to loss of nodal cilia generating leftward flow of extraembryonic fluid in mice lacking KIF3B motor protein. Cell 95, 829–837.

Nurnberger, J., Bacallao, R. L., and Phillips, C. L. (2002). Inversin forms a complex with catenins and N-cadherin in polarized epithelial cells. Mol. Biol. Cell 13, 3096–3106.

Nurnberger, J., Kribben, A., Saez, A. O., Heusch, G., Philipp, T., and Phillips, C. L. (2004). The Invs gene encodes a microtubule-associated protein. J. Am. Soc. Nephrol. 15, 1700–1710.

Ocbina, P. J. R., Tuson, M., and Anderson, K. V. (2008). Primary cilia are not required for normal canonical Wnt signaling in the mouse embryo. PLoS ONE 4, e6839–e6839.

Olbrich, H. et al. (2002). Mutations in DNAH5 cause primary ciliary dyskinesia and

randomization of left-right asymmetry. Nat. Genet. 30, 143–144.

Omori, Y., Zhao, C., Saras, A., Mukhopadhyay, S., Kim, W., Furukawa, T., Sengupta, P., Veraksa, A., and Malicki, J. (2008). Elipsa is an early determinant of ciliogenesis that links the IFT particle to membrane-associated small GTPase Rab8. Nat. Cell Biol. 10, 437–444.

Orozco, J. T., Wedaman, K. P., Signor, D., Brown, H., Rose, L., and Scholey, J. M. (1999). Movement of motor and cargo along cilia. Nature 398, 674.

Ortiz, D., Medkova, M., Walch-Solimena, C., and Novick, P. (2002). Ypt32 recruits the Sec4p guanine nucleotide exchange factor, Sec2p, to secretory vesicles; evidence for a Rab cascade in yeast. J. Cell Biol. 157, 1005–1015.

Ostermeier, C., and Brunger, A. T. (1999). Structural basis of Rab effector specificity: crystal structure of the small G protein Rab3A complexed with the effector domain of rabphilin-3A. Cell 96, 363–374.

Otto, E. A. et al. (2003). Mutations in INVS encoding inversin cause nephronophthisis type 2, linking renal cystic disease to the function of primary cilia and left-right axis determination. Nat. Genet. 34, 413–420.

Ounjai, P., Kim, K. D., Liu, H., Dong, M., Tauscher, A. N., Witkowska, H. E., and Downing, K. H. (2013). Architectural insights into a ciliary partition. Curr. Biol. 23, 339–344.

Overath, P., and Engstler, M. (2004). Endocytosis, membrane recycling and sorting of GPI-anchored proteins: Trypanosoma brucei as a model system. Mol. Microbiol. 53, 735–744.

Overath, P., Stierhof, Y. D., and Wiese, M. (1997). Endocytosis and secretion in trypanosomatid parasites - Tumultuous traffic in a pocket. Trends Cell Biol. 7, 27–33.

Palade, G. (1975). Intracellular aspects of the process of protein synthesis. Science 189, 867.

Pan, X., Eathiraj, S., Munson, M., and Lambright, D. G. (2006). TBC-domain GAPs for Rab GTPases accelerate GTP hydrolysis by a dual-finger mechanism. Nature 442, 303–306.

Papermaster, D. S., Schneider, B. G., and Besharse, J. C. (1985). Vesicular transport of newly synthesized opsin from the Golgi apparatus toward the rod outer segment. Ultrastructural immunocytochemical and autoradiographic evidence in Xenopus retinas. Invest. Ophthalmol. Vis. Sci. 26, 1386–1404.

Park, T. J., Mitchell, B. J., Abitua, P. B., Kintner, C., and Wallingford, J. B. (2008). Dishevelled controls apical docking and planar polarization of basal bodies in ciliated epithelial cells. Nat. Genet. 40, 871–879.

Parnell, S. C., Magenheimer, B. S., Maser, R. L., Zien, C. A., Frischauf, A.-M., and Calvet, J. P. (2002). Polycystin-1 activation of c-Jun N-terminal kinase and AP-1 is mediated by heterotrimeric G proteins. J. Biol. Chem. 277, 19566–19572.

Pasqualato, S., Renault, L., and Cherfils, J. (2002). Arf, Arl, Arp and Sar proteins: a family of GTP-binding proteins with a structural device for "front-back"

communication. EMBO Rep. 3, 1035–1041.

Pasqualato, S., Senic-Matuglia, F., Renault, L., Goud, B., Salamero, J., and Cherfils, J. (2004). The structural GDP/GTP cycle of Rab11 reveals a novel interface involved in the dynamics of recycling endosomes. J. Biol. Chem. 279, 11480–11488.

Pazour, G. J., Agrin, N., Leszyk, J., and Witman, G. B. (2005). Proteomic analysis of a eukaryotic cilium. J. Cell Biol. 170, 103–113.

Pazour, G. J., and Bloodgood, R. A. (2008). Targeting proteins to the ciliary membrane. Curr. Top. Dev. Biol. 85, 115–149.

Pazour, G. J., Baker, S. A., Deane, J. A., Cole, D. G., Dickert, B. L., Rosenbaum, J. L., Witman, G. B., and Besharse, J. C. (2002a). The intraflagellar transport protein, IFT88, is essential for vertebrate photoreceptor assembly and maintenance. J. Cell Biol. 157, 103–113.

Pazour, G. J., Dickert, B. L., and Witman, G. B. (1999). The DHC1b (DHC2) isoform of cytoplasmic dynein is required for flagellar assembly. J. Cell Biol. 144, 473–481.

Pazour, G. J., Dickert, B. L., Vucica, Y., Seeley, E. S., Rosenbaum, J. L., Witman, G. B., and Cole, D. G. (2000). Chlamydomonas IFT88 and its mouse homologue, polycystic kidney disease gene tg737, are required for assembly of cilia and flagella. J. Cell Biol. 151, 709–718.

Pazour, G. J., San Agustin, J. T., Follit, J. A., Rosenbaum, J. L., and Witman, G. B. (2002b). Polycystin-2 localizes to kidney cilia and the ciliary level is elevated in orpk mice with polycystic kidney disease. Curr. Biol. 12, R378–R380.

Pedersen, L. B., and Rosenbaum, J. L. (2008). Intraflagellar transport (IFT) role in ciliary assembly, resorption and signalling. Curr. Top. Dev. Biol. 85, 23–61.

Pedersen, L. B., Geimer, S., and Rosenbaum, J. L. (2006). Dissecting the molecular mechanisms of intraflagellar transport in chlamydomonas. Curr. Biol. 16, 450–459.

Pedersen, L. B., Veland, I. R., Schrøder, J. M., and Christensen, S. T. (2008). Assembly of primary cilia. Dev. Dyn. 237, 1993–2006.

Pereira-Leal, J. B., and Seabra, M. C. (2000). The mammalian Rab family of small GTPases: definition of family and subfamily sequence motifs suggests a mechanism for functional specificity in the Ras superfamily. J. Mol. Biol. 301, 1077–1087.

Pereira-Leal, J. B., and Seabra, M. C. (2001). Evolution of the Rab family of small GTP-binding proteins. J. Mol. Biol. 313, 889–901.

Perkins, L. A., Hedgecock, E. M., Thomson, J. N., and Culotti, J. G. (1986). Mutant sensory cilia in the nematode Caenorhabditis elegans. Dev. Biol. 117, 456–487.

Perrone, C. A., Tritschler, D., Taulman, P., Bower, R., Yoder, B. K., and Porter, M. E. (2003). A novel dynein light intermediate chain colocalizes with the retrograde motor for intraflagellar transport at sites of axoneme assembly in chlamydomonas and Mammalian cells. Mol. Biol. Cell 14, 2041–2056.

Peter, B. J., Kent, H. M., Mills, I. G., Vallis, Y., Butler, P. J. G., Evans, P. R., and McMahon, H. T. (2004). BAR domains as sensors of membrane curvature: the

amphiphysin BAR structure. Science 303, 495–499.

Pfeffer, S., and Aivazian, D. (2004). Targeting Rab GTPases to distinct membrane compartments. Nat. Rev. Mol. Cell Biol. 5, 886–896.

Pfister, K. K. et al. (2005). Cytoplasmic dynein nomenclature. J. Cell Biol. 171, 411–413.

Pigino, G., Geimer, S., Lanzavecchia, S., Paccagnini, E., Cantele, F., Diener, D. R., Rosenbaum, J. L., and Lupetti, P. (2009). Electron-tomographic analysis of intraflagellar transport particle trains in situ. J. Cell Biol. 187, 135–148.

Pinar, M., Arst, H. N., Pantazopoulou, A., Tagua, V. G., de los Ríos, V., Rodríguez-Salarichs, J., Díaz, J. F., and Peñalva, M. A. (2015). TRAPPII regulates exocytic Golgi exit by mediating nucleotide exchange on the Ypt31 ortholog RabERAB11. Proc. Natl. Acad. Sci. U.S.a. 112, 4346–4351.

Piperno, G., and Mead, K. (1997). Transport of a novel complex in the cytoplasmic matrix of Chlamydomonas flagella. Proc. Natl. Acad. Sci. U.S.a. 94, 4457–4462.

Piperno, G., Siuda, E., Henderson, S., Segil, M., Vaananen, H., and Sassaroli, M. (1998). Distinct mutants of retrograde intraflagellar transport (IFT) share similar morphological and molecular defects. J. Cell Biol. 143, 1591–1601.

Poole, C. A., Flint, M. H., and Beaumont, B. W. (1985). Analysis of the morphology and function of primary cilia in connective tissues: a cellular cybernetic probe? Cell Motil. 5, 175–193.

Porter, M. E., Bower, R., Knott, J. A., Byrd, P., and Dentler, W. (1999). Cytoplasmic dynein heavy chain 1b is required for flagellar assembly in Chlamydomonas. Mol. Biol. Cell 10, 693–712.

Praetorius, H. A., and Spring, K. R. (2001). Bending the MDCK cell primary cilium increases intracellular calcium. J. Membr. Biol. 184, 71–79.

Purves, D., Augustine, G. J., Fitzpatrick, D., and Katz, L. C. (2001). Hair Cells and the Mechanoelectrical Transduction of Sound Waves.

Pylypenko, O., Attanda, W., Gauquelin, C., Lahmani, M., Coulibaly, D., Baron, B., Hoos, S., Titus, M. A., England, P., and Houdusse, A. M. (2013). Structural basis of myosin V Rab GTPase-dependent cargo recognition. Proc. Natl. Acad. Sci. U.S.a. 110, 20443–20448.

Qin, H., Diener, D. R., Geimer, S., Cole, D. G., and Rosenbaum, J. L. (2004). Intraflagellar transport (IFT) cargo: IFT transports flagellar precursors to the tip and turnover products to the cell body. J. Cell Biol. 164, 255–266.

Qin, H., Rosenbaum, J. L., and Barr, M. M. (2001). An autosomal recessive polycystic kidney disease gene homolog is involved in intraflagellar transport in C. elegans ciliated sensory neurons. Curr. Biol. 11, 457–461.

Rajagopalan, V., Corpuz, E. O., Hubenschmidt, M. J., Townsend, C. R., Asai, D. J., and Wilkes, D. E. (2008). Analysis of properties of cilia using Tetrahymena thermophila. Methods Mol. Biol. 586, 283–299.

Ralston, K. S., and Hill, K. L. (2008). The flagellum of Trypanosoma brucei: new tricks from an old dog. Int. J. Parasitol. 38, 869–884.

Ramalho-Santos, M., Melton, D. A., and McMahon, A. P. (2000). Hedgehog signals regulate multiple aspects of gastrointestinal development. Development 127, 2763–2772.

Randazzo, P. A., and Hirsch, D. S. (2004). Arf GAPs: multifunctional proteins that regulate membrane traffic and actin remodelling. Cell. Signal. 16, 401–413.

Randazzo, P. A., Weiss, O., and Kahn, R. A. (1992). Preparation of recombinant ADP-ribosylation factor. Meth. Enzymol. 219, 362–369.

Raven, P. H., Evert, R. F., and Eichhorn, S. E. (1999). Biology of Plants & Offline Companion.

Recacha, R., Boulet, A., Jollivet, F., Monier, S., Houdusse, A., Goud, B., and Khan, A. R. (2009). Structural basis for recruitment of Rab6-interacting protein 1 to Golgi via a RUN domain. Structure 17, 21–30.

Recchi, C., and Seabra, M. C. (2012). Novel functions for Rab GTPases in multiple aspects of tumour progression. Biochemical Society Transactions 40, 1398–1403.

Reiners, J., Nagel-Wolfrum, K., Juergens, K., Maerker, T., and Wolfrum, U. (2006). Molecular basis of human Usher syndrome: Deciphering the meshes of the Usher protein network provides insights into the pathomechanisms of the Usher disease. Exp. Eye Res. 83, 97–119.

Reiter, J. F., Blacque, O. E., and Leroux, M. R. (2012). The base of the cilium: roles for transition fibres and the transition zone in ciliary formation, maintenance and compartmentalization. EMBO Rep. 13, 608–618.

Robinson, R. (2006). Ciliate genome sequence reveals unique features of a model eukaryote. PLoS Biol. 4, e304.

Rogers, K. K., Wilson, P. D., Snyder, R. W., Zhang, X., Guo, W., Burrow, C. R., and Lipschutz, J. H. (2004). The exocyst localizes to the primary cilium in MDCK cells. Biochem. Biophys. Res. Commun. 319, 138–143.

Rohatgi, R., Milenkovic, L., and Scott, M. P. (2007). Patched1 regulates Hedgehog signaling at the primary cilium. Science 317, 372–376.

Ronnett, G. V., and Moon, C. (2002). G proteins and olfactory signal transduction. Annu. Rev. Physiol. 64, 189–222.

Rosenbaum, J. L., and Witman, G. B. (2002). Intraflagellar transport. Nat. Rev. Mol. Cell Biol. 3, 813–825.

Rosenbaum, J. L., Cole, D. G., and Diener, D. R. (1999). Intraflagellar transport: The eyes have it. J. Cell Biol. 144, 385–388.

Ross, A. J. et al. (2005). Disruption of Bardet-Biedl syndrome ciliary proteins perturbs planar cell polarity in vertebrates. Nat. Genet. 37, 1135–1140.

Saadi-Kheddouci, S., Berrebi, D., Romagnolo, B., Cluzeaud, F., Peuchmaur, M., Kahn, A., Vandewalle, A., and Perret, C. (2001). Early development of polycystic

kidney disease in transgenic mice expressing an activated mutant of the beta-catenin gene. Oncogene 20, 5972–5981.

Sacher, M., Barrowman, J., Wang, W., Horecka, J., Zhang, Y., Pypaert, M., and Ferro-Novick, S. (2001). TRAPP I implicated in the specificity of tethering in ER-to-Golgi transport. Mol. Cell 7, 433–442.

Sakaguchi, A., Sato, M., Sato, K., Gengyo-Ando, K., Yorimitsu, T., Nakai, J., Hara, T., Sato, K., and Sato, K. (2015). REI-1 Is a Guanine Nucleotide Exchange Factor Regulating RAB-11 Localization and Function in C. elegans Embryos. Dev. Cell 35, 211–221.

Saraste, M., Sibbald, P. R., and Wittinghofer, A. (1990). The P-loop--a common motif in ATP- and GTP-binding proteins. Trends Biochem. Sci. 15, 430–434.

Satir, P., and Christensen, S. T. (2007). Overview of structure and function of mammalian cilia. Annu. Rev. Physiol. 69, 377–400.

Sato, Y., Shirakawa, R., Horiuchi, H., Dohmae, N., Fukai, S., and Nureki, O. (2007). Asymmetric coiled-coil structure with Guanine nucleotide exchange activity. Structure 15, 245–252.

Schafer, J. C., Haycraft, C. J., Thomas, J. H., Yoder, B. K., and Swoboda, P. (2003). XBX-1 encodes a dynein light intermediate chain required for retrograde intraflagellar transport and cilia assembly in Caenorhabditis elegans. Mol. Biol. Cell 14, 2057–2070.

Schiel, J. A., Simon, G. C., Zaharris, C., Weisz, J., Castle, D., Wu, C. C., and Prekeris, R. (2012). FIP3-endosome-dependent formation of the secondary ingression mediates ESCRT-III recruitment during cytokinesis. Nat. Cell Biol. 14, 1068–1078.

Schneider, L., Clement, C. A., Teilmann, S. C., Pazour, G. J., Hoffmann, E. K., Satir, P., and Christensen, S. T. (2005). PDGFRalphaalpha signaling is regulated through the primary cilium in fibroblasts. Curr. Biol. 15, 1861–1866.

Scholey, J. M. (2008). Intraflagellar transport motors in cilia: moving along the cell's antenna. J. Cell Biol. 180, 23–29.

Scholey, J. M. (2012). Kinesin-2 motors transport IFT-particles, dyneins and tubulin subunits to the tips of Caenorhabditis elegans sensory cilia: relevance to vision research? Vision Res. 75, 44–52.

Schonteich, E., Pilli, M., Simon, G. C., Matern, H. T., Junutula, J. R., Sentz, D., Holmes, R. K., and Prekeris, R. (2007). Molecular characterization of Rab11-FIP3 binding to ARF GTPases. Eur J Cell Biol 86, 417–431.

Schwartz, E. A., Leonard, M. L., Bizios, R., and Bowser, S. S. (1997). Analysis and modeling of the primary cilium bending response to fluid shear. Am. J. Physiol. Renal Physiol. 272, F132–F138.

Schwartz, S. L., Cao, C., Pylypenko, O., Rak, A., and Wandinger-Ness, A. (2007). Rab GTPases at a glance. J. Cell. Sci. 120, 3905–3910.

Seabra, M. C. (1996). Nucleotide dependence of Rab geranylgeranylation - Rab

escort protein interacts preferentially with GDP-bound Rab. J. Biol. Chem. 271, 14398–14404.

Seabra, M. C., and Wasmeier, C. (2004). Controlling the location and activation of Rab GTPases. Curr. Opin. Cell Biol. 16, 451–457.

Seixas, E., Barros, M., Seabra, M. C., and Barral, D. C. (2013). Rab and Arf proteins in genetic diseases. Traffic 14, 871–885.

Settembre, C., Fraldi, A., Medina, D. L., and Ballabio, A. (2013). Signals from the lysosome: a control centre for cellular clearance and energy metabolism. Nat. Rev. Mol. Cell Biol. 14, 283–296.

Sharma, N., Berbari, N. F., and Yoder, B. K. (2008). Ciliary dysfunction in developmental abnormalities and diseases. Curr. Top. Dev. Biol. 85, 371–427.

Shen, F., and Seabra, M. C. (1996). Mechanism of digeranylgeranylation of rab proteins - Formation of a complex between monogeranylgeranyl-rab and rab escort protein. J. Biol. Chem. 271, 3692–3698.

Shiba, T., Koga, H., Shin, H.-W., Kawasaki, M., Kato, R., Nakayama, K., and Wakatsuki, S. (2006). Structural basis for Rab11-dependent membrane recruitment of a family of Rab11-interacting protein 3 (FIP3)/Arfophilin-1. Proc. Natl. Acad. Sci. U.S.a. 103, 15416–15421.

Shida, T., Cueva, J. G., Xu, Z., Goodman, M. B., and Nachury, M. V. (2010). The major alpha-tubulin K40 acetyltransferase alphaTAT1 promotes rapid ciliogenesis and efficient mechanosensation. Proc. Natl. Acad. Sci. U.S.a. 107, 21517–21522.

Simons, M. et al. (2005). Inversin, the gene product mutated in nephronophthisis type II, functions as a molecular switch between Wnt signaling pathways. Nat. Genet. 37, 537–543.

Simón-Sánchez, J. et al. (2009). Genome-wide association study reveals genetic risk underlying Parkinson's disease. Nat. Genet. 41, 1308–1312.

Singla, V., and Reiter, J. F. (2006). The primary cilium as the cell's antenna: signaling at a sensory organelle. Science 313, 629–633.

Sivars, U., Aivazian, D., and Pfeffer, S. R. (2003). Yip3 catalyses the dissociation of endosomal Rab-GDI complexes. Nature 425, 856–859.

Sloboda, R. D. (2005). Intraflagellar transport and the flagellar tip complex. J. Cell. Biochem. 94, 266–272.

Soldati, T., Shapiro, A. D., Svejstrup, A. B., and Pfeffer, S. R. (1994). Membrane targeting of the small GTPase Rab9 is accompanied by nucleotide exchange. Nature 369, 76–78.

Song, A.-H., Wang, D., Chen, G., Li, Y., Luo, J., Duan, S., and Poo, M.-M. (2009). A selective filter for cytoplasmic transport at the axon initial segment. Cell 136, 1148–1160.

SOROKIN, S. (1962). Centrioles and the formation of rudimentary cilia by fibroblasts and smooth muscle cells. J. Cell Biol. 15, 363–377.

Sorokin, S. P. (1968). Reconstructions of centriole formation and ciliogenesis in mammalian lungs. J. Cell. Sci. 3, 207–230.

Stalder, D., Mizuno-Yamasaki, E., Ghassemian, M., and Novick, P. J. (2013). Phosphorylation of the Rab exchange factor Sec2p directs a switch in regulatory binding partners. Proc. Natl. Acad. Sci. U.S.a. 110, 19995–20002.

Stenmark, H. (2009). Rab GTPases as coordinators of vesicle traffic. Nat. Rev. Mol. Cell Biol. 10, 513–525.

Stenmark, H., Parton, R. G., Steele-Mortimer, O., Lütcke, A., Gruenberg, J., and Zerial, M. (1994). Inhibition of rab5 GTPase activity stimulates membrane fusion in endocytosis. Embo J. 13, 1287–1296.

Stewart, M. (2007). Molecular mechanism of the nuclear protein import cycle. Nat. Rev. Mol. Cell Biol. 8, 195–208.

Stroupe, C., and Brunger, A. T. (2000). Crystal structures of a Rab protein in its inactive and active conformations. J. Mol. Biol. 304, 585–598.

Sung, C. H., Makino, C., Baylor, D., and Nathans, J. (1994). A rhodopsin gene mutation responsible for autosomal dominant retinitis pigmentosa results in a protein that is defective in localization to the photoreceptor outer segment. J. Neurosci. 14, 5818–5833.

Szul, T., Grabski, R., Lyons, S., Morohashi, Y., Shestopal, S., Lowe, M., and Sztul, E. (2007). Dissecting the role of the ARF guanine nucleotide exchange factor GBF1 in Golgi biogenesis and protein trafficking. J. Cell. Sci. 120, 3929–3940.

Takao, D., Nemoto, T., Abe, T., Kiyonari, H., Kajiura-Kobayashi, H., Shiratori, H., and Nonaka, S. (2013). Asymmetric distribution of dynamic calcium signals in the node of mouse embryo during left-right axis formation. Dev. Biol. 376, 23–30.

Tam, B. M., Moritz, O. L., Hurd, L. B., and Papermaster, D. S. (2000). Identification of an outer segment targeting signal in the COOH terminus of rhodopsin using transgenic Xenopus laevis. J. Cell Biol. 151, 1369–1380.

Tanaka, Y., Okada, Y., and Hirokawa, N. (2005). FGF-induced vesicular release of Sonic hedgehog and retinoic acid in leftward nodal flow is critical for left-right determination. Nature 435, 172–177.

Tao, B., Bu, S., Yang, Z., Siroky, B., Kappes, J. C., Kispert, A., and Guay-Woodford, L. M. (2009). Cystin localizes to primary cilia via membrane microdomains and a targeting motif. J. Am. Soc. Nephrol. 20, 2570–2580.

Taylor, R. W., and Turnbull, D. M. (2005). Mitochondrial DNA mutations in human disease. Nat. Rev. Genet. 6, 389–402.

TerBush, D. R., Maurice, T., Roth, D., and Novick, P. (1996). The Exocyst is a multiprotein complex required for exocytosis in Saccharomyces cerevisiae. Embo J. 15, 6483–6494.

Tran, P. V. et al. (2008). THM1 negatively modulates mouse sonic hedgehog signal transduction and affects retrograde intraflagellar transport in cilia. Nat. Genet. 40, 403–410.

Tsao, C.-C., and Gorovsky, M. A. (2008). Tetrahymena IFT122A is not essential for cilia assembly but plays a role in returning IFT proteins from the ciliary tip to the cell body. J. Cell. Sci. 121, 428–436.

Tucker, R. W., Pardee, A. B., and Fujiwara, K. (1979). Centriole ciliation is related to quiescence and DNA synthesis in 3T3 cells. Cell 17, 527–535.

Udayar, V. et al. (2013). A paired RNAi and RabGAP overexpression screen identifies Rab11 as a regulator of β-amyloid production. Cell Rep 5, 1536–1551.

Ullrich, O., HORIUCHI, H., Bucci, C., and Zerial, M. (1994). Membrane association of Rab5 mediated by GDP-dissociation inhibitor and accompanied by GDP/GTP exchange. Nature 368, 157–160.

Ullrich, O., Reinsch, S., Urbé, S., Zerial, M., and Parton, R. G. (1996). Rab11 regulates recycling through the pericentriolar recycling endosome. J. Cell Biol. 135, 913–924.

Ullrich, O., Stenmark, H., ALEXANDROV, K., Huber, L. A., Kaibuchi, K., Sasaki, T., Takai, Y., and Zerial, M. (1993). Rab GDP dissociation inhibitor as a general regulator for the membrane association of rab proteins. J. Biol. Chem. 268, 18143–18150.

van Leeuwenhoek, A. (1677). Observations, Communicated to the Publisher by Mr. Antony Van Leewenhoeck, in a Dutch Letter of the 9th of Octob. 1676. Here English'd.

van's Gravesande, K. S., and Omran, H. (2005). Primary ciliary dyskinesia: Clinical presentation, diagnosis and genetics. Annals of Medicine 37, 439–449.

Veeman, M. T., Axelrod, J. D., and Moon, R. T. (2003). A second canon. Functions and mechanisms of beta-catenin-independent Wnt signaling. Dev. Cell 5, 367–377.

Vetter, I. R., and Wittinghofer, A. (2001). The guanine nucleotide-binding switch in three dimensions. Science 294, 1299–1304.

Vetter, M., Stehle, R., Basquin, C., and Lorentzen, E. (2015a). Structure of Rab11-FIP3-Rabin8 reveals simultaneous binding of FIP3 and Rabin8 effectors to Rab11. Nat. Struct. Mol. Biol.

Vetter, M., Wang, J., Lorentzen, E., and Deretic, D. (2015b). Novel topography of the Rab11-effector interaction network within a ciliary membrane targeting complex. Small GTPases 6, 165–173.

Vieira, O. V., Gaus, K., Verkade, P., Fullekrug, J., Vaz, W. L. C., and Simons, K. (2006). FAPP2, cilium formation, and compartmentalization of the apical membrane in polarized Madin-Darby canine kidney (MDCK) cells. Proc. Natl. Acad. Sci. U.S.a. 103, 18556–18561.

Vigil, D., Cherfils, J., Rossman, K. L., and Der, C. J. (2010). Ras superfamily GEFs and GAPs: validated and tractable targets for cancer therapy? Nat. Rev. Cancer 10, 842–857.

Walch-Solimena, C., Collins, R. N., and Novick, P. J. (1997). Sec2p mediates nucleotide exchange on Sec4p and is involved in polarized delivery of post-Golgi

vesicles. J. Cell Biol. 137, 1495–1509.

Walther, Z., Vashishtha, M., and Hall, J. L. (1994). The Chlamydomonas FLA10 gene encodes a novel kinesin-homologous protein. J. Cell Biol. 126, 175–188.

Wang, J., and Deretic, D. (2013). Molecular complexes that direct rhodopsin transport to primary cilia. Prog Retin Eye Res, –.

Wang, J., and Deretic, D. (2015). The Arf and Rab11 effector FIP3 acts synergistically with ASAP1 to direct Rabin8 in ciliary receptor targeting. J. Cell. Sci. 128, 1375–1385.

Wang, J., Morita, Y., Mazelova, J., and Deretic, D. (2012). The Arf GAP ASAP1 provides a platform to regulate Arf4- and Rab11-Rab8-mediated ciliary receptor targeting. Embo J.

Wang, W., and Ferro-Novick, S. (2002). A Ypt32p exchange factor is a putative effector of Ypt1p. Mol. Biol. Cell 13, 3336–3343.

Wang, W., Sacher, M., and Ferro-Novick, S. (2000). TRAPP stimulates guanine nucleotide exchange on Ypt1p. J. Cell Biol. 151, 289–296.

Wang, Z., Fan, Z.-C., Williamson, S. M., and Qin, H. (2009). Intraflagellar transport (IFT) protein IFT25 is a phosphoprotein component of IFT complex B and physically interacts with IFT27 in Chlamydomonas. PLoS ONE 4, e5384.

Ward, C. J. et al. (2002). The gene mutated in autosomal recessive polycystic kidney disease encodes a large, receptor-like protein. Nat. Genet. 30, 259–269.

Ward, C. J. et al. (2003). Cellular and subcellular localization of the ARPKD protein; fibrocystin is expressed on primary cilia. Hum. Mol. Genet. 12, 2703–2710.

Ward, H. H., Brown-Glaberman, U., Wang, J., Morita, Y., Alper, S. L., Bedrick, E. J., Gattone, V. H., Deretic, D., and Wandinger-Ness, A. (2011). A conserved signal and GTPase complex are required for the ciliary transport of polycystin-1. Mol. Biol. Cell 22, 3289–3305.

Ward, S., Thomson, N., White, J. G., and Brenner, S. (1975). Electron microscopical reconstruction of the anterior sensory anatomy of the nematode Caenorhabditis elegans.?2UU. J. Comp. Neurol. 160, 313–337.

Watanabe, D., Saijoh, Y., Nonaka, S., Sasaki, G., Ikawa, Y., Yokoyama, T., and Hamada, H. (2003). The left-right determinant Inversin is a component of node monocilia and other 9+0 cilia. Development 130, 1725–1734.

Waters, A. M., and Beales, P. L. (2011). Ciliopathies: an expanding disease spectrum. Pediatr. Nephrol. 26, 1039–1056.

Weirich, C. S., Erzberger, J. P., and Barral, Y. (2008). The septin family of GTPases: architecture and dynamics. Nat. Rev. Mol. Cell Biol. 9, 478–489.

Welz, T., Wellbourne-Wood, J., and Kerkhoff, E. (2014). Orchestration of cell surface proteins by Rab11. Trends Cell Biol. 24, 407–415.

Wennerberg, K., Rossman, K. L., and Der, C. J. (2005). The Ras superfamily at a glance. J. Cell. Sci. 118, 843–846.

West, A. B., Moore, D. J., Biskup, S., Bugayenko, A., Smith, W. W., Ross, C. A., Dawson, V. L., and Dawson, T. M. (2005). Parkinson's disease-associated mutations in leucine-rich repeat kinase 2 augment kinase activity. Proc. Natl. Acad. Sci. U.S.a. 102, 16842–16847.

Westlake, C. J. et al. (2011). Primary cilia membrane assembly is initiated by Rab11 and transport protein particle II (TRAPPII) complex-dependent trafficking of Rabin8 to the centrosome. Proc. Natl. Acad. Sci. U.S.a. 108, 2759–2764.

Wharton, K. A. (2003). Runnin' with the Dvl: Proteins that associate with Dsh/Dvl and their significance to Wnt signal transduction. Dev. Biol. 253, 1–17.

Wheatley, D. N., Wang, A. M., and Strugnell, G. E. (1996). Expression of primary cilia in mammalian cells. Cell Biol. Int. 20, 73–81.

Williams, C. L. et al. (2011). MKS and NPHP modules cooperate to establish basal body/transition zone membrane associations and ciliary gate function during ciliogenesis. J. Cell Biol. 192, 1023–1041.

Wilson, G. M., Fielding, A. B., Simon, G. C., Yu, X., Andrews, P. D., Hames, R. S., Frey, A. M., Peden, A. A., Gould, G. W., and Prekeris, R. (2005). The FIP3-Rab11 protein complex regulates recycling endosome targeting to the cleavage furrow during late cytokinesis. Mol. Biol. Cell 16, 849–860.

Witman, G. B. (1993). Chlamydomonas phototaxis. Trends Cell Biol. 3, 403–408.

Wong, S. T., Trinh, K., Hacker, B., Chan, G. C., Lowe, G., Gaggar, A., Xia, Z., Gold, G. H., and Storm, D. R. (2000). Disruption of the type III adenylyl cyclase gene leads to peripheral and behavioral anosmia in transgenic mice. Neuron 27, 487–497.

Wu, S., Mehta, S. Q., Pichaud, F., Bellen, H. J., and Quiocho, F. A. (2005). Sec15 interacts with Rab11 via a novel domain and affects Rab11 localization in vivo. Nat. Struct. Mol. Biol. 12, 879–885.

Xiong, B. et al. (2012). Crag is a GEF for Rab11 required for rhodopsin trafficking and maintenance of adult photoreceptor cells. PLoS Biol. 10, e1001438.

Xu, X. Z., Wes, P. D., Chen, H., Li, H. S., Yu, M., Morgan, S., Liu, Y., and Montell, C. (1998). Retinal targets for calmodulin include proteins implicated in synaptic transmission. J. Biol. Chem. 273, 31297–31307.

Yao, C. et al. (2013). Kinase inhibitors arrest neurodegeneration in cell and C. elegans models of LRRK2 toxicity. Hum. Mol. Genet. 22, 328–344.

Yip, C. K., Berscheminski, J., and Walz, T. (2010). Molecular architecture of the TRAPPII complex and implications for vesicle tethering. Nat. Struct. Mol. Biol. 17, 1298–1304.

Yoder, B. K., Hou, X., and Guay-Woodford, L. M. (2002). The polycystic kidney disease proteins, polycystin-1, polycystin-2, polaris, and cystin, are co-localized in renal cilia. J. Am. Soc. Nephrol. 13, 2508–2516.

Yoshiba, S. et al. (2012). Cilia at the node of mouse embryos sense fluid flow for left-right determination via Pkd2. Science 338, 226–231.

Yoshimura, S.-I., Egerer, J., Fuchs, E., Haas, A. K., and Barr, F. A. (2007). Functional dissection of Rab GTPases involved in primary cilium formation. J. Cell Biol. 178, 363–369.

Yoshimura, S.-I., Gerondopoulos, A., Linford, A., Rigden, D. J., and Barr, F. A. (2010). Family-wide characterization of the DENN domain Rab GDP-GTP exchange factors. J. Cell Biol. 191, 367–381.

Yuan, S., Zhao, L., Brueckner, M., and Sun, Z. (2015). Intraciliary Calcium Oscillations Initiate Vertebrate Left-Right Asymmetry. Curr. Biol. 25, 556–567.

Zariwala, M. A. et al. (2006). Mutations of DNAI1 in primary ciliary dyskinesia - Evidence of founder effect in a common mutation. Am. J. Respir. Crit. Care Med. 174, 858–866.

Zeng, J. et al. (1999). Identification of a putative effector protein for rab11 that participates in transferrin recycling. Proc. Natl. Acad. Sci. U.S.a. 96, 2840–2845.

Zerial, M., and McBride, H. (2001). Rab proteins as membrane organizers. Nat. Rev. Mol. Cell Biol. 2, 107–117.

Zhang, X.-M., Ellis, S., Sriratana, A., Mitchell, C. A., and Rowe, T. (2004). Sec15 is an effector for the Rab11 GTPase in mammalian cells. J. Biol. Chem. 279, 43027–43034.

Zhang, X.-M., Walsh, B., Mitchell, C. A., and Rowe, T. (2005). TBC domain family, member 15 is a novel mammalian Rab GTPase-activating protein with substrate preference for Rab7. Biochem. Biophys. Res. Commun. 335, 154–161.

Zimmermann, K. W. (1898). Beiträge zur Kenntniss einiger Drüsen und Epithelien. Archiv Für Mikroskopische Anatomie.

Zuo, X., Guo, W., and Lipschutz, J. H. (2009). The exocyst protein Sec10 is necessary for primary ciliogenesis and cystogenesis in vitro. Mol. Biol. Cell 20, 2522–2529.